Ministry of Education and Science of the Russian Federation
Saint Petersburg National Research University of Information Technologies, Mechanics, and Optics

NANOSYSTEMS:

PHYSICS, CHEMISTRY, MATHEMATICS

2015, volume 6(5)

Наносистемы: физика, химия, математика

2015, том 6, № 5

NANOSYSTEMS:

PHYSICS, CHEMISTRY, MATHEMATICS

ADVISORY BOARD MEMBERS

Chairman: V.N. Vasiliev *(St. Petersburg, Russia)*,
V.M. Ievlev *(Voronezh)*, P.S. Kop’ev*(St. Petersburg, Russia)*,
V.N. Parmon *(Novosibirsk)*, A.I. Rusanov *(St. Petersburg, Russia)*.

EDITORIAL BOARD

Editor-in-Chief: N.F. Morozov *(St. Petersburg, Russia)*
Deputy Editor-in-Chief: I.Yu. Popov *(St. Petersburg, Russia)*

Section Co-Editors:
Physics – V.M. Uzdin *(St. Petersburg, Russia)*,
Chemistry, material science –V.V. Gusarov *(St. Petersburg, Russia)*,
Mathematics – I.Yu. Popov *(St. Petersburg, Russia)*.

Editorial Board Members:
V.M. Adamyan *(Odessa, Ukraine)*; O.V. Al’myasheva *(St. Petersburg, Russia)*; A.P. Alodjants *(Vladimir, Russia)*; S. Bechta *(Stockholm, Sweden)*; J. Behrndt *(Graz, Austria)*; M.B. Belonenko *(Volgograd, Russia)*; V.G. Bespalov *(St. Petersburg, Russia)*; J. Brasche *(Clausthal, Germany)*; A. Chatterjee (*Hyderabad, India)*; S.A. Chivilikhin *(St. Petersburg, Russia)*; A.V. Chizhov *(Dubna, Russia)*; A.N. Enyashin *(Ekaterinburg, Russia)*, P.P. Fedorov *(Moscow, Russia)*; E.A. Gudilin *(Moscow, Russia)*; V.K. Ivanov *(Moscow, Russia)*, H. Jónsson *(Reykjavik, Iceland)*; A.A. Kiselev *(Madison, USA)*; Yu.S. Kivshar *(Canberra, Australia)*; S.A. Kozlov *(St. Petersburg, Russia)*; P.A. Kurasov *(Stockholm, Sweden)*; A.V. Lukashin *(Moscow, Russia)*; V.A. Margulis *(Saransk, Russia)*; I.V. Melikhov *(Moscow, Russia)*; G.P. Miroshnichenko *(St. Petersburg, Russia)*; I.Ya. Mittova *(Voronezh, Russia)*; H. Neidhardt *(Berlin, Germany)*; K. Pankrashkin *(Orsay, France)*; B.S. Pavlov *(Auckland, New Zealand)*; A.V. Ragulya *(Kiev, Ukraine)*; V. Rajendran *(Tamil Nadu, India)*; A.A. Rempel *(Ekaterinburg, Russia)*; V.Ya. Rudyak *(Novosibirsk, Russia)*; D Shoikhet *(Karmiel, Israel)*; P Stovicek *(Prague, Czech Republic)*; V.M. Talanov *(Novocherkassk, Russia)*; A.Ya. Vul’ *(St. Petersburg, Russia)*; V.A. Zagrebnov *(Marseille, France)*.

Editors:
I.V. Blinova; A.I. Popov; A.I. Trifanov; E.S. Trifanova *(St. Petersburg, Russia)*,
R. Simoneaux *(Philadelphia, Pennsylvania, USA)*.

Address: University ITMO, Kronverkskiy pr., 49, St. Petersburg 197101, Russia.
Phone: +7(812)232-67-65, **Journal site:** http://nanojournal.ifmo.ru/,
E-mail: popov1955@gmail.com

AIM AND SCOPE

The scope of the journal includes all areas of nano-sciences. Papers devoted to basic problems of physics, chemistry, material science and mathematics inspired by nanosystems investigations are welcomed. Both theoretical and experimental works concerning the properties and behavior of nanosystems, problems of its creation and application, mathematical methods of nanosystem studies are considered.

The journal publishes scientific reviews (up to 30 journal pages), research papers (up to 15 pages) and letters (up to 5 pages). All manuscripts are peer-reviewed. Authors are informed about the referee opinion and the Editorial decision.

Content

MATHEMATICS

PHYSICS

CHEMISTRY AND MATERIAL SCIENCE

NANOSYSTEMS: PHYSICS, CHEMISTRY, MATHEMATICS, 2015, 6 (5), P. 611–617

Waveguide bands for a system of macromolecules

V. M. Adamyan[1], I. V. Blinova[2], A. I. Popov[2], I. Yu. Popov[2]

[1] Odessa I. I. Mechnikov National University, Dvoryanskaya str., 2, Odessa, 65082, Ukraine

[2] ITMO University, Kronverkskiy, 49, Saint Petersburg, 197101, Russia

popov1955@gmail.com

PACS 72.80.Le; 03.65 Nk **DOI 10.17586/2220-8054-2015-6-5-611-617**

A system of parallel chain-type macromolecules (linear polymers) is considered. The spectrum of an electron in such a system is described. Waveguide bands are shown to be present, ensuring conductivity. Consideration is undertaken within the framework of a zero-range potentials model based on the theory of self-adjoint extensions of symmetric operators. Possible applications also discussed.

Keywords: spectrum, linear polymer, zero-range potential.

Received: 15 September 2015

Revised: 25 September 2015

1. Introduction

This paper deals with the theoretical investigation of a nanosystem which can be used for the creation of optically controlled magnetoresistance. The possibilities for this type of control were outlined in [1]. Layered structures having magnetic layers and a spacer filled with conducting polymer (linear molecules) with inserted banana-shaped photosensitive molecules were suggested to be used for this purpose. Linear polymeric molecules should ensure electronic conductivity between the magnetic layers. In the present paper, we investigate the electronic band structure for a system of linear molecules.

Consider an infinite periodic chain of impurity atoms placed along some line (let it be the axis OX) between two nanolayers (magnetic). We use the effective mass approximation, i.e. we take into account the influence of the nanolayers by changing the effective mass of the electron in the spacer (see, e.g., [2]). In chosen coordinate system, the position of $n-$th atom of the chain $(n = 0, \pm 1, \pm 2, \ldots)$ is given by a vector $n\mathbf{a} = (na, 0, 0)$, where a is the chain period. A simple but less accurate quantum graph model of such systems (see, e.g., [3, 4]) is used more often. To compute the energy spectrum of the chain, we use the zero-range potentials model. We mention that the spectrum for chain structures in $\mathbb{R}^3$ can be rather unusual (see, e.g., [5]), but in our periodic case it has a defined band structure. As for zero-range potentials, the background for the model is formed by the theory of self-adjoint extensions of symmetric operators (see, e.g., [6, 7]). Namely, one starts from a self-adjoint operator – the Laplacian in $L_2(\mathbb{R}^3)$ with the domain $W_2^2(\mathbb{R}^3)$. Here W_2^2 is the Sobolev space. Let us restrict the operator to the set of smooth functions which vanish at points $p_n = |\mathbf{r} - n\mathbf{a}|\,; \quad n = 0, \pm 1, \ldots$. The closure of this restricted operator is a symmetric operator with infinite deficiency indices. To construct a self-adjoint extension, it is more convenient to deal with the corresponding restriction of the adjoint operator. There are several ways to describe extensions, e.g., boundary triplets method ([8, 9], von Neumann formulas ([10]), Krein resolvent formula ([11, 12]). We will use here a variant of the second approach which allows one, in the case of semi-boundedness of the Hamiltonian, to present an element from the domain of the adjoint operator in the following form:

$$\psi(\mathbf{r}) = \psi_0(x) + \sum_{m=-\infty}^{\infty} C_m \cdot \frac{e^{-ik_0|\mathbf{r}-m\mathbf{a}|}}{4\pi\,|\mathbf{r}-m\mathbf{a}|}, \tag{1}$$

where ψ_0 belongs to the domain of the Friedrichs extension of the initial symmetric operator, C_m is some constant, $k_0 = \sqrt{\lambda_0}$, λ_0 is a regular value of the spectral parameter (particularly, one can choose real negative value of λ_0, $\Im k_0 > 0$). To explain the choice of extension, it is convenient to consider the simplest case of a single point-like potential (at $\mathbf{r} = 0$). In this case, one has the symmetric operator with the deficiency indices $(1, 1)$. The domain of the adjoint operator (A^*) consists of the following elements (compare with (1)):

$$\psi(\mathbf{r}) = \psi_0(x) + C_0 \frac{e^{-ik_0|\mathbf{r}|}}{4\pi\,|\mathbf{r}|}.$$

To construct a self-adjoint extension, one calculates the boundary form for elements ψ, ϕ from the domain of the adjoint operator:

$$(A^*\psi, \phi) - (\psi, A^*\phi) = \psi_0(0)\overline{C_0^{\phi}} - \overline{\phi_0(0)}C_0^{\psi}.$$

Evidently, one gets a self-adjoint extension (annihilation of this form) if there is the following relation between $\psi_0(0)$ and C_0^{ϕ}:

$$\psi_0(0) = b \quad C_0^{\psi}, \Im b = 0. \tag{2}$$

Formally, the condition (2) takes the form of a "boundary condition" at the point:

$$\lim_{|\mathbf{r}|\to 0} \left[\frac{\partial}{\partial\,|\mathbf{r}|} - b\right] |\mathbf{r}|\,\Psi = 0. \tag{3}$$

One often rewrites condition (3) as a condition for the logarithmic derivative:

$$\lim_{|\mathbf{r}|\to 0} \frac{1}{|\mathbf{r}|\,\Psi} \frac{\partial}{\partial\,|\mathbf{r}|}(|\mathbf{r}|\,\Psi) = b. \tag{4}$$

For the case of the periodic chain, one has:

$$\lim_{p_n\to 0} \left[\frac{\partial}{\partial p_n} - b\right] p_n\Psi = 0, \tag{5}$$

$$p_n = |\mathbf{r} - \mathbf{na}|; \quad n = 0, \pm 1, \ldots$$

Below we will use this form of the condition.

2. Two chains

Consider the spectral problem for two parallel chains of zero-range potentials in $\mathbb{R}^3$. We assume that centers of the chains are shifted by vector $\mathbf{g} = (g_1, g_2, 0)$. The first chain has centers at points $n\mathbf{a} = na\mathbf{e_1}$, the second chain - at points $n\mathbf{a} + \mathbf{g} = (na + g_1)\,\mathbf{e_1} + g_2\mathbf{e_2}$; $n = 0, \pm 1, \pm 2, \ldots$; $\mathbf{e_1}, \mathbf{e_2}$ are unit vectors of axis X and axis Y, correspondingly. The Green function for the operator with point-like potentials has the form:

$$G(\mathbf{r}, \mathbf{r}', E) = \frac{1}{4\pi} \frac{\exp\left[is\,|\mathbf{r}-\mathbf{r}'|\right]}{|\mathbf{r}-\mathbf{r}'|} +$$

$$\sum_{n=-\infty}^{+\infty} \left\{ C_n^{(1)} \frac{\exp\left[is\,|\mathbf{r}-n\mathbf{a}|\right]}{|\mathbf{r}-n\mathbf{a}|} + C_n^{(2)} \frac{\exp\left[is\,|\mathbf{r}-n\mathbf{a}-\mathbf{g}|\right]}{|\mathbf{r}-n\mathbf{a}-\mathbf{g}|} \right\}.$$

Coefficients $C_n^{(1)}$, $C_n^{(2)}$ are determined for the system given by conditions (5), which gives one the following system after the Fourier transform:

$$\begin{aligned} D(k,s)\,\xi_k^{(1)} + Q(k,s)\,\xi_k^{(2)} &= \varphi_k(\mathbf{r}') \\ \overline{Q(k,s)}\xi_k^{(1)} + D(k,s)\,\xi_k^{(2)} &= \varphi_k(\mathbf{r}') \end{aligned}$$

where

$$\xi_k^{(j)} = \sum_n C_n^{(j)} e^{ikna}; \quad j = 1, 2,$$

$$\varphi_k(\mathbf{r}) = -\frac{1}{4\pi}\sum_n \frac{\exp\left[is\left|\mathbf{r} - n\mathbf{a}\right| + ikna\right]}{\left|\mathbf{r} - n\mathbf{a}\right|}$$

$$D(k,s) = \sum_{n\neq 0} \tfrac{\exp[is|n|a + ikna]}{|n|a} + is - b$$

$$Q(k,s) = \sum_n \tfrac{\exp\left[is\left|n\vec{a} - \mathbf{g}\right| + ikna\right]}{|n\mathbf{a} - \mathbf{g}|}$$

Hence,

$$\begin{aligned} \xi_k^{(1)} &= \tfrac{1}{2}\left\{\tfrac{\varphi_k(\mathbf{r}') + \chi\varphi_k(\mathbf{r}' - \mathbf{g})}{D(k,s) + |Q(k,s)|} + \tfrac{\varphi_k(\mathbf{r}') - \chi\varphi_k(\mathbf{r}' - \mathbf{g})}{D(k,s) - |Q(k,s)|}\right\} \\ \xi_k^{(2)} &= \tfrac{\overline{\chi}}{2}\left\{\tfrac{\varphi_k(\mathbf{r}') + \chi\varphi_k(\mathbf{r}' - \mathbf{g})}{D(k,s) + |Q(k,s)|} - \tfrac{\varphi_k(\mathbf{r}') - \chi\varphi_k(\mathbf{r}' - \mathbf{g})}{D(k,s) - |Q(k,s)|}\right\} \end{aligned}$$

where

$$\chi = \chi(k,s) = \frac{Q(k,s)}{|Q(k,s)|}$$

Returning from $\xi_k^{(i)}$ to coefficients $C_n^{(i)}$ using formulas:

$$C_n^{(i)} = \frac{a}{2\pi}\int\limits_{-\pi/a}^{+\pi/a} \xi_k^{(i)} e^{-ikna} dk,$$

one obtains the following expression for the Green function:

$$G(\mathbf{r}, \mathbf{r}', E) = G_0(\mathbf{r} - \mathbf{r}', E) - a\int\limits_{-\pi/a}^{+\pi/a} dk \sum_{n,n'} \frac{\exp\left[-ik(n - n')a\right]}{D(k,s) + |Q(k,s)|}\times$$

$$\times\left[G_0(\mathbf{r} - n\mathbf{a}, E) + \overline{\chi}G_0(\mathbf{r} - n\mathbf{a} - \mathbf{g}, E)\right]\left[G_0(n\mathbf{a} - \mathbf{r}', E) + \chi G_0(n\mathbf{a} + \mathbf{g} - \mathbf{r}', E)\right]$$

$$-a\int\limits_{-\pi/a}^{+\pi/a} dk \sum_{n,n'} \frac{\exp\left[-ik(n - n')a\right]}{D(k,s) - |Q(k,s)|}\times$$

$$\times\left[G_0(\mathbf{r} - n\mathbf{a}, E) - \overline{\chi}G_0(\mathbf{r} - n\mathbf{a} - \mathbf{g}, E)\right]\left[G_0(n\mathbf{a} - \mathbf{r}', E) - \chi G_0(n\mathbf{a} + \mathbf{g} - \mathbf{r}', E)\right] \qquad (6)$$

where

$$G_0(\mathbf{r}, E) = \frac{e^{isr}}{4\pi r}$$

Expression (6) shows that two localized waveguide bands can appear near the chains. The dispersion law for one band is determined by roots of $D(k,s) + |Q(k,s)|$ of the second band - by $D(k,s) - |Q(k,s)|$. The corresponding wave functions have the forms:

$$\varphi_\pm(k, \mathbf{r}) =$$

$$\left[\frac{d}{dE}\left(D(k,s) \pm |Q(k,s)|\right)\right]_{E=\varepsilon_\pm(k)}^{-1/2}$$

$$\sum_n \exp\left(-ikna\right)\left[G_0\left(\mathbf{r}-n\mathbf{a},E\right) \pm \overline{\chi} G_0\left(\mathbf{r}-n\mathbf{a}-\mathbf{g},E\right)\right]_{E=\varepsilon_\pm(k)}$$

where $\varepsilon_\pm(k)$ is determined from the equations:

$$D\left(k,\sqrt{\frac{2\mu E_\pm}{h^2}}\right) \pm \left|Q\left(k,\sqrt{\frac{2\mu E_\pm}{h^2}}\right)\right| = 0 \tag{7}$$

Consider the particular case for which the distance between the chains g_2 is greater than the distance between neighboring centers of one chain. Let us find the approximate expression for function $Q(k,s)$ if $s = i\chi$, χ is real. Using the formula:

$$\frac{e^{-\chi\Delta}}{\Delta} = \frac{1}{\pi}\int_{-\infty}^{+\infty}\frac{e^{ip\Delta}dp}{p^2+\Delta^2},$$

one transforms the expression for $Q(k,i\chi)$ to the following form:

$$Q(k,i\chi) = \frac{1}{\pi}\sum_{n=-\infty}^{+\infty} e^{ikna}\int_{-\infty}^{+\infty}\frac{e^{i\xi\chi}d\xi}{\xi^2+(na-g_1)^2+g_2^2} =$$

$$\frac{1}{\pi}\int_{-\infty}^{+\infty} e^{i\xi\chi}\left(\sum_{n=-\infty}^{+\infty}\frac{e^{ikna}}{\xi^2+(na-g_1)^2+g_2^2}\right)d\xi$$

If $0 \leqslant ka < \pi$ then:

$$\sum_{n=-\infty}^{+\infty}\frac{e^{ikna}}{\alpha^2+(na-\beta)^2} =$$

$$-\frac{\pi}{2a\alpha}\left\{\left[cth\left[\frac{\pi}{a}(\beta-i\alpha)\right]-i\right]\exp\left[ik(\beta+i\alpha)\right]-\left[cth\left[\frac{\pi}{a}(\beta-i\alpha)\right]-i\right]\exp\left[ik(\beta-i\alpha)\right]\right\}$$

for $\alpha > 0$. However, for $\alpha \to 0$:

$$\sum_{n=-\infty}^{+\infty}\frac{e^{ikna}}{\alpha^2+(na-\beta)^2} \simeq$$

$$\frac{\pi\exp(ik\beta)}{a\alpha}\left[\exp(-k\alpha)-\exp(k\alpha)\exp\left[-\frac{2\pi}{a}(\alpha+\beta)\right]\right].$$

for $\alpha \to 0$.

Hence,

$$Q(k,i\chi) \approx \frac{e^{ikg_1}}{a}\int_{-\infty}^{+\infty}\frac{e^{i\xi\chi}}{\sqrt{\xi^2+g_2^2}}\left[e^{-k\sqrt{\xi^2+g_2^2}}-e^{-2\pi g_1/a}e^{(k-2\pi/a)\sqrt{\xi^2+g_1^2}}\right]d\xi =$$

$$= \frac{e^{ikg_1}}{a}\int_{-\infty}^{+\infty}\frac{e^{i\eta\chi g_2}}{\sqrt{1+\eta^2}}\left[e^{-kg_2\sqrt{1+\eta^2}}-e^{-2\pi g_1/a}e^{(k-2\pi/a)g_2\sqrt{1+\eta^2}}\right]d\eta \tag{8}$$

The last integral in (8) can be transformed to the integral over the curve which comprises the half-axis (i, i_∞) in upper half-plane. Thus,

$$Q(k,i\chi) \approx \frac{2e^{ikg_1}}{a}\int_{1}^{\infty}\frac{e^{-\theta\chi g_2}}{\sqrt{\theta^2-1}}\left[\cos(kg_2)\sqrt{\theta^2-1}-e^{-2\pi g_1/a}\cos\left(\left(\frac{2\pi}{a}-k\right)g_2\sqrt{\theta^2-1}\right)\approx\right]$$

$$\approx \sqrt{\frac{2\pi}{g_2}}\frac{e^{ikg_1-kg_2}}{a}\left\{\frac{\sqrt{\chi+\sqrt{\chi^2+2k^2}}}{\sqrt{\chi^2+2k^2}}-e^{i2\pi g_1/a}\frac{\sqrt{\chi+\sqrt{\chi^2+2\left(2\pi/a-k\right)^2}}}{\sqrt{\chi^2+2\left(2\pi/a-k\right)^2}}\right\} \tag{9}$$

Substituting (9) into (7) one determines the value of the waveguide band splitting caused by the existence of the second chain. Taking into account the smallness of $\left|Q\left(,i\chi\right)\right|$ for sufficiently remote chains, one finds that the level $\varepsilon_0\left(k\right)$ of single chain is split in the following manner:

$$\varepsilon_{\pm}\left(k\right)=\varepsilon_0\left(k\right)\pm\frac{hd\sqrt{2\left|\varepsilon_0\left(k\right)\right|}}{\sqrt{\mu}\sqrt{\left(d+\cos\left(ka\right)\right)^2-1}}\left|Q\left(k,\frac{i}{h}\sqrt{2\mu\left|\varepsilon_0\left(k\right)\right|}\right)\right|$$

A gap in the waveguide band can appear if the top of the band $\varepsilon_-\left(k\right)$, i.e. $\varepsilon_-\left(\pi/a\right)$ is greater than the bottom $\varepsilon_+\left(0\right)$ of the band $\varepsilon_+\left(k\right)$, i.e. if $\varepsilon_-\left(\pi/a\right)<\varepsilon_+\left(0\right)$.

3. The case of many chains

We now consider the system of $M-1$ $\left(M=2,3,...\right)$ parallel identical chains. Let the position of centers be given by vectors $n\mathbf{a_1}+m\mathbf{a_2}$, $n,m-$ integer. In the framework of the zero-range potential approach, the wave function of the electron is $\Psi\left(\mathbf{r}\right)$:

$$\lim_{p_{nm}\to 0}\left[\frac{\partial}{\partial p_{nm}}-b\right]p_{nm}\Psi=0, \tag{10}$$

where $p_{nm}=\left|\mathbf{r}-n\mathbf{a_1}-m\mathbf{a_2}\right|$. We will seek the perturbed Green function $G\left(\mathbf{r},\mathbf{r}',E\right)$ for $\Im E>0$ in the following form:

$$G\left(\mathbf{r},\mathbf{r}',E\right)=G_0\left(\mathbf{r}-\mathbf{r}',E\right)+4\pi\sum_{n,m}C_{nm}G_0\left(\mathbf{r}-n\mathbf{a_1}-m\mathbf{a_2},E\right),$$

where $G_0(\mathbf{r},E)$ is the Green function for free space. Conditions (10) gives one a system for coefficients C_{nm}:

$$\left(is-b\right)C_{nm}+\sum_{n'\neq n,m'\neq m}C_{n'm'}\frac{\exp\left[is\left|\left(n-n'\right)\mathbf{a_1}+\left(m-m'\right)\overrightarrow{a_2}\right|\right]}{\left|\left(n-n'\right)\mathbf{a_1}+\left(m-m'\right)\mathbf{a_2}\right|}=\varphi_{nm}\left(\mathbf{r}'\right),$$

where

$$\varphi_{nm}\left(\mathbf{r}'\right)=-\frac{1}{4\pi}\frac{\exp\left[is\left|\mathbf{r}'-n\mathbf{a_1}-m\mathbf{a_2}\right|\right]}{\left|\mathbf{r}'-n\mathbf{a_1}-m\mathbf{a_2}\right|}.$$

The prime sign near the sum means that it is sufficient to satisfy only one from the conditions $n'\neq n$ or $m\neq m'$. ,,To simplify formulas for C_{nm}, we assume that $\left|C_{n,m\pm p}\right|\ll\left|C_{n,m\pm 1}\right|$ for $p>1$. Then, after the Fourier transform along the chain, one obtains:

$$D\left(k,s\right)\xi_m\left(k\right)+D_1\left(k,s\right)\left[\xi_{m+1}\left(k\right)+\xi_{m-1}\left(k\right)\right]=\eta_m\left(k,\mathbf{r}'\right), \tag{11}$$

where

$$\xi_m\left(k\right)=\sum_n C_{nm}\exp\left(ikna\right),$$

$$D\left(k,s\right)=\frac{1}{a}\ln\frac{d}{\cos\left(a_1 s\right)-\cos\left(a_2 k\right)},$$

$$D_1\left(k,s\right)=\sum_{n=-\infty}^{+\infty}\frac{\exp\left[is\left|n\mathbf{a_1}+\mathbf{a_2}\right|+ikna_1\right]}{\left|n\mathbf{a_1}+\mathbf{a_2}\right|}, \tag{12}$$

$$\eta_m\left(k,\mathbf{r}'\right) = -\frac{1}{4\pi}\sum_n \varphi_{nm}\left(\mathbf{r}'\right)\exp\left(ikna\right).$$

The dispersion equation is obtained from the solvability condition for the following homogeneous difference equation:

$$D\xi_m + D_1\left(\xi_{m+1}+\xi_{m-1}\right) = 0. \tag{13}$$

The solution of (13) has the form:

$$\xi_m\left(k\right) = \Xi_1\left(k\right)\cos\left(k_2 m a_2\right) + \Xi_2\left(k\right)\sin\left(k_2 m a_2\right).$$

The range for k_2 and value of Ξ_1 (for $M-1$ chains) are determined from the boundary conditions $C_{n0} = C_{nM} = 0$. Consequently, $\xi_0\left(k\right) = \xi_M\left(k\right) = 0$, $\Xi_1\left(k\right) = 0$ and

$$k_2 = \pi l/\left(M a_2\right); \quad l = 1, 2, \ldots, M-1.$$

If one inserts the solution:

$$\xi_m\left(k\right) = \Xi\left(k\right)\sin\left(\pi m l/M\right),$$

into (11), the dispersion equation is obtained:

$$D\left(k,s\right) + 2D_1\left(k,s\right)\cos\left(\pi l/M\right) = 0. \tag{14}$$

Waveguide bands are given by the solution $s = i\chi$, $\chi > 0$, of (14). Taking into account (12), one reduces (14) to the following form:

$$cosh\left(a_1\chi\right) = \cos\left(a_1 k\right) + d_1\left(\chi,l\right), \tag{15}$$

where $d_1\left(\chi,l\right) = d\exp\left[2a_1 D_1\cos\left(\pi l\right)/M\right]$, or, correspondingly, to the form:

$$E_1\left(k\right) = -\frac{h^2}{2\mu a_1}\left\{\ln\left[d_1\left(\chi,l\right)+\cos\left(a_1 k\right)+\sqrt{\left[d_1\left(\chi,l\right)+\cos\left(a_1 k\right)\right]^2-1}\right]\right\}^2,$$

where $E_1\left(k\right) = -\frac{h^2\chi^2}{2\mu}$. Note that for small k, χ, one can replace the sum for D_1 from (12) by the integral:

$$D_1 \approx \int\limits_{-\infty}^{+\infty}\frac{\exp\left[-\chi\left|\nu\mathbf{a_1}+\mathbf{a_2}\right|+ik\nu a_1\right]}{\left|\nu\mathbf{a_1}+\mathbf{a_2}\right|}d\nu = \frac{2}{a_1}K_0\left(\sqrt{\left(\chi a_1\right)^2+\left(k a_2\right)^2}\right),$$

where $K_0\left(z\right)$ is the Macdonald function of zero order. Due to the integer parameter l, equation (15) determines, generally speaking, $M-1$ waveguide bands. The conductivity is determined by such bands which are empty or partially filled, i.e. contain the Fermi level E_F. If each atom of the chain has one "free" electron, then the Fermi level E_F is determined from the equation:

$$\frac{\pi\left(M-1\right)}{2a_1} = \sum_{l=1}^{M-1}\int\limits_{E_0}^{E_F}\frac{dk}{dE}dE. \tag{16}$$

Taking into account (15), one rewrites (16) in the form:

$$\frac{\pi}{2a_1} = \frac{1}{M-1}\sum_{l=1}^{M-1}\int\limits_{\chi_0}^{\chi_F}\frac{sh\left(\chi a_1\right)-d_1'\left(\chi,l\right)}{\sqrt{1-\left[ch\left(\chi a_1\right)-d_1\right]^2}}d\chi, \tag{17}$$

where $d'_1(\chi, l) = \frac{\partial d_1(\chi,l)}{\partial(\chi a_1)}$. If one ignores the difference between $d_1(\chi, l)$ and d, then equation (17) gives one the following value of the Fermi level:

$$E_F^0 = -\frac{h^2}{2\mu a_1^2}\ln^2\left[d + \sqrt{d^2-1}\right],$$

which corresponds to the case of single chain.

Acknowledgments

This work was partially financially supported by the Government of the Russian Federation (grant 074-U01), by Ministry of Science and Education of the Russian Federation (GOSZADANIE 2014/190, Projects No 14.Z50.31.0031 and No. 1.754.2014/K), by grant MK-5001.2015.1 of the President of the Russian Federation, and by grant of St. Petersburg.

References

[1] I.Yu. Popov. On the possibility of magnetoresistance governed by light. *Nanosystems: Phys. Chem. Math.*, 2013, **4**(6), P. 795–799.

[2] U. Wulf, M. Krahlisch, J. Kucera, H. Richter, J. Hontschel. A quantitative model for quantum transport in nano-transistors. *Nanosystems: Phys. Chem. Math.*, 2013, **4**(6), P. 800–809.

[3] I. S. Lobanov, A. I. Trifanov, E. S. Trifanova. Genetic algorithm for constructing graphene nanoribbon with given electronic transport properties. *Nanosystems: Phys. Chem. Math.*, 2013, **4**(4), P. 512–523.

[4] I.Yu.Popov, A.N.Skorynina, I.V.Blinova. On the existence of point spectrum for branching strips quantum graph. *J. Math. Phys.*, 2014, **55**, 033504/1-20.

[5] A.A.Boitsev, I.Yu.Popov, O.V.Sokolov. Hamiltonian with zero-range potentials having infinite number of eigenvalues. *Nanosystems: Phys. Chem. Math.*, 2012, **3**(4), P. 9–19.

[6] S.Albeverio, F.Gesztesy, R.Hoegh-Krohn, H.Holden with an appendix by P.Exner 2005 *Solvable Models in Quantum Mechanics: Second Edition.* (Providence, R.I.: AMS Chelsea Publishing)

[7] B.S.Pavlov, Extensions theory and explicitly solvable models. *Uspekhi. Mat. Nauk.*, 1987, 42(6), P. 99–131.

[8] J.Berndt , M. M. Malamud, H. Neidhardt. Scattering matrices and Weyl functions. *Proc. London Math. Soc.*, 2008, **97**(3), P. 568–598.

[9] A.A. Boitsev, H. Neidhardt, I.Yu. Popov. Weyl function for sum of operators tensor products. *Nanosystems: Phys. Chem. Math.*, 2013, **4**(6), P. 747–759.

[10] M. S. Birman, M. Z. Solomyak. *Spectral Theory of Self-Adjoint Operators in Hilbert Space* (D. Reidel Publishing Company, Dordrecht-Boston-Lancaster, 1987).

[11] A. Alonso, B. Simon. The Birman-Krein-Vishik theory of selfadjoint extensions of semi-bounded operators. *J. Oper. Theory*, 1980, **4**, P. 251–270.

[12] V.M. Adamyan, B.S. Pavlov. Null-range potentials and M.G. Krein's formula for generalized resolvents. *Journal of Soviet Mathematics*, 1988, **42**(2), P. 1537–1550.

NANOSYSTEMS: PHYSICS, CHEMISTRY, MATHEMATICS, 2015, 6 (5), P. 618–627

On positive solutions of the homogeneous Hammerstein integral equation

Yu. Kh. Eshkabilov, F. H. Haydarov

National University of Uzbekistan, Tashkent, Uzbekistan

yusup62@mail.ru, haydarov_imc@mail.ru

PACS 02.30.Rz **DOI 10.17586/2220-8054-2015-6-5-618-627**

In this paper the existence and uniqueness of positive fixed points operator for a nonlinear integral operator are discussed. We prove the existence of a finite number of positive solutions for the Hammerstein type of integral equation. Obtained results are applied to the study of Gibbs measures for models on a Cayley tree.

Keywords: integral equation of Hammerstein type, fixed point of operator, Gibbs measure, Cayley tree.

Received: 2 April 2015

Revised: 18 July 2015

1. Introduction

It is well known that integral equations have wide application in engineering, mechanics, physics, economics, optimization, vehicular traffic, biology, queuing theory and so on (see [1–5]). The theory of integral equations is rapidly developing with the help of tools in functional analysis, topology and fixed point theory. Therefore, many different methods are used to obtain the solution of the nonlinear integral equation. Moreover, some methods can be found in Refs. [6–13], to discuss and obtain a solution for the Hammerstein integral equation. In [11], J.Appell and A.S. Kalitvin used fixed point methods and methods of nonlinear spectral theory to obtain a solution for integral equations of the Hammerstein or Uryson type. The existence of positive solutions of abstract integral equations of Hammerstein type is discussed in [9]. In [7], M.A. Abdou, M.M. El-Borai and M.M. El-Kojok discuss the existence and uniqueness of a solution for the nonlinear integral equation of the Hammerstein type with a discontinuous kernel.

In this present paper, we study the solvability of an homogeneous integral equation of the Hammerstein type. An integral equation of the form:

$$\int_0^1 K(t,u)\Psi\left(t,f(u)\right)du = f(t), \tag{1.1}$$

is called the homogeneous Hammerstein integral equation, where $K(t,u)$ is continuous real-valued function defined on $0 \le t \le 0$, $0 \le u \le 1$, $\Psi : [0,1] \times \mathbb{R} \to \mathbb{R}$ is a continuous function and $f(t)$ is unknown function from $C[0,1]$.

Let $\Psi(t,z)$, $\dfrac{\partial}{\partial z}\Psi(t,z)$ be continuous and bounded for $t \in [0,1]$ and for all z. Then [14], the Hammerstein integral equation (1.1) has a solution, assuming that $\Psi(t,z)$ is a bounded continuous function for $t \in [0,1]$ and $z \in \mathbb{R}$. In this case, the Hammerstein integral equation (1.1) also has a solution [15]. For the necessary details of this theorem and for more results on the Hammerstein integral equation, we refer to Petryshyn and Fitzpatrik [16], Browder [17], Brezis and Browder [18].

Recently, the case $\Psi(t,z) = \Psi(z)$ was considered [19]. Let $\Psi(z)$ be a monotonous left-continuous function on $[0,+\infty)$ and $\lim\limits_{x\to 0}\dfrac{\Psi(z)}{z} = +\infty$, $\lim\limits_{x\to+\infty}\dfrac{\Psi(z)}{z} = 0$. Then, the integral equation of Hammerstein type (1.1) has a solution [19].

In this work, we will consider the following integral equation of Hammerstein type (i.e. in (1.1) $\Psi(t,z) = \Psi(z) = z^{\vartheta}$):

$$\int\limits_0^1 K(t,u)f^{\vartheta}(u)du = f(t),\ \ \vartheta > 1, \tag{1.2}$$

on the $C[0,1]$, where $K(t,u)$ is a strictly positive continuous function.

By Theorem 44.8 from [4], the existence of a nontrivial positive solution for the Hammerstein equation (1.2) follows. We study the problem of the existence of a finite number of positive solutions for the integral equation of the Hammerstein type (1.2).

Consider the nonlinear operator R_α on the cone of positive continuous functions on $[0,1]$:

$$\left(R_\alpha f\right)(t) = \left(\frac{\int_0^1 K(t,u)f(u)du}{\int_0^1 K(0,u)f(u)du}\right)^{\alpha}, \tag{1.3}$$

where $K(t,u)$ is given in the integral equation of Hammerstein type (1.2) and $\alpha > 0$. An operator of the form (1.3) arises in the theory of Gibbs measures (see [20–22]). Positive fixed points of the operator R_k, $k \in \mathbb{N}$ and their numbers are very important to study Gibbs measures for models on a Cayley tree.

In [21], for the case $\alpha = 1$, the uniqueness of positive fixed points of the nonlinear operator R_α (1.3) was proved. In [20], in the case $\alpha = k \in \mathbb{N}$, $k > 1$, for the nonlinear operator R_α, the existence of positive fixed point and the existence Gibbs measure for some mathematical models on a Cayley tree were proved.

The aim of this work is to study the existence of a finite number of positive solutions for the Hammerstein equation (1.2) on the space of continuous functions on $[0,1]$. The plan of this paper is as follows: in the second section, using properties of Hammerstein equation (1.2), we reduce some statements on the positive fixed point of the operator R_α; in the third section, we construct the strictly positive continuous kernel $K(t,u)$, such that, for given $n \in \mathbb{N}$, the corresponding Hammerstein equation (1.2) has n number of positive Solutions; in the fourth section, the obtained results for the operator R_α are applied to study Gibbs measures for models on a Cayley tree.

2. Existence and uniqueness of positive fixed points for the operator R_α

In this section, we study the existence and the uniqueness of positive fixed points for the nonlinear operator R_α (1.3). We set:

$$C^{+}[0,1] = \{f \in C[0,1] : f(x) \geq 0\},\ \ C_0^{+}[0,1] = C^{+}[0,1] \setminus \{\theta \equiv 0\},$$

where the set $C^{+}[0,1]$ is the cone of positive continuous functions on $[0,1]$.

We define the Hammerstein operator H_ϑ on $C[0,1]$ by the equality:

$$H_\vartheta f(t) = \int\limits_0^1 K(t,u)f^{\vartheta}(u)du = f(t),\ \ \vartheta > 1.$$

Clearly, by Theorem 44.8 from [4], we obtain:

Theorem 1. *Let* $\vartheta > 1$. *The equation:*

$$H_\vartheta f = f \tag{2.1}$$

has at least one solution in $C_0^+[0,1]$.

We set:

$$\mathcal{M}_0 = \left\{f \in C^+[0,1] : f(0) = 1\right\}.$$

Lemma 1. *Let* $\alpha > 1$. *The equation*

$$R_\alpha f = f, \ \ f \in C_0^+[0,1] \tag{2.2}$$

has a positive solution iff the Hammerstein operator has a positive eigenvalue, i.e. the Hammerstein equation:

$$H_\alpha g = \lambda g, \ \ f \in C^+[0,1], \tag{2.3}$$

has a positive solution in $\mathcal{M}_0$ *for some* $\lambda > 0$.

Proof. We define the linear operator W and the linear functional ω on the $C[0,1]$ by the following equalities:

$$(Wf)(t) = \int_0^1 K(t,u)f(u)du, \ \ \omega(f) = \int_0^1 K(0,u)f(u)du.$$

Necessariness. Let $f_0 \in C_0^+[0,1]$ be a solution of the equation (2.2). We have:

$$(Wf_0)(t) = \omega(f_0)\sqrt[\alpha]{f_0(t)}.$$

From this equality, we get:

$$(H_\alpha h)(t) = \lambda_0 h(t),$$

where $h(t) = \sqrt[\alpha]{f_0(t)}$ and $\lambda_0 = \omega(f_0) > 0$.

It is easy to see that $h \in \mathcal{M}_0$ and $h(t)$ is an eigenfunction of the Hammerstein's operator H_α, corresponding the positive eigenvalue λ_0.

Sufficiency. Let $h \in \mathcal{M}_0$ be an eigenfunction of the Hammerstein's operator H_α. Then, there is a number $\lambda_0 > 0$ such that $H_\alpha h = \lambda_0 h$. From $h(0) = 1$, we get $\lambda_0 = (H_\alpha h)(0) = \omega(h^\alpha)$. Then:

$$h(t) = \frac{(H_\alpha h)(t)}{\omega(h^\alpha)}.$$

From this equality, we get $R_\alpha f_0 = f_0$ with $f_0 = h^\alpha \in C_0^+[0,1]$. This completes the proof. □

Theorem 2. *The equation (2.2) has at least one solution in* $C_0^+[0,1]$.

Let λ_0 be a positive eigenvalue of the Hammerstein operator H_α, $\alpha > 1$. Then, there exists $f_0 \in \mathcal{M}_0$ such that $H_\alpha f_0 = \lambda_0 f_0$. We take $\lambda \in (0,+\infty)$, $\lambda \neq \lambda_0$. We define function $h_0(t) \in C_0^+[0,1]$ by

$$h_0(t) = \sqrt[\alpha-1]{\frac{\lambda}{\lambda_0}} f_0(t), \ \ t \in [0,1].$$

Then:

$$H_\alpha h_0 = H_\alpha\left(\sqrt[\alpha-1]{\frac{\lambda}{\lambda_0}} f_0\right) = \lambda h_0,$$

i.e. the number λ is an eigenvalue of Hammerstein operator H_α corresponding the eigenfunction $h_0(t)$. This can be easily verified: if the number $\lambda_0 > 0$ is an eigenvalue of the operator

H_α, $\alpha > 1$, then an arbitrary positive number is an eigenvalue of the operator H_α. Therefore, we have:

Lemma 2. *a) Let $\alpha > 1$.The equation $R_\alpha f = f$ has a nontrivial positive solution iff the Hammerstein equation $H_\alpha g = g$ has a nontrivial positive solution.*

Let $\alpha > 1$. We denote by $N_{fix.p}(H_\alpha)$ and $N_{fix.p}(R_\alpha)$ numbers of nontrivial positive solutions of the equations (2.1) and (2.2), respectively.

Theorem 3. *Let $\alpha > 1$. The equality $N_{fix.p}(H_\alpha) = N_{fix.p}(R_\alpha)$ is held.*

We denote:

$$m = \min_{t,u\in[0,1]} K(t,u), \quad M_0 = \max_{u\in[0,1]} K(0,u),$$

$$M = \max_{t,u\in[0,1]} K(t,u), \quad m_0 = \min_{u\in[0,1]} K(0,u).$$

Theorem 4. *Let $\alpha > 1$. If the following inequality holds:*

$$\left(\frac{M}{m}\right)^\alpha - \left(\frac{m}{M}\right)^\alpha < \frac{1}{\alpha},$$

then the homogenous Hammerstein equation (2.1) and the equation (2.2) have a unique non-trivial positive solution.

An analogous theorem was proved for $\alpha = k \in \mathbb{N}, k \geq 2$ in [20] and proof of Theorem 4 is analogously obtained.

3. The existence of a finite number of positive solutions for the homogeneous Hammerstein equation

In this section, for a given $n \in \mathbb{N}$, we'll show the existence of n number of positive solutions of homogeneous integral equation of Hammerstein type (1.2).

For all $p, n \in \mathbb{N}$ we define following matrices:

$$\mathbf{A}_n^{(p)} = \left\{ \frac{1}{2(2p+i+j)-3} \left(\frac{1}{2}\right)^{2(2p+i+j-2)} \right\}_{i,j=\overline{1,n}}, \quad n,p \in \mathbb{N}. \tag{3.1}$$

$$\mathbf{B}\left[a_1, ..., a_n; b_1, ...b_n\right] = \left(\frac{1}{a_i + b_j}\right)_{i,j=\overline{1,n}}, \quad a_i, b_j > 0. \tag{3.2}$$

$$\mathbf{C}_n^{(p)} = B\left[4p, 4(p+1), ..., 2(p+n-1); 1, 5, ..., 4n-3\right]. \tag{3.3}$$

Lemma 3. *[25] Let $n \geq 2$. Then:*

$$\det \mathbf{B}\left[a_1, ..., a_n; b_1, ..., b_n\right] = \frac{\prod_{1\leq i<j\leq n}\left[(a_i - a_j)(b_i - b_j)\right]}{\prod_{i,j=1}^{n}(a_i + b_j)}.$$

Corollary 1. $\det \mathbf{A}_n^{(p)} = \left(\frac{1}{2}\right)^{2n(2p+n-1)} \det \mathbf{C}_n^{(p)}$.

Proof. Let $i, j \in 1, 2, ..., n$. We multiply by $2^{2(p+j-1)}$ the jth column of the matrix $\mathbf{A}_n^{(p)}$, after that, we multiply by $2^{2(i-1)}$ the i-th row of the matrix obtained. As a result, we get $\mathbf{C}_n^{(p)}$. □

Lemma 4. *Let* $\mathbf{B}^{-1}[a_1, a_2, ..., a_n; b_1, b_2, ..., b_n] = \{\beta_{ij}\}_{i,j=\overline{1,n}}$ *be an inverse matrix of* $\mathbf{B}[a_1, a_2, ..., a_n; b_1, b_2, ..., b_n]$*. Then:*

$$\beta_{ji} = \frac{\prod_{s=1}^{n}(a_s + b_j)\prod_{s=1,s\neq i}^{n}(a_i + b_s)}{\prod_{s=1,s\neq j}^{n}(b_j - b_s)\prod_{s=1,s\neq i}^{n}(a_i - a_s)}.$$

Proof. Subtracting the jth column of $\mathbf{B}[a_1, a_2, ..., a_n; b_1, b_2, ..., b_n]$ from every other column, we get the following equality:

$$\det \mathbf{B}[a_1, a_2, ..., a_n; b_1, b_2, ..., b_n] =$$

$$\frac{\prod_{s=1,s\neq j}^{n}(b_j - b_s)}{\prod_{s=1}^{n}(a_s + b_j)}\begin{pmatrix} \frac{1}{a_1+b_1} & \cdots & \frac{1}{a_1+b_{j-1}} & 1 & \frac{1}{a_1+b_{j+1}} & \cdots & \frac{1}{a_1+b_n} \\ \frac{1}{a_2+b_1} & \cdots & \frac{1}{a_2+b_{j-1}} & 1 & \frac{1}{a_2+b_{j+1}} & \cdots & \frac{1}{a_2+b_n} \\ & \cdots & & \cdots & & \cdots & \\ \frac{1}{a_n+b_1} & \cdots & \frac{1}{a_n+b_{j-1}} & 1 & \frac{1}{a_n+b_{j+1}} & \cdots & \frac{1}{a_n+b_n} \end{pmatrix}.$$

Next, we subtract from the j-th row the i-th row for every $j \in \{1, 2..., i-1, i+1, ...n\}$. Then,

$$\det \mathbf{B}[a_1, ..., a_n; b_1, ..., b_n] = \frac{\prod_{s=1,s\neq j}^{n}(b_j - b_s)\prod_{s=1,s\neq i}^{n}(a_i - a_s)}{\prod_{s=1}^{n}(a_s + b_j)\prod_{s=1,s\neq i}^{n}(a_i + b_s)} \times \det \mathbf{B}^{(i,j)}[a_1, ..., a_n; b_1, ..., b_n],$$

where $\mathbf{B}^{(j,i)}[a_1, ..., a_n; b_1, ..., b_n]$ is the cofactor of the element $\dfrac{1}{a_i + a_j}$ in $\mathbf{B}[a_1, ..., a_n; b_1, ..., b_n]$, since:

$$\beta_{ji} = \frac{\det \mathbf{B}^{(i,j)}[a_1, ..., a_n; b_1, ..., b_n]}{\det \mathbf{B}[a_1, ..., a_n; b_1, ..., b_n]}.$$

This completes the proof. □

We let:

$$\left(\mathbf{A}_n^{(p)}\right)^{-1} = \{\alpha_{ij}\}_{i,j\in\overline{1,n}}.$$

Remark 1. *For each* α_{ji} *element of* $\left(\mathbf{A}_n^{(p)}\right)^{-1}$*, the following equality holds:*

$$\alpha_{ji} = 4^{2p+i+j-n+1} \cdot \frac{\prod_{s=1}^{n}(4p + 2s + 2j - 3)\prod_{s=1,s\neq j}^{n}(4p + 2s + 2j - 3)}{\prod_{s=1,s\neq j}^{n}(j - s)\prod_{s=1,s\neq i}^{n}(i - s)}.$$

Proof. By Corollary 1 and Lemma 4 we get:

$$\alpha_{ji} = 4^{2p+i+j} \cdot \frac{\det \mathbf{B}^{(i,j)}[4p, 4p+2, ...4p+2(n-1); 1, 3, ...2n-1]}{\det \mathbf{B}[4p, 4p+2, ...4p+2(n-1); 1, 3, ...2n-1]} =$$

$$4^{2p+i+j} \cdot \frac{\prod_{s=1}^{n}(4p + 2s + 2j - 3)\prod_{s=1,s\neq i}^{n}(4p + 2s + 2i - 3)}{\prod_{s=1,s\neq j}^{n}(2j - 2s)\prod_{s=1,s\neq i}^{n}(2i - 2s)}.$$

□

Here, we denote

$$\varphi_{(s,n,p)}(u)=\alpha_{s1}u^{2p-1}+...+\alpha_{sn}u^{2(n+p)-3},\quad s,n,p\in\mathbb{N},\ u\in[0,1],$$

$$K_{(n,p)}(t,u;k)=1+\sum_{s=1}^{n}\left(\sqrt[k]{1+t^{2(p+s)-1}}-1\right)\varphi_{(s,n,p)}(u),\quad k\in\mathbb{N},k\geq 2,\ t,u\in[0,1].$$

Remark 2. *For the given* $k\in\mathbb{N},k\geq 2$. *the following inequality holds:*

$$K_{(n,p)}\left(t-\frac{1}{2},u-\frac{1}{2};k\right)\leq K_{(n,1)}\left(t-\frac{1}{2},u-\frac{1}{2};k\right),\quad (t,u)\in[0,1]^2,n,p\in\mathbb{N}.$$

We set:

$$\zeta_0(n)=\frac{64}{9}\cdot\frac{4^n-1}{4n+1}\left(\frac{(4n+1)!!}{(n-1)!(2n+1)!!}\right)^2.$$

Lemma 5. *Let* $n\in\mathbb{N}$. *If* $k\geq\zeta_0(n)$, *then the following inequality holds:*

$$K_{(n,p)}\left(t-\frac{1}{2},u-\frac{1}{2};k\right)>0,\ (t,u)\in[0,1]^2,p\in\mathbb{N}.$$

Proof. For $p=1$ from Remark 1, we have:

$$\alpha_{ij}=4^{i+j-n+3}\frac{\prod_{s=1}^{n}(2i+2s+1)\prod_{s=1,s\neq j}^{n}(2j+2s+1)}{\prod_{s=1,s\neq i}^{n}(i-s)\prod_{s=1,s\neq j}^{n}(j-s)}.$$

Then:

$$\left|\frac{\alpha_{i,j+1}}{\alpha_{i,j}}\right|=\frac{4(4j+1)(2j+2n+3)}{(2j+3)(4j+5)},\ i=\overline{1,n},\ j=\overline{1,n-1}$$

and

$$\left|\frac{\alpha_{i+1,j}}{\alpha_{i,j}}\right|=\frac{4(n-i)(2i+2n+3)}{i(2i+3)},\ i=\overline{1,n},\ j=\overline{1,n-1}.$$

From the above, one has: $\max_{i,j=\overline{1,n}}|\alpha_{ij}|=|\alpha_{nn}|$. By Remark 1, we can take:

$$K_{(n,p)}\left(t-\frac{1}{2},u-\frac{1}{2};k\right)\geq 1-\frac{2}{3}\max_{i,j=\overline{1,n}}|\alpha_{ij}|\sum_{s=1}^{n}\left(\sqrt[k]{1+\left(\frac{1}{2}\right)^{2s+1}}-1\right)\geq$$

$$1-\frac{2|a_{nn}|}{3k}\sum_{s=1}^{n}\left(\frac{1}{2}\right)^{2s+1}\geq 1-(4^n-1)\cdot\frac{64(2n+3)^2(2n+5)^2...(4n-1)^2(4n+1)}{9k\left((n-1)!\right)^2}.$$

Since $k\geq\zeta_0(n)$, one gets $K_{(n,p)}\left(t-\frac{1}{2},u-\frac{1}{2};k\right)>0$. This completes the proof.

$\square$

Proposition 1. *Let $n \in \mathbb{N}$. If $k \geq \zeta_0(n)$, then the Hammerstein's nonlinear operator H_k with kernel $K_{(n,p)}\left(t-\frac{1}{2}, u-\frac{1}{2}; k\right)$ $(p \in \mathbb{N})$ has at least n number of positive fixed points.*

Proof. Let $f_j(u) = \sqrt[k]{1+u^{2(p+j)-1}}$, $j = \overline{1,n}$ and $u_1 = u - \frac{1}{2}$, $t_1 = t - \frac{1}{2}$. Put $g_j(t) = f_j\left(t-\frac{1}{2}\right)$. We will show functions $g_j(t)$ are fixed points of the Hammerstein operator H_k with the kernel $K_{(n,p)}\left(t-\frac{1}{2}, u-\frac{1}{2}; k\right)$:

$$\int\limits_0^1 K_{(n,p)}\left(t-\frac{1}{2}, u-\frac{1}{2}; k\right) g_j^k(u)du =$$

$$\int\limits_0^1 K_{(n,p)}\left(t-\frac{1}{2}, u-\frac{1}{2}; k\right) f_j^k\left(u-\frac{1}{2}\right) du = \int\limits_{-\frac{1}{2}}^{\frac{1}{2}} K_{(n,p)}\left(t_1, u_1; k\right) f_j^k(u_1)du_1 =$$

$$\int\limits_{\frac{1}{2}}^{-\frac{1}{2}} \left[1+\sum_{s=1}^{n}\left(\sqrt[k]{1+t_1^{2(p+s)-1}}-1\right)\varphi_{(s,n,p)}(u_1)\right]\left(1+u_1^{2(p+j)-1}\right)du_1 =$$

$$1+\sum_{s=1}^{n}\left(\sqrt[k]{1+t_1^{2(p+s)-1}}-1\right)\int\limits_{\frac{1}{2}}^{\frac{1}{2}}\left(\alpha_{s1}u_1^{4(p-1)+2s+2j}+\ldots+\alpha_{sn}u_1^{4p+2(s+j+n)-6}\right)du_1 =$$

$$1+\sum_{s=1}^{n}\left(\sqrt[k]{1+t_1^{2(p+s)-1}}-1\right)\left(\alpha_{sj}\beta_{s1}+\ldots+\alpha_{nj}\beta_{sn}\right) = \sqrt[k]{1+t_1^{2(p+j)-1}}.$$

Hence:

$$\int\limits_0^1 K_{(n,p)}\left(t-\frac{1}{2}, u-\frac{1}{2}; k\right) g_j^k(u)du = g_j(t), \quad j \in \{1, 2, ..., n\}.$$

□

Theorem 5. *For each $n \in \mathbb{N}$, there exists $\vartheta > 1$ and a positive continuous kernel $K(t,u)$ such that, the number of positive solutions for the Hammerstein integral equation (1.2) is equal to at least n.*

4. Gibbs measures for models on Cayley tree Γ^k

In this section we study Gibbs measures for models on Cayley tree. You may be familiar with the definitions and properties of Gibbs measures in books [22–24]. A Cayley tree (Bethe lattice) Γ^k of order $k \in \mathbb{N}$ is an infinite homogeneous tree, i.e., a graph without cycles, such that exactly $k+1$ edges originate from each vertex. Let $\Gamma^k = (V, L)$ where V is the set of vertices and L that of edges (arcs). Two vertices x and y are called nearest neighbors if there exists an edge $l \in L$ connecting them. We will use the notation $l = \langle x, y\rangle$. A collection of nearest neighbor pairs $\langle x, x_1\rangle, \langle x_1, x_2\rangle, ...\langle x_{d-1}, y\rangle$ is called a *path* from x to y. The distance $d(x,y)$ on the Cayley tree is the number of edges of the shortest path from x to y.

For a fixed $x^0 \in V$, called the root, we set:

$$W_n = \{x \in V | d(x, x^0) = n\}, \qquad V_n = \bigcup_{m=0}^{n} W_m$$

and denote:

$$S(x) = \{y \in W_{n+1} : d(x, y) = 1\}, x \in W_n,$$

the set of $direct\ successors$ of x.

Consider models where the spin takes values in the set $[0, 1]$, and is assigned to the vertices of the tree. For $A \subset V$ a configuration σ_A on A is an arbitrary function $\sigma_A : A \to [0, 1]$. We denote $\Omega_A = [0, 1]^A$ the set of all configurations on A and $\Omega = [0, 1]^V$. The Hamiltonian on Γ^k of the model is:

$$H(\sigma) = -J \sum_{\langle x,y\rangle \in L} \xi\left(\sigma(x), \sigma(y)\right), \quad \sigma \in \Omega, \tag{4.1}$$

where $J \in R \setminus \{0\}$ and $\xi : (u, v) \in [0, 1]^2 \to \xi_{u,v} \in \mathbb{R}$ is a given bounded, measurable function.

Let λ be the Lebesgue measure on $[0, 1]$. On the set of all configurations on A the a priori measure λ_A is introduced as the $|A|$ fold product of the measure λ. Here and subsequently, $|A|$ denotes the cardinality of A. We consider a standard sigma-algebra $\mathcal{B}$ of subsets of $\Omega = [0, 1]^V$ generated by the measurable cylinder subsets.

Let $\sigma_n : x \in V_n \mapsto \sigma_n(x)$ be a configuration in V_n and $h : x \in V \mapsto h_x = (h_{t,x}, t \in [0, 1]) \in \mathbb{R}^{[0,1]}$ be mapping of $x \in V \setminus \{x^0\}$. Given $n = 1, 2, \ldots$, consider the probability distribution $\mu^{(n)}$ on Ω_{V_n} defined by:

$$\mu^{(n)}(\sigma_n) = Z_n^{-1} \exp\left(-\beta H(\sigma_n) + \sum_{x \in W_n} h_{\sigma(x),x}\right). \tag{4.2}$$

Here, as before, $\sigma_n : x \in V_n \mapsto \sigma(x)$ and Z_n is the corresponding partition function:

$$Z_n = \int\limits_{\Omega_{V_n}} \exp\left(-\beta H(\widetilde{\sigma}_n) + \sum_{x \in W_n} h_{\widetilde{\sigma}(x),x}\right) \lambda_{V_n}(\widetilde{\sigma}_n), \tag{4.3}$$

where $\beta = T^{-1}$, $T > 0$ – temperature. The probability distributions $\mu^{(n)}$ are compatible [21] if for any $n \geq 1$ and $\sigma_{n-1} \in \Omega_{V_{n-1}}$:

$$\int\limits_{\Omega_{W_n}} \mu^{(n)}\left(\sigma_{n-1} \vee \omega_n\right) \lambda_{W_n}\left(d(\omega_n)\right) = \mu^{(n-1)}\left(\sigma_{n-1}\right). \tag{4.4}$$

Here, $\sigma_{n-1} \vee \omega_n \in \Omega_{V_n}$ is the concatenation of σ_{n-1} and ω_n. In this case, there exists [21] a unique measure μ on Ω_V such that, for any n and $\sigma_n \in \Omega_{V_n}$, $\mu\left(\left\{\sigma\Big|_{V_n} = \sigma_n\right\}\right) = \mu^{(n)}(\sigma_n)$. The measure μ is called the *splitting Gibbs measure*, corresponding to Hamiltonian (4.1) and function $x \mapsto h_x$, $x \neq x^0$.

The following statement describes conditions on h_x guaranteeing compatibility of the corresponding distributions $\mu^{(n)}(\sigma_n)$.

Proposition 2. *[21] The probability distributions* $\mu^{(n)}(\sigma_n)$, $n = 1, 2, \ldots$, *in (4.2) are compatible iff for any* $x \in V \setminus \{x^0\}$ *the following equation holds:*

$$f(t,x)=\prod_{y\in S(x)}\frac{\int_0^1 \exp(J\beta\xi_{t,u})f(u,y)du}{\int_0^1 \exp(J\beta\xi_{0,u})f(u,y)du}. \tag{4.5}$$

Here and below, $f(t,x)=\exp(h_{t,x}-h_{0,x}),\ t\in[0,1]$ *and* $du=\lambda(du)$ *is the Lebesgue measure.*

We consider ξ_{tu} as a continuous function and we are going to solve equation (4.5) in the class of $translation-invariant$ functions $f(t,x)$ (i.e. $f(t,x)=f(t)$ for all $x\in\Gamma^k\setminus\{x_0\}$). We'll show that there exists a finite number of $translation-invariant$ Gibbs measures for model (4.1).

For $translation-invariant$ functions, equation (4.5) can be written as:

$$\left(R_k f\right)(t)=f(t),\ \ k\in\mathbb{N}, \tag{4.6}$$

where $K(t,u)=Q(t,u)=\exp(J\beta\xi_{tu})$, $f(t)\in C_0^{+}[0,1]$, $t,u\in[0,1]$ (see [20,21]).

Consequently, for each $k\in\mathbb{N}$, $k\geq 2$, the Hammerstein integral equation corresponding to the equation (4.6) has the following form:

$$\int_0^1 Q(t,u)f^k(u)du=f(t). \tag{4.7}$$

By Theorem 3 and Propositions 1and 2 we'll obtain the following Theorem:

Theorem 6. *Let* $n\in\mathbb{N}$. *If* $k\geq\zeta_0(n)$, *then number of translation-invariant Gibbs measures for the model:*

$$H(\sigma)=-\frac{1}{\beta}\sum_{<x,y>} ln\left(K_{(n,p)}\left(\sigma(x)-\frac{1}{2},\sigma(y)-\frac{1}{2};k\right)\right),\quad \sigma\in\Omega(p\in\mathbb{N}),$$

on the Cayley tree Γ^k *is equal to at least* n.

References

[1] M.A. Abdou, A.A. Badr. On a method for solving an integral equation in the displacement contact problem. *J. Appl. Math Comput.*, 2002, **127**, P. 65–78.

[2] R. Grimmer, J.H. Liu. Singular perturbations in viscoelasticity. *Rocky Mountain J. Math.*, 1994, **24**, P. 61–75.

[3] J.B. Keller, W.E. Olmstead. Temperature of nonlinearly radiating semi-infinite solid. *Quart. Appl. Math.*, 1972, **29**, P. 559–566.

[4] M.A. Krasnoselskii, P.P. Zabrejko. *Geometrical methods of Nonlinear Analysis*. Springer-Verlag, 1984.

[5] W.E. Olmstead, R.A. Handelsman. Diffusion in a semi-infinite region with nonlinear surface dissipation. *SIAM Rev.*, 1996, **18**, P. 275–291.

[6] M.A. Abdou. On the solution of linear and nonlinear integral equation. *J. Appl. Math. Comput.*, 2003, **146**, P. 857–871.

[7] M.A. Abdou, M.M. El-Borai, M.M. El-Kojok. Toeplitz matrix method and nonlinear integral equation of Hammerstein type. *Journal of Computational and Applied Mathematics*, 2009, **223**, P. 765–776.

[8] M.A. Abdou, W.G. El-Sayed, E.I. Deebs. A solution of nonlinear integral equation. *J. Appl. Math. Comput.*, 2005, **160**, P. 1–14.

[9] A. Horvat-Marc. Positive solutions for nonlinear integral equations of Hammerstein type. *Carpathian J. Math.*, 2008, **24** (2), P. 54–62.

[10] J.A. Appell, E. de Pascale, P.P. Zabrejko. On the unique solvability of Hammerstein integral equations with non-symmetric kernels. *Progress in Nonlinear Differential Equations and Their Applications*, 2000, **40**, P. 27–34.

[11] J. Appell, A.S. Kalitvin. Existence results for integral equations: spectral methods VS. *Fixed point theory*, 2006, **7** (2), P. 219–234.

[12] D. Bugajewski. On BV-Solutions of some nonlinear integral equations. *Integral Equations Operator Theory*, 2003, **46**, P. 387–398.

[13] P.S. Milojevic. Solvability and the number of solutions of Hammerstein equations. *Electronic J. Diff. Equat.*, 2004, **54**, P. 1–25.

[14] H.K. Pathak, G.S. Jeong, Y.J. Cho. Recent fixed point theorems and their applications. *Proceedings of nonlinear functional analysis and applications*, 1997, **2**, P. 89–114.

[15] P. Kumlin. A note on fixed point theory. *Functional Analysis. Mathematics, Chalmers $\wp$ GU*, 2003/2004, TMA 401/MAN 670.

[16] W.V. Petryshyn, P.M. Fitzpatrik. New existence theorems for nonlinear integral equations of Hammerstein type. *Trams. Amer. Math. Soc.*, 1970, **160**, P. 39–63.

[17] F.E. Browder. Nonlinear functional analysis and nonlinear integral equations of Hammerstein and Urysohn type. *Contributions to Nonlinear Functional Analysis* (ed. C.H. Zarantonello, Academic Press), 1971, P. 99–154.

[18] H. Brezis, F.E. Browder. Nonlinear integral equations and systems of Hammerstein type. *Advances in Math*, 1975, **18**, P. 115–147.

[19] E.Yu. Elenskaya. The existence fixed point of monoton left-continuous operators in space with right cone. *Izvestiya vuzov. Matematika*, 2011, **10**, P. 40–47 [in Russian].

[20] Yu.Kh. Eshkabilov, F.H. Haydarov, U.A. Rozikov. Uniqueness of Gibbs Measure for Models With Uncountable Set of Spin Values on a Cayley Tree. *Math. Phys. Anal. Geom.*, 2013, **16** (1), P. 1–17.

[21] Yu.Kh. Eshkabilov, U.A. Rozikov. On models with uncountable set of spin values on a Cayley tree: Integral equations. *Math. Phys. Anal. Geom.*, 2010, **13**, P. 275–286.

[22] U.A. Rozikov. *Gibbs measures on a Cayley trees*. World Sci. Pub, Singapore, 2013.

[23] H.O. Georgii. *Gibbs measures and phase transitions*. Second edition, de Gruyter Studies in Mathematics, 9. Walter de Gruyter, Berlin, 2011.

[24] C. Preston. *Gibbs states on countable sets*. Cambridge University Press, London, 1974.

[25] I.V. Proskuryakov. *Problems in Linear Algebra*. MIR Publishers Moscow, 1978 (English translation).

NANOSYSTEMS: PHYSICS, CHEMISTRY, MATHEMATICS, 2015, 6 (5), P. 628–636

The optical properties of the cobalt nanoparticles in the transparent condensed matrices

M. V. Ananyeva[1], A. V. Kalenskii[1], A. A. Zvekov[2], A. P. Nikitin[2], I. Yu. Zykov[1]

[1]Kemerovo state University, Kemerovo, 650043, Russia,
[2]Institute of Coal Chemistry and Material Science SB RAS, Kemerovo, 650000, Russia

kriger@kemsu.ru

PACS 61.46.+w, 82.33.Vx **DOI 10.17586/2220-8054-2015-6-5-628-636**

The absorption and scattering efficiency factors for cobalt nanoparticles over wavelengths ranging from 400 – 1200 nm were calculated. The maximum values and corresponding radii of the absorption efficiency were shown to be dependent upon the incident light wavelength. The highest scattering factor values in the studied spectral range were between 2.2 and 2.4. If the absorptivity of the matrix increases, absorption of the light by cobalt nanoparticles begins to dominate over scattering process. The obtained results allow us to predict the optical properties for composite materials based on a transparent matrix with cobalt nanoparticles, which is essential for the accurate modeling of such systems' behavior under laser irradiation.

Keywords: optical properties, Mie theory, nanoparticles, cobalt, composite materials, laser irradiation.

Received: 5 July 2015

Revised: 27 September 2015

1. Introduction

Nanoparticles have unique thermochemical, physical and optical properties. Their inclusion into condensed matrices significantly changes the properties of the obtained composite materials. The composites, based on metal nanoparticles and transparent matrix, are of the great interest for the optical physics and optoelectronics [1]. Both experimental and theoretical investigations of such composites' optical properties are presented in [2–4]. The problem is important today because of the possible practical use of the absorption and scattering of light by nanoparticles in timing devices of nonlinear optical equipment [5], application to the thermal cancer therapy, and optical detonators [6, 7].

It is known that iron-group element nanoparticles may be used in the high-speed optical devices [7, 8]. Aluminium nanoparticles in pentaerythritol tetranitrate (PETN) reduce the explosive decomposition threshold by more than 100-fold in case of initiation by the first and second harmonics of the Nd:YAG laser [6, 9, 10]. The possibility of using cobalt nanoparticle-based composites in secondary explosives as an optical detonator cup was mentioned in [3, 11, 12]. Methods for synthesizing cobalt nanoparticles with definite sizes have been previously described [13]. In order to calculate the illumination intensity in the composite's volume, it is necessary to take into account multiple scattering of light by the metal nanoparticles [14, 15]. This point was verified experimentally for the pressed PETN-aluminium pellets [4]. In order to find the optimal material for an optical detonator cup and compositions for the nonlinear optical equipment, it is necessary to calculate the relationships of the absorption and scattering efficiency factors by varying particle size and the wavelength of the incident light [16].

2. Calculation procedure and Results

The interaction of metal nanoparticles and electromagnetic radiation is traditionally described by using the absorption efficiency (Q_{abs}) and scattering efficiency factors (Q_{sca}). These dimensionless parameters are equal to the ratio of the particle's cross-section and its geometrical cross-section $Q = \sigma/\sigma_g$. The Q_{abs} was calculated in terms of Mie theory as the difference of the absorption efficiency (Q_{ext}) and scattering efficiency factors (Q_{sca}) [16–18].

The main parameters of the theory are the complex refractive index (m_i) of cobalt, which depends on the wavelength of the incident light (λ), and the refractive index of the medium (m_0) [19]. These data over the range 400 – 1210 nm with increments of $\sim$ 100 nm are presented in [20]. In order to calculate the absorption and scattering efficiency factors for the wavelengths, which were not presented in [19], work we used the spline interpolation with 1 nm increments, obtaining a smooth dependence $m_i(\lambda)$ in this manner [18, 19]. The range of nanoparticle radii studied is dictated by their potential use in optic initiation systems where values of $20 < R < 200$ nm are utilized.

Figures 1 and 2 show the dependences of the absorption efficiency (Q_{abs}) and scattering efficiency factors (Q_{sca}) respectively on the cobalt particle's radius in a transparent medium with m_0 equal to 1.54 calculated for the light wavelengths of 400, 600, 800, 1000, and 1200 nm.

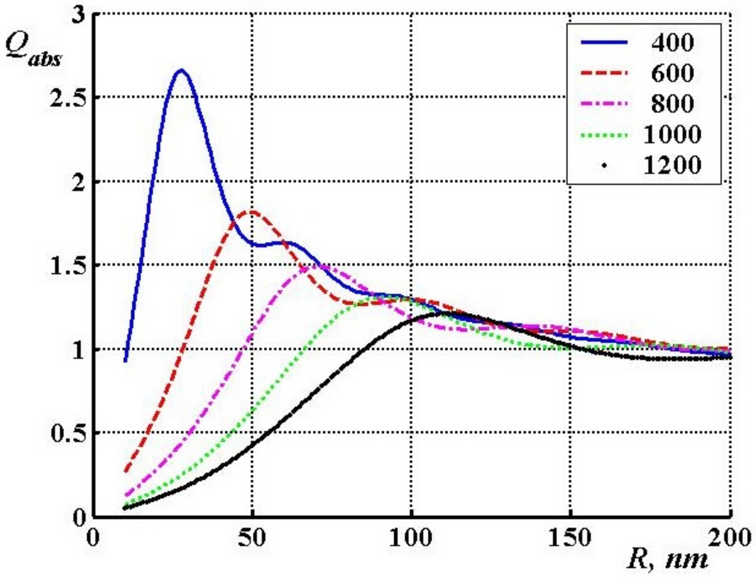

FIG. 1. The dependence of the absorption efficiency factor of the cobalt nanoparticles in the PETN matrix on their radius for the wavelengths in nm presented in the legend.

This refractive index was chosen as a typical value for dielectric media and is equal to the refractive index of pentaerythritol tetranitrate (PETN), which is one of the most important compounds among secondary explosives. As seen, Q_{abs} values increase for small particle radii values and tend to steady-state value with oscillations in the $R \to \infty$ limit [21, 22]. The dependence has a well-marked maximum which tends to shift to larger radii when the wavelength increases. At the same time, the maximum's amplitude decreases significantly. The dependence Q_{sca} vs. R increases for the small radii, then it achieves constant value and remains close to that value with minor fluctuations. The curve $Q_{\text{sca}}(R)$ has several local maxima. One can see the shift of the principal maximum position in Fig. 3. Enumerating the maxima from

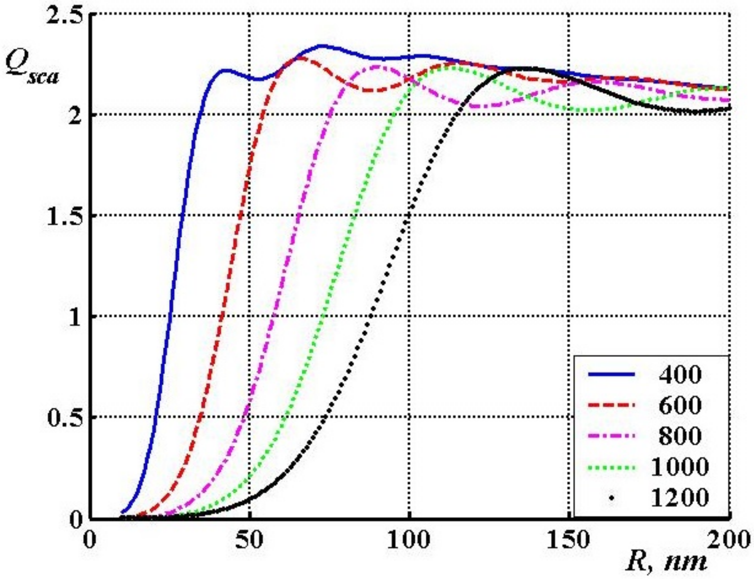

FIG. 2. The dependence of the scattering efficiency factor of the cobalt nanoparticles in the PETN matrix on their radius for the wavelengths in nm presented in the legend.

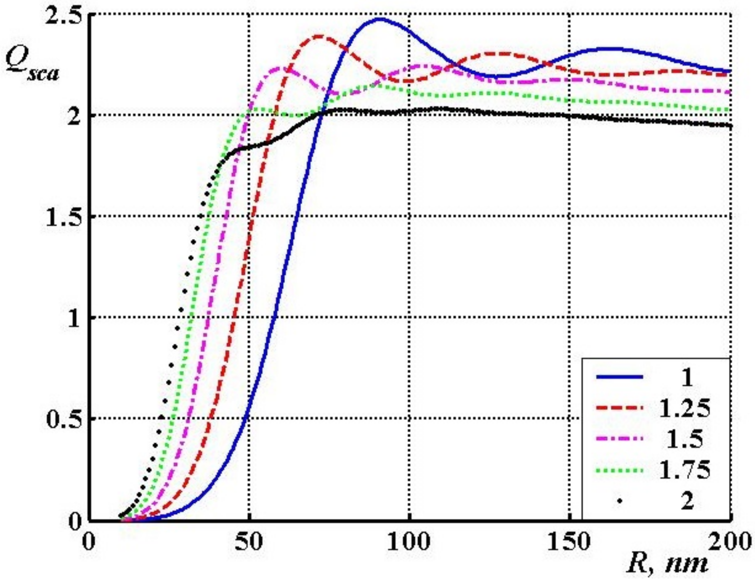

FIG. 3. The dependence of the scattering efficiency factor of the cobalt nanoparticles for of the second harmonics of Nd:YAG laser irradiation. The refractive indexes of the media are 1, 1.25, 1.5, 1.75, and 2

small to higher R values it is seen that for $\lambda > 463$ nm, the principal maximum is the first one, while in the spectral range $\lambda \leq 463$ nm the highest maximum is the second one.

Figures 3 and 4 show the dependences of the absorption and scattering efficiency factors of the cobalt nanoparticles upon their radii for 532 nm light and for different refractive indices. This value of λ coincides with the second harmonics wavelength for the Nd:YAG laser, which is widely used in many applications [6–8]. The displays show that increasing the medium's refractive index results in an increase of the maximum amplitude for $Q_{\text{abs}}(R)$ and a shift to smaller radii values. The increasing of the refraction index of the media results in the shift

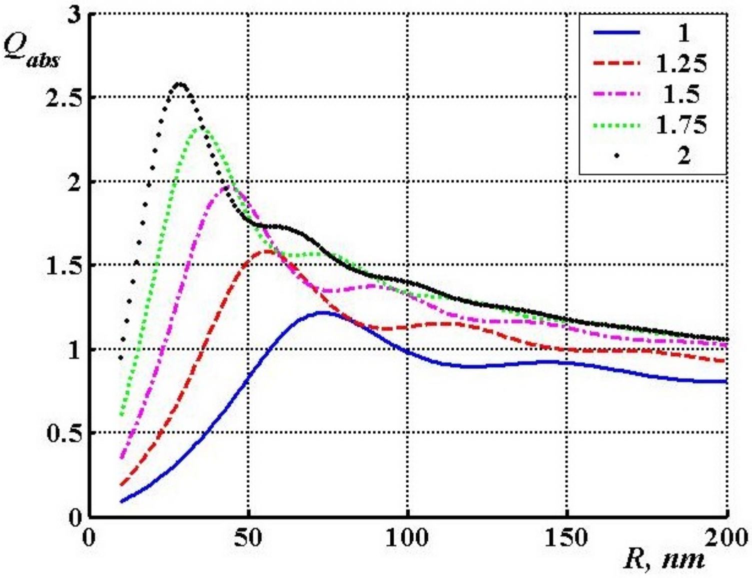

FIG. 4. The dependence of the cobalt nanoparticle absorption factor in case of irradiation of the second harmonic of Nd:YAG laser, refractive indexes of the media are 1, 1.25, 1.5, 1.75, and 2

of the initial ascending part of the $Q_{\text{sca}}(R)$ curve to the smaller radii values. Additionally, the oscillations' amplitude decreases for larger particle radius values and one can see a small decrease for the Q_{sca} stationary value when $R \to \infty$.

Based on the data presented above, the maximum values of absorption ($Q_{\text{abs max}}$) and scattering efficiency factors ($Q_{\text{sca max}}$) were calculated for cobalt nanoparticles for different wavelengths. These calculations for the positions of the maxima were done assuming a refractive index 1.54 for the medium. The results are presented in Table 1. These data show that the absorption exceeds the scattering for shorter wavelength values. The maximum values of absorption and scattering efficiency factor coincide for cobalt nanoparticles at a wavelength of 482.5 nm. Increasing of wavelength from 400 up to 1200 nm results in monotonic $Q_{\text{abs max}}(\lambda)$ decreasing in ~ 2.2 fold, from 2.6589 to 1.2065. If the wavelength increases, the radius of the particles with the largest absorption efficiency factor ($R_{\text{abs max}}$) increases linearly from 27.7 nm for $\lambda = 400$ nm up to 111.5 nm for $\lambda = 1200$ nm. For $Q_{\text{sca max}}(\lambda)$, this dependence is dissimilar. $Q_{\text{sca max}}$ is almost independent of the wavelength and shows small oscillations in the vicinity of the stationary value. For all wavelengths, the values of $Q_{\text{sca max}}(\lambda)$ are 2.1992 – 2.3371, and the minimum is observed at $\lambda = 471$ nm. The radius of the nanoparticles having the greatest scattering efficiency factor for a given wavelength ($R_{\text{sca max}}$) increases from 73.3 nm to 105.3 nm in the $400 < \lambda < 550$ nm range and from 63.2 nm to 136.3 nm in the $575 < \lambda < 1200$ nm range. In the 550 – 575 nm wavelength range, a two fold decreasing of $R_{\text{sca max}}$ values was observed. This might be explained by the fact that in the $400 < \lambda < 550$ nm range, the second maximum dominates for the $Q_{\text{sca}}(R)$ dependence, and if the wavelength is longer than 550 nm, the first one dominates.

The contributions of the harmonics to the scattering efficiency factor were calculated for a wavelength of 532 nm and $m_0 = 1.54$ in an attempt to explain the shift of the maximum (Fig. 5). Letters c denotes the electric-type oscillations of the electron density on the surface of the metal, letters b – magnetic-type oscillations. The figures show the harmonics index: 1 – dipole, 2 – quadrupole, 3 – octopole, etc. One can readily see that when the radius of the cobalt nanoparticles is less than 70 nm, the first electric oscillation predominates. When the radius

TABLE 1. Spectral regularities for maximum absorption and scattering factor values for cobalt nanoparticles

λ, nm	m_i	$Q_{\text{abs max}}$	$R_{\text{abs max}}$, nm	$Q_{\text{sca max}}$	$R_{\text{sca max}}$, nm
400	$1.2000 - 3.0000i$	2.6589	27.7	2.3371	73.3
450	$1.5070 - 3.1721i$	2.3400	33.5	2.2070	85.0
500	$1.7000 - 3.4000i$	2.1355	38.9	2.2079	95.3
532	$1.7932 - 3.5609i$	2.0249	42.2	2.2286	101.7
550	$1.8430 - 3.6529i$	1.9662	44.1	2.2402	105.3
600	$2.0000 - 3.9000i$	1.8172	49.4	2.2777	66.0
650	$2.2148 - 4.1164i$	1.6973	54.9	2.2787	71.8
700	$2.4500 - 4.3000i$	1.6086	60.3	2.2613	77.8
750	$2.6628 - 4.4567i$	1.5434	65.6	2.2469	83.7
800	$2.8700 - 4.6000i$	1.4907	70.9	2.2333	89.6
850	$3.0914 - 4.7444i$	1.4432	76.2	2.2196	95.6
900	$3.3000 - 4.9000i$	1.3978	81.4	2.2134	101.4
950	$3.4667 - 5.0719i$	1.3528	86.5	2.2191	107.2
1000	$3.6000 - 5.2500i$	1.3096	91.6	2.2304	112.9
1050	$3.7178 - 5.4203i$	1.2708	96.5	2.2411	118.7
1064	$3.7505 - 5.4647i$	1.2611	97.9	2.2433	120.3
1100	$3.8381 - 5.5688i$	1.2391	101.5	2.2463	124.5
1150	$3.9789 - 5.6816i$	1.2170	106.5	2.2421	130.4
1200	$4.1580 - 5.7446i$	1.2065	111.5	2.2255	136.3

increases, the contribution of the second electric and the first magnetic oscillations become noticeable, these oscillations become dominant when $R > 100$ nm. Competition between the electric and magnetic oscillations results in two different effects:

i) the maximum on the dependence $Q_{\text{abs}}(R)$ shifts with increasing wavelength;
ii) local maxima for the dependence $Q_{\text{sca}}(R)$ have almost the same amplitude and for large cobalt nanoparticle radii; there is almost no dependence on R. Since there are several oscillations of comparable intensity, their sum changes only slightly.

Figures 6 and 7 present spectral dependencies of the absorption and scattering efficiency factors for cobalt nanoparticles of different radii in a PETN matrix. The line descriptions and radii values are represented on the legend. For 30 nm nanoparticles, Q_{abs} decreases monotonically. For the 50 nm nanoparticles, a maximum for Q_{abs} occurs at 553 nm and that of the scattering efficiency factor at 400 nm. Increasing the nanoparticle radius causes the appearance of a second maximum. It is worth pointing out the difference between our results and those obtained for gold nanoparticles [16]. Spectral regularities of the latter have a narrow band (half-width $\sim$ tens nm) due to plasmon resonance. In the case of cobalt, there are wide bands in the absorption spectra and scattering efficiency factor, as for other iron-group elements [7,8,15].

In the visible region of the spectrum and for larger cobalt nanoparticles, the standard deviation of the absorption and scattering factors is about 10 – 20 %. The weak dependence

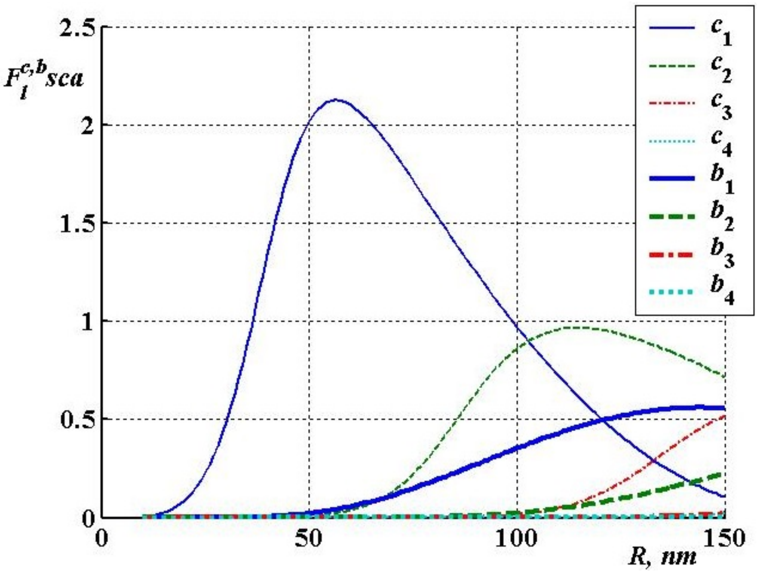

FIG. 5. Dependences of electric (c) and magnetic (b) oscillations of the scattering factor upon the cobalt nanoparticle radius at 532 nm

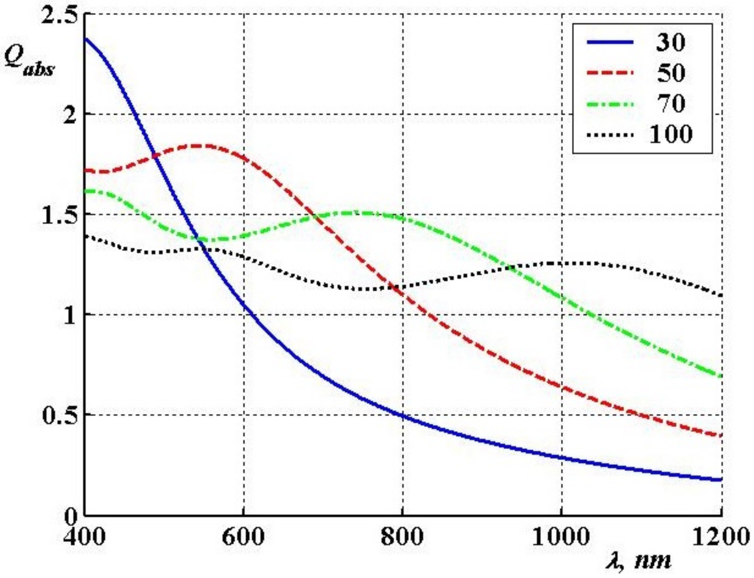

FIG. 6. Spectral dependencies of the absorption efficiency factors for cobalt nanoparticles with 30, 50, 70, and 100 nm radii

of the mentioned parameters upon the wavelength proves that the composite materials, based on the transparent media and cobalt nanoparticles with radius of ~ 100 nm, are neutral-density filters. So, this differs from the gold or silver colloidal solutions, which are colored and are used as a band-pass filter. Thus, it appears that a light filter with cobalt nanoparticles decreases the light's intensity primarily by scattering but not because of the absorption.

Figure 8 displays the calculated spectral regularities for the absorptivity of 1.5 nm cobalt nanoparticles and the experimental values of the molar absorptivity ε presented in [23]. The figure shows that the absorption predominates considerably over the scattering and the comparison of the extinction and the absorption is incorrect. As it follows from Fig. 8, in both cases, decreasing the wavelength results in increased absorptive properties. The region of

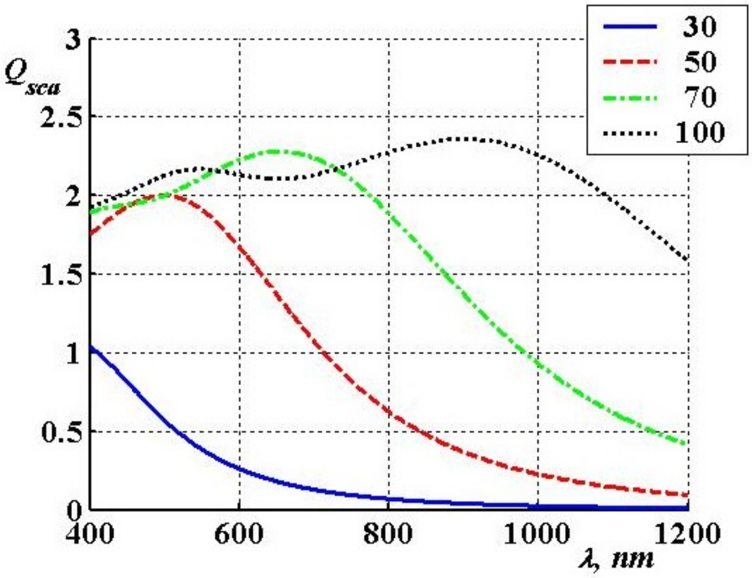

FIG. 7. Spectral dependencies of the scattering efficiency factors for cobalt nanoparticles with radii of 30, 50, 70, and 100 nm

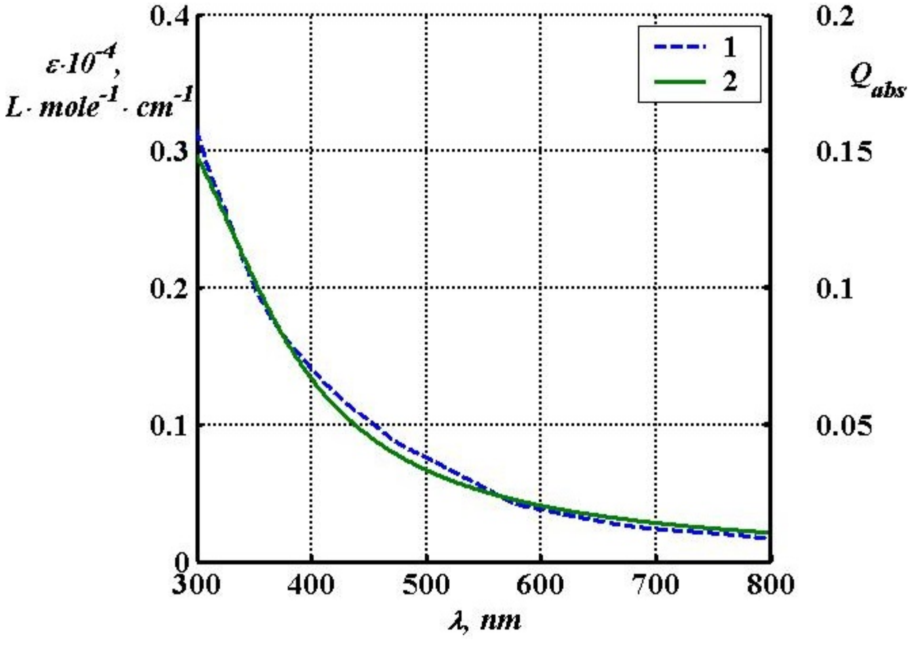

FIG. 8. Experimental spectral regularities for the molar absorptivity of 2 – 4 nm radii cobalt nanoparticles (1) [23]; calculated spectral regularities of the absorption factor for 1.5 nm radii cobalt nanoparticles (2)

the increase coincides, but the quantitative results do not coincide because of the three reasons. First, cobalt is partially lost during the synthesis (yield is always less than 100 %), this makes the calculated molar absorptivity larger than that which is observed. Second, cobalt nanoparticles are covered by a mixed oxide-hydroxide film [13]. Third, the existing size distribution of the particles can distort the spectrum. When these considerations are taken into account, the calculated values and the experimental results are in good agreement.

3. Conclusion

The absorption and scattering of light by cobalt nanoparticles with variation of wavelength and radius values was studied in terms of Mie theory. The optimal nanoparticles' radii performing maximal absorption and scattering efficiency factors, which are of practical interest in different applications including light filters and optic detonators, were determined for different wavelengths. The spectral dependencies of cobalt nanoparticles' scattering and absorption efficiency factors show wide bands or continuum spectrum, thus exhibiting a vast difference relative to gold or silver nanoparticles.

Acknowledgments

This work was supported by Ministry of Education and Science of the Russian Federation (governmental project No. 2014/64), grant of the Russian President (MK-4331.2015.2) and Russian Foundation for Basic Research for the financial support (grant 14-03-31648).

References

[1] Pomogajlo A.D., Rozenberg A.S., et al. *Metal Nanoparticles in Polymers*. Moscow, Himija, 2000, 672 p.

[2] Rey J.M., Kottman J., et al. Photothermal diffuse reflectance: a new tool for spectroscopic investigation in scattering solids. *Applied Physics B*, 2013, **112**, P. 547–551.

[3] Kalenskii A.V., Anan'eva M.V., et al. Explosive decomposition kinetics of aluminum tetranitropentaerytrite pellets. *Zhurnal Tekhnicheskoi Fiziki*, 2015, **85** (3), P. 119–123.

[4] Aduev B.P., Nurmukhametov D.R., et al. Integrating Sphere study of the optical properties of aluminum nanoparticles in tetranitropentaerytrite. *Zhurnal Tekhnicheskoi Fiziki*, 2014, **84** (9), P. 126–131.

[5] Sarkhosh L., Aleali H. et al. Large thermally induced nonlinear refraction of gold nanoparticles stabilized by cyclohexanone. *Physica Status Solidi A*, 2010, **207** (10), P. 2303–2310.

[6] Kalenskii A.V., Zvekov A.A., et al. Laser Wavelength Influence on the Critical Density of Initiation Energy of Energetic Materials. *Fizika Goreniya i Vzryva*, 2014, **50** (3), P. 98–104.

[7] Kalenskii A.V., Ananyeva M.V. Spectral regularities of the critical energy density of the pentaerythriol tetranitrate-aluminium nanosystems initiated by the laser pulse. *Nanosystems: Physics, Chemistry, Mathematics*, 2014, **5** (6), P. 803–810.

[8] Ananyeva M.V., Kalenskii A.V., et al Kinetic regularities of explosive decomposition of PETN contaning aluminium, cobalt and nickel nanoparticles. *Bulletin of Kemerovo State University*, 2014, **1-1** (57), P. 194–200.

[9] Kalenskii A.V., Zykov I.Yu., et al. Explosive sensitivity of petn-aluminum composites to pulsed laser radiation. *Bulletin of Kemerovo State University*, 2014, **3-3** (59), P. 211–217.

[10] Aduev B.P., Nurmukhametov D.R. et al. Explosive decomposition of PETN with nanoaluminum additives under the influence of pulsed laser radiation at different wavelengths. *Russian Journal of Physical Chemistry B*, 2013, **7** (4), P. 453–456.

[11] Ananyeva M.V., Zvekov A.A., et al. Promising compounds for the cap of optical detonator. *Perspektivnye materialy*, 2014, **7**, P. 5–12.

[12] Kalenskii A.V., Kriger V.G., et al. The Microcenter Heat Explosion Model Modernization. *Izvestia Vuzov Fizika*, 2012, **55** (11/3), P. 62–65.

[13] Zaharov, Yu.A., Pugachev, V.M., et al. Chemical synthesis, structure and magnetic properties of nanocrystalline Fe-Co alloys. *Materials Letters*, 2012, **74**, P. 173–175 .

[14] Zvekov A.A., Kalenskii A.V., et al. Radiance distribution simulation in a transparent medium with fresnel boundaries containing aluminum nanoparticles. *Komp'juternaja optika*, 2014, **38** (4), P. 749–756.

[15] Zvekov A.A., Ananyeva M.V., et al. Regularities of light diffusion in the composite material pentaery thriol tetranitrate-nickel. *Nanosystems: Physics, Chemistry, Mathematics*, 2014, **5** (5), P. 685–691.

[16] Lukatova S.G. Calculation of the PETN-gold composites' absorptivity for the second harmonic of the ND:YAG laser. *Sovremennye fundamental'nye i prikladnye issledovanija*, 2014, **1** (12), P. 95–98.

[17] Kriger, V.G., Kalenskii A.V., et al. Effect of Laser Radiation Absorption E?ciency on the Heating Temperature of Inclusions in Transparent Media. *Combustion, Explosion, and Shock Waves*, 2012, **48** (6), P. 705–708.

[18] Gazenaur N.V., Zykov I.Yu., et al. The wavelength dependence of copper absorption. *Aspirant*, 2014, **5**, P. 89–94.

[19] Kalenskii A.V., Ananyeva M.V. Absorptivity of the cobalt nanoparticles in a transparent media. *Spravochnik. Inzhenernyj zhurnal s prilozheniem*, 2015, **5**, P. 56–60.

[20] Zolotarev V.M., Morozov V.N., et al. *Optical Constants of Natural and Technical Media*. 1984, Leningrad: Himija, 216 p.

[21] Nikitin A.P. Calculations of chemical parameters of thermal explosion iniciation for samples with copper nanoparticles for different wave lengths. *Sovremennye fundamental'nye i prikladnye issledovanija*, 2013, **4** (11), P. 68–75.

[22] Odincova O.V. Calculation of laser sensitivity of the pentaerythriol tetranitrate-silver composites. *Sovremennye fundamental'nye i prikladnye issledovanija*, 2014, **4** (15), P. 38–43.

[23] Ershov B.G. Metal nanoparticles in water solutions: electronic, optical and catalytic properties. *Rossijskij himicheskij zhurnal*, 2001, **45** (3), P. 20–30.

NANOSYSTEMS: PHYSICS, CHEMISTRY, MATHEMATICS, 2015, 6 (5), P. 637–643

Periodic chain of disks in a magnetic field: bulk states and edge states

E. N. Grishanov[1], D. A. Eremin[1], D. A. Ivanov[1],
I. Yu. Popov[2], P. I. Smirnov[2]

[1] Department of Mathematics and IT,
Ogarev Mordovia State University
Bolshevistskaya Str. 68, Saransk, Russia
[2]Department of Higher Mathematics, ITMO University,
Kroverkskiy pr. 49, St. Petersburg, 197101, Russia
popov1955@gmail.com

PACS 73.23.Ad, 02.30.Tb **DOI 10.17586/2220-8054-2015-6-5-637-643**

An explicitly solvable model for periodic chain of coupled disks in orthogonal magnetic field is considered. The spectrum for the Hamiltonian is compared with the spectrum for the corresponding chain of circles. These models are used for the comparison of the bulk and edge states. It is found that for some range of the magnetic field values the lowest band for the circles system lies below the spectrum for the corresponding disks system, i.e. the edge band is below and is separated from the lowest bulk band.

Keywords: nanostructure; magnetic field; explicitly solvable model.

Received: 1 September 2015

1. Introduction

The difference between surface and bulk conductivities for materials and nanostructures is a subject of numerous experimental and theoretical investigations due to intriguing prospects (high-temperature superconductivity, topological insulator, etc.). In many cases, low-dimensional nanostructures have unusual electronic properties, see, e.g., results of recent experiments with highly ordered organometallic nanoribbons, whose intrinsic (defect-free) conductivity is found to be three orders of magnitude higher than that of macroscopic crystals [1]. It should be mentioned that in many cases there is no adequate mathematical model of the corresponding nanosystem, and the theoretical description is complex. Our goal is to construct a mathematical model for chain type periodic nanostructure and to describe its spectrum. Ideally, we would like to have a band (preferably, the lowest band) for the surface (edge) states be in the gap (or below the first band) for the bulk states. The corresponding system is described in the present paper. This case is, in some sense, similar to a topological insulator (TI). TIs are electronic materials that have a bulk band gap like an ordinary insulator, but have protected conducting states on their edge or surface [2–5]. We have similar phenomenon for surface state protection as in TI, although the physical nature is different.

We consider a periodic system of coupled disks as a basic geometry. As for the problem of edge states, our consideration is in the framework of a model of quantum graphs (periodic system of coupled circles). This model was used intensively in previous publications (starting from works [6, 7]) due to its advantages: in one way, it is quasi-one-dimensional and rather simple, however, despite this apparent simplicity, it preserves the properties of the corresponding physical system, particularly, its spectral properties [8–13]. As for the problem of bulk states, we deal with the model of quantum resonators coupled through point-like window. This model is based on the theory of self-adjoint extensions of symmetric operators (see, e.g., [21]). We compare the spectra of the Landau operators for these two models and observe that for some values of the magnetic field, one has an edge state band below the first bulk band. The structure of the paper is rather natural. We describe, consequently, the models for chain of circles and for chain of disks, and then compare the corresponding spectra.

2. Chain of circles

Consider an infinite chain of circles $C_n,\ n = 1, 2, \dots$ of radii a. The state space is $\mathcal{H} = \bigoplus\limits_{n=1}^{+\infty} L^2(C_n)$. To construct the Hamiltonian of the charge particle for the chain of coupled circles, we start from self-adjoint operator H_{cc}, $H_{cc} = \bigoplus\limits_{n=1}^{+\infty} H_c^n$. Here H_c^n is the Landau operator for the circle C_n. Using the standard polar coordinates (r, φ) on the circle, one can represent the Hamiltonian in the following form:

$$H_c^n = \frac{\hbar^2}{2ma^2}\left(-\imath\frac{\partial}{\partial\varphi} + \frac{\Phi}{\Phi_0}\right)^2 .$$

Here, m is an electron mass, $\Phi = \pi a^2 B$ is a magnetic flux, $\Phi_0 = \dfrac{\hbar}{2c}$ is the quantum of the magnetic flux. We use the unit system such that the factor $\dfrac{\hbar^2}{2ma^2}$ is equal to 1 (i.e. $\hbar = 1\ , m = 1/2,\ a = 1$).

A rigorous mathematical model of our system of coupled circles is constructed by a conventional way by use of the operator extensions theory (see, e.g., [14–19]). We assume that the contacts are located at the opposite points (a, φ_1) and (a, φ_2), where $\varphi_1 = 0,\ \varphi_2 = \pi$ (see Fig. 1). We restrict the initial operator H_{cc} on the set $D_0 = \bigcup\limits_{n=1}^{+\infty}\{f \in D(H_{cc}) : f(q_n) = 0\}$, where q_n is the contact point. The model Hamiltonian is given by a self-adjoint extension of this symmetric operator. We choose the extension corresponding to the following boundary conditions:

$$\begin{cases} \psi^{n+1}(\varphi_2^{n+1}) = e^{\imath ql}\psi^n(\varphi_2^n), \\ \psi'^{n+1}(\varphi_2^{n+1}+0) - \psi'^{n+1}(\varphi_2^{n+1}-0) = e^{\imath ql}[\psi'^n(\varphi_2^n+0) - \psi'^n(\varphi_2^n-0)], \\ \psi^{n+1}(\varphi_2^{n+1}) = \psi^n(\varphi_1^n) = \\ \beta[\psi'^{n+1}(\varphi_2^{n+1}+0) - \psi'^{n+1}(\varphi_2^{n+1}-0) + \psi'^n(\varphi_1^n+0) - \psi'^n(\varphi_1^n-0)], \end{cases} \tag{1}$$

where $l = 2a = 2$, q is the quasi-momentum, β is the coupling parameter for the contact points.

Taking into account the expression for the electron wave function $\psi(\varphi)$:

$$\psi(\varphi) = \alpha_1 G(\varphi, \varphi_1, E) + \alpha_2 G(\varphi, \varphi_2, E),$$

and (1), we obtain the following dispersion equation:

$$4Q_{21}\cos(ql) + \beta^{-1}\det Q - 2\operatorname{Tr} Q = 0, \tag{2}$$

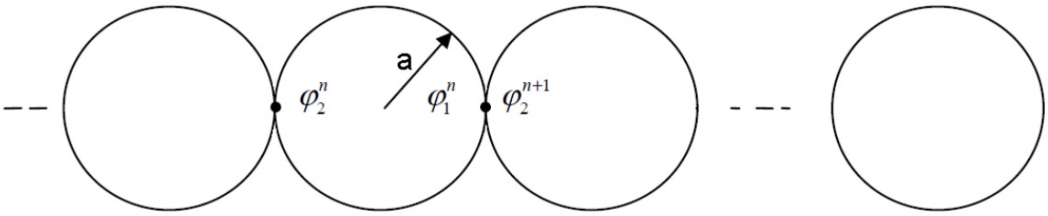

FIG. 1. Chain of circles (disks)

where Q is the Krein Q-matrix:

$$Q_{11}(E) = Q_{22}(E) = \frac{1}{kr}\left[\frac{\sin\pi kr\cos\pi kr}{\sin^2\pi\eta-\sin^2\pi kr}\right],$$

$$Q_{12}(E) = Q_{21}(E) = \frac{1}{kr}\left[\frac{\sin\pi kr\cos\pi\eta}{\sin^2\pi\eta-\sin^2\pi kr}\right].$$

Solutions of (1) for various quasi-momenta give us the spectral bands.

3. Chain of disks

In this section, we consider a system with similar geometrical structure but circles in the chain are replaced by disks of the same radius $D_n = \{(r,\varphi) : r \le a\}$. Here, r,φ are the standard polar coordinates. The initial Hamiltonian for our procedure is $H_{cd} = \bigoplus_{n=1}^{+\infty} H_d^n$, where H_d^n is the Landau operator for the disk D_n with the Dirichlet boundary conditions:

$$H_d = -\frac{1}{2m}\left(\imath\hbar\nabla - \frac{e}{2c}B\times\mathbf{r}\right)^2.$$

We introduce the following notations:

$$\omega = \frac{|eB|}{cm},\ \mu = \left(\frac{\hbar c}{|eB|}\right)^{1/2},\ x_0 = \frac{a}{2\mu^2}.$$

An eigenfunction of the operator H_{cd} with the Dirichlet boundary condition is as follows:

$$\psi(r,\varphi) = \left(\frac{m\omega}{2\pi\hbar c_{ln}}\right)^{1/2}\frac{r^{|l|}}{(2\mu^2)^{|l|/2}}\exp\left(\imath l\varphi - \frac{r^2}{4\pi\mu^2}\right)\Phi\left(\varepsilon_{ln}, |l|+1, \frac{r^2}{2\mu^2}\right).$$

We denote by $E_{ln},\ l = 0, \pm1, \pm2, \dots$ the corresponding eigenvalue:

$$E_{ln} = \hbar\omega\left(\frac{l+|l|+1}{2} - \varepsilon_{ln}\right),$$

where ε_{ln} is the $n-$th root of the equation $\Phi(\varepsilon, |l|+1, x_0) = 0$, Φ is the Kummer function. Here, c_{ln} is the normalization constant:

$$c_{ln} = \int_0^{x_0}\exp(-x)x^{|l|}\Phi^2(\varepsilon_{ln}, |l|+1, x)dx.$$

The Green function for a single disk has the following form [20]:

$$G(r,\varphi,r',\varphi';E)=\frac{m\omega}{2\pi\hbar}\exp\left(-\frac{r^2+r'^2}{4\mu^2}\right)\sum_{l=-\infty}^{+\infty}\frac{(rr')^{|l|}}{(2\mu^2)^{|l|}}\exp(\imath l(\varphi-\varphi'))\times$$
$$\sum_{n=1}^{+\infty}\frac{\Phi(\varepsilon_{ln},|l|+1,\frac{r^2}{2\mu^2})\Phi(\varepsilon_{ln},|l|+1,\frac{r'^2}{2\mu^2})}{c_{ln}(E_{ln}-E)}. \tag{3}$$

To construct the model for coupled disks, we use the operator extensions theory model, more precisely, the model of zero-width slit [21]. This model faces difficulties for the Dirichlet boundary condition. In this case, one has to extend the initial Hilbert space to the Pontryagin space with indefinite metrics. The mathematical structure of this model has been described previously, e.g., in [22]. Here, we present the resulting formulas for our case.

The wave function for the j-th disk has the form:

$$\psi_j(r,\varphi)=\alpha_1^j\left.\frac{\partial G(r,\varphi;r',\varphi';E)}{\partial r'}\right|_{r'=1,\varphi'=0}+\alpha_2^j\left.\frac{\partial G(r,\varphi;r',\varphi';E)}{\partial r'}\right|_{r'=1,\varphi'=\pi}.$$

The asymptotics of this function near the chosen (contact) points $(r,\varphi)=(1,0)$, $(r,\varphi)=(1,\pi)$ contain a singular term. To construct a self-adjoint extension in the Pontryagin space (i.e. the model Hamiltonian), one should introduce a linear relation between the main singular and regular terms of the asymptotics from the both sides of the contact points (i.e. in neighbor disks).

We assume the existence of the δ-potentials at the contact points. This gives us a rule for selection of the self-adjoint extension from the family of extensions.

As for the chain, we should take into account the periodicity. This can be made using the Bloch's theory (similarly to the case of circles) or by the transfer-matrix technique (see, e.g. [14]). The transfer-matrix M is determined as follows:

$$\begin{pmatrix} a_{j+1} \\ b_{j+1} \end{pmatrix}=M\begin{pmatrix} a_j \\ b_j \end{pmatrix}, \tag{4}$$

where:

$$\begin{cases} a_j=\alpha_2^j, \\ a_{j+1}=\alpha_2^{j+1}, \\ b_j=q_{12}\alpha_2^j+q_{11}\alpha_1^j, \\ b_{j+1}=q_{12}\alpha_2^{j+1}+\alpha_1^{j+1}q_{11}. \end{cases} \tag{5}$$

In this formula, the following notation is used:

$$q_{11}=\frac{\partial}{\partial r}\left(\left.\frac{\partial G(r,\varphi;r',\varphi';E)}{\partial r'}\right|_{r'=1,\varphi'=0}-\left.\frac{\partial G(r,\varphi;r',\varphi';E_0)}{\partial r'}\right|_{r'=1,\varphi'=0}\right)\Bigg|_{r=1,\varphi=0},$$

$$q_{12}=\frac{\partial}{\partial r}\left(\left.\frac{\partial G(r,\varphi;r',\varphi';E)}{\partial r'}\right|_{r'=1,\varphi'=0}\right)\Bigg|_{r=1,\varphi=\pi}.$$

The above mentioned selection rule for the extension leads to the following relations:

$$\begin{cases} \alpha_2^{j+1}+\alpha_1^j=\alpha(\alpha_2^jq_{12}+\alpha_1^jq_{11}), \\ \alpha_2^jq_{12}+\alpha_1^jq_{11}=\alpha_1^{j+1}q_{21}+\alpha_2^{j+1}q_{22}. \end{cases} \tag{6}$$

Here, α is the parameter describing the strength of the $\delta-$potential at the contact point.

Taking into account (5) and (6), we express a_{j+1}, b_{j+1} in terms of a_j, b_j:

$$a_{j+1} = \frac{q_{12}}{q_{11}} a_j - \frac{1-\alpha q_{11}}{q_{11}} b_j, \tag{7}$$

$$b_{j+1} = a_j \left(q_{11} + \frac{\alpha q_{11} - 1}{1 - \alpha q_{11}} - \frac{q_{11}^2 - q_{22}^2}{q_{11}} \right) + b_j \left(\frac{1}{q_{12}} + \frac{(1-\alpha q_{11})(q_{11}^2 - q_{22}^2)}{q_{11} q_{12}} \right). \tag{8}$$

Using (4), one obtains from (7), (8) the formula for the transfer-matrix M:

$$M = \begin{pmatrix} \dfrac{q_{12}}{q_{11}} & -\dfrac{1-\alpha q_{11}}{q_{11}} \\ q_{11} - 1 - \dfrac{\det Q}{q_{11}} & \dfrac{1}{q_{12}} + \dfrac{(1-\alpha q_{11}) \det Q}{q_{11} q_{12}} \end{pmatrix}, \tag{9}$$

where $\det Q = q_{11}^2 - q_{12}^2$. One can check that $\det M = 1$. In order for E to belong to the continuous spectrum of the Hamiltonian, the modula of the eigenvalues of the matrix $M = M(E)$ must be equal to 1 (see, e.g. [14]). In our case, it reduces to the following inequality:

$$|TrM(E)| \leq 2.$$

4. Results and discussion

The spectral bands of the Hamiltonian for the periodic chain of circles are obtained by solving equation (2) for various quasi-momenta q. The dependence of the dispersion equation solution upon the quasi-momentum is shown in Fig. 2. The picture depends on the value of the magnetic flux $\dfrac{\Phi}{\Phi_0}$. For the semi-integer flux (Fig. 2a), one has only levels (so-called, flat bands, i.e. infinitely degenerate eigenvalues). Fig. 2b shows the band structure for $\dfrac{\Phi}{\Phi_0} = 0.2$.

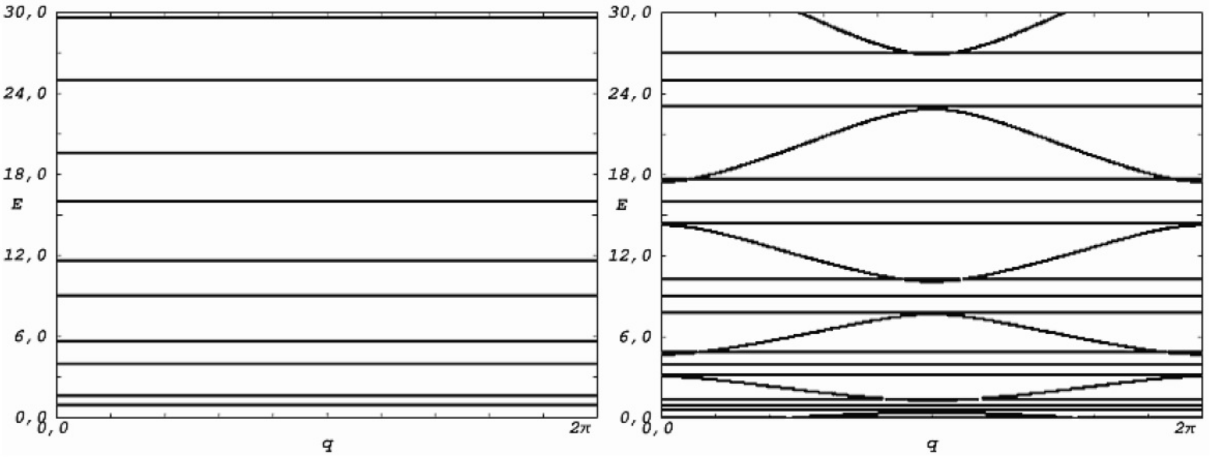

FIG. 2. The band structure for the circles chain for different values of the magnetic flux: a – for $\dfrac{\Phi}{\Phi_0} = 0.5$; b – for $\dfrac{\Phi}{\Phi_0} = 0.2$.

The dependence of the bands on the magnetic field for the disks system for different α parameter values is shown in Fig. 3.

The dependence of the magnetic field bands for both systems is shown in Fig. 4. Bands correspond to the dark areas. One can see that for chosen range of the magnetic field, the lowest band for the chain of circles lies below the lowest band for the chain of disks. Hence,

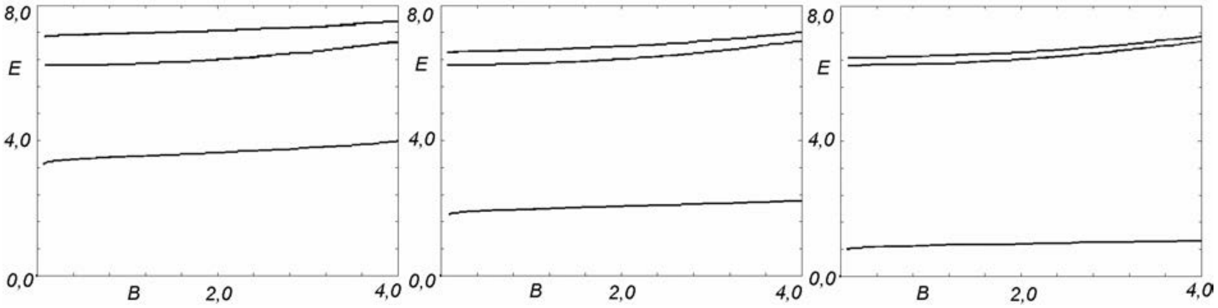

FIG. 3. The dependence of the bands on the magnetic field for the disks system for different α parameter values: a – for $\alpha = 0.5$; b – for $\alpha = 1$; for $\alpha = 2$.

for these magnetic field values, one has something similar to the topological insulator effect; the edge state lies below all bulk states.

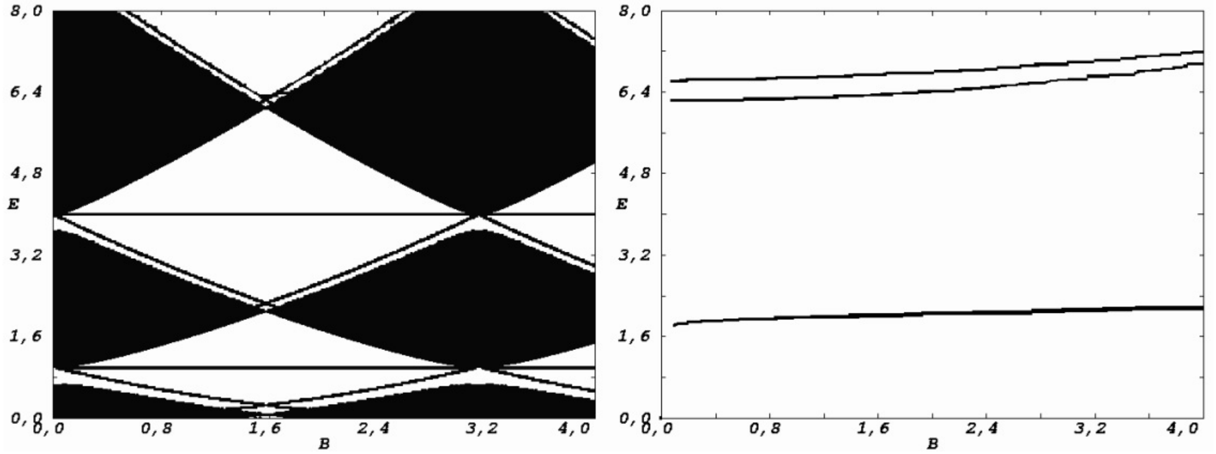

FIG. 4. The dependence of the energy bands on the magnetic field B: a – for the chain of disks; b – for the chain of circles.

Acknowledgements

This work was partially financially supported by the Government of the Russian Federation (grant 074-U01), by the Ministry of Science and Education of the Russian Federation (GOSZADANIE 2014/190, Project 14.Z50.31.0031), by grants of the President of Russia (state contracts 14.124.13.2045-MK and 14.124.13.1493-MK).

References

[1] C. Hermosa, J.V. Alvarez, et al. Intrinsic electrical conductivity of nanostructured metal-organic polymer chains. *Nature Comm.*, 2013, **4**, P. 1709.

[2] A. Medhi, V.B. Shenoy. Continuum theory of edge states of topological insulators: variational principle and boundary conditions. *J. Phys.: Condens. Matter*, 2012, **24** (35), P. 355001.

[3] M.Z. Hasan, C.L. Kane. Topological insulators. *Rev. Mod. Phys.*, 2010, **82** P. 3045-3067.

[4] S. Mao, Y. Kuramoto, K.-I. Imura, A. Yamakage. Analytic theory of edge modes in topological insulators. *J. Phys. Soc. Japan*, 2010, **79**, P. 124709.

[5] J.J. Cha, K.J. Koski, Yi. Cui. Topological insulator nanostructures. *Phys. Status Solidi RRL*, 2013, **7** (1-2), P. 15–25.

[6] N.I. Gerasimenko, B.S. Pavlov. Scattering problems on noncompact graphs. *Theoret. Math. Phys.*, 1988, **74**, P. 230–240.

[7] P. Exner, P. Seba. Free quantum motion on a branching graph. *Rep. Math. Phys.*, 1989, **28**, P. 7–26.

[8] P. Exner, et al. (Eds.) Analysis on Graphs and Its Applications. *Proc. Symp. Pure Math.*, (AMS, Providence, Rhode Island, 2008).

[9] O. Post. *Spectral Analysis on Graph-like Spaces*. Springer, Berlin, 2010.

[10] I.S. Lobanov, I.Yu. Popov. Scattering by zigzag-armchair nanotube junction. *Nanosystems: Physics, Chemistry, Mathematics*, 2012, **3** (2), P. 6–28.

[11] I.Yu. Popov, A.N. Skorynina, I.V. Blinova. On the existence of point spectrum for branching strips quantum graph. *J. Math. Phys.*, 2014, **55**, P. 033504/1–20.

[12] V. Kostrykin, R. Schrader. Kirchhoff's rule for quantum wires. *J. Physics A: Math. Gen.*, 1999, **32**, P. 595–630.

[13] K. Pankrashkin. On the Robin eigenvalues of the Laplacian in the exterior of a convex polygon. *Nanosystems: Phys., Chem., Math.*, 2015, **6** (1), P. 46–56.

[14] P. Duclos, P. Exner, O. Turek. On the spectrum of a bent chain graph. *J. Phys. A: Math. Theor.*, 2008, **41**, P. 415206.

[15] I.Yu. Popov, P.I. Smirnov. Spectral problem for branching chain quantum graph. *Phys. Lett. A*, 2013, **377**, P. 439–442.

[16] I.S. Lobanov, E.S. Trifanova. Direct and inverse problems in the model of quantum graphs. *Nanosystems: Phys., Chem., Math.*, 2012, **3** (5), P. 6–32.

[17] I.S. Lobanov, A.I. Trifanov, E.S. Trifanova. Genetic algorithm for constructing graphene nanoribbon with given electronic transport properties. *Nanosystems: Phys., Chem., Math.*, 2013, **4**, P. 512–523.

[18] D.A. Eremin, I.Yu. Popov. Quantum ring with wire: a model of two-particles problem. *Nanosystems: Phys., Chem., Math.*, 2012, **2** (2), P. 6–32.

[19] M.A. Kokoreva, V.A. Margulis, M.A. Pyataev. Electron transport in a two-terminal AharonovBohm ring with impurities. *Physica E*, 2011, **43**, P. 1610.

[20] B.S. Pavlov, I.Yu. Popov, V.A. Geyler, O.S. Pershenko. Possible construction of a quantum multiplexer. *Europhys. Lett.*, 2000, **52**, P. 196.

[21] I.Yu. Popov. The resonator with narrow slit and the model based on the operator extensions theory. *J.Math. Phys.*, 1992, **33** (11), P. 3794–3801.

[22] I.Yu. Popov. Model of point-like window for electromagnetic Helmholtz resonator. *Zeitschrift fur Analysis und ihre Anwendungen*. 2013, **32** (2), P. 155–162.

NANOSYSTEMS: PHYSICS, CHEMISTRY, MATHEMATICS, 2015, 6 (5), P. 644–649

Nano-ZnS thin films for solar cell

M. A. Jafarov, E. F. Nasirov, S. A. Jahangirova, R. Jafarli
Baku State University, Baku, Azerbaijan
maarif.jafarov@mail.ru

PACS 71.55.Gs, 78.20.e, 85.30.z, 85.60.Dw DOI 10.17586/2220-8054-2015-6-5-644-649

In this paper, we report the effect of deposition time on the properties of zinc sulfide thin films. The ZnS thin films have been grown on amorphous glass substrates and at various deposition periods ranging from 30 to 120 min by chemical bath deposition technique. Other parameters, such as reactant concentration, solution pH, and bath temperature were kept constant for the all depositions. Morphological characterizations of the surface were studied using the atomic force microscopy (AFM). The AFM images confirmed that the grain size of ZnS increased with increased deposition time. Average diameter of nanoparticles was between 60 and 90 nm, while the roughness ranged from 6 to 11 nm. Optical properties, which were determined from UV–VIS spectrophotometry, were obtained by analyzing the measured absorbance and transmittance spectrum. The zinc sulfide thin films show high transmittance in the visible region and the ZnS band gap value was estimated to be in range of 3.99 – 4.05 eV.

Keywords: zinc sulfide, nanoparticles, chemical bath deposition.

Received: 10 June 2015

Revised: 25 June 2015

1. Introduction

Zinc sulfide (ZnS) is an important II – VI semiconducting material with a wide direct band gap of 3.65 eV in the bulk [1–5]. This new class of materials has not only provided many unique opportunities but also exhibited novel optical and transport properties, which are potentially useful for technological applications. These materials have potential application in optoelectronic devices, such as blue light emitting diodes, electroluminescent devices and photovoltaic cells [1–3] and more recently as n-type nonreflecting window materials in heterojunction solar cells. The efficiency of heterojunction solar cells depend largely on the interfacial properties between absorber and buffer layers. The wider bandgap of ZnS enables high energy incident photons to reach the window-absorber junction, enhancing the blue response of the photovoltaic cells and thus contributes to a better cell performance [4]. Recently, efficiency enhancement of solar cells has become more important due to the need for environmentally benign renewable energy sources. To improve the light harvesting in solar cells, it is crucial to minimize undesirable Fresnel surface reflection losses at the interface between air and the top layer of solar cells over the entire range of the solar spectrum.

Zinc sulfide has found wide use as a thin film coating in the optical and microelectronic industries, having a high refractive index (2×25 at 632 nm), high effective dielectric constant (9 at 1 MHz) and wide wavelength pass band (0×4 – 13 mm) [5]. There have been various studies on the bulk and thin film characteristics of ZnS, including optical and electrical properties [6]. The optical properties of the prepared film depend strongly on the manufacturing technique. Two of the most important optical properties; refractive index and the extinction coefficient are generally called optical constants. The amount of light which is transmitted through thin film material depends on the amount of the reflection and absorption that takes place along the light path [7].

Many growth techniques have been reported for the preparation of ZnS thin films, such as sputtering, pulsed-laser deposition, metal organic chemical vapor deposition, electron beam evaporation, photochemical deposition, thermal evaporation, sol-gel processing, co-precipitation and chemical bath deposition [8]. These doped ZnS semiconductor materials have a wide range of applications in electroluminescence devices, phosphors, light emitting displays, and optical sensors. Doped nanoparticles with dimensions below that of the Bohr diameter exhibit interesting optoelectronic properties due to quantum size effect and are potential candidates for a variety of applications. The characteristics and concentrations of dopants are responsible for particular luminescence emission and efficiency of semiconductor nanoparticles [9]. Hence, investigation of the role that dopant concentration has on doped semiconductor nanoparticle optical properties of is very important from the viewpoints of basic and applied physics [10]. Recently, 2D nanostructure P-N junctions have attracted a great deal of attention for their potential application in photovoltaic devices. Zinc sulfide (ZnS) was one of the first semiconductors discovered and is also an important semiconductor material with direct wide band gaps for cubic and hexagonal phases of 3.72 and 3.77 eV, respectively [9, 11]. It has a high absorption coefficient in the visible range of the optical spectrum and reasonably good electrical properties. This property makes ZnS a very attractive as an absorber in heterojunction thin-film solar cells. Among various other methods, the chemical bath deposition – CBD that we use in present case is a well known deposition process for some chalcogenides, it is well known as prevented low temperature aqueous technique for deposition large area of semiconductor thin films and has gained renewed interest due to the good quality and high purity of the deposited films. CBD of ZnS is a highly reproducible and controllable technique, thus it is considered the simplest and the most economical one. CBD results good deposits on suitable substrates by controlled precipitation of the compound from the solution.

2. Experiment

The basic principle of the CBD technique consists in the controlled generation of the metal and chalcogenide ions in an alkaline medium and their ion by ion deposition on the substrate in order to form a film. In our CBD experiment, the deposition of ZnS film was based on the reaction between zinc sulfate ($ZnSO_4$) as a source of Zn^{2+}, Thiourea ($SC(NH_2)_2$) as a source of S^{2-} and ammonia (NH_4OH) that used as complexing agent to vary the pH of the reaction bath and to control the Zn^{2+} concentration.

ZnS films were deposited on commercial glass substrates (75 mm × 25 mm × 1 mm) by chemical bath deposition technique. Prior to deposition, the substrate was degreased in ethanol for 10 min, followed by ultrasonic cleaning with doubly-distilled water for another 10 min, rinsed in de-ionized water and finally air dried in. In a typical deposition set up of ZnS, the CBD was achieved by mixing 10 ml of 0.025 M $ZnSO_4$ solution, 10 ml of 0.27 M $SC(NH_2)_2$ solution, and 2.9 M NH_4OH solution. Firstly, ammonia solution was added slowly to the required quantity of zinc sulfate, after stirring for several minutes the solution becomes colorless and homogeneous, thereafter, a thiourea solution was added under stirring. Lastly, the reaction solution was placed in 50 ml beaker (sealed with a Teflon tape) into the water bath pot. The glass substrates were then immersed vertically inside this beaker and supported against the wall of the beaker without disturbing it. The deposited film was carried out water bath temperature at $T_b = 70$ °C, for different durations, (30, 60, 90, 120 min) that were selected to study the characteristics of ZnS thin films. After complete film deposition, each sample was removed from the beaker and was cleaned with de-ionized water to remove the white, loosely, adherent powders precipitate in the solution during the deposition. The structural properties of ZnS films are studied by using X-ray diffractometer (XRD) using Cu-Kα radiation with wavelength 1.5418 Å. Surface morphology was examined by Scanning Electron Microscope (SEM). The atomic force microscopy (AFM) was used to investigate the surface morphology and surface roughness. AFM imaging is performed on the Nanosurf system (easyScan2) operating in a tapping mode in air at room temperature. The optical transmission and absorption studies of the deposited ZnS thin films were carried out with a UV–VIS spectrophotometer (Varian carry 5000). Absorption coefficient corrected for scattering contribution versus wavelength. The error bars represent the standard deviation.

3. Results and discussion

AFM allows us to obtain microscopic information on the surface structure and to plot topographies representing the surface relief. In this work, we have used this technique to visualize the surface relief, specify the growth, and determine the contribution of the deposition time (t_d) to the quality of the film. AFM images of the surface morphology recorded on samples of the ZnS–NPs thin films deposited with different deposition times for ($t_d = 10, 40$ min) are shown in Fig. 1. In all cases the prepared thin films have good quality, uniform morphology and covered the entire substrate surface. We can expect this result due to the increase of the film thickness with the deposition time.

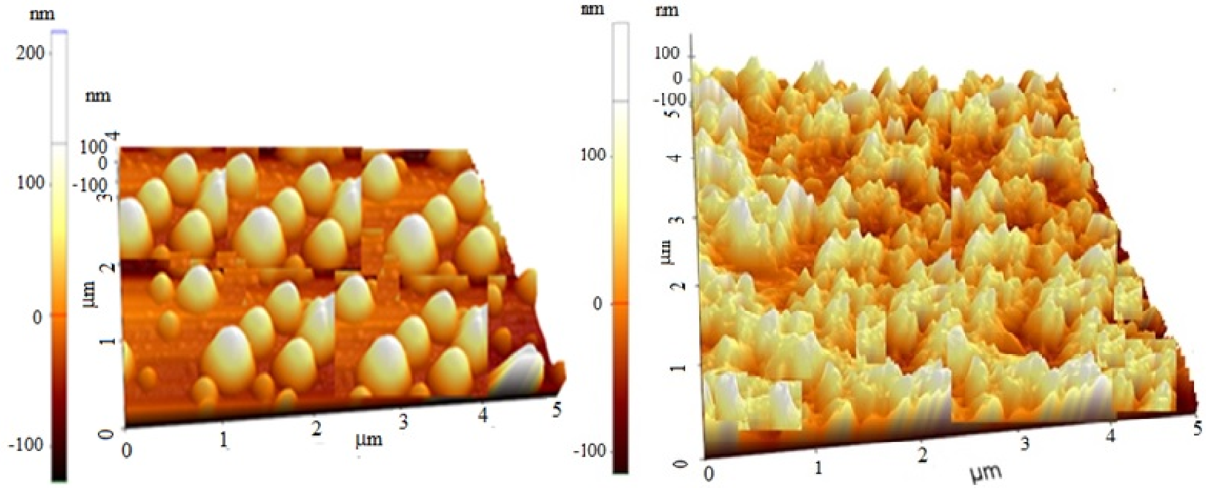

FIG. 1. AFM images of the surface morphology recorded on samples of the ZnS–NPs thin films deposited with different deposition time periods for (t, min: 10, 40)

The same relation between the mean height of ZnS–NPs and the deposition time has been observed. This can be seen in the increasing roughness with increased deposition time and that because new bigger domed grains are formed, the layer is more complete and has fewer voids. It is important to note that these obtained values are averaged and there is a statistical variation associated with them, which depends on the location of the measurement that is performed on the samples. To minimize these errors, we performed many measurements of each parameter at several different locations on the surface of samples.

The optical properties evolution for the prepared ZnS thin films was determined after obtaining the absorbance and transmittance spectrum with a UV–VIS spectrophotometer. UV–VIS transmittance spectra of ZnS–NPs formed at bath or reaction temperature of 70 °C with different reaction times (30, 60 min) are given in Fig. 2. Transmittance was recorded from 300 – 800 nm. The transmission of the zinc sulfide thin films decreases with increased deposition times. The average transmittance of these films is calculated to be 99 %, 97.5 %, 96 %, and 95 %, respectively. These results are related to the increased deposition time; as a result of the voids in the ZnS thin layer filling up with new ZnS grains, film thickness is increased, thus reducing the transmittance. In general, the layers produced in this work exhibit high transmittance, which depends on low film thickness. In addition, the decreased transmittance can be linked with agglomeration and increased grain size, indicating its high surface roughness. The ZnS thin films have a steep optical absorption feature, indicating good homogeneity in the shape and size of the ZnS–NPs and low defect density.

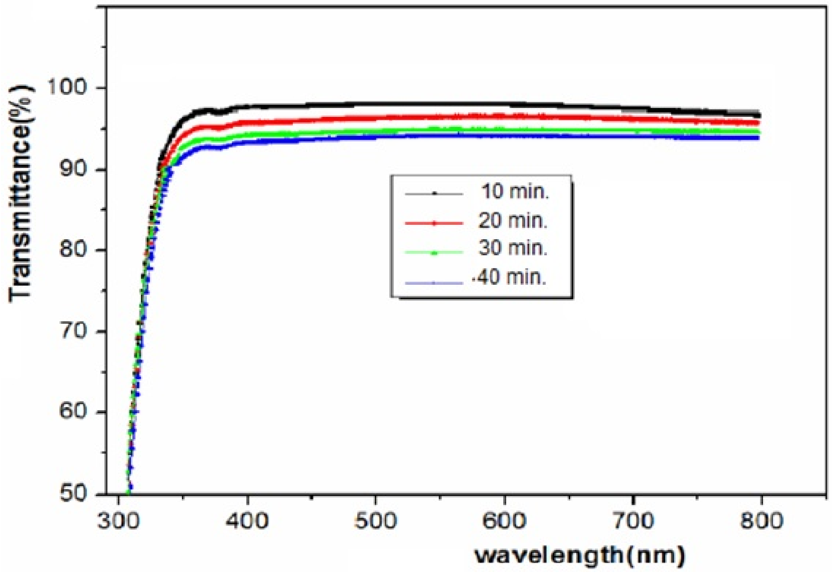

FIG. 2. Transmittance spectra of ZnS thin film at different deposition times (10, 20, 30, 40 min)

Figure 3 shows the absorption coefficient a as a function of photon energy; at low photon energies, a decreases the probability of electrical transfer between the valance and conduction bands, making it very rare and conversely, will increase at the absorbance edge, towards high energy photons.

Using the last data, the band gap energy of ZnS thin film was estimated by plotting, as in Fig. 4. The linear nature of the plot indicates that ZnS is a direct band gap material. The films' optical band gaps can be evaluated by extrapolating the straight portion to the axis.

In this work, the band gap energy (E_g) was determined to be in the range of 4.05 – 3.6 eV for the ZnS films with different deposition times, from 10 to 40 min, respectively which closely agree with the values reported for ZnS thin films obtained by CBD. The band gap values of the as deposited ZnS films are somewhat larger than the typical band gap for bulk ZnS ($\sim$ 3.6 eV) at 300 K. In Fig. 4, we have reported the variation of band gap energy and thickness of thin film ZnS–NPs as a function of deposition time. We note a reduction in the gap with the deposition time this due to the quantum size effect as expected for the nanoparticles nature of the films. In fact, it is observed that the band gap energy values of ZnS thin layers decrease slightly from 4.05 to 3.99 eV with increased deposition time. There was good agreement between the structural and optical properties and calculated band energy gap. The thickness of ZnS thin film slightly increased from 65 to 90 nm when the deposition time was increased from 10 to 40 min. This may be due to processes of heterogeneous and homogenous precipitation, which increase with time, leading to higher ZnS thin film growth rates.

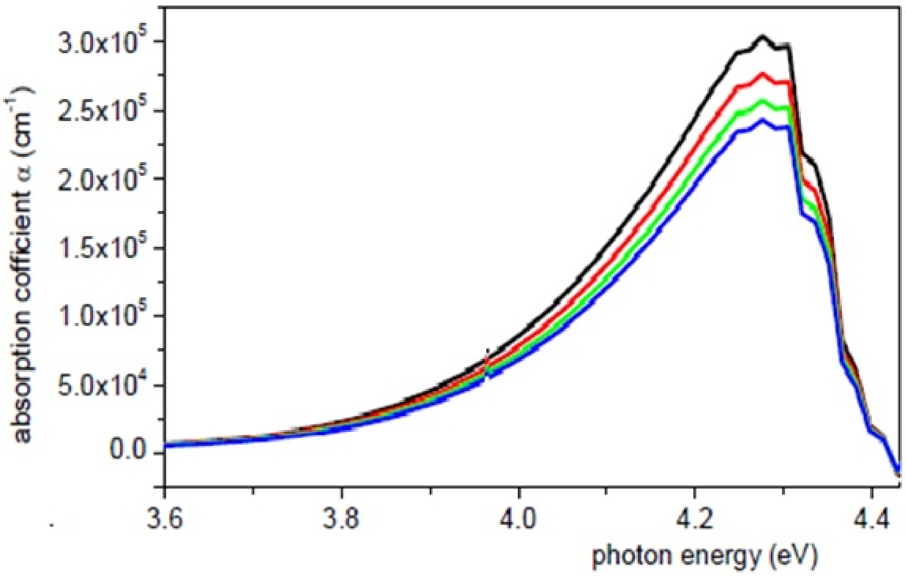

FIG. 3. Absorption coefficient versus photon energy for ZnS thin films deposited at different times (10, 20, 30, 40 min)

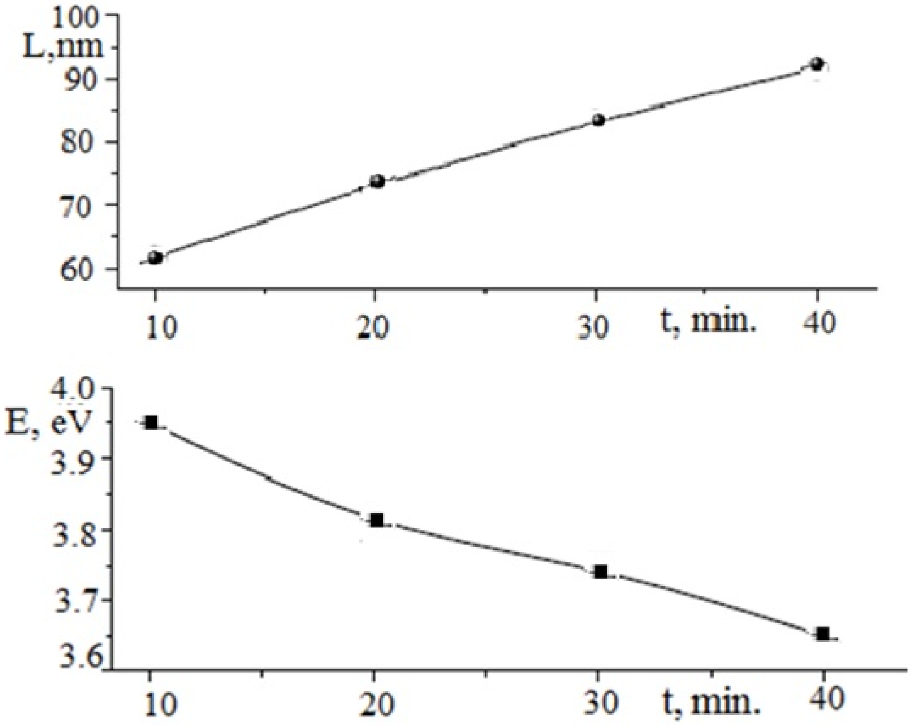

FIG. 4. Variation of ZnS thin films thickness and band gap with deposition times at fixed bath temperature $T_b = 70$ °C

4. Conclusion

We have successfully used chemical bath deposition to obtain ZnS/glass thin films. AFM showed that the films were of good quality and have uniform distribution of ZnS–NPs over the glass substrate. Images revealed that the particle size increased with increasing of deposition time, the average diameter was 180 nm. The high transparency of the films, over 90 %, was investigated using a UV–VIS spectrophotometer. The optical direct band gap energy was calculated to be between 3.99 – 4.05 eV for the ZnS films with different thicknesses. Structural and optical properties were in agreement with each other. From these studies, we are able to optimize the process in order to produce the antireflection layer of ZnS suitable for optical window in solar cells.

References

[1] T. Ben Nasr, N. Kamoun, M. Kanzari, R. Bennaceur. Effect of pH on the properties of ZnS thin films grown by chemical bath deposition. *Thin Solid Films*, 2006, **500**, P. 4–8.

[2] A.U. Ubale, D.K. Kulkarni. Preparation and study of thickness dependent electrical Characteristics of zinc sulfide thin films. *Bull. Mater. Sci.*, 2005, **28** (1), P. 43–47.

[3] N.M. Saeed. Structural and Optical Properties of ZnS Thin Films Prepared by Spray Pyrolysis Technique. *Journal of Al-Nahrain University*, 2011, **14** (2), P. 86–92.

[4] R. Sharma, B.P. Chandra, D.P. Bisen. Optical properties of ZnS: Mn nanoparticles prepared by chemical bath routs. *Chalcogenide Letters*, 2009, **6** (8), P. 339–342.

[5] J. Hasanzadeh, A. Taherkhani, M. Ghorbani. Luminescence and Structural Properties of ZnS: Cu Nanocrystals Prepared Using a Wet Chemical Technique. *Chinese journal of physics*, 2013, **51** (3), P. 540–550.

[6] X. Wu, F. Lai, et al. Effects of substrate temperature and annealing on the structure and optical properties of ZnS film. *Proc. of SPIE*, 2007, **6722**, 67222L(1–5).

[7] K. Jayanthi, S. Chawla, H. Chander, D. Haranath. Structural, optical and photoluminescence properties of ZnS: Cu nanoparticle thin films as a function of dopant concentration and quantum confinement effect. *Cryst. Res. Technol.*, 2007, **42** (10), P. 976–982.

[8] L.-W. Ji, Y.-J. Hsiao, et al. Annealing effect and photovoltaic properties of nano-ZnS/textured p-Si heterojunction. *Nanoscale Research Letters*, 2013, **8** (470), P. 1–6.

[9] S.P. Patel, J.C. Pivin, et al. Grain growth and structural transformation in ZnS nanocrystalline thin films. *Vacuum*, 2010, **85**, P. 307–311.

[10] M. Ashrat, M. Mehmood, A. Qayyum. Influence of source-to-substrate distance on the properties of ZnS films grown by close-space sublimation. *Semiconductors*, 2012, **46** (10), P. 1326–1330.

[11] H. Abdullah, N. Saadah, S. Shaari. Effect of Deposition Time on ZnS Thin Films Properties by Chemical Bath Deposition (CBD) Techinique. *World Applied Sciences Journal*, 2012, **19** (8), P. 1087–1091.

NANOSYSTEMS: PHYSICS, CHEMISTRY, MATHEMATICS, 2015, 6 (5), P. 650–660

Prediction of glass forming ability in Cu_xZr_{1-x} alloys using molecular dynamics

M. M. Khandpekar[1*], A. Shrivastava[1], D. S. Gowtam[2], M. Mohape[2], V. P. Deshmukh[2]

[1]Materials Research Lab, Department of Physics, Birla College,
Kalyan – 421304, India
[2]Naval Material Research Lab, Shil-Badlapur Road Ambernath,
Thane, Maharashtra – 42150, India
*dr_mmk1968@yahoo.com

PACS 61.43.Bn, 61.43.Dq, 61.43.Fs, 61.66.Dk DOI 10.17586/2220-8054-2015-6-5-650-660

Binary Cu_xZr_{1-x} ($x = 0.46, 0.50, 0.58, 0.62$) alloy systems were developed using a conventional melting route. Molecular dynamics (MD) simulations have been carried out using the embedded atom method (EAM) potentials. Radial distribution function (RDF) and Voronoi calculations have been conceded for amorphous structure verification. The reduced glass transition temperature (T_{rg}) has been determined in order to predict the glass forming ability (GFA) of these alloys. T_l is found to be a better substitute for T_m and the simulated T_{rg} values are seen to be in good agreement with the experimental results in limits of 0.8 – 5.4 %.

Keywords: Amorphous materials, Simulation and Modelling, Structural and thermal properties.

Received: 4 June 2015

Revised: 3 July 2015

Final revision: 15 September 2015

1. Introduction

The excellent properties of metallic glasses over their crystalline counterparts have attracted the attention of the scientific and industrial communities [1–4]. The challenge lies in predicting the glass forming compositions and thus, has been an active area of research [5–10]. Several empirical rules and criteria such as, an alloy must contain more than two elements, negative heat of mixing between the constituent atoms, low liquid eutectic, have been proposed to predict the glass forming ability (GFA) followed by rigorous experimentation [11–14]. Certainly, these rules have played an important role in providing enough information to synthesize bulk metallic glasses (BMGs), but experiments have also suggested that a minor change in composition can effectively change GFA [15].

Hence, it is essential to employ simulations and modeling methods for the prediction of GFA in order to reduce the associated time, energy and costs associated with these studies. Binary alloys are basically simple to model and as a result of the possibility of wide glass-forming compositions in Cu–Zr binary systems, they may be considered to be perfect systems for the prediction of GFA [16]. Additionally, Cu–Zr systems have experimental data availability (Table 1) [13, 14] for the comparison, and accessibility of EAM potentials for Cu and Zr elements for simulation.

One such simulation method which can be used to understand the behavior of metallic glasses at the atomic level and to predict GFA is Molecular dynamics (MD). In the present work, MD simulations have been applied to binary Cu_xZr_{1-x} alloys in order to predict their GFA. Reduced glass transition temperature criteria ($T_{rg} = T_g/T_l$ or T_g/T_m, where T_m is the

TABLE 1. EAM potential parameters [13, 14]

Elements	Structure	a (Å)	E_C (eV)	C_{11} (GPA)	C_{12} (GPA)	C_{44} (GPA)
Cu	fcc	3.6149^a	-3.5400	168.062	123.754	78.84
		3.61^b	3.49	168.4	121.4	75.4
Zr	hcp	3.230^c	-5.150	143.4	72.8	32
		3.232^d	-6.32	153	67	36

^{a,c} EAM, ^{b,d} Experiments

onset melting temperature T_g is the glass transition temperature, T_l is the liquidus temperature) have been employed in the GFA prediction process [14]. T_g and T_l are calculated using Wendt-Abraham (WA) parameter [17] and volume temperature ($V-T$) curve. The relationship between the melting temperature (obtained from the MD simulation) and experimental T_l values have been correlated and compared with those reported previously [18, 19].

2. Simulation and experimental methods

2.1. Simulation

To obtain an atomic description of the crystallization process and glass formation during rapid cooling of alloys, the MD simulation technique was adopted. The embedded atom method [20] (EAM)-based potential was used to represent the pair-wise atomic interaction between Cu and Zr atoms in the liquid and amorphous states.

The molecular dynamics simulation (MD) of the copper-zirconium alloy was carried out using constant number of particles-pressure-temperature (NPT) ensemble. To model the atomic interactions, EAM potentials provided with in Large-scale atomic/molecular massively parallel simulator software (LAMMPS) [21] was used to simulate the $\mathrm{Cu}_x\mathrm{Zr}_{1-x}$ ($x = 0.46, 0.50, 0.58,$ 0.62) alloy systems. The simulated system consisted of 5000 atoms in a cubic unit cell of B2 structure with in periodic boundary conditions. The number of Cu atoms was replaced with number of Zr atoms according to the atomic percentage defined for the system under study. First, the model system was heated at 300 K to relax the system, then temperature was raised up to 3000 K and held there for 400 picoseconds (ps) in order to allow atoms to forget their initial structure. After that, the system was rapidly cooled to 2100 K and then slowly cooled from liquid state to 300 K at a cooling rate of 1×1011 K/s. At each temperature, the quantities of interest were obtained by taking averages over 80 ps. The MD time step selected for the simulation was 2 fs (1 fs = 1×10^{-15} second). The Voronoi atomic clusters of each composition were analyzed at 600K using OVITO [22].

In order to check the size effect, a system of 10000 atoms was also utilized for calculation. The simulation shows very small finite size effect on the on the structural properties. A schematic approach has been displayed adopted in this work in Fig. 1.

2.2. Experiments

In order to validate the simulation results, experiments were also performed. To prepare the alloy ingots of the system studied in present work, first Cu and Zr ingots (Sigma-Aldrich, India) of purity percentage 99.99 % and 99.95 % respectively were ultrasonically cleaned; then, each ingot was melted in vacuum arc plasma melting furnace on a water cooled copper

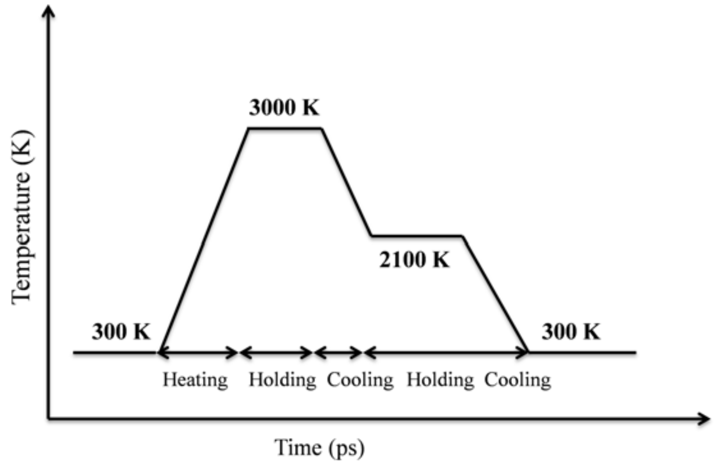

FIG. 1. Simulation schedule for studied alloy systems

plate under T_i gettered with a high purity argon atmosphere (6 bar). Each ingot was flipped over and remelted at least 4 – 5 times to obtain chemical homogeneity. The ingots were then melted again under high vacuum in glass test tube and casted in the form of amorphous ribbons using melt spinning. The prepared ribbons were then examined by a Panalytical 3040/60 X-ray diffractometer (XRD) using Cu–K$_\alpha$ source to investigate the present phase of the system. A differential scanning calorimeter (Hitachi DSC 6300) with heating rate of 20 °C/minute and argon atmosphere was used to confirm the amorphous structure by studying the glass transition temperature and crystallization temperature.

3. Results and discussion

3.1. Radial distribution function (RDF) and Voronoi tessellation

RDF is one of the most powerful techniques used for analyzing the inherent structure of liquids and amorphous alloys. It describes the spatial distribution of all other atoms with respect to the origin atom. For the bulk materials, it is given by:

$$G\left(r\right) = \frac{V}{N^2}\left\langle \sum_i \sum_{i \neq j} \delta(r - r_{ij}) \right\rangle , \tag{1}$$

where N is the number of atoms, V is volume of the cell, r and r_{ij} are the position of reference and other atoms, $G(r)$ is the probability of finding the atoms in the simulation box. For a random distribution, $G(r)$ always tends to unity. For a binary alloy system i.e. alloy containing at least atom 1 and atom 2, the radial distribution function (RDF) was calculated in the following manner:

$$G_{12}\left(r\right) = \frac{V}{N_1 N_2}\left\langle \sum_1 \sum_{1 \neq 2} \delta(r - r_{12}) \right\rangle . \tag{2}$$

Figures 2a and 2b represent the characteristic RDF's of pure copper and Zirconium at room temperature, at liquid state and in super cooled state. The sharp maxima observed in the RDF of pure copper and Zirconium at room temperature is found to correspond to the minimum bond length and crystalline state can be identified by sharp maxima. With an increase in temperature, the height of first peak of $G(r)$ is found to decrease. The broadening in the second peak indicates that the model system is in a disordered or liquid state; though first nearest neighbors were almost equivalent to their crystalline counterpart. The difference however was observed in the lower and diffuse second peaks. Cooling of the melt rapidly down to 300 K, shows a slight increase in bond length which is attributable to the rearrangement of atoms. Due to this, the values of $G(r)_{\text{Cu–Cu}}$ and $G(r)_{\text{Zr–Zr}}$ are lower in super cooled state as compared to its ordered structure.

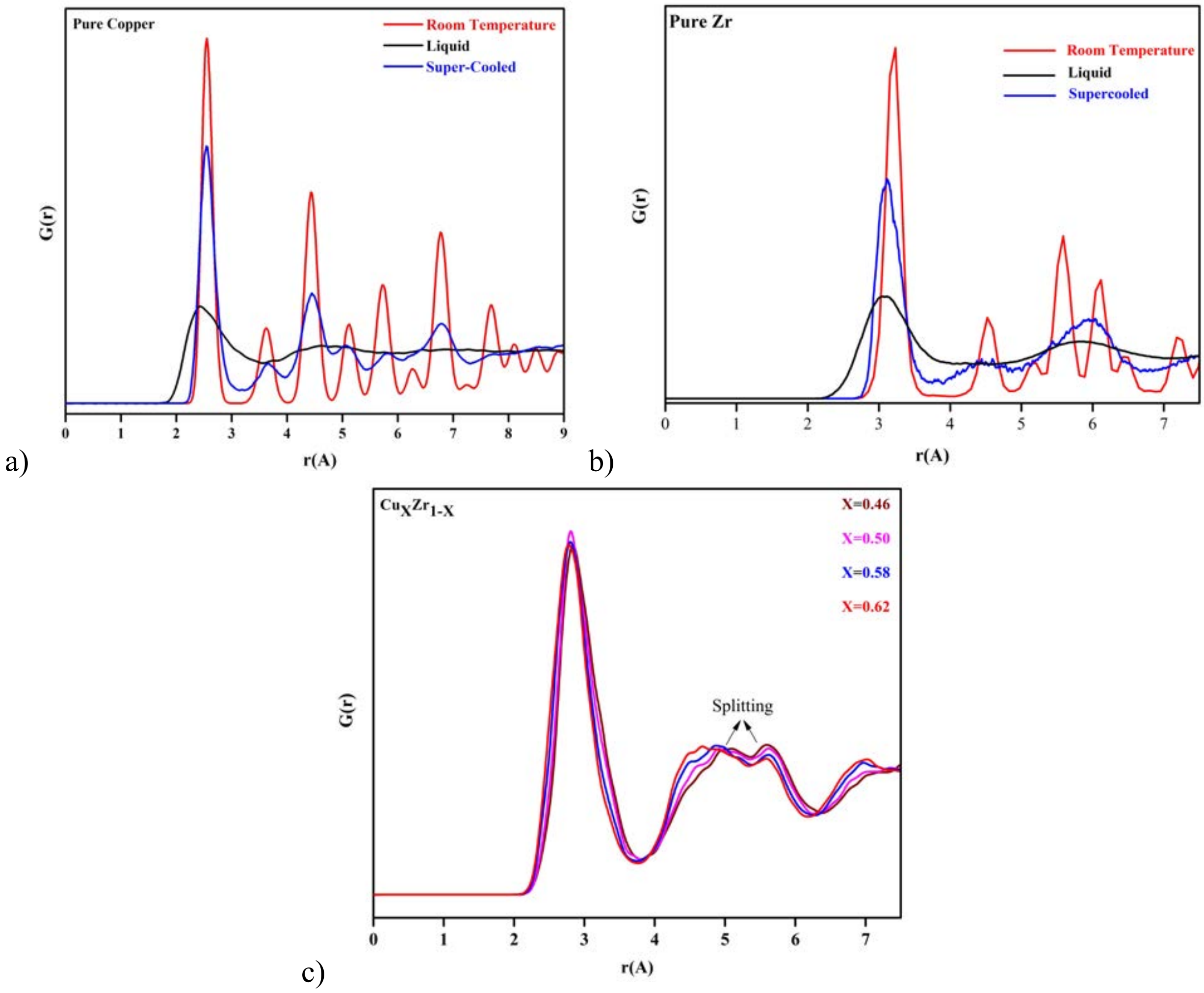

FIG. 2. RDF of Copper at (a) the room temperature, liquid state and super cooled state, Zirconium at (b) the room temperature, liquid state and super cooled state (c) Cu_xZr_{1-x} ($x = 0.46, 0.50, 0.58, 0.62$) in super cooled state

From Fig. 2c, it is clear that the addition of zirconium to copper shifts the first peak towards the higher ‘r’ values. This is due to the lower atomic radius of Cu (1.27 Å) as compared to that of Zr (1.60 Å). A splitting (marked) indicating characteristic of metallic glasses [23] is seen to make its presence in the second peak of the Copper alloy RDF plot. Further analysis of Fig. 2c showed that, upon super-cooling, there was no change in the height of the first peak, while second peak showed very slight variation. This led us to the conclusion that the super-cooled state is characterized by a local atomic arrangement to that of a liquid state.

To further analyze the local atomic arrangement, the Voronoi tessellation [24,25] method was employed. The Voronoi index is represented by a vector notation $\langle n_3, n_4, n_5, n_6\rangle$ where n_i

denotes the number of shell atoms which are connected by other shell atoms defined by RDF. A cut off distance of 5 Å [26] was selected for Voronoi polyhedra (VP) calculation. The total fractions of various VP around Cu and Zr are shown in the Fig. 3 and Fig. 4.

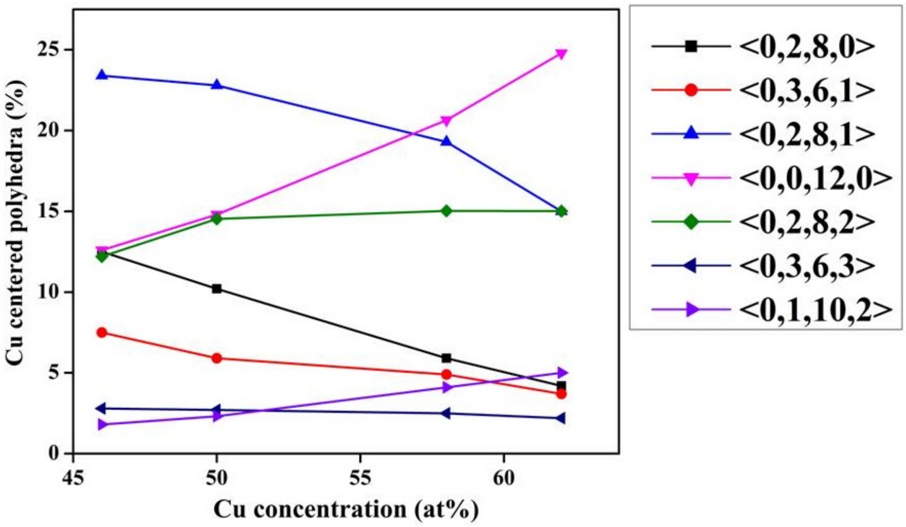

FIG. 3. Voronoi Fractions of around Cu in simulated Cu–Zr MGs at 600 K

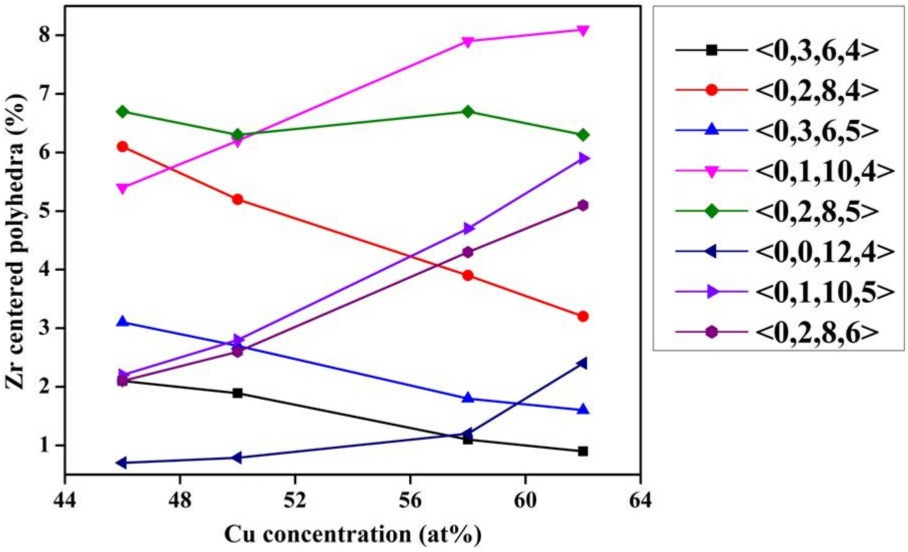

FIG. 4. Voronoi Fractions of around Zr in simulated Cu–Zr MGs at 600 K

From Fig. 3 it was observed, as concentration of Cu atoms increases from 46 at % (atomic percent) to 62 at %, the population of Cu centered five edges icosahedra face i.e., $\langle 0, 0, 12, 0\rangle$ and icosadihedra $\langle 0, 1, 0, 12\rangle$ increases, while the population of other polyhedra the such as $\langle 0, 2, 8, 0\rangle$, $\langle 0, 2, 8, 1\rangle$, $\langle 0, 3, 6, 1\rangle$ decreases, except to $\langle 0, 2, 8, 2\rangle$ which increases only to 50 at % and remains constant along with $\langle 0, 3, 6, 3\rangle$ polyhedra. This population variation of Cu center clusters was found to be consistent with the GFA of CuZr systems [27–29].

Some investigation of Zr centered VP clusters, shown in Fig. 4, suggested that the population of Zr polyhedra $\langle 0, 1, 10, 4\rangle$, $\langle 0, 1, 10, 5\rangle$, $\langle 0, 2, 8, 6\rangle$ and $\langle 0, 0, 12, 4\rangle$ gradually increased maximum up to 8 % , while the population of $\langle 0, 2, 8, 4\rangle$, $\langle 0, 3, 6, 4\rangle$, $\langle 0, 3, 6, 5\rangle$ lowered to 2 –

4 % and $\langle 0, 2, 8, 5\rangle$ remained fairly constant at 7 %. This supports the hypothesis of Peng [24], which asserts that the population of these Zr centered clusters may fundamentally determine the dynamics in the CuZr system. The analysis of both Cu- and Zr- centered VP clusters implies that the Cu-centered $\langle 0, 0, 12, 0\rangle$ VP enhances the stability of the system with Cu concentration, while other clusters slow the dynamics and both are responsible for amorphous structure evolution in the CuZr system.

The amorphous nature of our model system was experimentally confirmed by the XRD analysis of melt spin ribbons. Fig. 5 shows the XRD patterns of the melt spun ribbons of Cu$_x$Zr$_{1-x}$ ($x = 0.46, 0.50, 0.58, 0.62$). It can clearly be seen from the figure, that all exhibit broad diffraction maxima with no sign of the crystalline peak, thus confirming the amorphous nature.

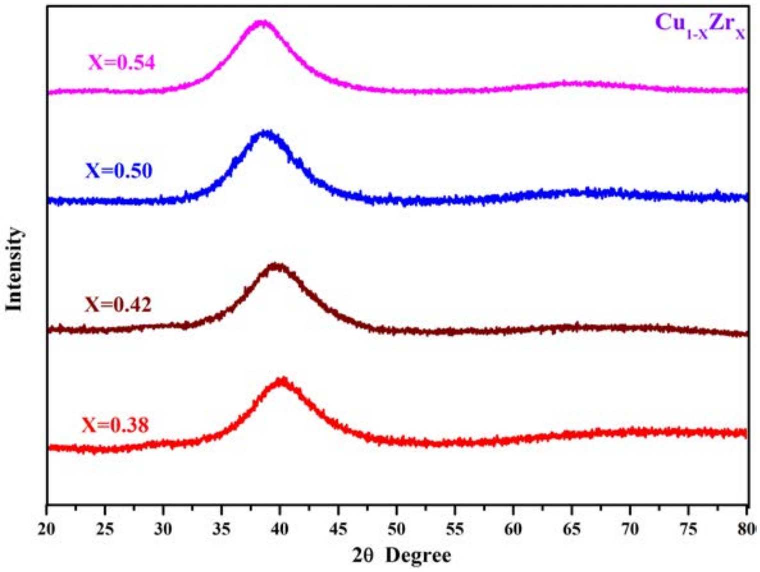

FIG. 5. X-ray diffraction pattern of melt spun ribbons of Cu$_x$Zr$_{1-x}$ ($x = 0.46, 0.50, 0.58, 0.62$)

3.2. Melting and Glass Transition temperatures

To further explain the melting and glass transition in amorphous Cu–Zr system, volume temperature ($V - T$) curves were calculated during heating and cooling (not shown in figure). Fig. 6 displays the change in volume as a function of temperature for simulated alloy systems. As the temperature of the model system is raised from 300 to 3000 K at a constant heating rate, the volume is found to increase linearly. A sudden jump in the $V - T$ curves occurs, indicating a rapid increase in volume. This sudden jump is an indication of a phase transformation; i.e. it corresponds to the melting (T_l) of the system.

A parameter known as the Wendt-Abraham (WA) parameter ($R_{WA} = G_{\min}/G_{\max}$), often used as a measure of glass transition, was used to determine T_g of the system under study. $G_{\min}$ represents the value of $G(r)$ at the first minimum and $G_{\max}$ the value of $G(r)$ at the first maximum in the RDF curve. Fig. 7 shows a plot between RWA against temperature. The point of intersection was determined and adopted as T_g. The WA parameter provides direct comparison to structures since it emphasizes the local character of $G(r)$, leading to better estimation of the glass transition temperature. It is well known, that the glass transition temperature is not a true second order phase transition, since it is dependent on the cooling rates. Faster cooling rate results the higher glass transition temperature due to less time available for

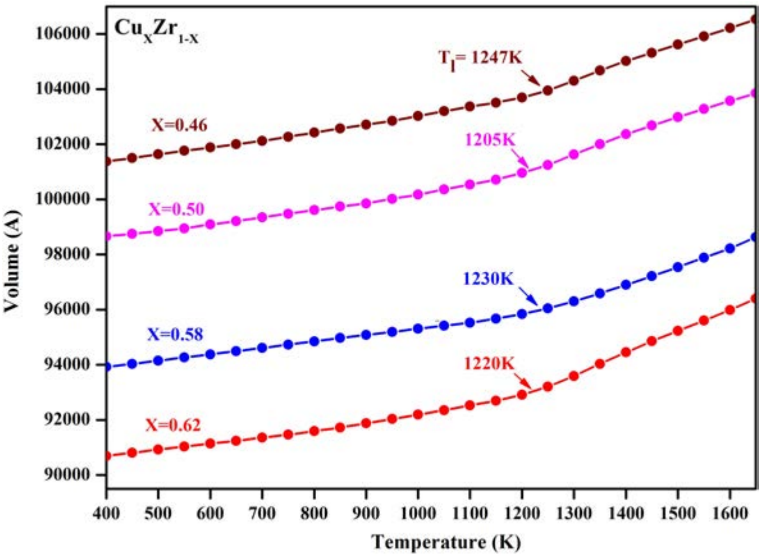

FIG. 6. Variation in cell volume with temperature for Cu$_x$Zr$_{1-x}$

atoms to relax. Around T_g, a change in volume, enthalpy and entropy are continuous, but their derivatives such as heat capacity and thermal expansion coefficient are discontinuous. With the chosen cooling rates in present work, the calculated T_g was found to be close to the laboratory-determined experimental values and the simulated T_g was believed be reliable for Cu–Zr system. Furthermore, Duan et al. [30] have used tight binding potentials to simulate T_g for Cu$_{0.46}$Zr$_{0.54}$, and Su-Wen Kao et. al. [17], using the same potentials, have also calculated T_g for Cu$_x$Zr$_{100-x}$ ($x = 46, 50, 62$) and found that these values are similar to those determined experimentally (i.e. differs by 2 – 8 %).

The DSC curves of the synthesized alloy systems are depicted in Fig. 8. A strip of sample amorphous ribbon was heated at a constant rate. The DSC curve shows a clear endothermic peak, which is characteristic of a glass transition temperature (T_g) followed by an exothermic crystallization peak. The other deep endothermic peak, of which starting point is solidus melting temperature (T_m) and end point is liquidus temperature (T_l), were associated with the simulated melting. The deviation in the T_g, and T_l obtained from MD and experimental values are found to lie between 1.3 – 6.2 %, and 1 – 2.5 % respectively. Despite the very high heating and cooling rate, the precision between the simulated and experimental value implies that a viscosity change from solid to super cooled liquid is not a second order phase transition and involves no latent heat of transition, thus further confirming the accuracy of simulation against the experimentation.

3.3. Reduced glass transition temperature

When a liquid alloy is cooled from the molten state down to a temperature below T_g, the viscosity of the melt increases to a high value and a glass is formed. Based on nucleation kinetics viscosity calculation, Turnbull [15] have mentioned, an alloy with high value of T_g and low value of T_l would easily form a glass. This ratio has been designated as reduced glass transition temperature (T_{rg}). The higher the T_{rg} value, the higher the viscosity of melt is and it is more easily solidified into a glassy state at a lower cooling rate.

Table 2 shows simulated and experimental T_g, T_m, T_l, and T_{rg} for Cu$_x$Zr$_{1-x}$ ($x = 0.46, 0.50, 0.58, 0.62$) alloys. It was rather difficult to distinguish between T_m and T_l, as the $V - T$ plot (generated by MD simulation) indicated a single shift for the melting in

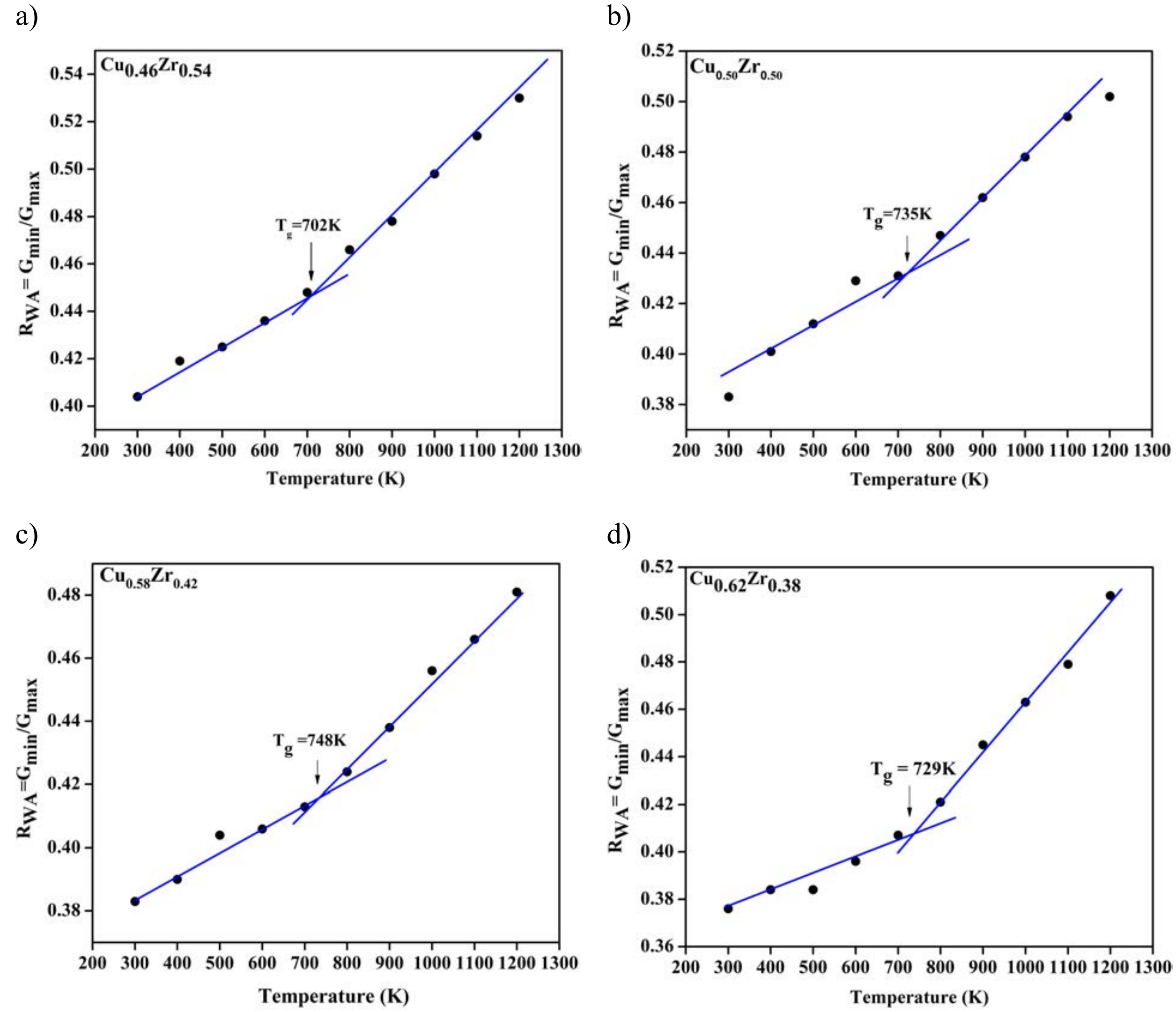

FIG. 7. Wendt Abraham (RWA) parameter as a function of temperature for $Cu_{0.46}Zr_{0.54}$

Cu–Zr alloy system. Additionally, the simulated melting temperature values were found to lie closer to experimental T_l values rather than T_m. Hence, the T_{rg} values were calculated using T_g/T_l as emphasized by Turnbull instead of the T_g/T_m ratio. Simulated T_{rg} values are well found to be in good agreement with experimental values with deviation lying between 0.8 – 5.4 %. These results further support our assumption that T_l is a better substitute for T_m. That is, when calculating T_{rg} from MD, for a Cu–Zr binary alloy, one should avoid the interchange of T_m to T_l and melting temperature (obtained from MD) should be considered as the liquidus temperature instead of solidus temperature. It is also clear from the Fig. 9 that T_{rg} obtained from the simulation and experiments follow the same trend against the copper content, which confirms the consistency between the theoretical and experimental results.

4. Conclusion

The relationship between GFA and T_{rg} for Cu_xZr_{1-x} ($x = 0.46, 0.50, 0.58, 0.62$) alloys has been studied by MD simulations. The amorphous structure of the alloy system was confirmed by RDF and Voronoi calculation. It was found that the population of Cu centered Voronoi

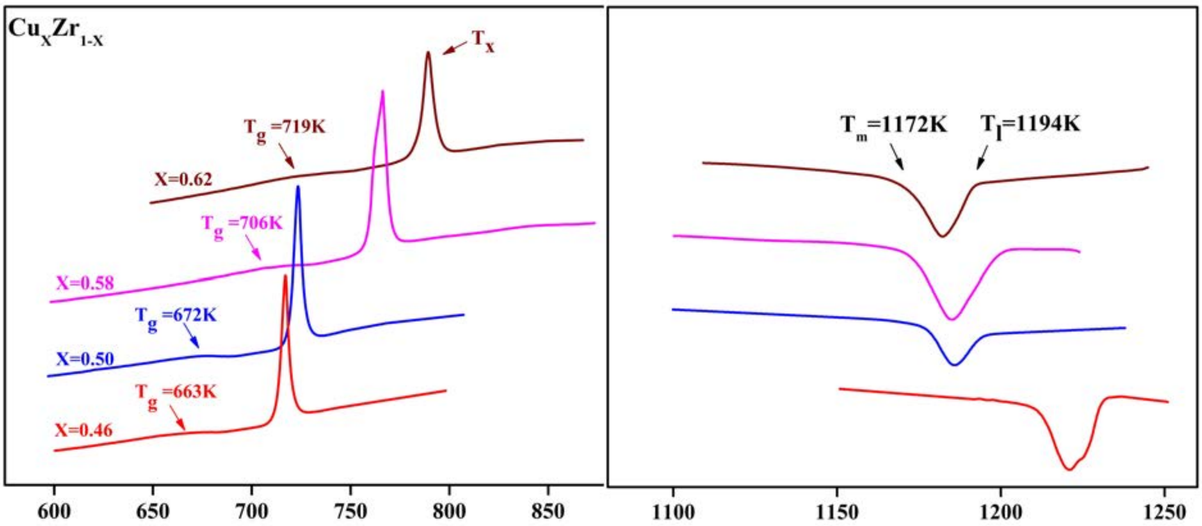

FIG. 8. DSC scan of melt spin ribbons of Cu$_x$Zr$_{1-x}$

TABLE 2. The simulated and calculated T_l, T_g and T_{rg} values for Cu$_x$Zr$_{1-x}$ alloys

Compositions	MD (K)			Experiments (K)			
	T_l	T_g	T_{rg}	T_m	T_l	T_g	T_{rg}
$Cu_{0.46}Zr_{0.54}$	1247	702	0.562	1209	1232	663	0.538
$Cu_{0.50}Zr_{0.50}$	1205	717	0.595	1178	1193	672	0.563
$Cu_{0.58}Zr_{0.42}$	1230	733	0.596	1173	1199	706	0.588
$Cu_{0.62}Zr_{0.38}$	1220	729	0.597	1172	1194	719	0.602

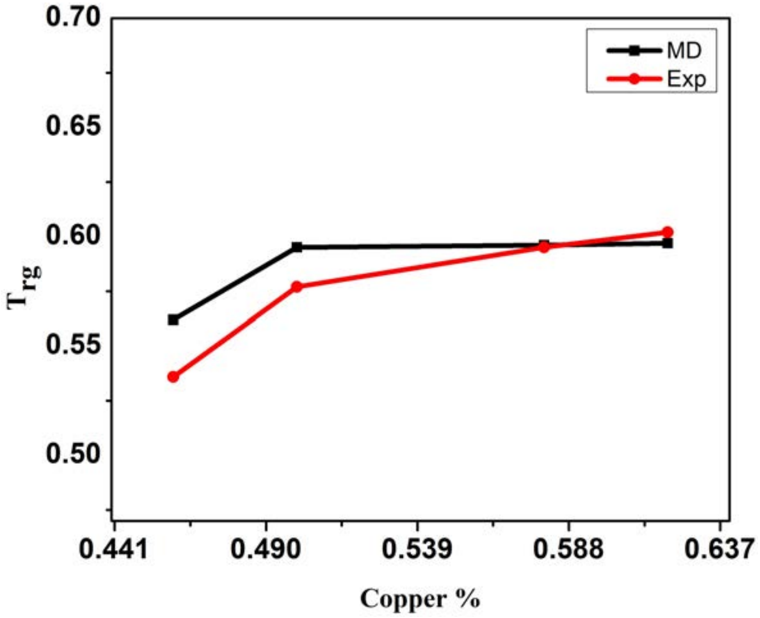

FIG. 9. Experimental versus Simulated T_{rg} of Cu$_x$Zr$_{1-x}$

polyhedra $\langle 0, 0, 12, 0\rangle$ increases the amorphous phase stability, with Cu content. Experiments were carried out in order to validate the accuracy of the simulated quantities. The difference between the experimental and simulated T_l, T_g and T_{rg} values lies within the accuracy limit of 1.3 – 6.2 %, 1 – 2.5 % and 0.8 – 5.4 % respectively, better than those reported [6]. Nearly same trend has been attained in simulated and experimental T_{rg} values. Thus MD simulation offers a reliable way to predict the GFA of alloys systems whose constituent elements have well defined EAM potentials.

Acknowledgments

The authors are grateful to Dr. R. S. Hastak, Director NMRL, for his research support, Dr. B. C. Chakraborthy, Dr. G. Gunasekaran, Dr. S. Rath of NMRL, M. Bharadwaj of CSTEP, Bangalore and Dr. S. Subramanian, DMRL, Hyderabad for their useful discussions.

References

[1] Guo F.Q., Poon S.J., Shiflet G. J. CaAl-based bulk metallic glasses with high thermal stability. *Appl. Phys. Lett.*, 2004, **84**, P. 37–39.

[2] Fan C., Takeuchi A., Inoue A. Preparation and mechanical properties of Zr-based bulk nanocrystalline alloys containing compound and amorphous phases. *Mater. Trans. JIM*, 1999, **40**, P. 42–51.

[3] Drehman A.J., Greer A.L., Turnbull D. Bulk formation of a metallic glass: palladium-nickel-phosphorus ($Pd_{40}Ni_{40}P_{20}$). *Appl. Phys. Lett.*, 1982, **41**, P. 716.

[4] Inoue A., Zhang T., Masumoto T. Production of amorphous cylinder and sheet of $La_{55}Al_{25}Ni_{20}$ alloy by metallic mould casting method. *Mater. Trans. JIM*, 1990, **31**, P. 425–428.

[5] Pecker A., Johnson W.L. A highly processable metallic glass: $Zr_{41.2}Ti_{13.8}Cu_{12.5}Ni_{10.0}Be_{22.5}$. *Appl. Phys. Lett.*, 1993, **63**, P. 2342–2344.

[6] Zhang T., Inoue. A, Masumoto T. Amorphous Zr–Al–Tm (Tm=Co, Ni, Cu) alloys with significant supercooled liquid region of over 100 K. *Mater Trans. JIM*, 1991, **32**, P. 1005–1010.

[7] Johnson W.L. Bulk glass-forming metallic alloys: science and technology. *Mater. Res. Bull.*, 1999, **24**, P. 42–56.

[8] Loffler J.F. Bulk metallic glasses. *Intermetallics*, 2003, **11**, P. 529–540.

[9] Lu Z.P., Liu. C.T. Glass formation criterion for various glass-forming systems. *Phys. Rev. Lett.*, 2003, **91**, P. 115505.

[10] Inoue A. Stabilization of metallic supercooled liquid and bulk amorphous alloys. *Acta Mater.*, 2000, **48**, P. 279–306.

[11] Inoue A., Zhang T., Masumoto T. Glass-forming ability of alloys. *J. Non-Cryst. Solids.*, 1993, **156**, P. 473–480.

[12] Cheng Y.Q., Sheng H.W., Ma E. Relationship between structure, dynamics, and mechanical properties in metallic glass-forming alloys. *Phys. Rev. B*, 2008, **78**, P. 014207.

[13] Li Y., Poon S.J., et al. Formation of bulk metallic glasses and their composites. *MRS Bull.*, 2007, **32**, P. 624–628.

[14] Kittel C. *Introduction to Solid State Physics*. Wiley, New York, 2005, 704 p.

[15] Cohen E.R., Lide D.R., Trigg G.L. *AIP Physics Desk Reference*. AIP Press, New York, 2003, 843 p.

[16] Turnbull D. Under What Conditions can a Glass be Formed? *Cont. Phys.*, 1969, **10** (5), P. 473–488.

[17] Wendt H.R., Abraham F.F. Empirical Criterion for the Glass Transition Region Based on Monte Carlo Simulations. *Phys. Rev. Lett.*, 1978, **41**, P. 1244.

[18] Kao S.W., Hwang C.C., Chi T.S. Simulation of reduced glass transition temperature of Cu–Zr alloys by molecular dynamics. *J. Appl. Phys.*, 2009, **105**, P. 064913.

[19] Gunawardana K.G.S.H., Wilson S.R., Mendelev M.I., Song X. Theoretical calculation of the melting curve of Cu–Zr binary alloys. *Phys. Rev. E*, 2014, **90**, P. 052403.

[20] Mendelev M.I., Sordelet D.J., Kramer M.J. Using atomistic computer simulations to analyze X-ray diffraction data from metallic glasses. *J. Appl. Phys.*, 2007, **102**, P. 043501.

[21] Plimpton S.J. Fast parallel algorithms for short-range molecular dynamics. *Comp. Phys.*, 1995, **117**, P. 1–19.

[22] Stukowski A. Visualization and analysis of atomistic simulation data with OVITO – the Open Visualization Tool. *Mater. Sci. Eng.*, 2010, **18**, P. 015012.

[23] Qi Y., Cagin T., Kimura Y., Goddard W.A. Molecular-Dynamics Simulations of Glass Forming and Crystallization in Binary Liquid Metals: Cu–Ag and Cu–Ni. *Phys. Rev. B*, 1999, **59**, P. 3527–3533.

[24] Finney J.L. Modelling the structures of amorphous metals and alloys. *Nature*, 1977, **266**, P. 309–314.

[25] Stepanyuk V.S., Katsnelson A.A., et al. Microstructure and its relaxation in FeB amorphous system simulated by moleculular dynamics. *J. Non-Cryst. Solids.*, 1993, **159**, P. 80–87.

[26] Peng H.L., Li M.Z., et al. Effect of local structures and atomic packing on glass forming ability in $\mathrm{Cu}_x\mathrm{Zr}_{100-x}$ metallic glasses. *Appl. Phys. Lett.*, 2010, **96**, P. 021901.

[27] Tang M.B., Zhao D.Q., Pan M.X., Wang W.H. Binary Cu–Zr bulk metallic glasses. *Chin. Phys. Lett.*, 2004, **21**, P. 901–903.

[28] Park K.W., Jang J.I., et al. Atomic packing density and its influence on the properties of Cu–Zr amorphous alloys. *Scr. Mater.*, 2007, **57**, P. 805–808.

[29] Ma D., Stoica A.D., et al. Efficient local atomic packing in metallic glasses and its correlation with glass-forming ability. *Phys. Rev. B*, 2009, **80**, P. 014202.

[30] Duan G., Xu D., et al. Molecular dynamics study of the binary $\mathrm{Cu}_{46}\mathrm{Zr}_{54}$ metallic glass motivated by experiments: Glass formation and atomic-level structure. *Phys. Rev. B*, 2005, **71**, P. 224208.

NANOSYSTEMS: PHYSICS, CHEMISTRY, MATHEMATICS, 2015, 6 (5), P. 661–671

The motion of a charged particle in the field by a frequency-modulated electromagnetic wave

G. F. Kopytov, A. A. Martynov, N. S. Akintsov
Kuban State University, Krasnodar, Russia
g137@mail.ru, martynov159@yandex.ru, akintsov777@mail.ru

PACS 52.38.Kd; 52.27.Ny **DOI 10.17586/2220-8054-2015-6-5-661-671**

In this article, the exact solutions of equations of motion for a charged particle in a frequency-modulated wave are presented. We performed an analysis of the results for the motion of a charged particle in the field of frequency-modulated electromagnetic waves. A point of interest was a solution for the equations of the motion for a charged particle in the field of a plane electromagnetic wave. We investigated the interaction of high intensity laser pulses with solid targets in relation to the practical development of multi-frequency lasers and laser modulation technology. This study was undertaken because of the wide practical application of high-temperature plasma formed on the surface of the target and the search for new modes of laser plasma interaction

Keywords: charged particle, plane electromagnetic wave, modulation frequency, average kinetic energy, ultrashort laser pulse.

Received: 3 March 2015

Revised: 2 August 2015

1. Introduction

The creation of petawatt level laser systems in recent years, has allowed the study of a new unique physical object – relativistic laser plasma, produced when gas, clusters or solid targets are exposed to intense laser radiation [1]. Developments in different fields of physics and engineering; e.g. plasma physics, astrophysics, powerful relativistic high-frequency electronics and appliances. have increased the interest in studying the interaction between charged particles and electromagnetic waves. A special role in such interactions is assigned to relativistic charged particles in strong electromagnetic waves. The energy characteristics of a charged particle in the field of a frequency-modulated electromagnetic wave are of interest as a result of the practical development of multifrequency lasers and laser modulation techniques [2–4]. In this paper, we consider the dynamics of an electron in an intense frequency-modulated electromagnetic field of linear and circular polarization. The interaction of charged particles with ultrashort femtosecond laser pulses with radiation intensities of up to 1022 W/cm^2 is one of the main areas of laser physics at the moment. Previous literature [5] discussed the consistent derivation of a particle's average kinetic energy in an intense electromagnetic field by a frequency-modulated electromagnetic wave, but was not found by averaging coordinate, momentum, and energy values for the particle over the period of the particle's oscillation in the field plane of a monochromatic frequency-modulated electromagnetic wave.

The problem of the motion of a charged particle in the field of a plane monochromatic frequency-modulated electromagnetic wave was formulated and solved for linear and circular polarization of the wave [6], but the interest in this topic has appeared presently in connection with the development of high-power lasers. The peculiarity of this work lies in the fact that there are considered highly-fields for review before the end of the simple modes of interaction of charged particles with a frequency-modulated electromagnetic wave.

The aim of this work is to analyze the motion of a particle in the external field of frequency-modulated electromagnetic wave of high intensity and to derive the average kinetic energy of a particle over the oscillation period of the field.

2. Problem Statement

The equation of motion of a particle of mass m and charge q placed in an external field of a plane monochromatic wave has a known form (see, for example [7], paragraph 17). The equation of motion for a charged particle being acted upon by a high-Lorentz force is given by:

$$\frac{d\boldsymbol{p}}{dt} = q\boldsymbol{E} + \frac{q}{c}\left[\boldsymbol{V} \times \boldsymbol{H}\right], \tag{1}$$

where $\boldsymbol{p}$ – momentum of charged particle; $\boldsymbol{E}$ and $\boldsymbol{H}$ – electric and magnetic intensity of the laser field; $q > 0$ the absolute value of the electron charge. Equation (1) is supplemented by the initial conditions for the velocity and position of the electron:

$$\boldsymbol{V}(0) = \boldsymbol{V}_0, \quad \boldsymbol{r}(0) = \boldsymbol{r}_0.$$

The particle momentum $\boldsymbol{p}$ and velocity $\boldsymbol{V}$ are related by equality ([7], paragraph 9):

$$\boldsymbol{p} = \frac{m\boldsymbol{V}}{\sqrt{1 - \frac{V^2}{c^2}}}. \tag{2}$$

The change in the particle energy:

$$\varepsilon = \frac{mc^2}{\sqrt{1 - \frac{V^2}{c^2}}} = \sqrt{m^2c^4 + p^2c^2}, \tag{3}$$

is determined by the equation:

$$\frac{d\varepsilon}{dt} = q\boldsymbol{E}\boldsymbol{V}. \tag{4}$$

It follows from (2) and (3) that the energy ε, momentum $\boldsymbol{p}$, and velocity $\boldsymbol{V}$ of the particle are related by equations:

$$\boldsymbol{p} = \frac{\varepsilon\boldsymbol{V}}{c^2}, \quad \boldsymbol{V} = \frac{c^2\boldsymbol{p}}{\varepsilon}. \tag{5}$$

In this paper, it is assumed that the frequency of the electromagnetic wave is modulated harmonically $\phi = \mu\sin(\omega'\xi + \psi)$, where $\mu = \Delta\omega_m/\omega'$ – modulation index equal to the ratio of frequency deviation to the frequency of the modulating wave; ω' – frequency modulation; $\xi = t - z/c$; ψ – constant phase. We assign the plane wave as propagating along the axis$z$, then the vector components of electric and magnetic fields of plane monochromatic wave are given by:

$$\begin{cases} E_x = H_y = b_x \exp\big(-i\left(\omega\xi + \alpha + \mu\sin\left(\omega'\xi + \psi\right)\right)\big); \\ E_y = -H_x = f b_y \exp\big(-i\left(\omega\xi + \alpha + \mu\sin\left(\omega'\xi + \psi\right)\right)\big); \\ E_z = H_z = 0, \end{cases} \tag{6}$$

where ω is carrier frequency of the wave; α – constant phase; the x and y axes coincide with the b_x and b_y axes of the polarization ellipse of the wave and $b_x \geq b_y \geq 0$; $f = \pm 1$ is a polarization parameter (the upper and lower signs in the expression for E_y correspond to right and left polarization [5]).

We take the real part form (6) and apply the Jacobi-Anger expansion then obtain:

$$\begin{cases} E_x = H_y = b_x \sum\limits_{n=-\infty}^{+\infty} J_n(\mu) \cos \Phi_n, \\ E_y = -H_x = f b_y \sum\limits_{n=-\infty}^{+\infty} J_n(\mu) \cos \Phi_n, \\ E_z = H_z = 0, \end{cases} \tag{7}$$

where $J_n(\mu)$ is the n-th Bessel function; $\Phi_n = (\omega + n\omega')\,\xi + \alpha + n\psi$.

As can be seen from (7), the frequency spectrum of the modulated wave is symmetrical and is not theoretically limited, but when $n \gg \mu$ Bessel function becomes negligible and the width of the spectrum can be limited. Practical spectral width is determined by the expression $\Delta\omega = 2(\mu + 1)\,\omega'$. In (7), index n can vary from $-N$ to N, where the number $N \approx \mu + 1$. Thus, if $\mu \ll 1$ and $N = 1$, then spectrum width $\Delta\omega = 2\omega'$ coincides with the width of the spectrum of a harmonic amplitude-modulated wave [5]. When $\mu \gg 1$ and $N = \mu$, spectral width is equal to twice the frequency deviation $\Delta\omega = 2\Delta\omega_m$.

3. Solution of the equation of the charge motion

The solution of equations (1) and (4) with $\boldsymbol{E}$ and $\boldsymbol{H}$ from (7) has the form:

$$\begin{gathered} p_x = \frac{q b_x}{\omega} \sum_{n=-N}^{N} \frac{J_n(\mu) \sin \Phi_n}{(1 + n\eta)} + \chi_x, \\ p_y = \frac{f q b_y}{\omega} \sum_{n=-N}^{N} \frac{J_n(\mu) \sin \Phi_n}{(1 + n\eta)} + \chi_y, \\ p_z = \gamma g; \\ \varepsilon = c\gamma(1 + g), \end{gathered} \tag{8}$$

where χ_x, χ_y and γ are constants ($\gamma \geq 0$ because $\varepsilon \geq mc^2$):

$$g = h + \frac{q}{\gamma^2 \omega}(b_x \chi_x + f b_y \chi_y) \sum_{n=-N}^{N} \frac{J_n(\mu) \sin \Phi_n}{(1 + n\eta)} + \\ \frac{q^2 \left(b_x^2 + b_y^2\right)}{2\gamma^2 \omega^2} \sum_{\substack{n,k=-N \\ n \neq k}}^{N} \frac{J_n(\mu) J_k(\mu) \sin \Phi_n \sin \Phi_k}{(1 + n\eta)(1 + k\eta)} - \frac{q^2 \left(b_x^2 + b_y^2\right)}{4\gamma^2 \omega^2} \sum_{n=-N}^{N} \frac{J_n^2(\mu) \cos(2\Phi_n)}{(1 + n\eta)^2}; \tag{9}$$

$$h = \frac{1}{2} \left\{ \frac{m^2 c^2 + \chi_x^2 + \chi_y^2}{\gamma^2} - 1 + \frac{q^2 \left(b_x^2 + b_y^2\right)}{2\gamma^2 \omega^2} \sum_{n=-N}^{N} \frac{J_n^2(\mu)}{(1 + n\eta)^2} \right\}. \tag{10}$$

$\Phi_k = (\omega + k\omega')\,\xi + \alpha + k\psi$, k is index of the Bessel function.

From (8) and (5), we obtain the parametric representation (the parameter ξ) of the particle velocity:

$$\begin{gathered}
V_x = \frac{dx}{dt} = \frac{c}{\gamma}\left(1 - \frac{V_z}{c}\right)\left(\frac{qb_x}{\omega}\sum_{n=-N}^{N}\frac{J_n(\mu)\sin\Phi_n}{(1+n\eta)} + \chi_x\right) = \\
\frac{c}{(1+g)\gamma}\left(\frac{qb_x}{\omega}\sum_{n=-N}^{N}\frac{J_n(\mu)\sin\Phi_n}{(1+n\eta)} + \chi_x\right), \\
V_y = \frac{dy}{dt} = \frac{c}{\gamma}\left(1 - \frac{V_z}{c}\right)\left(\frac{fqb_y}{\omega}\sum_{n=-N}^{N}\frac{J_n(\mu)\sin\Phi_n}{(1+n\eta)} + \chi_y\right) = \\
\frac{c}{(1+g)\gamma}\left(\frac{fqb_y}{\omega}\sum_{n=-N}^{N}\frac{J_n(\mu)\sin\Phi_n}{(1+n\eta)} + \chi_y\right), \\
V_z = \frac{dz}{dt} = \frac{cg}{1+g}.
\end{gathered} \tag{11}$$

Through the constants χ_x, χ_y and γ, determined by the initial phase of the wave:

$$\Phi_{n0} = -\left(\omega + n\omega'\right)\frac{z}{c} + \alpha + n\psi, \tag{12}$$

and the initial velocity of the particle V_0; from (3), (8) and (11) we find:

$$\begin{gathered}
\chi_x = \frac{mV_{x0}}{\sqrt{1 - V_0^2/c^2}} - \frac{qb_x}{\omega}\sum_{n=-N}^{N}\frac{J_n(\mu)\sin\Phi_{n0}}{(1+n\eta)}; \\
\chi_y = \frac{mV_{y0}}{\sqrt{1 - V_0^2/c^2}} - \frac{fqb_y}{\omega}\sum_{n=-N}^{N}\frac{J_n(\mu)\sin\Phi_{n0}}{(1+n\eta)}; \\
\gamma = \frac{mc\left(1 - v_{z0}/c\right)}{\sqrt{1 - v_0^2/c^2}}.
\end{gathered} \tag{13}$$

From (11), we obtain the following solutions for coordinates of the particles as functions of the parameter ξ:

$$\begin{gathered}
x = x_0 + \sum_{n=-N}^{N}\frac{\chi_x\left(\Phi_n - \Phi_{n0}\right)}{\gamma k\left(1+n\eta\right)} - \frac{qb_x}{\gamma\omega k}\sum_{n=-N}^{N}\frac{J_n(\mu)}{\left(1+n\eta\right)^2}\left(\cos\Phi_n - \cos\Phi_{n0}\right), \\
y = y_0 + \sum_{n=-N}^{N}\frac{\chi_y\left(\Phi_n - \Phi_{n0}\right)}{\gamma k\left(1+n\eta\right)} - \frac{fqb_y}{\gamma\omega k}\sum_{n=-N}^{N}\frac{J_n(\mu)}{\left(1+n\eta\right)^2}\left(\cos\Phi_n - \cos\Phi_{n0}\right), \\
z = z_0 + \sum_{n=-N}^{N}\frac{h\left(\Phi_n - \Phi_{n0}\right)}{k\left(1+n\eta\right)} - \frac{2q}{\gamma^2 k\omega}\left(b_x\chi_x + fb_y\chi_y\right)\sum_{n=-N}^{N}\frac{J_n(\mu)\left(\cos\Phi_n - \cos\Phi_{n0}\right)}{\left(1+n\eta\right)^2} - \\
\frac{q^2\left(b_x^2 + b_y^2\right)}{2\gamma^2 k\omega}\sum_{n=-N}^{N}\frac{J_n^2(\mu)\left(\sin\left(2\Phi_n\right) - \sin\left(2\Phi_{n0}\right)\right)}{\left(1+n\eta\right)^3} + \\
\frac{q^2\left(b_x^2 + b_y^2\right)}{2\gamma^2\omega k}\sum_{\substack{n,k=-N \\ n\neq k}}^{N}\frac{J_n(\mu)\,J_k(\mu)}{\left(1+n\eta\right)\left(1+k\eta\right)} \times \\
\left(\frac{\sin\Phi_{(n-k)}}{n-k} - \frac{\sin\Phi_{(n-k)0}}{n-k} - \frac{\sin\Phi_{(n+k)}}{n+k} + \frac{\sin\Phi_{(n+k)0}}{n+k}\right),
\end{gathered} \tag{14}$$

where $\Phi_{(n-k)} = \Phi_n - \Phi_k$, $\Phi_{(n+k)} = \Phi_n + \Phi_k$; $\Phi_{(n-k)0} = \Phi_{n0} - \Phi_{k0}$, $\Phi_{(n+k)0} = \Phi_{n0} + \Phi_{k0}$.

From (11) and (14), we determine that the motion of a particle in the external field of the plane monochromatic electromagnetic wave is the imposition of movement with the constant velocity $\boldsymbol{V}$ and vibrational motion with the frequency $\tilde{\omega} = 2\pi/\tilde{T}$ different from the frequency of the field ω and the frequency modulation ω':

$$x(t) = \tilde{x} + \tilde{V}_x t + \xi\left(t\right), \quad y(t) = \tilde{y} + \tilde{V}_y t + \eta\left(t\right), \quad z(t) = \tilde{z} + \tilde{V}_z t + \zeta\left(t\right), \tag{15}$$

where $\tilde{x}$, $\tilde{y}$, $\tilde{z}$ are constants and

$$\xi\left(t + \tilde{T}\right) = \xi\left(t\right), \quad \eta\left(t + \tilde{T}\right) = \eta\left(t\right), \quad \zeta\left(t + \tilde{T}\right) = \zeta\left(t\right) \tag{16}$$

are periodic function with same period.

We seek the solution of the equation for the coordinate z in (14) from (15). By substituting $z(t)$ from (15) into (14) and selecting constants $\tilde{z}$ and $\tilde{V}_z$ in the form:

$$\begin{aligned}\tilde{z} = z_0 + \Bigg[& \frac{2q}{\gamma^2 k\omega}\left(b_x\chi_x + f b_y\chi_y\right)\sum_{n=-N}^{N}\frac{J_n\left(\mu\right)\cos\Phi_{n0}}{\left(1+n\eta\right)^2} - \frac{q^2\left(b_x^2+b_y^2\right)}{2\gamma^2 k\omega}\sum_{n=-N}^{N}\frac{J_n^2\left(\mu\right)\sin\left(2\Phi_{n0}\right)}{\left(1+n\eta\right)^3} - \\ & \frac{q^2\left(b_x^2+b_y^2\right)}{2\gamma^2\omega k}\sum_{\substack{n,k=-N\\ n\neq k}}^{N}\frac{J_n\left(\mu\right)J_k\left(\mu\right)}{\left(1+n\eta\right)\left(1+k\eta\right)}\left(\frac{\sin\Phi_{(n-k)0}}{n-k} - \frac{\sin\Phi_{(n+k)0}}{n+k}\right)\Bigg]\frac{1}{1+h};\end{aligned} \tag{17}$$

$$\tilde{V}_z = \frac{ch}{1+h}, \tag{18}$$

we obtain the equation for $\zeta\left(t\right)$:

$$\begin{aligned}&\left(1+h\right)\zeta\left(t\right) = \\ &-\frac{q}{\gamma^2\omega}\Bigg[\frac{2}{k}\left(b_x\chi_x + f b_y\chi_y\right)\sum_{n=-N}^{N}\frac{J_n\left(\mu\right)\cos\Phi_n}{\left(1+n\eta\right)^2} + \frac{q\left(b_x^2+b_y^2\right)}{2k}\sum_{n=-N}^{N}\frac{J_n^2\left(\mu\right)\sin\left(2\Phi_n\right)}{\left(1+n\eta\right)^3} + \\ &\qquad \frac{q\left(b_x^2+b_y^2\right)}{2k}\sum_{\substack{n,k=-N\\ n\neq k}}^{N}\frac{J_n\left(\mu\right)J_k\left(\mu\right)}{\left(1+n\eta\right)\left(1+k\eta\right)}\left(\frac{\sin\Phi_{(n-k)}}{n-k} - \frac{\sin\Phi_{(n+k)}}{n+k}\right)\Bigg].\end{aligned} \tag{19}$$

It follows from (19) that $\zeta\left(t\right)$ is a periodic function defined by the period $\tilde{T}$. Let us find its period. The period $\tilde{T}$ of particle oscillation in the field of a frequency-modulated electromagnetic wave is determined from the formulae $\Phi\left(t + \tilde{T}\right) = \Phi(t) + 2\pi$, from which, taking into account (7), (15) and (16), it follows that:

$$\tilde{T}_n = \frac{2\pi}{\omega}\frac{\left(1+h\right)}{\left(1+n\eta\right)} = T\frac{\left(1+h\right)}{\left(1+n\eta\right)}. \tag{20}$$

One can see that the oscillation period of the particle differs from that of the field of the frequency-modulated electromagnetic wave.

We will seek the solution of the first equation in (14) in the form $x(t)$ from (14). By representing constants $\tilde{x}$ and $\tilde{V}_x$ in the form:

$$\begin{gathered}\tilde{x} = x_0 + \sum_{n=-N}^{N} \frac{\chi_x (z_0 - \tilde{z})}{\gamma k (1+n\eta)} + \frac{qb_x}{\gamma\omega k}\sum_{n=-N}^{N}\frac{J_n(\mu)}{(1+n\eta)^2}\cos\Phi_{n0},\\ \tilde{V}_x = \chi_x \frac{c}{\gamma}\left(1-\frac{\tilde{V}_z}{c}\right) = \frac{\chi_x}{\gamma}\frac{c}{(1+h)},\end{gathered} \tag{21}$$

we find that:

$$\xi(t) = -\sum_{n=-N}^{N}\frac{\chi_x}{\gamma(1+n\eta)}\zeta(t) - \frac{qb_x}{\gamma\omega k}\sum_{n=-N}^{N}\frac{J_n(\mu)}{(1+n\eta)^2}\cos\Phi_n. \tag{22}$$

Similarly, we obtain for $y(t)$ in (15):

$$\begin{gathered}\tilde{y} = y_0 + \sum_{n=-N}^{N} \frac{\chi_y (z_0 - \tilde{z})}{\gamma k (1+n\eta)} + \frac{fqb_y}{\gamma\omega k}\sum_{n=-N}^{N}\frac{J_n(\mu)}{(1+n\eta)^2}\cos\Phi_{n0},\\ V_y = \chi_y \frac{c}{\gamma}\left(1-\frac{V_z}{c}\right) = \frac{\chi_y}{\gamma}\frac{c}{(1+h)\gamma},\\ \eta(t) = -\sum_{n=-N}^{N}\frac{\chi_y}{\gamma k(1+n\eta)}\zeta(t) - \frac{fqb_y}{\gamma\omega k}\sum_{n=-N}^{N}\frac{J_n(\mu)}{(1+n\eta)^2}\cos\Phi_n.\end{gathered} \tag{23}$$

4. The motion of a particle averaged over an oscillation period

In this section, we will perform the averaging of the coordinate $\boldsymbol{r}(t)$, velocity $\boldsymbol{V}(t)$, momentum $\boldsymbol{p}(t)$, and energy $\varepsilon(t)$ of the particles over its oscillation period (20) with (8), (11) and (14) in the field of a frequency-modulated electromagnetic wave.

Consider a new variable of the integration $\xi' = \xi(t')$, then:

$$\begin{gathered}\Phi'_n = \Phi_n(t');\\ dt' = \frac{d\Phi'_n}{\omega(1+n\eta)}\frac{1}{1-V_z/c} = \frac{1+g}{\omega(1+n\eta)}d\Phi'_n.\end{gathered} \tag{24}$$

Since the motion of particle is a superposition of two kinds of periodic motion with frequencies ω and ω', averaging will be carried out according to the formula:

$$\bar{f}(t) = \frac{1}{\tilde{T}_n}\int\limits_{\Phi(t)}^{\Phi(\tilde{t})} f(t')\frac{1+g}{\omega(1+n\eta)}d\Phi'_n, \tag{25}$$

where $f(t')$ is an arbitrary function taking into account (7), (15) and (20).

For the coordinate x in (14), we have:

$$\begin{gathered}\bar{x}(t) = \frac{1}{\tilde{T}}\int\limits_{t}^{\tilde{t}} x(t')\,dt' = \left(x_0 - \sum_{n=-N}^{N}\frac{\chi_x\Phi_{n0}}{\gamma k(1+n\eta)} + \frac{qb_x}{\gamma\omega k}\sum_{n=-N}^{N}\frac{J_n(\mu)}{(1+n\eta)^2}\cos\Phi_{n0}\right) +\\ \frac{\chi_x}{\gamma k}\sum_{n=-N}^{N}\frac{1}{\tilde{T}_n}\int\limits_{t}^{\tilde{t}}\frac{\Phi_n(t')}{(1+n\eta)}dt' - \frac{qb_x}{\gamma\omega k}\sum_{n=-N}^{N}\frac{1}{\tilde{T}_n}\int\limits_{t}^{\tilde{t}}\frac{J_n(\mu)}{(1+n\eta)^2}\cos\Phi_n(t')\,dt',\end{gathered} \tag{26}$$

where

$$\tilde{t} = t + \tilde{T}_n \tag{27}$$

see (7), (15) and (28).

$$\begin{gathered}\Phi_n(t) = (1+n\eta)\left[\omega t - k\left(\tilde{z} + \tilde{V}_z t + \zeta(t)\right)\right] + \alpha + n\psi = \\ (1+n\eta)\left[\tilde{\omega} t - k\tilde{z} - k\zeta(t)\right] + \alpha + n\psi.\end{gathered} \tag{28}$$

By using (27) and (28), we obtain the expression:

$$\int_t^{\tilde{t}} \Phi_n(t')\,dt' = (\alpha + n\psi + (1+n\eta)[\tilde{\omega}t - k\tilde{z}])\,\tilde{T} - (1+n\eta)\,k\int_t^{\tilde{t}} \zeta(t)\,dt' \tag{29}$$

for the first integral in the right-hand side of (26). The integral in the right-hand side of (29) is independent of t, because $\zeta(t)$ is periodic function with a period $\tilde{T}_n$. This integral is zero. The Fourier component of the function $\zeta(t)$ multiplied by $\tilde{T}_n$.

Expression (29) can then be transformed to:

$$\int_t^{\tilde{t}} \Phi_n(t')\,dt' = \left(\alpha + n\psi - (1+n\eta)\,k\left(\tilde{z} + \bar{\zeta}\right)\right)\tilde{T} + 2\pi t, \tag{30}$$

where $\bar{\zeta}$ is the average value of the function $\zeta(t)$ in the time interval equal the period $\tilde{T}_n$.

By substituting into (26) the values of integrals from (30) with $\bar{\zeta} = 0$, we finally obtain:

$$\bar{x}(t) = \tilde{x} + \tilde{V}_x\left(t + \tilde{T}_n/2\right), \tag{31}$$

where $\tilde{x}$ and $\tilde{V}_x$ are defined by expressions (21).

In the same way, we find:

$$\bar{y}(t) = \tilde{y} + \tilde{V}_y\left(t + \tilde{T}/2\right), \tag{32}$$

from (32) $\tilde{y}$ and $\tilde{V}_y$ are defined by expressions in (23).

Finally, taking into account that $\bar{\zeta} = 0$, the expression for:

$$\bar{z}(t) = \tilde{z} + \tilde{V}_z\left(t + \tilde{T}/2\right), \tag{33}$$

where $\tilde{z}$ and $\tilde{V}_z$ are defined by expressions (17) and (18).

Averaging the components (11) of the particle velocity, we obtain:

$$\bar{V}_x = \tilde{V}_x, \quad \bar{V}_y = \tilde{V}_y, \quad \bar{V}_z = \tilde{V}_z. \tag{34}$$

As might be expected, the speed of the particle $\bar{\boldsymbol{V}}$ in (26) corresponds $\tilde{\boldsymbol{V}}$ with (18), (21) and (23).

From the average value of the longitudinal component of the particle momentum, we obtain the expression:

$$\begin{gathered}
\bar{p}_x = \chi_x + \frac{q^2 b_x \left(b_x \chi_x + f b_y \chi_y\right)}{\gamma^2 \omega^2 (1+h)} \sum_{n=-N}^{N} \frac{J_n^2(\mu)}{(1+n\eta)^2};\\
\bar{p}_y = \chi_y + \frac{q^2 b_y \left(b_x \chi_x + f b_y \chi_y\right)}{\gamma^2 \omega^2 (1+h)} \sum_{n=-N}^{N} \frac{J_n^2(\mu)}{(1+n\eta)^2};\\
\bar{p}_z = \frac{\gamma}{1+h} \left\{ h + h^2 + \frac{q^2}{2\gamma^4\omega^2} \left(b_x \chi_x + f b_y \chi_y\right)^2 \sum_{n=-N}^{N} \frac{J_n^2(\mu)}{(1+n\eta)^2} + \right.\\
\left. \frac{q^4 \left(b_x^2 + b_y^2\right)^2}{16\gamma^4\omega^4} \sum_{\substack{n,k=-N\\ n\neq k}}^{N} \frac{J_n^2(\mu) J_k^2(\mu)}{(1+n\eta)^2 (1+k\eta)^2} + \frac{q^4 \left(b_x^2 + b_y^2\right)^2}{32\gamma^4\omega^4} \sum_{n=-N}^{N} \frac{J_n^4(\mu)}{(1+n\eta)^4} \right\}.
\end{gathered} \tag{35}$$

The average energy $\bar{\varepsilon}$ of the particles is determined by formula:

$$\begin{gathered}
\bar{\varepsilon} = \frac{c\gamma}{1+h} \left\{ (1+h)^2 + \frac{q^2}{2\gamma^4\omega^2} \left(b_x \chi_x + f b_y \chi_y\right)^2 \sum_{n=-N}^{N} \frac{J_n^2(\mu)}{(1+n\eta)^2} + \right.\\
\left. \frac{q^4 \left(b_x^2 + b_y^2\right)^2}{16\gamma^4\omega^4} \sum_{\substack{n,k=-N\\ n\neq k}}^{N} \frac{J_n^2(\mu) J_k^2(\mu)}{(1+n\eta)^2 (1+k\eta)^2} + \frac{q^4 \left(b_x^2 + b_y^2\right)^2}{32\gamma^4\omega^4} \sum_{n=-N}^{N} \frac{J_n^4(\mu)}{(1+n\eta)^4} \right\}.
\end{gathered} \tag{36}$$

5. The case of an arbitrary polarization for a particle being initially at rest

Consider the case when the particle is initially at rest ($V_0 = 0$) and the Bessel functions indices are equal to each other ($k = n$). Formula (13) expresses χ_x, χ_y, γ and taking into account that:

$$\Phi_n(0) = \Phi_{n0} = (\omega + n\omega')\,\xi_0 + \alpha + n\psi; \quad \xi_0 = -z_0/c,$$

we obtain:

$$\begin{gathered}
\chi_x = -\frac{q b_x}{\omega} \sum_{n=-N}^{N} \frac{J_n(\mu) \sin \Phi_{n0}}{(1+n\eta)};\\
\chi_y = -\frac{f q b_y}{\omega} \sum_{n=-N}^{N} \frac{J_n(\mu) \sin \Phi_{n0}}{(1+n\eta)};\\
\gamma = mc.
\end{gathered} \tag{37}$$

For a wave with an arbitrary polarization [8]:

$$b_x^2 \pm b_y^2 = \rho^2 b^2, \tag{38}$$

where ρ is the ellipticity parameter ($\rho = \pm 1$ corresponds to the linear polarization and $\rho = \pm 1/\sqrt{2}$ does to the circular one).

In other cases, the value ρ corresponds to an elliptical polarization ($0 \le \rho \le 1$), in which:

$$\chi_x^2 + \chi_y^2 = \frac{q^2 \rho^2 b^2}{\omega^2} \sum_{n=-N}^{N} \frac{J_n^2(\mu) \sin^2 \Phi_{n0}}{(1+n\eta)^2}, \tag{39}$$

$$(b_x\chi_x + f b_y\chi_y)^2 = \frac{q^2\rho^4 b^4}{\omega^2}\sum_{n=-N}^{N}\frac{J_n^2(\mu)\sin^2\Phi_{n0}}{(1+n\eta)^2}. \tag{40}$$

From (10), we obtain the value of h at the initial time:

$$h = \frac{1}{4}\left\{\sigma\left(\sum_{n=-N}^{N}\frac{J_n^2(\mu)\left(1+2\sin^2\Phi_{n0}\right)}{(1+n\eta)^2}\right)\right\}, \tag{41}$$

and according to (41):

$$\sigma = \frac{q^2\rho^2 b^2}{m^2c^2\omega^2} = \frac{2q^2}{\pi m^2 c^5} I\lambda^2, \tag{42}$$

where $I = c\rho^2 b^2/4\pi$ is the intensity of the elliptically polarized electromagnetic wave, and $\lambda = 2\pi c/\omega$ is the wavelength.

The oscillation period of a particle is:

$$\tilde{T}_n = T\left(\frac{1}{(1+n\eta)} + \frac{\sigma}{4}\left(\sum_{n=-N}^{N}\frac{J_n^2(\mu)\left(1+2\sin^2\Phi_{n0}\right)}{(1+n\eta)^3}\right)\right). \tag{43}$$

By substituting (37) – (41) in (36), we obtain the average energy of a particle at rest in the initial wave of arbitrary polarization:

$$\begin{gathered}\bar{\varepsilon} - mc^2 = \frac{mc^2\sigma}{4}\left\{\sum_{n=-N}^{N}\frac{J_n^2(\mu)\left(1+2\sin^2\Phi_{n0}\right)}{(1+n\eta)^2} + \right.\\ \left.\sum_{n=-N}^{N}\frac{J_n^4(\mu)}{(1+n\eta)^4}\frac{\sigma\left(2\sin^2\Phi_{n0}+1/8\right)}{\left(1+\left(\sigma J_n^2(\mu)\left(1+2\sin^2\Phi_{n0}\right)\right)/\left(4(1+n\eta)^2\right)\right)}\right\}.\end{gathered} \tag{44}$$

The maximum average energy is obtained for the phase $\Phi_{n0} = \pi/2$ or $3\pi/2$, when the field at the point where a particle in located initially zero. In this case, we have:

$$\bar{\varepsilon} - mc^2 = \frac{3mc^2\sigma}{4}\left\{\sum_{n=-N}^{N}\frac{J_n^2(\mu)}{(1+n\eta)^2} + \sum_{n=-N}^{N}\frac{J_n^4(\mu)}{(1+n\eta)^4}\frac{17\sigma}{\left(24+18\sigma J_n^2(\mu)/\left((1+n\eta)^2\right)\right)}\right\}. \tag{45}$$

The minimum average energy corresponds to the phase $\Phi_{n0} = 0$ or π and is determined by the expression:

$$\bar{\varepsilon} - mc^2 = \frac{mc^2\sigma}{4}\left\{\sum_{n=-N}^{N}\frac{J_n^2(\mu)}{(1+n\eta)^2} + \sum_{n=-N}^{N}\frac{J_n^4(\mu)}{(1+n\eta)^4}\frac{\sigma}{\left(8+2\sigma J_n^2(\mu)/(1+n\eta)^2\right)}\right\}. \tag{46}$$

The energy $\langle\bar{\varepsilon}\rangle$ of the charged particle, being further averaged over the initial phase Φ_{n0}, in the plane monochromatic arbitrarily polarized wave is given by:

$$\begin{gathered}\langle\bar{\varepsilon}\rangle - mc^2 = \frac{mc^2\sigma}{4}\left\{\sum_{n=-N}^{N}\frac{6J_n^2(\mu)}{(1+n\eta)^2} - \right.\\ \left.\sum_{n=-N}^{N}\frac{7\sigma J_n^4(\mu) + 32J_n^2(\mu)(1+n\eta)^2}{2(1+n\eta)^2\sqrt{3J_n^4(\mu)\sigma^2 + 16\sigma J_n^2(\mu)(1+n\eta)^2 + 16(1+n\eta)^4}}\right\}.\end{gathered} \tag{47}$$

For the private case of wave circular polarization when the difference between E_x and E_y corresponds to $\pi/2$ or $3\pi/2$ (see (6) and (7)). This means that waves are located in opposite phases and cancel each other out. We obtain the average energy $\bar{\varepsilon}$ of the particle:

$$\bar{\varepsilon} - mc^2 = \frac{\sigma mc^2}{2}\left\{\sum_{n=-N}^{N}\frac{J_n^2(\mu)}{(1+n\eta)^2} + \sigma\sum_{n=-N}^{N}\frac{J_n^4(\mu)}{(1+n\eta)^4\left(4+2\sigma\sum\limits_{n=-N}^{N}\frac{J_n^2(\mu)}{(1+n\eta)^2}\right)}\right\}. \quad (48)$$

The resulting formulas (44), (45), (46) (47) and (48) for the average kinetic energy of the particles comprise an explicit dependence on the initial particle velocity, amplitude of the electromagnetic wave, a frequency modulation index, the frequency of the carrier wave, frequency modulation, intensity and polarization, which allow one to make practical calculations. When $\mu \ll 1$, $N = 1$, the formulas (44), (45), (46) (47) and (48) become the special case of linear and circular polarization form [6].

6. Conclusions

This article offers the exact solution for the equations of a charged particle's motion in the external field of a frequency-modulated electromagnetic wave. This solution indicates the dependence of the electron velocity on the intensity of the monochromatic frequency-modulated electromagnetic wave for the cases of elliptical polarization which are, therefore, the cases of different initial conditions of the charged particle motion and wave polarization. In the electromagnetic wave (7) of the field $\boldsymbol{E}$ and $\boldsymbol{H}$ is periodic with average electric and magnetic field values of zero. One would assume that such fields will have an alternating effect on charged particles and the average deviation caused by this influence is also zero. However, this assumption is incorrect. In particular, in the field of a plane frequency-modulated electromagnetic wave, the particle performs a systematic drift in the direction of the electromagnetic field, as well as the drift direction of wave propagation. The values of the momentum and energy of the particle, averaged over the period of vibration, were calculated. The oscillation period of the particle differs from that of the field. As the field intensity is increased, the frequency of the oscillatory motion of the particle tends to zero according to (20). The motion of the particle was shown to be the superposition of motion at a constant velocity and vibrational motion with the frequency of the electromagnetic field and the frequency modulation different from the field frequency. In the absence of the frequency modulation, all the formulae go to the appropriate formulae given in [6]. The solutions obtained are presented in the explicit dependence on the initial data, the amplitude of the electromagnetic wave, the wave intensity and its polarization parameter that allows practical application of the solutions. We have obtained the exact criterion for the applicability of relativistic equations of motion for a charged particle in a frequency-modulated electromagnetic field, depending on the intensity and duration of the pulse. This implies that the accuracy of the analytical calculation increases with its time duration and decreases with the intensity of the electromagnetic pulse. The practical significance of the research is that the results can be used to develop relativistic electronic devices. In addition, the results may be of interest for astrophysical research or studies involving plasma in an external electromagnetic field.

References

[1] Mourou G., Tajima T., Bulanov S.V. Optics in the Relativistic Regime. *Rev. Mod. Phys.*, 2006, **78**, P. 309–371.

[2] Yariv A. *Quantum Electronics and Nonlinear Optics*. Moscow, Soviet radio engineering, 1980, 488 p.

[3] Ready J. *Effects of High-Power laser Radiation*. Moscow, Mir, 1974, 468 p.

[4] Koroteev N.I., Shumay I.L. *Physics of intense laser radiation*. Moscow, Nauka, 1991, 312 p.

[5] Kopytov G.F., Oksuzyan S.S., Tlyachev V.B. On the radiation characteristics of electron in modulated electromagnetic field. *Izvestiya vuzov. Fizika. Tomsk*, 1987, **7** (20), P. 15–18.

[6] Andreev S.N., Makarov V.P., Rukhadze A.A. On the motion of a charged particle in a plane monochromatic electromagnetic wave. *Quantum Electronics*, 2009, **1** (39), P. 68–72.

[7] Landau L.D., Lifshits E.M. *The Classical Theory of Fields*. Moscow, Nauka, 2004, 536 p.

[8] Azzam R.M., Bashara N.M. *Ellipsometry and Polarized Light*. Moscow, Mir, 1981, 583 p.

NANOSYSTEMS: PHYSICS, CHEMISTRY, MATHEMATICS, 2015, 6 (5), P. 672–679

Analytical benchmark solutions for nanotube flows with variable viscosity

I. V. Makeev, I. V. Blinova, I. Yu. Popov

ITMO University, 49, Kronverkskiy, St. Petersburg, 197101, Russia

popov1955@gmail.com

PACS 68.90.+g, 05.60.-k **DOI 10.17586/2220-8054-2015-6-5-672-679**

Three-dimensional Stokes equations with variable viscosity in cylindrical coordinates are considered. This case is natural for flow through a nanotube in biological applications. We obtain exact particular solutions – a benchmark for numerical approache.

Keywords: Stokes flow, variable viscosity, multigrid methods, benchmark solutions.

Received: 10 October 2015

1. Introduction

Flow through nanotubes are intensively investigated, particularly due to its biological applications, e.g., as a transport channel for some compounds into the cell (see, e.g., [1]). Although there is no general approach in nanohydrodynamics [2-6], the Stokes approximation (with variable viscosity) is available in many cases. We consider the axisymmetric case, which is natural for the nanotube flow. Biologists need a reliable computational approach to describe and predict the mass transport through a nanotube "to" and "from" the cell. There are several computational schemes for solution of the Stokes and continuity equations, but in the case of strongly varying viscosity, these schemes are plagued by difficulties. One would like to have an instrument for testing of these algorithms. One convenient method is to suggest benchmark solutions for some particular cases [7-9]. In this paper, such a benchmark solution is constructed for the axisymmetric case. It is interesting to note that the same mathematical problem appears in geophysics [10, 11].

This paper deals with the Stokes and continuity equations for the case of variable viscosity and density having the following form:

$$(\nabla \cdot \sigma) = -\rho G \quad , \tag{1}$$

$$\nabla(\rho v) = 0, \tag{2}$$

where v is velocity, η is a dynamic viscosity, σ is the total stress tensor, p is a pressure, G is a gravitational force. We consider equations (1), (2) in cylindrical coordinates (r, φ, z) and construct a solution for the case when the variables depend only on the radius r.

2. Benchmark solutions

We construct particular solutions of the system of Stokes and continuity equations for specific density and viscosity distributions: $\eta = \eta(r)$, $\rho = \rho(r)$. Let $v_r = v_r(r)$, $v_\varphi = v_\varphi(r)$, $v_z = v_z(r)$, $P = P(r)$, $\eta = \eta(r)$, $\rho = \rho(r)$, $G = G(r)$. Then equation (1) simplifies considerably:

$$2\eta\frac{1}{r}v'_r + 2\eta' v'_r + 2\eta v''_r - 2\eta\frac{1}{r^2}v_r - P' = -\rho G_r \tag{3}$$

$$\eta' v'_\varphi - \frac{1}{r}\eta' v_\varphi + \eta v''_\varphi + \frac{1}{r}\eta v'_\varphi - \eta\frac{1}{r^2}v_\varphi = -\rho G_\varphi \tag{4}$$

$$\eta\frac{1}{r}v'_z + \eta' v'_z + \eta v''_z = -\rho G_z. \tag{5}$$

The continuity equation takes the form:

$$\rho\frac{1}{r}v_r + \rho' v_r + \rho v'_r = 0. \tag{6}$$

In this case, we obtain the following solutions of equations (1), (2):

$$\begin{aligned} &v_r = \tfrac{c}{r\rho}, \quad v_\varphi = c_1 f(r) + c_2 r + C_1(r)f(r) + C_2(r)r, \\ &v_z = -\int\limits_1^r \tfrac{1}{\eta r_2}\Big(\int\limits_1^{r_2} r_1\rho G_z dr_1 + c_1\Big)dr_2 + c_2, \end{aligned} \tag{7}$$

$$P(r) = \int(\rho G_r + 2\eta\frac{1}{r}v'_r + 2\eta' v'_r + 2\eta v''_r - 2\eta\frac{1}{r^2}v_r)dr, \tag{8}$$

where

$$f(r) = \exp\Big(\int\limits_1^r \Big(\frac{1}{r_2} + \frac{1}{\eta r_2^3}\frac{1}{\int\limits_1^{r_2}\frac{1}{\eta r_1^3}dr_1 + C}\Big)dr_2\Big),$$

$$C_1(r) = \int\frac{r\rho G_\varphi}{\eta(f - f'r)}dr, \quad C_2(r) = -\int\frac{f\rho G_\varphi}{\eta(f - f'r)}dr.$$

Formulas (7), (8) gives us the solution of equations (1), (2). Derivation of the solution is presented in Appendix A in detail.

3. Multigrid method

In this work, we derive a procedure of multigrid method for solving the Stokes equations with variable viscosity in cylindrical coordinates. The analogous algorithm for the Cartesian coordinates was described in [10]. We derive a similar scheme for cylindrical coordinates.

As usual, the multigrid method algorithm contains three steps: 1) smoothing operation 2) restriction operation 3) prolongation operation. Cylindrical coordinates are orthogonal coordinates, thus the implementation of the prolongation and restriction operations in our method is not different from that in the case of the Cartesian coordinates. As for the smoothing operation, it differs. This procedure is described in Appendix B in detail.

The scheme for algorithm testing is as follows. Let us consider some particular analytical solutions (7), (8): $v_r = -\frac{1}{r}$, $v_\varphi = r^2$, $v_z = -\frac{1}{10}\rho G_z r^5 - \frac{1}{3}r^3$, $P(r) = \rho G_r r + 1.2\frac{1}{r^2}$ in the domain $1 \leqslant r \leqslant 2$, $0 \leqslant \phi \leqslant 1$, $0 \leqslant z \leqslant 1$ ($\rho = const$, $G_r = 10$, $G_\varphi = 0$, $G_z = 10$, $\eta = r^{-3}$). We calculate the values for velocity and pressure given by our analytical solution and take these values as the boundary conditions for the numerical algorithm. The deviation of the numerical solution values from the analytical solution is related to the error of the multigrid scheme. The dependence of the relative error on the grid step for the multigrid scheme is shown in Figure.1. Positive curve slopes indicate a convergence for the algorithm.

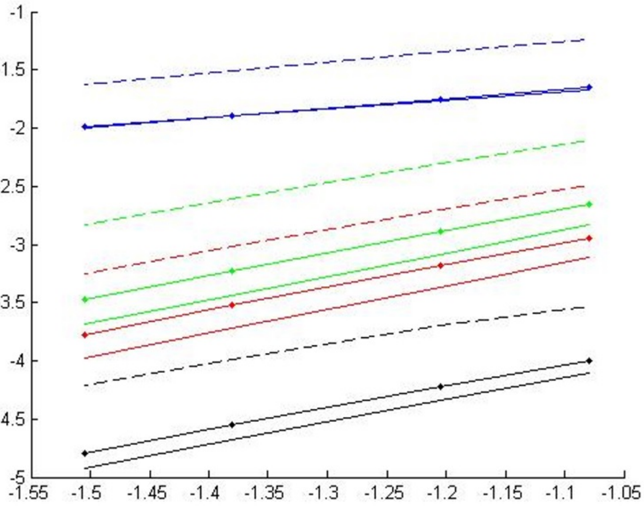

FIG. 1. Error norm via the grid resolution in logarithmic scale: blue lines- pressure, red lines- v_r , black lines - v_φ , green lines - v_z; solid lines - L_1-error, dashed lines- L_∞ -error, solid dotted lines- L_2-error

Appendix A. Derivation of the Stokes equations solution

Integration of (6) gives us:

$$v_r = \frac{c}{r\rho}. \tag{9}$$

Substitution of (9) in (3) gives us the expression for pressure:

$$P(r) = \int (\rho G_r + 2\eta\frac{1}{r}v_r' + 2\eta' v_r' + 2\eta v_r'' - 2\eta\frac{1}{r^2}v_r)dr. \tag{10}$$

Consider equation (4). Simple transformation gives us:

$$v_\varphi'' + v_\phi'(\frac{\eta'}{\eta} + \frac{1}{r}) - v_\phi(\frac{1}{r}\frac{\eta'}{\eta} + \frac{1}{r^2}) = \frac{-\rho G_\varphi}{\eta} \tag{11}$$

We seek a solution of (11) in the form $v_\varphi(r) = v_{\varphi 0}(r) + v_{\varphi 1}(r)$, where $v_{\varphi 0}(r)$ is particular solution of (11) and $v_{\varphi 1}(r)$ is the general solution of the corresponding homogeneous equation:

$$v_\varphi'' + v_\varphi'(\frac{\eta'}{\eta} + \frac{1}{r}) - v_\varphi(\frac{1}{r}\frac{\eta'}{\eta} + \frac{1}{r^2}) = 0. \tag{12}$$

Let us make a replacement:

$$z = \frac{v_\varphi'}{v_\varphi} \tag{13}$$

in (12). It transforms into the first-order equation:

$$z' + z(\frac{\eta'}{\eta} + \frac{1}{r}) + z^2 - \frac{1}{r}\frac{\eta'}{\eta} - \frac{1}{r^2} = 0. \tag{14}$$

If one makes the substitution $z = \frac{1}{\eta r}y$, where $y = y(r)$ then (14) transforms into the Riccati equation:

$$y' + y^2\frac{1}{\eta r} - \eta' - \frac{\eta}{r} = 0. \tag{15}$$

Function $y = \eta$ is a particular solution of (15). Keeping this in mind, we seek the solution in the form $y = u + \eta$. For function $u = u(r)$ one obtains the Bernoulli equation:

$$u' = -2\frac{1}{r}u - \frac{1}{\eta r}u^2. \tag{16}$$

Note that $u(r) = 0$ is a solution. We seek a non-trivial solution of (16) in the form $u = \frac{1}{r^2}q$, where $q = q(r)$. The equation simplifies:

$$q' + \frac{1}{\eta r^3}q^2 = 0,$$

giving us:

$$q = \frac{1}{\int \frac{1}{\eta r^3}dr}$$

Coming back to (12), we get:

$$\frac{v_\varphi'}{v_\varphi} = \frac{1}{\eta r}(\eta + \frac{1}{r^2}\frac{1}{\int \frac{1}{\eta r^3}dr})$$

After integration, one obtains:

$$\ln(|v_\varphi|) = \int\limits_1^r (\frac{1}{r_2} + \frac{1}{\eta r_2^3}\frac{1}{\int\limits_1^{r_2} \frac{1}{\eta r_1^3}dr_1 + c_{11}})dr_2 + c_{21}$$

Solution $u(r) = 0$ of (16) leads to the following solution of (12):

$$v_\varphi = cr$$

As a result, we obtain the general solution of (12) in the following form:

$$v_{\varphi 1}(r) = c_1 f(r) + c_2 r,$$

where $f(r) = \exp(\int\limits_1^r (\frac{1}{r_2} + \frac{1}{\eta r_2^3}\frac{1}{\int\limits_1^{r_2} \frac{1}{\eta r_1^3}dr_1 + C})dr_2)$.

We seek a particular solution of equation (11) by the Lagrange method in the form $v_{\varphi 0}(r) = C_1(r)f(r) + C_2(r)r$.

Here $C_1(r)$, $C_2(r)$ satisfy the system of equation:

$$\begin{array}{l} C_1' f(r) + C_2' r = 0 \\ C_1' f'(r) + C_2' = \frac{-\rho G_\varphi}{\eta} \end{array}.$$

Correspondingly, $C_1(r) = \int \frac{r\rho G_\varphi}{\eta(f - f'r)}dr$, $C_2(r) = -\int \frac{f\rho G_\varphi}{\eta(f - f'r)}dr$

As a result, we come to the following solution of equation (4):

$$v_\varphi(r) = c_1 f(r) + c_2 r + C_1(r)f(r) + C_2(r)r, \tag{17}$$

we let $v_z = w(r)$, equation (8) takes the form:

$$w' + (\frac{\eta'}{\eta} + \frac{1}{r})w = -\frac{\rho}{\eta}G_z \tag{18}$$

If one makes the substitution $w = \varpi\frac{1}{\eta r}$, where $\varpi = \varpi(r)$, then (11) transforms into equation:

$$\varpi'\frac{1}{\eta r} = -\frac{\rho}{\eta}G_z$$

Integration gives us:

$$w = -\frac{1}{\eta r}\left(\int_1^r r_1 \rho G_z dr_1 + c_1\right),$$

As a result, we get the following expression for the velocity component:

$$v_z = -\int_1^r \frac{1}{\eta r_2}\left(\int_1^{r_2} r_1 \rho G_z dr_1 + c_1\right) dr_2 + c_2. \tag{19}$$

Appendix B. Gauss-Seidel smoother

Smoothing operation can be implemented on the basis of Gauss-Seidel iterations. The respective iterative pressure and velocity update schemes for a regularly spaced grid can be derived:

$$P^{new}_{(i,j,l)} = P_{(i,j,l)} + \eta_{n(i,j,l)} \Delta R^{continuity}_{i,j,l} \theta^{continuity}_{relaxation} \tag{20}$$

$$\Delta R^{continuity}_{i,j,l} = R^{continuity}_{i,j,l} - \frac{v_r}{r} - \frac{\partial v_r}{\partial r} - \frac{1}{r}\frac{\partial v_\varphi}{\partial \varphi} - \frac{\partial v_z}{\partial z}, \tag{21}$$

$$v^{new}_{r(i,j,l)} = v_{r(i,j,l)} + \frac{\Delta R^{r-Stokes}_{i,j,l}}{C_{v_r(i,j,l)}} \theta^{Stokes}_{relaxation} \tag{22}$$

$$v^{new}_{\phi(i,j,l)} = v_{\varphi(i,j,l)} + \frac{\Delta R^{\varphi-Stokes}_{i,j,l}}{C_{v_\varphi(i,j,l)}} \theta^{Stokes}_{relaxation} \tag{23}$$

$$v^{new}_{z(i,j,l)} = v_{z(i,j,l)} + \frac{\Delta R^{z-Stokes}_{i,j,l}}{C_{v_z(i,j,l)}} \theta^{Stokes}_{relaxation} \tag{24}$$

where $\theta^{continuity}_{relaxation}, \theta^{Stokes}_{relaxation}$ are relaxation parameters. $C_{v_r(i,j,l)}$, $C_{v_\varphi(i,j,l)}$,$C_{v_z(i,j,l)}$ is the coefficients at $v_{r(i,j,l)} v_{\varphi(i,j,l)}$, $v_{z(i,j,l)}$ in Stokes equations (1). For models with variable viscosity, the respective residuals in Eqs.(22)–(24) become:

$$\Delta R^{r-Stokes}_{i,j,l} = R^{r-Stokes}_{i,j,l} - \frac{\partial \tau_{rr}}{\partial r} - \frac{\tau_{rr} - \tau_{\varphi\varphi}}{r} - \frac{1}{r}\frac{\partial \tau_{r\varphi}}{\partial \varphi} - \frac{\partial \tau_{rz}}{\partial z} + \frac{\partial P}{\partial r}, \tag{25}$$

$$\Delta R^{\varphi-Stokes}_{i,j,l} = R^{\varphi-Stokes}_{i,j,l} - \frac{\partial \tau_{r\varphi}}{\partial r} - \frac{2\tau_{r\varphi}}{r} - \frac{1}{r}\frac{\partial \tau_{\varphi\varphi}}{\partial \varphi} - \frac{\partial \tau_{\varphi z}}{\partial z} + \frac{1}{r}\frac{\partial P}{\partial \varphi}, \tag{26}$$

$$\Delta R^{z-Stokes}_{i,j,l} = R^{z-Stokes}_{i,j,l} - \frac{\partial \tau_{rz}}{\partial r} - \frac{\tau_{rz}}{r} - \frac{1}{r}\frac{\partial \tau_{\varphi z}}{\partial \varphi} - \frac{\partial \tau_{zz}}{\partial z} + \frac{\partial P}{\partial z} \tag{27}$$

where τ is a deviatoric stress tensor.

B.1 Discretization of the continuity equation

Fig. 2 shows an elementary volume (cell) of a 3D staggered grid that can be used for discretization. Using the stencil with six velocity nodes around a cell (Fig.2), equation (21) takes the form:

$$\Delta R^{continuity}_{i,j,l} = R^{continuity}_{i,j,l} - \frac{1}{r_j + \Delta r/2}\frac{v_{r(i+1,j+1,l+1)} + v_{r(i+1,j,l+1)}}{2} - \frac{v_{r(i+1,j+1,l+1)} - v_{r(i+1,j,l+1)}}{\Delta r} -$$
$$- \frac{1}{r_j + \Delta r/2}\frac{v_{\varphi(i+1,j+1,l+1)} - v_{\varphi(i,j+1,l+1)}}{\Delta \varphi} - \frac{v_{z(i+1,j+1,l+1)} - v_{z(i+1,j+1,l)}}{\Delta z}$$

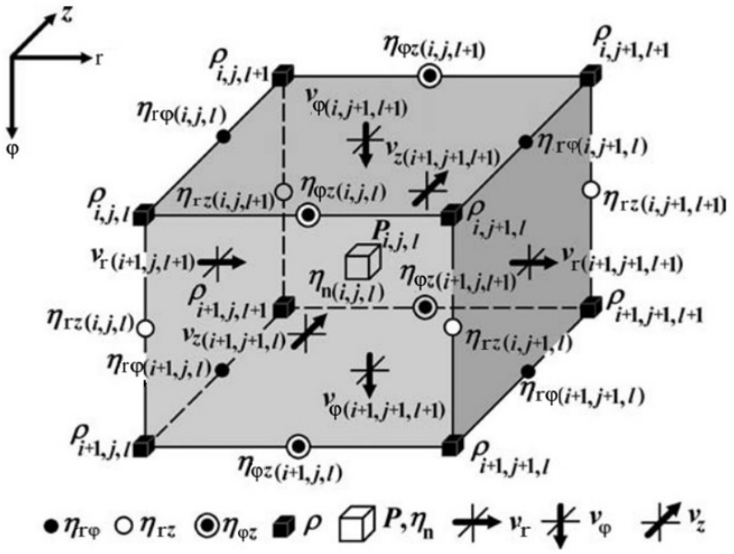

FIG. 2. Indexing of different variables for a 3D staggered grid

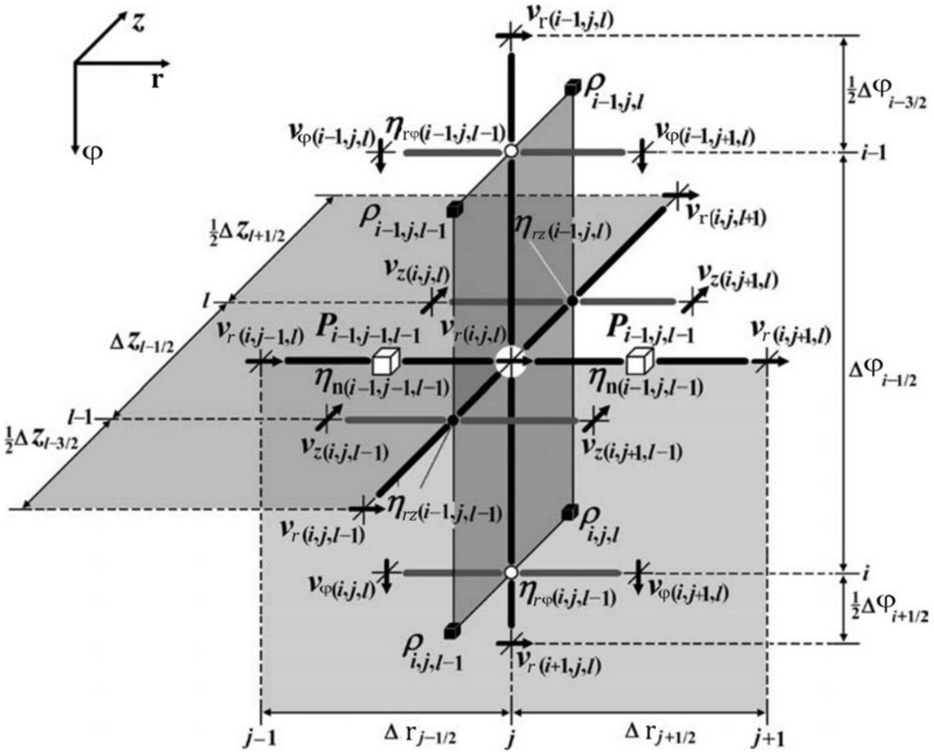

FIG. 3. Stencil of a 3D staggered grid used for the discretization of the r-Stokes equation with variable viscosity

B.2 Discretization of Stokes equations

An example of stencil for the discretization of the r-Stokes equation is shown in Fig.3. For terms in equations (22), (25), we obtain the following discretization:

1. Pressure derivative:

$$\frac{\partial P}{\partial r} = \frac{P_{(i-1,j,l-1)} - P_{(i-1,j-1,l-1)}}{\Delta r}$$

Discretization for terms which contain deviatoric stress tensor components:

2.

$$(\frac{\partial \tau_{rr}}{\partial r})_{i,j,l} = (\frac{\partial}{\partial r}(2\eta\frac{\partial v_r}{\partial r}))_{i,j,l} = 2\frac{1}{\Delta r}(\eta_{(i-1,j,l-1)}\frac{v_{r(i,j+1,l)} - v_{r(i,j,l)}}{\Delta r} - \eta_{(i-1,j-1,l-1)}\frac{v_{r(i,j,l)} - v_{r(i,j-1,l)}}{\Delta r})$$

3.

$$(\tau_{rr})_{i,j,l} = (2\eta\frac{\partial v_r}{\partial r})_{i,j,l} = (\eta_{n(i-1,j,l-1)} + \eta_{n(i-1,j-1,l-1)})\frac{v_{r(i,j+1,l)} - v_{r(i,j-1,l)}}{2\Delta r}$$

4.

$$(\tau_{\varphi\varphi})_{i,j,l} = (2\eta(\tfrac{1}{r}\tfrac{\partial v_\varphi}{\partial \varphi} + \tfrac{v_r}{r}))_{i,j,l} = \tfrac{1}{r_j}(\eta_{n(i-1,j,l-1)} + \eta_{n(i-1,j-1,l-1)})(\tfrac{1}{\Delta\varphi}(\tfrac{v_{\varphi(i,j+1,l)}+v_{\varphi(i,j,l)}}{2} - \\ - \tfrac{v_{\varphi(i-1,j+1,l)}+v_{\varphi(i-1,j,l)}}{2}) + v_{r(i,j,l)})$$

5.

$$(\tfrac{\partial \tau_{r\varphi}}{\partial \varphi})_{i,j,l} = (\tfrac{\partial}{\partial\varphi}(\eta(\tfrac{1}{r}\tfrac{\partial v_r}{\partial\varphi} + \tfrac{\partial v_\varphi}{\partial r} - \tfrac{v_\varphi}{r})))_{i,j,l} = \tfrac{1}{\Delta\varphi}(\eta_{r\varphi(i,j,l-1)}(\tfrac{1}{r_j}\tfrac{v_{r(i+1,j,l)}-v_{r(i,j,l)}}{\Delta\varphi} + \tfrac{v_{\varphi(i,j+1,l)}-v_{\varphi(i,j,l)}}{\Delta r} \\ - \tfrac{1}{r_j}\tfrac{v_{\varphi(i,j+1,l)}+v_{\varphi(i,j,l)}}{2}) - \eta_{r\varphi(i-1,j,l-1)}(\tfrac{1}{r_j}\tfrac{v_{r(i,j,l)}-v_{r(i-1,j,l)}}{\Delta\varphi} + \tfrac{v_{\varphi(i-1,j+1,l)}-v_{\varphi(i-1,j,l)}}{\Delta r} - \tfrac{1}{r_j}\tfrac{v_{\varphi(i-1,j+1,l)}+v_{\varphi(i-1,j,l)}}{2}))$$

6.

$$(\tfrac{\partial \tau_{rz}}{\partial z})_{i,j,l} = (\tfrac{\partial}{\partial z}(\eta(\tfrac{\partial v_z}{\partial r} + \tfrac{\partial v_r}{\partial z})))_{i,j,l} = \tfrac{1}{\Delta z}\eta_{rz(i-1,j,l)}(\tfrac{v_{z(i,j+1,l)}-v_{z(i,j,l)}}{\Delta r} + \tfrac{v_{r(i,j,l+1)}-v_{r(i,j,l)}}{\Delta z}) - \\ - \eta_{rz(i-1,j,l-1)}(\tfrac{v_{z(i,j+1,l-1)}-v_{z(i,j,l-1)}}{\Delta r} + \tfrac{v_{r(i,j,l)}-v_{r(i,j,l-1)}}{\Delta z}) .$$

Discretization for coefficient $C_{v_r(i,j,l)}$ in equation (16) takes the form:

$$C_{v_r(i,j,l)} = -2\tfrac{\eta_{n(i-1,j,l-1)}+\eta_{n(i-1,j-1,l-1)}}{\Delta r^2} - \tfrac{\eta_{n(i-1,j,l-1)}+\eta_{n(i-1,j-1,l-1)}}{r_j^2} - \\ - \tfrac{1}{r_j^2}\tfrac{\eta_{r\varphi(i,j,l-1)}+\eta_{r\varphi(i-1,j,l-1)}}{\Delta\varphi^2} - \tfrac{\eta_{rz(i-1,j,l)}+\eta_{rz(i-1,j,l-1)}}{\Delta z^2}$$

Discretization for the φ-Stokes and z-Stokes equations can be constructed and indexed analogously.

Acknowledgements

This work was partially financially supported by the Government of the Russian Federation (grant 074-U01), by Ministry of Science and Education of the Russian Federation (GOSZADANIE 2014/190, Projects No 14.Z50.31.0031 and No. 1.754.2014/K)), by grant MK-5001.2015.1 of the President of the Russian Federation. The authors thank Prof. P. Tackley and Prof. T. Gerya for interesting discussions.

References

[1] Zhang H., Xu Sh., Jeffries G.D.M., Orwar O., Jesorka A. Artificial nanotube connections and transport of molecular cargo between mammalian cells. *Nano Comm. Net.*, 2013, **4**(4), P. 197–204.

[2] Li T.-D., Gao J., Szoszkeiwicz R., Landman U., Riedo E. Structured and viscous water in subnanometr gaps. *Phys. Rev. B*, 2007, **75**, P. 115415.

[3] Popov I.Yu., Chivilikhin S.A., Rodygina O.A., Gusarov V.V. Crystallite model for flow in nanotube caused by wall soliton. *Nanosystems: Phys. Chem. Math.*, 2014, **5**(3), P. 400–404.

[4] Popov I. Statistical derivation of modified hydrodynamic equations for nanotube flows. *Phys. Scripta*, 2011, **83**, P. 045601/1-5.

[5] Mashl R.J., Joseph S., Aluru N.R., Jacobsson E. Anomalously immobilized water: A new water phase induced by confinement in nanotubes. *Nano Letters*, 2003, **3**(5), P. 589–592.

[6] Kolesnikova S.A., Loonga C.K., de Souzaa N.R., Burnhamb C.J., Moravskyc A.P. Anomalously soft dynamics of water in carbon nanotubes, *Physica B*, 2006, **385-386**, P. 272–274.

[7] Popov I., Makeev I. A benchmark solution for 2-D Stokes flow over cavity, *Z. Angew. Math.Phys.*, 2014, **65**, P. 339–348.

[8] Popov A.I., Gerya T., Lobanov I.S., Popov I.Yu. Benchmark solutions for nanoflows. *Nanosystems: Phys. Chem. Math.*, 2014, **5**(2), P. 391–399.

[9] Popov A.I., Gerya T., Lobanov I.S., Popov I.Yu. On the Stokes flow computation algorithm based on Woodbury formula. *Nanosystems: Phys. Chem. Math.* 2015, **6**(1), P. 140–145.

[10] Gerya T. *Introduction to Numerical Geodynamic Modelling.* Cambridge: Cambridge University Press, 2010.

NANOSYSTEMS: PHYSICS, CHEMISTRY, MATHEMATICS, 2015, 6 (5), P. 680–688

Encapsulation of iron atoms between framgments of graphene planes

[1]A. V. Siklitskaya, [2]V. I. Ivanov-Omskii, [2]M. S. Chekulaev, [2]S. G. Yastrebov, [3]R. Smith, [4]A. Slav, [4]C. Morosanu, [5]S. V. Kozyrev

[1] Institute of Theoretical Physics, University of Warsaw, Warsaw, Poland

[2] Ioffe Institute, St.Petersburg, Russia

[3] Loughborough University, Department of Mathematical Sciences, Loughborough, United Kingdom

[4] National Institute of Materials Physics, Bucharest, Romania

[5] Center for advanced studies, Peter the Great St.Petersburg Polytechnic University, St.Petersburg, Russia

Yastrebov@mail.ioffe.ru, SVKozyrev@spbcas.ru

PACS 81.05.ue **DOI 10.17586/2220-8054-2015-6-5-680-688**

In this paper, we apply results of analysis of the Raman spectrum from an amorphous carbon film modified with iron ($a - C : Fe$) which leads to construction of clusters containing fragments of graphene and a layer of iron atoms. Such clusters may be candidates for the role of microwave radiation absorbers. For the Raman experiments we performed deposition of a thin film of $a - C : Fe$. Details of the film deposition process, together with the corresponding Raman experiments are presented in this paper. Comparison with a literature model was performed for the intensity ratio of the maxima for specific Raman bands, using the letter D to represent “disorder” and the letter G to represent “graphite”. Comparison gives evidence for the existence of nanosize fragments of graphene embedded in an amorphous matrix of the $a - C : Fe$ film. The diameter of the fragments is predicted to attain a value of about 1.2 nm. Moreover, in a comparison with experimental data for defective graphite, the position of the maximum of the D band for $a - C : Fe$ appeared to be red shifted. This could support the proposition that damping of Raman-active oscillations occurs by an electron gas in fragments of graphene after introduction of iron, e.g. after intercalation. On the basis of these estimates, we modeled a symmetrical polycyclic aromatic hydrocarbon having a similar size and converted it into fragment of a graphene plane by removal of hydrogen atoms occupying the edge states. To preserve symmetry, we placed atoms of iron on top of the fragment, situating them exactly above the centers of hexagons at a certain distance and placed another fragment of graphene on the top of the iron atoms, symmetrically. For a distance of 2.52 Åbetween the centers of the hexagon and the iron atom, distortions of carbon-carbon valence bonds and angles were found to be minimal, as shown through optimization of the system's geometry using the *Avogadro* molecular editor. This result supports an hypothesis of graphene fragments during the growth of an amorphous carbon film modified by simultaneous addition of a dopant metal such as iron. This example may illustrate the stability of a two-dimensional electron gas confined between the fragments.

Keywords: graphene, iron, intercalation, carbon, nanoclusters, encapsulation.

Received: 1 October 2015

1. Introduction

Academic interest has recently been growing for the relatively new nanocomposites formed from clusters of graphene and metals. For example, two dimensional inclusions of iron were incorporated between planar fragments of graphene due to the lattice parameter match between graphene and two-dimensional iron [1, 2]. On the other hand, routine technological methods to achieve similar goals have so far not been reported. Simultaneous magnetron sputtering of graphite and metal targets may be one way in which such clusters may be formed. In this case, a stacking between two dimensional metal and graphene plane fragments may occur, usually termed intercalation. The metal atoms can be situated either between two graphene planes or above a single fragment [3,4]. However, experimental evidence for the existence of such fragments is limited to exploiting arguments concerning the activation of D and G Raman bands in infrared spectra of the composites [3–7]. The authors of these papers term the incorporation of metal atoms in a carbon environment as 'encapsulation'. For the case of pairs of graphene planes and iron metal atoms fragments placed between them, one may consider these planes as outer "shells" of a capsule and use this term. However, there has until now been no direct observations of the intercalated graphene clusters, although some modelling results have been published [3, 4].

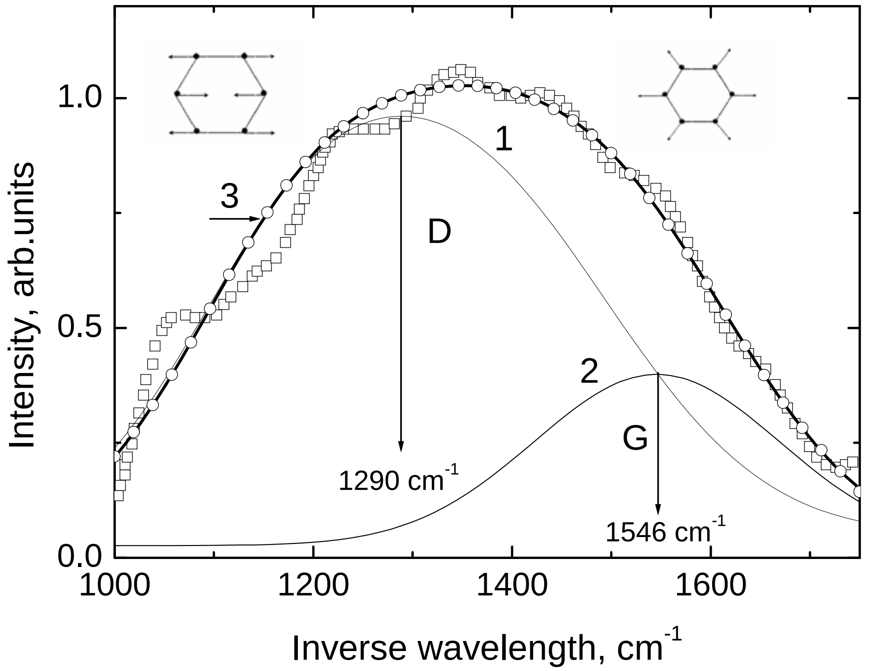

Fig. 1. Raman spectrum of a thin film of a-:Fe ([Fe]/[C]=0.62) and its Gaussian decomposition: empty squares stand for experimental data. Insets show two types of oscillations of carbon atoms in a hexagon contributing to D and G Raman bands, correspondingly. An interference pattern is distinctly recognizable. Result of smoothing [17] is presented by empty circles. Solid lines depict Gaussian decomposition discriminating D and G bands as contour 1 and (contour 2), correspondingly; curve 3 portrays the sum of contours 1 and 2

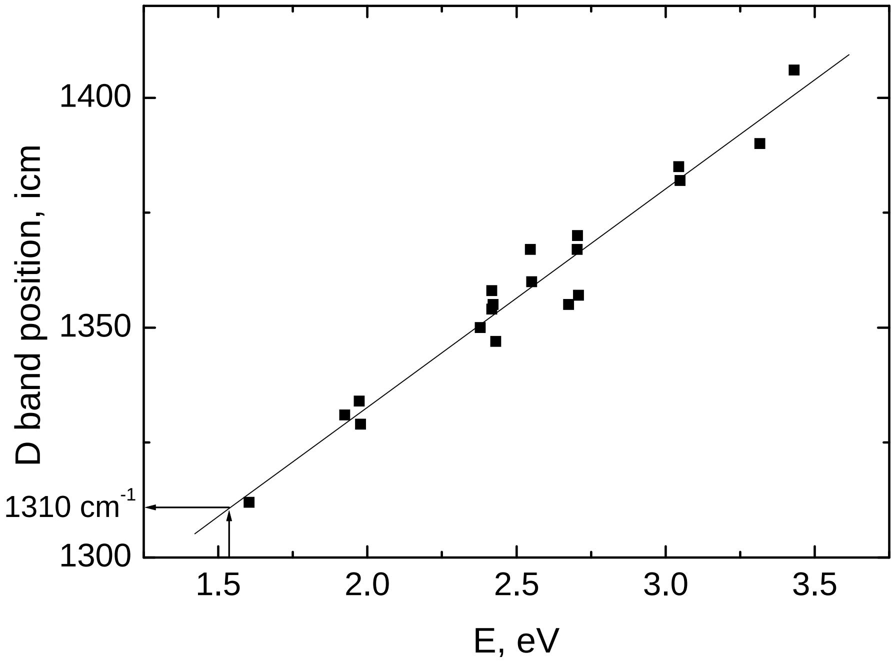

FIG. 2. Dependence of the spectral position of the Raman D band for defective graphite as a function of energy of photons exciting the Raman spectra, [18]. Arrows depict the position of the D band for the photon energy used in this paper

Practical interest in amorphous carbon containing encapsulated clusters of magnetic metals was linked to the intriguing possibility of electromagnetic radiation absorption in the microwave spectral region (frequency $\sim$ 10 GHz) [8]. This could provide opportunities to use nanocomposite films for purposes of electromagnetic shielding in many different areas, including stealth technology [9]. This effect might be linked to the excitation of Frőlich-like resonance because of either the specific magnetic properties of nanosize portions of ferromagnetic materials [10] or their special dielectric characteristics. Among valuable magnetic properties, hysteresis losses play the most important role for contribution to the absorption of microwaves. However, for magnetic clusters of several nanometers in size, the hysteresis losses are negligibly small [11]. Thus, the observed effect of microwave absorption might be simply explained by the peculiarities of electromagnetic absorption by particles of special shapes. These could be e.g., flat nanoclusters confining a two-dimensional electron gas embedded in the nanocomposite because the Frőlich resonance shifts for this particular case to the microwave region (see, e.g. [12]). It is natural to postulate the existence of two-dimensional conductive clusters that may absorb microwave radiation and real fragments of graphene. Thus, in this study, we investigate fragments of graphene and ordered layers of iron atoms. If a single layer of iron is absorbed by a single fragment of graphene, one may term this situation as decoration. When two or more fragments are involved, this situation might be termed as intercalation. For symmetry reasons, we present the case of intercalation when a layer of iron atoms is placed between a pair of fragments of graphene. To be precise, iron atoms are situated above the centers of the carbon hexagons. A similar geometrical picture was considered [13], but more fragments of graphene planes were considered there.

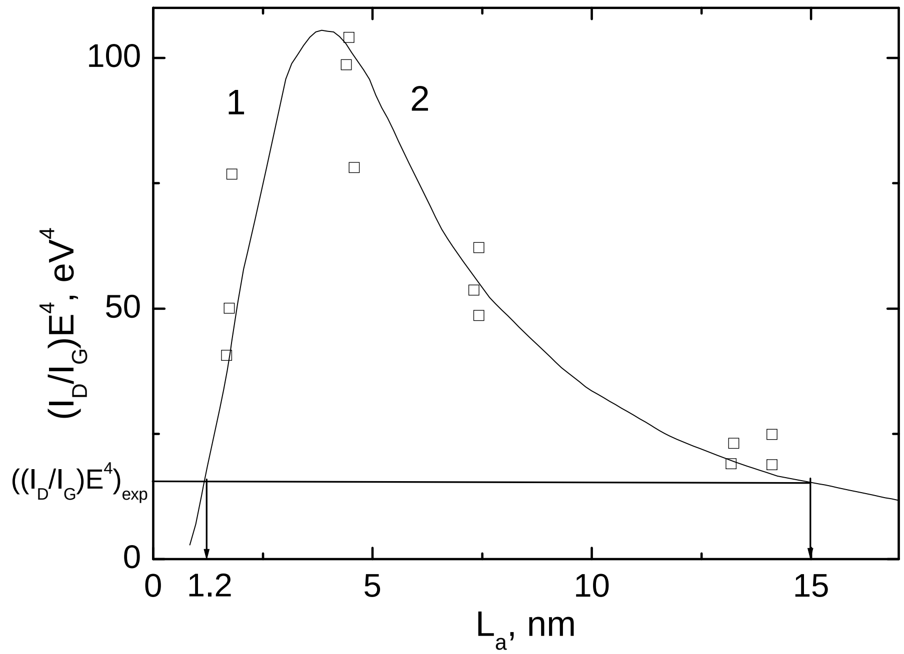

FIG. 3. Dependence of the ratio $\frac{I_D}{I_G}E^4$ on the distance L_a between defects in exfoliated graphene exposed to ion bombardment. The left hand part of the curve to the maximum represents fragmented graphene embedded in the amorphous matrix; points to the right from the maximum characterize passage through the percolation threshold; here I_D and I_G are intensities of Raman scattering measured at the maxima of the contours of D and G correspondingly; E is the energy of the photon used for excitation of the Raman spectrum. Empty squares depict experimental data from [14], [15]. The solid line shows the best fit to the equation in [15]. The left arrow gives the size of graphene fragments for the case of an amorphous film of a-C : Fe: $(\frac{I_D}{I_G}E^4)_{exp}$ as determined from Fig.1. The right arrow shows the hypothetical case when the percolation cluster consists of linking fragments of graphene

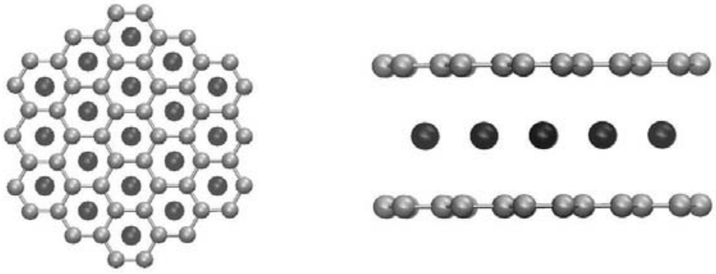

FIG. 4. A view of a pair of fragments of graphene planes encapsulating a layer of iron atoms after structure optimization performed by the *Avogadro* package. Gray and dark gray circles portray atoms of carbon and iron correspondingly

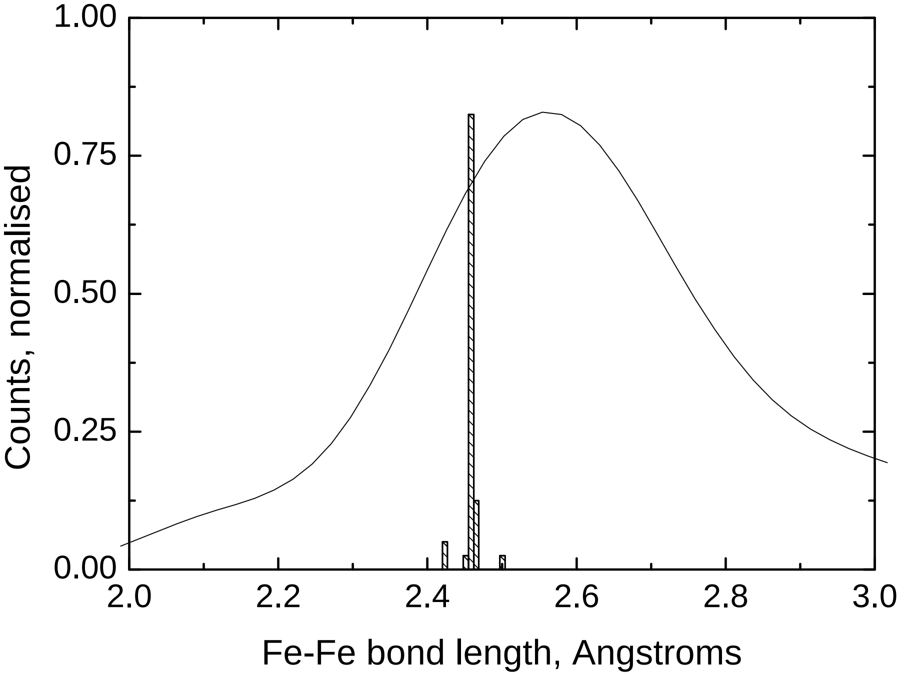

Fig. 5. The Fe bond angle distribution in the graphene layers. Bars represent the Fe-Fe interatomic distance after optimizing the geometry of the atomic configuration as in Fig. 4. The full line corresponds to part of the radial distribution function for amorphous iron [20]

Here we derive geometric parameters of the cluster by comparison of the ratio of specific Raman bands obtained from our experimental data and calibration curve suggested recently in ([14], [15]).The geometric optimization of the model of the cluster was performed using the *Avogadro* molecule editor [16]. This is useful for qualitative investigation of the stability of new materials. The statistical distributions of bond length between atoms forming the cluster are also presented and discussed here.

2. Experimental

The film was grown by the simultaneous sputtering of graphite and iron with an alternating current magnetron system operating at a frequency of 1.78 MHz. More technical details are presented in [11]. Here we note that the chemical composition of film, thickness and specific density were obtained using both Rutherford backscattering and nuclear reactions with a deuteron beam of energy 1 MeV. Analysis of the experimental data shows a concentration ratio [Fe]/[C] of 0.62 and traces of oxygen with a corresponding ratio $[O]/[C]$ of 0.05. The film was $\sim 1\mu m$ in thickness and the density $\varrho = 3.9 g/cm^3$. Raman spectra were obtained using an Ocean Optics R-2001 spectrometer operating at 785 nm and 500 mW radiation. The radiation was delivered to the investigating sample by a fiber waveguide. A similar waveguide was used for detection of the scattered radiation.

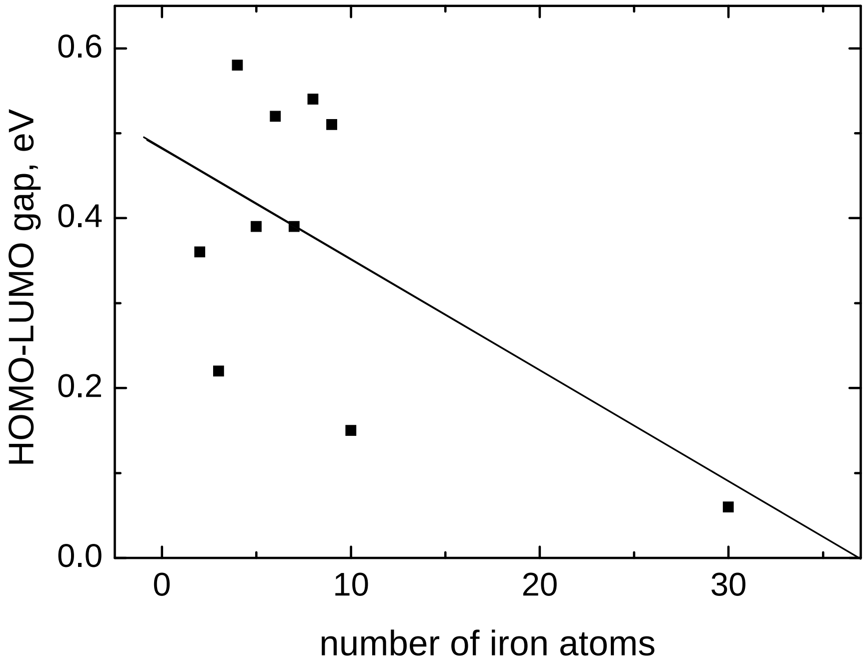

Fig. 6. Dependence of the HOMO-LUMO gap as a function of the number of atoms in the iron nanocluster [21], [22]. The gap becomes zero for N=37

3. Results and discussion

3.1. Geometrical characteristics of graphene fragment

Figure 1 shows the Raman spectrum for $a - C : Fe$ in the area corresponding to atomic vibrations of the carbon matrix where specific bands D and G manifest themselves. The spectrum looks like a wide band slightly modified with an interference pattern. We applied the Swanepoel method [8] for smoothing the interference and the result is presented in Fig.1 by empty circles. The decomposition of the resulting function was performed using the best fit by a sum of two Gaussians extracting the contribution of D and G lines from the background. A comparison was performed between the spectral position of the Raman band D extracted from the experiment presented in Fig.1 and the dispersion dependence for the position of the D band for disordered graphite depicted in Fig.2. The dependence presented in Fig.2 is plotted for the position of the D band measured in inverse wavelength versus the exciting Raman spectra photon energies. The arrow in Fig.2 shows the prediction for the position of the D band for our experiment, equal to $\sim 1310 cm^{-1}$. However, the Gaussian decomposition of data presented in Fig.1, gives a different inverse wavelength value, $1290 cm^{-1}$. It means that the position of the D band presented in Fig.1 is red-shifted in comparison with the prediction. That might be used as evidence of a damping process of the $C - C$ vibrations that might be realized through excitation of a free electron gas in the vicinity of the conducting cluster. This fact may be used as evidence for the existence of conductive inclusions embedded in an amorphous carbon matrix. Among them, the iron-decorated or iron-intercalated fragments of graphene might occur. Note that the ratio of $\frac{I_D}{I_G}$ characterizes the size of the graphene fragment forming the amorphous carbon matrix, as was demonstrated in recent papers [14], [15] where a correction to the energy of photons exciting the Raman spectrum E was performed. Here I_D and I_G are the intensities for Raman scattering measured at the maxima of the contours of D and G correspondingly. To be precise, the calibration curve from [15] establishing a link between the ratio and distance between defects in exfoliated graphene is depicted in Fig.3. This dependence consists of two parts: that of the left side of the maximum and that of the right part. The right part corresponds to the case when a percolation cluster containing linking graphene fragments has formed. The left part characterizes an ensemble of graphene fragments separated from each other by an amorphous matrix. Therefore, a direct comparison of the experimental the value obtained from Fig.1, $(\frac{I_D}{I_G}E^4)_{exp}$, with the dependence presented in Fig.3 by a solid line, is valid. The left arrow in Fig.3 corresponds to the case of an amorphous structure and gives an estimation for the graphene fragment size for our sample of ≈ 1.2 nm. The right arrow corresponds to the hypothetical case of formation of the infinite percolation cluster in an amorphous carbon matrix.

3.2. Optimisation of geometry

Based on the above information for the size of a fragment of graphene, we chose as a model a polycyclic aromatic hydrocarbon $C_{54}H_{18}$ [19] having almost the same size as predicted by Raman spectroscopy. We made a slight modification with the hydrocarbon, removing atoms of hydrogen occupying the edge states. Afterwards we constructed the layered system. The iron atoms were placed exactly above the centers of each hexagon belonging to a basal fragment of graphene maintaining a certain distance L above the plane. Another fragment of graphene was placed symmetrically on the top of the layer of iron atoms keeping the same distance from the each hexagon center to each iron atom of L. Thus, we investigate case of "intercalation", but one may reduce the system size to obtain results for the case "decoration" without loss of generality.

Different occupations of empty places above hexagons may occur in reality. Here, we considered maximal occupation of empty places by analogy with previous paper where we modeled the interaction of cobalt with unsymmetrical graphene fragments.

A schematic view of the carbon-iron cluster after optimization of the geometry by *Avogadro* is portrayed in Fig.4. Note that after optimization both the Fe-Fe and C-C bond lengths only slightly deviate from their initial values of $2.61 \mathring{A}$ and $1.42 \mathring{A}$ respectively. It is seen in the Figure 5 that the interplanar distances are slightly changed after optimization, deviating from the initial value of $L = 2.52 \mathring{A}$. It might be interesting to exploit *ab initio* modeling to investigate details of the electronic structure of carbon-iron clusters more exactly before a firm conclusion on the possibility of absorption of microwaves by the clusters can be formed. However, for ab initio modeling, computation time is expensive. Thus, we analyze here the electronic spectrum qualitatively. First of all it is important to estimate with more details the degree of amorphization of the iron layer obtained after optimization of the geometry because electronic properties are very sensitive to this parameter. For this purpose, we present in Fig.5 an histogram of the Fe-Fe interatomic distribution in comparison with a similar distribution for amorphous iron. One may see in Fig.5 that the distribution of Fe-Fe bonds is very sharp in comparison with amorphous iron itself.

Furthermore, since we are dealing with nano-dimensional clusters, it is interesting to see how the effects of electron spectrum size quantization can affect the electrical conductivity of the iron layer and adjacent graphene plane fragment.

Figure 6 shows the dependence of the energy gap between the free and occupied states in iron nanoclusters (HOMO-LUMO gap), as a function of the number of atoms forming them. It is seen that the dependence may be approximated by a linear trend that reaches zero when the number of atoms is approximately equal to M = 37. In this case, the cluster of iron is metallic. Note that this cluster will differ only slightly in size from the analog, shown in Figure 4. This may indicate a good estimation of the size of the cluster size performed by analyzing the Raman spectrum. Because a possible difference may exist between the work functions of the graphene plane fragments and two-dimensional layer of iron metal, electrons can be either localized in the vicinity of iron layer or may delocalize within a whole fragment of graphene -iron - fragment of the graphene sandwich.

When electrons in an iron cluster behave as they do in a bulk metal, one may use a value known for a bulk iron: 4.5-4.7 eV [23]. In turn, to evaluate the work function W of a fragment of graphene one can use the expression: $W = I_p + \frac{E_g}{2}$, where I_p is ionization potential for the fragment and E_g is its width of optical gap.

The value of I_p might be estimated using a well-known equation for polycyclic aromatic hydrocarbons: $I_p = 5.1 + 0.7E_g$ (eV) [24]. For a fragment of graphene containing 37 hexagonal rings (37 is number of atoms when the layer of iron becomes conductive), the value for E_g might be estimated using an approximate equation for symmetric hydrocarbons [25]: $E_g = 2|\beta|M^{-1/2}$; here $2|\beta| \approx 2.9$ eV is the energy of interaction between pair of adjacent π orbitals. M is number of hexagons in the fragment. $E_g \approx 0.95$ eV for $M = 37$, thus $W =$ 6.24 eV. That is the work function for a fragment of graphene supporting a conductive iron layer is bigger than that for bulk iron. One may expect for this situation some smearing of the free electron gas from the iron layer to the graphene fragments.

4. Conclusions

The estimations performed in this paper lead to two preliminary conclusions:

1. Flat particles containing fragments of graphene planes separated by a layer of iron may be present in an a-C:Fe structure.

2. Whether the fragment would be metallic or not will depend upon the possibility of the formation of the iron layer with dimensions that are sufficient for suppression of quantum effects.

The paper was presented at the 10th Simposium “Thermodynamics and Material Science” 7-11.09.2015, St. Petersburg, Russia.

References

[1] Kosugi K., Bushiri M. J., Nishi N. Formation of air stable carbon-skinned iron nanocrystals from FeC_2. *Appl. Phys. Lett*, 2004, **84**, P. 1753–55.

[2] Zhao J., Deng Q., Bachmatiuk A., et al. Free-Standing Single-Atom-Thick Iron Membranes Suspended in Graphene Pores. *Science*, 2014, **343**, P. 1228–32.

[3] Ivanov-Omskii V. I., Smorgonskaya E. A. Charge displacement induced by intercalation of graphite-like nanoclusters in amorphous carbon with copper. *Physics of the Solid State*, 1999, **41**(3), P. 786–88.

[4] Ivanov-Omskii V. I., Smorgonskaya E. A. Modification of the electron spectrum and vibrational properties of amorphous carbon by copper doping. *Semiconductors*, 1998, **32**(8), P. 831–37.

[5] Ivanov-Omskii V. I., Zvonareva T. K., Frolova G. S. Vibration modes of carbon in hydrogenated amorphous carbon modified with copper. *Semiconductors*, 2000, **34**(12), P. 1391–96.

[6] Zvonareva T. K., Ivanova E. I., Frolova G. S. et al. Vibratonal spectroscopy of $aC : H(Co)$. *Semiconductors*, 2002, **36**(6), P. 695–00.

[7] Ivanov-Omskii V. I., Frolova G. S. IR spectroscopy of copper-intercalated graphite nanoclusters in amorphous carbon. *Tech. Phys. Lett.*, 2000, **26**(7), P. 623–24.

[8] Lutsev L. V., Yakovlev S. V., Zvonareva T. K. et al. Microwave properties of granular amorphous carbon films with cobalt nanoparticles. *J. Appl. Phys.*, 2005, **97**, P. 104327/1-6.

[9] Alexeev A. G., Shtager E. A., Kozyrev S. V. Physical Principles of Stealth Technology. St.Petersburg.: VVM, 2007. 283 p.

[10] Draine B. T., Lazarian A. Magnetic dipole microwave emission from dust grains. *Astrophys. J.*, 1999, **512**, P. 740–54.

[11] Yastrebov S. G, Ivanov-Omskii V. I., Pop V, et al. Magnetic properties of iron-modified amorphous carbon. *Semiconductors*, 2005, **39**(7), P. 840–44.

[12] Bohren C. F., Huffman D. R. Absorption and Scattering of Light by Small Particles. Weinheim.: Wiley-VCH Verlag GmbH, 1998, 545 p.

[13] Belenkov E. A. Formation of Graphite Structure in Carbon Crystallites. *Inorganic Materials*, 2001, **37**(9), P. 928–34.

[14] Lucchese M. M., Stavale F, Ferreira Martins E. H., Vilani C. et al Quantifying ion-induced defects and Raman relaxation length in graphene. *Carbon*, 2010, **4**(8), P. 1592–97.

[15] Cancado L. G., Jorio A., Ferreira Martins E. H. et. al. Quantifying Defects in Graphene via Raman Spectroscopy at Different Excitation Energies. *Nanoletters*, 2011, **11**(8), P. 3190–3196.

[16] Hanwell M. D., Curtis D. E., Lonie D. C., et al. Avogadro: An advanced semantic chemical editor, visualization, and analysis platform. *J Cheminform*, 2012, **4**(1), P. 1–17.

[17] Swanepoel R. Determination of the thickness and optical constants of amorphous silicon. *J. Phps. E: Sci. Instrum.*, 1983, **16**, P. 1214–33.

[18] Ferrari A. C. Raman spectroscopy of graphene and graphite: Disorder, electron-phonon coupling, doping and nonadiabatic effects. *Solid State Communications*, 2007, **143**, P. 47–57

[19] Alberty R., A., Chung M., B., Reif A. K. Standard Chemical Thermodynamic properties of Polycyclic Aromatic Hydrocarbons and their Isomer Groups. III. Naphthocoronene Series, Ovalene Series, and First Members of Some Higher Series. *Phys Chem Ref Data*, 1990, **19**(2), P. 350–70.

[20] Yamamoto R., Shibuta H., Doyama M. Computer simulation of radiation damage in amorphous metals. *J.Nucl.Mater.*, 1979, **85-86**, P. 603–06.

[21] Wang L., Hudson G. A. Advanced Molecular Dynamics Simulations on the Formation of Transition Metal Nanoparticles. In: Molecular Dynamics - Theoretical Developments and Applications in Nanotechnology and Energy; Ed. Lichang Wang L.- INTECH Open Access Publisher, 2012, 424 p.

[22] Cervantes-Salguero K., Seminario J. M. Structure and energetics of small iron clusters. *J. Mol. Model.*, 2012, **18**, P. 4043–52.

[23] Hölzl J., Schulte F. K. Work function of metals In Solid Surface Physics. *Springer Tracts in Modern Physics*, 2006, **85**, P. 1–150

[24] Kuroda H. Ionisation potential of polyciclic aromatic hydrocarbons. *Nature*, 1964, P. 1214–15.

[25] Robertson J., O'Reilly E. P. Electronic and atomic structure of amorphous carbon. *Phys.Rev.B*, 1987, **35**(6), P. 2946–57.

NANOSYSTEMS: PHYSICS, CHEMISTRY, MATHEMATICS, 2015, 6 (5), P. 689–696

Numerical solution of Schrödinger equation for biphoton wave function in twisted waveguide arrays

D. N. Vavulin[1], A. A. Sukhorukov[2]

[1]ITMO University, St. Petersburg, Russia
[2]Nonlinear Physics Centre, Research School of Physics and Engineering,
Australian National University, Canberra, ACT 2601, Australia

dima-vavulin@mail.ru, Andrey.Sukhorukov@anu.edu.au

PACS 42.50.Tx, 42.65.Wi, 42.65.Lm DOI 10.17586/2220-8054-2015-6-5-689-696

We consider the generation of entangled biphoton states with orbital-angular-momentum in triangular quadratic waveguide arrays with twisted geometry. For this purpose, we derive the Shrödinger equation for biphoton wave function and equation for pump field profile. We describe numerically the process of biphoton generation through spontaneous four-wave mixing. We suggest that biphoton correlations can be controlled by the amount of twist and pump field profile.

Keywords: entangled states, orbital-angular-momentum, optical vortices, twisted waveguides, spontaneous four-wave mixing.

Received: 30 June 2015

Revised: 5 August 2015

1. Introduction

Quantum biphoton states with orbital-angular-momentum (OAM) can be used in quantum communications to extend the alphabet of quantum cryptography, which can increase the transmission rate [7]. Of particular interest are quantum walks, where the interference of several walkers can be used to realize various simulations, including database search [1,12], quantum teleportation, and quantum cryptography [2–4], enabling absolutely secure communications. Quantum walks and generation of biphoton states with OAM can be implemented in arrays of coupled waveguides with closed-loop boundary conditions [5]. Recently, a new type of coupled waveguide with a twisted geometry was demonstrated in a photonic-crystal fiber [6]. Such waveguides are able to effectively provide the transfer of OAM states. The behavior and generation of biphotons in twisted waveguides can be described by the Shrödinger equation and evolution of the pump profile can be desribed by the classical coupled-mode equations. The biphoton entanglement with OAM was first experimentally demonstrated by Zeilinger et al. using the process of spontaneous parametric down-conversion (SPDC) [7]. We consider a linear polarization of light and small twist of waveguides, with the amount of twist $\lesssim 1^\circ$, and in this case the structure of the pump and biphoton modes is essentially the same as in the straight array. We formulate the mathematical model under such conditions.

In our work, we consider generation of biphonons through spontaneous four-wave mixing (SFWM) through $\chi^{(3)}$ nonlinearity in optical fibers. We have not considered $\chi^{(2)}$ nonlinearity, because it requires a crystal lattice without a center of inversion and it is difficult to realize in the optical fiber, unlike $\chi^{(3)}$ nonlinearity which occurs in conventional optical fibers. However, in the case of $\chi^{(3)}$ nonlinearity, the frequencies of pump wave and biphotons may be close to each other, which requires narrow-band filtering before the single-photon detectors [15].

We numerically solve the classical coupled-mode equations for pump profile and Shrödinger equation for biphotons in twisted waveguides.

2. Derivation of Schrödinger equation for biphoton wave function in a twisted waveguide array

The normalized pump field profile evolution along the propagation distance z is defined through the classical coupled-mode equations [8]:

$$i\frac{dE_n}{dz} + C(\omega)\exp\left[-i\omega\dot{\chi}_0(z)\right]E_{n+1} + C(\omega)\exp\left[i\omega\dot{\chi}_0(z)\right]E_{n-1} = 0, \tag{1}$$

where E_n is the complex field amplitude in the nth waveguide, and E_N maps to E_0, and E_{-1} maps to E_{N-1} due to closed-loop boundary conditions [9], n is the waveguide number, N is the total number of waveguides, $\chi_0(z) \equiv \chi_0(z+L)$ is the periodic waveguide bending profile, L is the modulation period, coefficient $C(\omega)$ defines a coupling strength between the neighboring waveguides (it characterizes diffraction strength in a straight waveguide array (WGA) with $\chi_0 \equiv 0$) [10]. In our case, $\dot{\chi}_0(z) = const$, because the waveguide bending profile is the same for all values of z.

The eigenmode solutions of Eqs. (1) are $E_{n(z)}^{(m)} = \varepsilon_n^{(m)}\exp(i\beta_m z)$, where $m = 0, \ldots, N-1$ is the mode number, $\varepsilon_n^{(m)} = \exp(i2\pi mn/N)$ are the mode profiles, and $\beta_m = 2C\cos(2\pi m/N - \phi_0)$ (where $\phi_0 = \omega\dot{\chi}_0(z)$) are the propagation constants. The eigenmodes $E_{n(z)}^{(m)}$ represent discrete optical vortices [14], or states with OAM due to a twisted structure of their phase profiles. Here, the supermode number m corresponds to the OAM.

Generation of photon pairs in cubic nonlinear WGAs through SFWM in the absence of multiple photon pairs can be characterized by the evolution of a bi-photon wave function $\psi_{n_s,n_i}(z)$ in a Schrödinger-type equation. The equation is obtained from the Hamiltonian, and has a form similar to that of quadratic media [13]:

$$\begin{aligned} i\frac{d\psi_{n_s,n_i}(z)}{dz} = \\ -C\Big[\exp\left[i\omega\dot{\chi}_0(z)\right]\psi_{n_{s-1},n_i}(z) + \exp\left[i\omega\dot{\chi}_0(z)\right]\psi_{n_s,n_{i-1}}(z) + \exp\left[-i\omega\dot{\chi}_0(z)\right]\psi_{n_{s+1},n_i}(z) \\ + \exp\left[-i\omega\dot{\chi}_0(z)\right]\psi_{n_s,n_{i+1}}(z)\Big] - \Delta\beta^{(0)}\psi_{n_s,n_i}(z) + i\gamma E_{n_s}^{(p)}(z)E_{n_s}^{(p)}(z)\delta_{n_s,n_i}, \end{aligned} \tag{2}$$

where n_s and n_i are the waveguide numbers describing the positions of the signal and the idler photons, and $E_{n_s}^{(p)}(z)$ is the pump amplitude in waveguide number n_s. $\Delta\beta^{(0)}$ is the linear four-wave mixing phase-mismatch in a single waveguide, γ is a nonlinear coefficient [11]. Dimensionless quantities $\Delta\beta^{(0)}$ and γ in the numerical simulations were considered equal to 1.

It is convenient to make a transformation $\psi_{n_s,n_i}(z) = \psi_{n_s,n_i}(z)\exp(-i\Delta\beta^{(0)}z)$. Then, (2) takes the form:

$$i\frac{d\psi_{n_s,n_i}(z)}{dz} = \\ -C\Big[\exp\left[i\omega\dot{\chi}_0(z)\right]\psi_{n_{s-1},n_i}(z) + \exp\left[i\omega\dot{\chi}_0(z)\right]\psi_{n_s,n_{i-1}}(z) + \exp\left[-i\omega\dot{\chi}_0(z)\right]\psi_{n_{s+1},n_i}(z) \\ + \exp\left[-i\omega\dot{\chi}_0(z)\right]\psi_{n_s,n_{i+1}}(z)\Big] + i\gamma E^{(p)}_{n_s}(z)E^{(p)}_{n_s}(z)\delta_{n_s,n_i}\exp(i\Delta\beta^{(0)}z). \quad (3)$$

3. Numerical solution

3.1. Numerical solution for pump field

We consider the algorithm for solving equation (1) for a system of three waveguides with closed-loop boundary conditions. Schematically, the system appears as shown in Fig. 1.

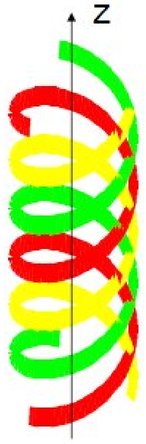

FIG. 1. Scheme of coupled twisted waveguides

Firstly, we consider a system with open boundary conditions, which is described by a three-diagonal matrix of the form:

$$\begin{pmatrix} B_1 & C_2 & 0 \\ A_2 & B_2 & C_2 \\ 0 & A_3 & B_3 \end{pmatrix}\begin{pmatrix} E_1 \\ E_2 \\ E_3 \end{pmatrix} = \begin{pmatrix} D_1 \\ D_2 \\ D_3 \end{pmatrix}, \quad (4)$$

where $A_n = -i(\Delta z/2)C\exp\left[i\omega\dot{\chi}_0(z)\right]$; $B_n = 1$; $C_n = -i\,(\Delta z/2)\,C\exp\left[-i\omega\dot{\chi}_0(z)\right]$; $E_n = E_n(z)$; $D_n = -A_nE_{n-1}\,(z-\Delta z) + B_nE_n\,(z-\Delta z) - C_nE_{n+1}\,(z-\Delta z)$; $n = 1, 2, \ldots, N$; Δz – step along z axis.

This matrix ratio is equivalent to the system of linear equations of the form $AE = D$, where E is a column vector with unknown values, and the matrix A and a column vector D are known. The solution can be found by the shuttle method or, for example, by the formula $E = A^{(-1)}D = \mathrm{linsolve}(A, D)$, which is implemented in a software package Matlab.

In the case of closed-loop boundary conditions, we obtain the following matrix relation:

$$\begin{pmatrix} B_1 & C_2 & A_1 \\ A_2 & B_2 & C_2 \\ C_3 & A_3 & B_3 \end{pmatrix} \begin{pmatrix} E_1 \\ E_2 \\ E_3 \end{pmatrix} = \begin{pmatrix} D_1 \\ D_2 \\ D_3 \end{pmatrix}. \tag{5}$$

The solution can also be found by the formula $E = A^{(-1)}D = \mathrm{linsolve}(A, D)$. For clarity, we give the matrix ratio for the system of five waveguides, which is constructed by a similar algorithm:

$$\begin{pmatrix} B_1 & C_1 & 0 & 0 & A_1 \\ A_2 & B_2 & C_2 & 0 & 0 \\ 0 & A_3 & B_3 & C_3 & 0 \\ 0 & 0 & A_4 & B_4 & C_4 \\ C_5 & 0 & 0 & A_5 & B_5 \end{pmatrix} \begin{pmatrix} E_1 \\ E_2 \\ E_3 \\ E_4 \\ E_5 \end{pmatrix} = \begin{pmatrix} D_1 \\ D_2 \\ D_3 \\ D_4 \\ D_5 \end{pmatrix}. \tag{6}$$

Thus, we can similarly obtain the numerical solution for the system of any number of waveguides. The figures show the numerical solutions for the direct (Fig. 2) and twisted (Fig. 3) arrays of the three waveguides.

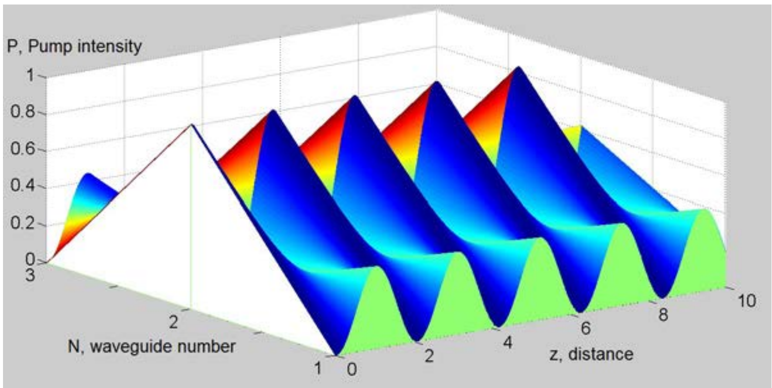

FIG. 2. Pump power ($|E_n|^2$), in the system of three straight waveguides

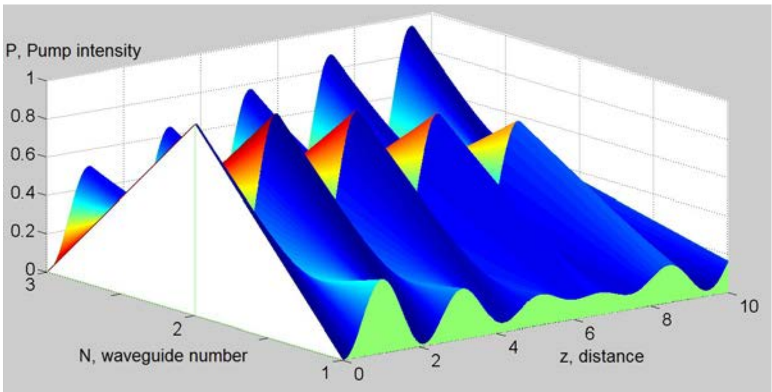

FIG. 3. Pump power ($|E_n|^2$), in the system of three twisted waveguides

3.2. Numerical solution of Schrödinger equation for biphoton wave function

Now, we consider the numerical algorithm for Schrödinger equation (3) for system of three twisted waveguides with closed boundary conditions.

We transform this equation by the Crank-Nicolson scheme to the following form:

$$\begin{aligned} i\psi^{j+1}_{n_s,n_i} &= i\psi^{j}_{n_s,n_i} - \frac{\Delta z}{2}\Big[\alpha_2\left(\psi^{j}_{n_{s-1},n_i} + \psi^{j}_{n_s,n_{i-1}}\right) + \alpha_1\left(\psi^{j}_{n_{s+1},n_i} + \psi^{j}_{n_s,n_{i+1}}\right) \\ &+ \alpha_2\left(\psi^{j+1}_{n_{s-1},n_i} + \psi^{j+1}_{n_s,n_{i-1}}\right) + \alpha_1\left(\psi^{j+1}_{n_{s+1},n_i} + \psi^{j+1}_{n_s,n_{i+1}}\right)\Big] \\ &+ \frac{\Delta z}{2} i\gamma\left(E^{j}_{n_s}\right)^2 \delta_{n_s,n_i} \exp\left(i\Delta\beta^{(0)}\Delta z j\right) + \frac{\Delta z}{2} i\gamma\left(E^{j+1}_{n_s}\right)^2 \delta_{n_s,n_i} \exp\left(i\Delta\beta^{(0)}\Delta z (j+1)\right), \end{aligned} \tag{7}$$

where $\alpha_1 = C\exp[-i\omega\dot{\chi}_0], \alpha_2 = C\exp[i\omega\dot{\chi}_0]$.

Furthermore:

$$\begin{aligned} &- r_2\cdot\psi^{j+1}_{n_s-1,n_i} - r_2\cdot\psi^{j+1}_{n_s,n_i-1} + \psi^{j+1}_{n_s,n_i} - r_1\cdot\psi^{j+1}_{n_s+1,n_i} - r_1\cdot\psi^{j+1}_{n_s,n_i+1} \\ &= r_2\cdot\psi^{j}_{n_s-1,n_i} + r_2\cdot\psi^{j}_{n_s,n_i-1} + \psi^{j}_{n_s,n_i} + r_1\cdot\psi^{j}_{n_s+1,n_i} + r_1\cdot\psi^{j}_{n_s,n_i+1} \\ &+ r_3\left(E^{j}_{n_s}\right)^2\exp(r_4 j) + r_3\left(E^{j+1}_{n_s}\right)^2\exp\left(r_4(j+1)\right), \end{aligned} \tag{8}$$

where $r_1 = i\dfrac{\Delta z}{2}\alpha_1, r_2 = i\dfrac{\Delta z}{2}\alpha_2, r_3 = \dfrac{\Delta z}{2}\gamma, r_4 = i\Delta\beta^{(0)}\Delta z$.

Thus, we obtain the following numerical scheme:

$$-r_2\cdot\psi^{j+1}_{n_s-1,n_i} - r_2\cdot\psi^{j+1}_{n_s,n_i-1} + \psi^{j+1}_{n_s,n_i} - r_1\cdot\psi^{j+1}_{n_s+1,n_i} - r_1\cdot\psi^{j+1}_{n_s,n_i+1} = D^{j}_{n_s,n_i}, \tag{9}$$

where

$$\begin{aligned} D_{n_s,n_i} &= r_2\cdot\psi^{j}_{n_s-1,n_i} + r_2\cdot\psi^{j}_{n_s,n_i-1} + \psi^{j}_{n_s,n_i} + r_1\cdot\psi^{j}_{n_s+1,n_i} + r_1\cdot\psi^{j}_{n_s,n_i+1} \\ &+ r_3\left(E^{j}_{n_s}\right)^2\exp(r_4 j) + r_3\left(E^{j+1}_{n_s}\right)^2\exp(r_4(j+1)). \end{aligned}$$

As a result, we now have a two-dimensional problem. Next, we can obtain the one-dimensional problem by reshaping matrix for the psi-function in a column vector:

$$\begin{pmatrix} \psi_{1,1} & \psi_{1,2} & \psi_{1,3} \\ \psi_{2,1} & \psi_{2,2} & \psi_{2,3} \\ \psi_{3,1} & \psi_{3,2} & \psi_{3,3} \end{pmatrix} \longrightarrow \begin{pmatrix} \psi_{1,1} \\ \psi_{1,2} \\ \psi_{1,3} \\ \psi_{2,1} \\ \psi_{2,2} \\ \psi_{2,3} \\ \psi_{3,1} \\ \psi_{3,2} \\ \psi_{3,3} \end{pmatrix}. \tag{10}$$

Finally, we have a five-diagonal matrix. In matrix form, the problem takes the following form:

$$\begin{pmatrix} 1 & -r_1 & -r_2 & -r_1 & 0 & 0 & -r_2 & 0 & 0 \\ -r_2 & 1 & -r_1 & 0 & -r_1 & 0 & 0 & -r_2 & 0 \\ -r_1 & -r_2 & 1 & 0 & 0 & -r_1 & 0 & 0 & -r_2 \\ -r_2 & 0 & 0 & 1 & -r_1 & -r_2 & -r_1 & 0 & 0 \\ 0 & -r_2 & 0 & -r_2 & 1 & -r_1 & 0 & -r_1 & 0 \\ 0 & 0 & -r_2 & -r_1 & -r_2 & 1 & 0 & 0 & -r_1 \\ -r_1 & 0 & 0 & -r_2 & 0 & 0 & 1 & -r_1 & -r_2 \\ 0 & -r_1 & 0 & 0 & -r_2 & 0 & -r_2 & 1 & -r_1 \\ 0 & 0 & -r_1 & 0 & 0 & -r_2 & -r_1 & -r_2 & 1 \end{pmatrix} \begin{pmatrix} \psi_{1,1} \\ \psi_{1,2} \\ \psi_{1,3} \\ \psi_{2,1} \\ \psi_{2,2} \\ \psi_{2,3} \\ \psi_{3,1} \\ \psi_{3,2} \\ \psi_{3,3} \end{pmatrix} = \begin{pmatrix} D_{1,1} \\ D_{1,2} \\ D_{1,3} \\ D_{2,1} \\ D_{2,2} \\ D_{2,3} \\ D_{3,1} \\ D_{3,2} \\ D_{3,3} \end{pmatrix}. \qquad (11)$$

This matrix ratio is equivalent to the matrix system of linear equations of the form $A\Psi = D$, where Ψ is a vector-column with unknown values, and the matrix A and a column vector D are known. The solution can be found by splitting methods or, for example, by the formula $\Psi = A^{(-1)}D = \mathrm{linsolve}(A, D)$, implemented in the Matlab software package.

Figures 4 and 5 show the numerical solutions for the squared modulus of the biphoton wave function respectively for forward and twisted arrays of three waveguides. In Figs. 4 and 5, we see 9 imaginary waveguides, which corresponds to the 3 real waveguides. Thus, waveguides with numbers 1–3 correspond to the biphoton wave function with signal photon located in the 1st wavegude and idler photon located in 1–3 waveguides respectively. Similarly, waveguides 4–6 correspond to the signal photon located in the2nd waveguide and the idler photon located in waveguides 1–3, and waveguides 7–9 correspond to the signal photon located in the 3rd waveguide and the idler photon located in waveguides 1–3.

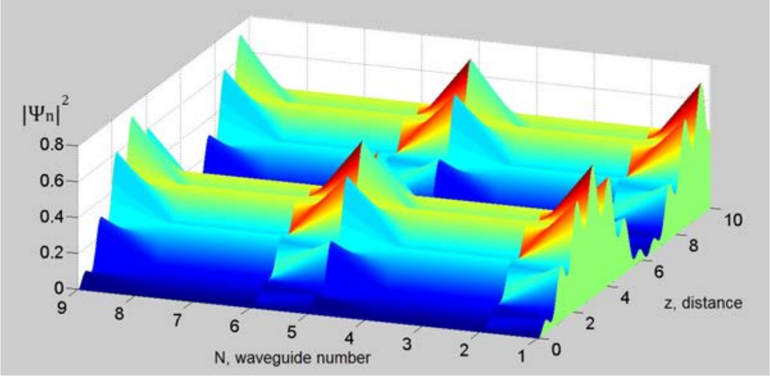

Fig. 4. Two-photon correlations ($|\Psi_{n_s,n_i}|^2$), in case of photon generation by SFWM from a pump inside the array for system of three straight waveguides

If we transform the Fig. 5 to a more convenient form Fig. 6, we can see the two-photon correlations ($|\Psi_{n_s,n_i}|^2$) at three different distances, which are of practical interest (a: $z = 0$; b: $z = 0.375L$; c: $z = 0.604L$, where L is the distance at which the biphoton wave function restores its initial state, when photons propagate in the regime of quantum walks in the absence of pumping). At $z = 0$ (a), there are no photons. At distance (b), the generated photons are mostly bunched: appearing in the same waveguides. In (c), the photons are anti-bunched; appearing at different waveguides.

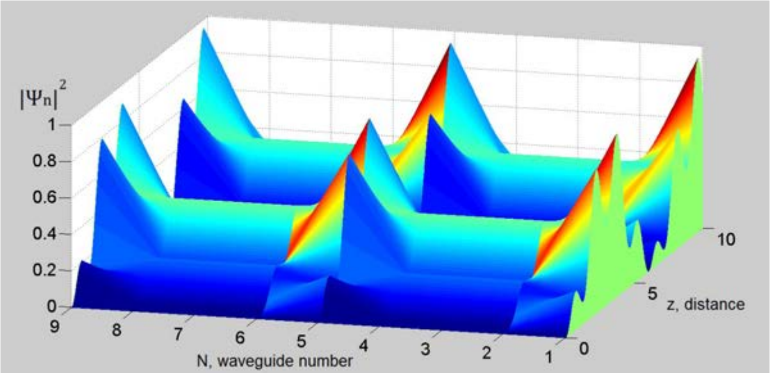

FIG. 5. Two-photon correlations ($|\Psi_{n_s,n_i}|^2$), in case of photon generation by SFWM from a pump inside the array for system of three twisted waveguides

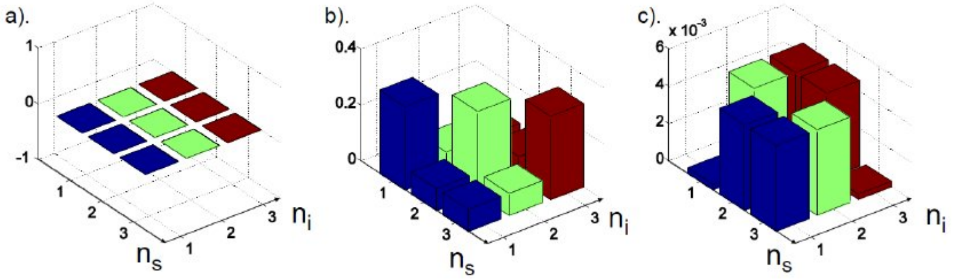

FIG. 6. Two-photon correlations ($|\Psi_{n_s,n_i}|^2$), in case of photon generation by SFWM from a pump inside the array. (a) $z = 0$, (b) $z = 0.375L$, (c) $z = 0.604L$. At $z = 0$ (a), there are no photons. At distance (b), the generated photons are mostly bunched; appearing in the same waveguides. In (c), the photons are anti-bunched.

Thus, we obtain that in the case of photon generation by SFWM from a pump inside the array, the signal and idler photons can be bunched at some distances and anti-bunched at other distances.

4. Conclusion

We have numerically solved the classical equation of coupled modes for the pump wave and the Schrödinger equation for biphoton wave function of three twisted waveguides. We analyzed integrated photon generation through spontaneous four-wave mixing. We have shown that the generated photons can demonstrate bunching behavior at some distances and anti-bunching behavior at other distances. These features can be controlled by the amount of twist and the input pump profile. Also, in the future, it is of interest to consider the effects of nonlinear phase modulation and self-focusing due to the pumping.

Acknowledgements

Authors wishing to acknowledge the Dynasty foundation for their financial support.

References

[1] Hamilton C.S., Kruse R., et al. Driven Quantum Walks. *Phys. Rev. Lett.*, 2014, **113**, P. 083602-5.

[2] Ekert A.K., Rarity J.G., Tapster P.R., Palma G.M. Practical quantum cryptography based on two-photon interferometry. *Phys. Rev. Lett.*, 1992, **69**, P. 1293.

[3] Egorov V.I., Vavulin D.N., et al. Analysis of a sidebands based quantum cryptography system with different detector types. *Nanosystems: Phys., Chem., Math.*, 2013, **4** (2), P. 190–195.

[4] Vavulin D.N., Egorov V.I., Gleim A.V., Chivilikhin S.A. Determining influence of fourwave mixing effect on quantum key distribution. *Journal of Physics: Conference Series*, 2014, **541**, P. 012066.

[5] Owens J.O. et al. Two-photon quantum walks in an elliptical direct-write waveguide array. *New J. Phys.*, 2011, **13**, P. 075003-13.

[6] Xi X.M., Wong G.K.L., et al. Orbital-angular-momentum-preserving helical Bloch modes in twisted photonic crystal fiber. *Optica*, 2014, **1** (3), P. 165–169.

[7] Mair A., Vaziri A., Weihs G., Zeilinger A. Entanglement of the orbital angular momentum states of photons. *Nature*, 2001, **412**, P. 313.

[8] Christodoulides D.N., Lederer F., Silberberg Y.. Discretizing light behaviour in linear and nonlinear waveguide lattices. *Nature*, 2003, **424**, P. 817–823.

[9] Markin D.M., Solntsev A.S., Sukhorukov A.A. Generation of orbital-angular-momentum-entangled biphotons in triangular quadratic waveguide arrays. *Phys. Rev. A*, 2013, **87**, P. 063814-5.

[10] Garanovich I.L., Longhi S., Sukhorukov A.A., Kivshar Yu.S. Light propagation and localization in modulated photonic lattices and waveguides. *Phys. Rep.*, 2012, **518**, P. 1–79.

[11] Solntsev A.S., Sukhorukov A.A., Neshev D.N., Kivshar Yu.S. Photon-pair generation in arrays of cubic nonlinear waveguides. *Optics Express*, 2012, **20** (24), P. 27441.

[12] Jonathan C.F., Thompson M. and Thompson M.G. Quantum optics: An entangled walk of photons. *Nature*, 2012, **484**, P. 47–48.

[13] Grafe M., Solntsev A.S., et al. Biphoton generation in quadratic waveguide arrays: A classical optical simulation. *Scientific Reports*, 2012, **2** (562), P. 1–5.

[14] Desyatnikov A.S., Dennis M.R., Ferrando A. All-optical discrete vortex switch. *Phys. Rev. A*, 2011, **83**, P. 063822.

[15] Agrawal G. *Applications of Nonlinear Fiber Optics*. San Diego, Academic Press, 2001, 472 p.

NANOSYSTEMS: PHYSICS, CHEMISTRY, MATHEMATICS, 2015, 6 (5), P. 697–703

Heat-stimulated transformation of zirconium dioxide nanocrystals produced under hydrothermal conditions

O. V. Almjasheva
Saint Petersburg Electrotechnical University "LETI", St. Petersburg, Russia
almjasheva@mail.ru

PACS 61.46.+w **DOI 10.17586/2220-8054-2015-6-5-697-703**

Processes occurring during the thermal treatment of nanocrystalline zirconium dioxide are reviewed. Changes in the dimensions and structure of ZrO_2 that occur depend upon the calcination conditions used.

Keywords: zirconium dioxide, ZrO_2, hydrothermal synthesis, phase formation, formation mechanism.
Received: 1 October 2015

1. Introduction

Many publications (see, e.g., [1- 12]) have studied the formation of various structural forms of ZrO_2 nanocrystals and have analyzed the reasons for the relatively high stability of the thermodynamically non-equilibrium modifications in nanocrystalline zirconium dioxide at relatively low temperatures. Publications [1-3] link this peculiarity of zirconium dioxide nanocrystals to a dimensional effect. Publications [4-12] examined the impact of the methods and parameters of ZrO_2 nanocrystal synthesis on their structure, morphology and properties. Studies on the mechanism for nanocrystalline zirconium dioxide formation [4, 5, 14, 15] and its behavior during heating [3, 7, 16] indicated that a more detailed analysis was needed of the impact of the reaction system prehistory on the process of ZrO_2 nanoparticle crystallisation.

The study of zirconium dioxide nanocrystals by comprehensive thermal analysis [16-19] has revealed a number of unusual effects in their behavior. Numerous publications [16-19] that have used this method to study the processes occurring in ZrO_2 particles obtained by different methods have reported an intensive exothermic effect in the 200–500°C temperature range which was accompanied by a loss of mass. The appearance of an exothermic effect in the 400–500°C temperature range is explained in publications [15-18] by the crystallisation of X-ray amorphous ZrO_2. The authors of publications [19, 20] attribute the exothermic effect to oxidation of carbon-containing compounds because nanocrystalline ZrO_2 was produced using zirconium oxalate, butanediol or other organic reagents. Publications [4, 5, 7, 8, 16, 21-27] explain the stabilization of the tetragonal (pseudo-cubic) modification of zirconium dioxide in the low-temperature range by the inclusion of water into the nanoparticle structure, while removal of water during heating initiates a structural rearrangement, accompanied by an exothermic effect.

The lack of a clear interpretation of the reasons for structural changes in the zirconium dioxide-based nanocrystals, including those accompanied by an exothermic effect with a simultaneous loss in mass during heating, requires a detailed study of these transformations.

2. Experimental methods

Zirconium dioxide nanocrystals were produced by hydrothermal processing of zirconium oxyhydroxide precipitated from a $ZrOCl_2$ solution by the technique described in [28].

The "isothermic calcination-quenching" method, using a specially designed furnace to ensure high sample heating and cooling rates, studied the structural change kinetics in the condition and dimensions of the zirconium dioxide nanocrystals depending on temperature and heat treatment duration.

The X-ray diffraction study was made on a DRON-3M diffractometer, CuK_α-radiation. Quantitative analysis of the tetragonal (t-ZrO_2) and monoclinic (m-ZrO_2) forms of zirconium dioxide and precise determination of the position of the diffraction maximums were conducted using the method of an internal reference introduction (α-Al_2O_3). The size and shape of the crystallites were determined in accordance with the recommendations of publication [9] based on the data on expansion of the X-ray diffraction line and high-resolution transmission electron microscopy (Jeol JEM-200).

3. Results and discussion

Based on X-ray phase analysis (Fig. 1), the nanoparticles produced under hydrothermal conditions consisted of two structural modifications: t-ZrO_2 and m-ZrO_2. Quantitative calculation of the t-ZrO_2 and m-ZrO_2 content, performed by the technique described in publication [28], showed that 80±5 % t-ZrO_2 and 20±5 % m-ZrO_2 are present in the system.

It should be noted that this ratio of t-ZrO_2/m-ZrO_2 is fairly stable and typical for the technique used to obtain the nanoparticles, as confirmed by the results of previous studies [4, 5, 7, 14-16, 25, 27, 28].

The dimensions of ZrO_2 nanocrystals, which were determined by both transmission electron microscopy (Fig. 2) and based on data from the expansion of the X-ray diffraction lines (Fig. 1) for t-ZrO_2 and m-ZrO_2, essentially coincided and were 20±3 nm, on the basis of which it can be concluded that the nanoparticles produced under hydrothermal conditions were monocrystalline. Structural analysis results for individual nanoparticles by high-resolution transmission electron microscopy also attest to the monocrystalline nature of the produced zirconium dioxide nanoparticles and the fusion on the edges of individual nanocrystals. It is noted that the resulting ZrO_2 nanocrystal dimensions are reproduced fairly consistently when ZrO_2 nanocrystals are synthesised under hydrothermal conditions, as follows from the results of previous studies (see, e.g., [5, 9, 14, 28]). The dimensions of the ZrO_2 nanocrystals may be reduced somewhat to 15–18 nm by reducing the duration of hydrothermal treatment [5], however in this case, zirconium oxyhydroxide is generally not completely dehydrated [5]. We therefore used such hydrothermal processing conditions for zirconium oxyhydroxide which result in its complete dehydration with the formation of ZrO_2 nanocrystals, according to the data of publication [5].

The results from the kinetic study of the change in zirconium dioxide nanocrystal structure and size when heated in the "isothermic calcination-quenching" mode are shown in Fig. 2. Three temperature regions with varying nanoparticle behavior are isolated, based on analysis of the resulting dependences of the quantity of tetragonal modification and particle size of zirconium dioxide on the temperature and duration of treatment (Fig. 2). This temperature ranges to 500°C, from 600 to 800°C and from 900 to 1100°C.

After thermal treatment of the nanoparticles at temperatures up to 500°C, there are no noticeable changes in the structure or particle size of ZrO_2 (Fig. 2). It is also precisely in this temperature range that significant exothermic effects are observed, accompanied by simultaneous water release [16]. Since the total quantity of crystalline ZrO_2, the ratio of metastable tetragonal and monoclinic zirconium dioxide modifications, and the sizes of the nanocrystals during thermal treatment in the examined temperature range do not essentially

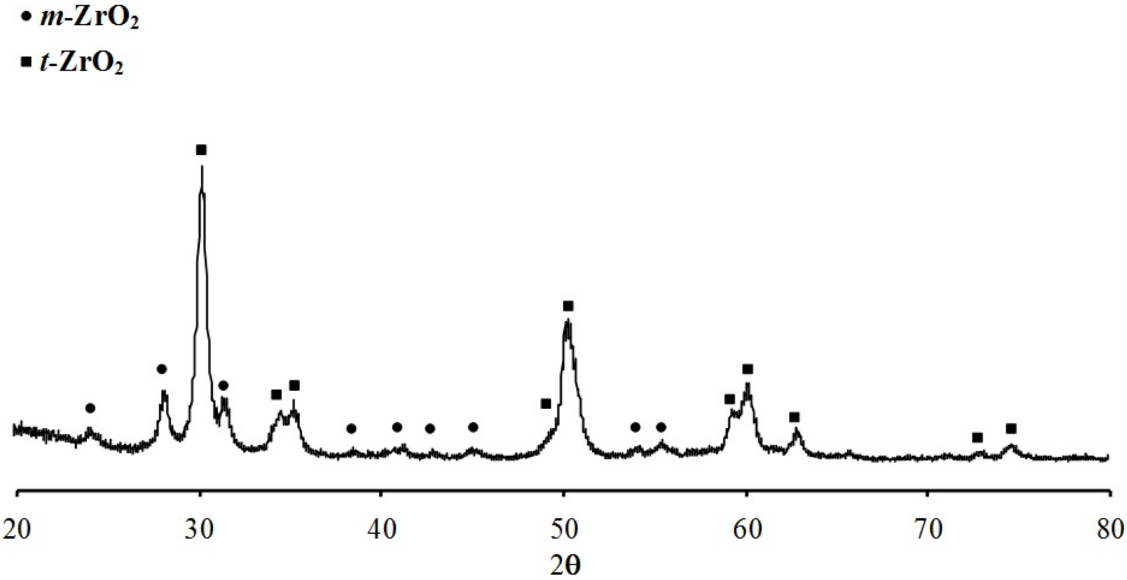

FIG. 1. X-ray diffraction of the nanocrystalline zirconium dioxide, obtained by hydrothermal synthesis

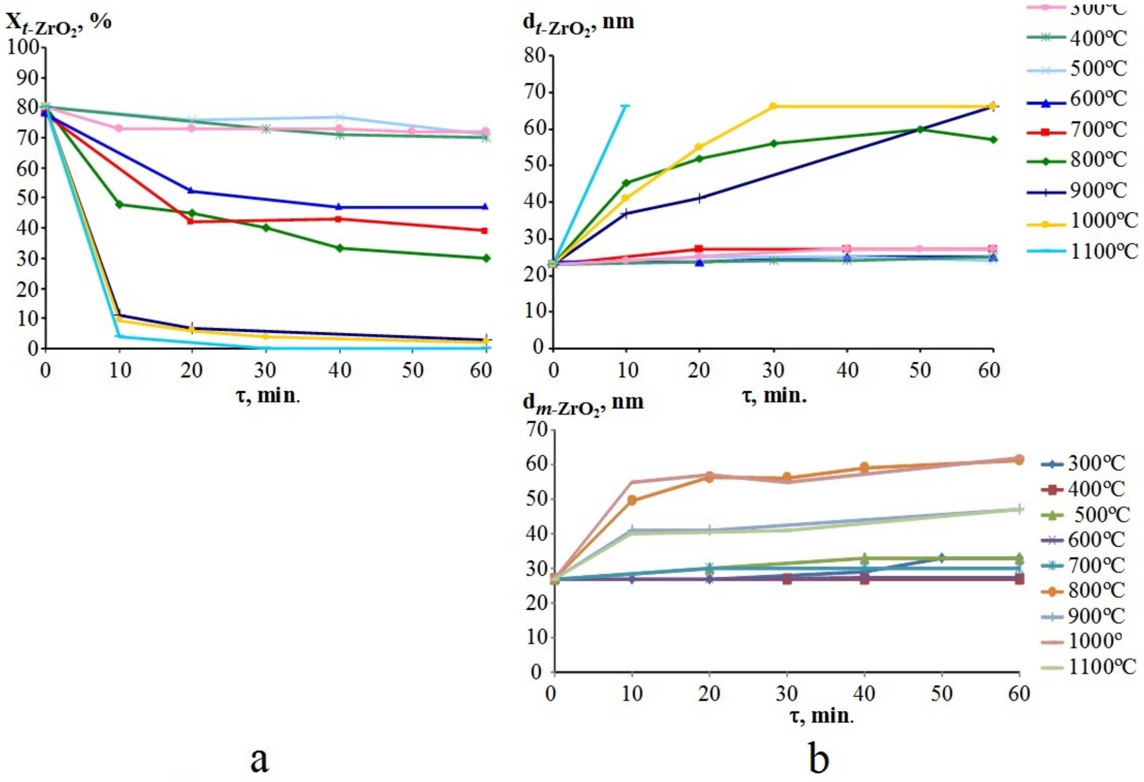

FIG. 2. The dependence of the amount of t-ZrO$_2$ (a) and crystallite size t-ZrO$_2$ and m-ZrO$_2$ (b) of the duration and temperature of heat treatment

change (Fig. 2), there are no grounds to classify the observed thermal effects as crystallization of amorphous zirconium dioxide, polymorphous transition t-ZrO$_2 \rightarrow m$-ZrO$_2$ or change in surface energy because of growth in nanoparticle grains. The process leading to heat release could be structural rearrangement in the nanocrystals, which does not cause transformation of one polymorphous modification of zirconium dioxide nanoparticles into another, and linked, for example, to relaxation processes in nanoparticle sublattices, primarily and apparently in the anion sublattice. The structural changes in the anion sublattice may be initiated, in particular, by certain dehydration reactions in the nanocrystals:

$$\mathrm{ZrO_2} \cdot n\mathrm{H_2O} \rightarrow \mathrm{ZrO_2} + n\mathrm{H_2O} \tag{1}$$

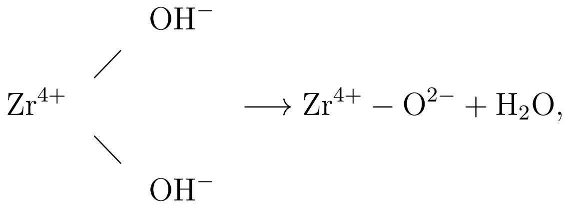

$$\mathrm{Zr^{4+}}\begin{matrix} \diagup\,\mathrm{OH^-} \\ \\ \diagdown\,\mathrm{OH^-} \end{matrix} \longrightarrow \mathrm{Zr^{4+}} - \mathrm{O^{2-}} + \mathrm{H_2O}, \tag{2}$$

which alter the anion sublattice structure, and consequently, create conditions for the occurrence of relaxation processes, which reduce the system internal energy, i.e., occurring with an exothermic effect. The presence of structural changes in the nanocrystals, accompanying the dehydration process is confirmed by data indicating a change in the position and ratio of the intensity of X-ray diffraction lines in t-ZrO$_2$.

t-ZrO$_2$	**h k l**	**d/n**	**h k l**	**d/n**
Standard (24-1164)	1 0 1	2.995	0 0 2	2.635
Original sample		2.971		2.601
Sample after heat treatment at 500°C		2.951		2.592

The proposed interpretation of t-ZrO$_2$ nanocrystal behavior in the 500°C temperature range correlates with previous zirconium dioxide structural study results indicating that its structure in the planes (1 0 1) coincides with the t-ZrO$_2$ structure [29]. The difference in the structure between zirconium X-ray amorphous hydroxide and tetragonal dioxide, according to publication [28-30] is that in the first case, the planes (1 0 1) are arranged randomly. Since, according to data [10, 11, 26], during zirconium hydroxide dehydration under hydrothermal conditions, the formed ZrO$_2$ nanoparticles inherit the structure of the hydrate precursor, one can thus hypothesize that the formed t-ZrO$_2$ nanoparticles also inherit the random arrangement of anions between the planes (1 0 1). This random atom arrangement in the anion sublattice will thus be stabilized by the presence of water in it [2, 7, 14, 16], while the dehydration processes (1) and/or (2) initiate a more orderly arrangement of O^{2-} ions, which, apparently, also causes the corresponding exothermic effects [16].

Heat treatment in the 600–700°C temperature range results in a noticeable increase in the amount of ZrO$_2$ monoclinic modification (up to 50%), while the particle size does not essentially change. Mass loss by the sample due to water release during t-ZrO$_2 \rightarrow m$-ZrO$_2$ transformation, which is slight in this temperature range, is only about 0.5 mass% [16]. At the same time, as shown by the nanoparticle study using high-resolution transmission electron microscopy, after heat treatment of nanoparticles in this temperature range, their morphology changes significantly (Fig. 3). They are converted from essentially non-faced particles into well-faced particles with the characteristic shape for crystallites of the relevant structural modifications (Fig. 3). This is apparently caused by activation of atom movement in the nanoparticles in this temperature range. We also note that an increase in the percentage of m-ZrO_2 nanoparticles to 50% without a change in their mean size was observed previously [29] for the behavior of zirconium dioxide nanoparticles by thermal radiography when heated to 800°C.

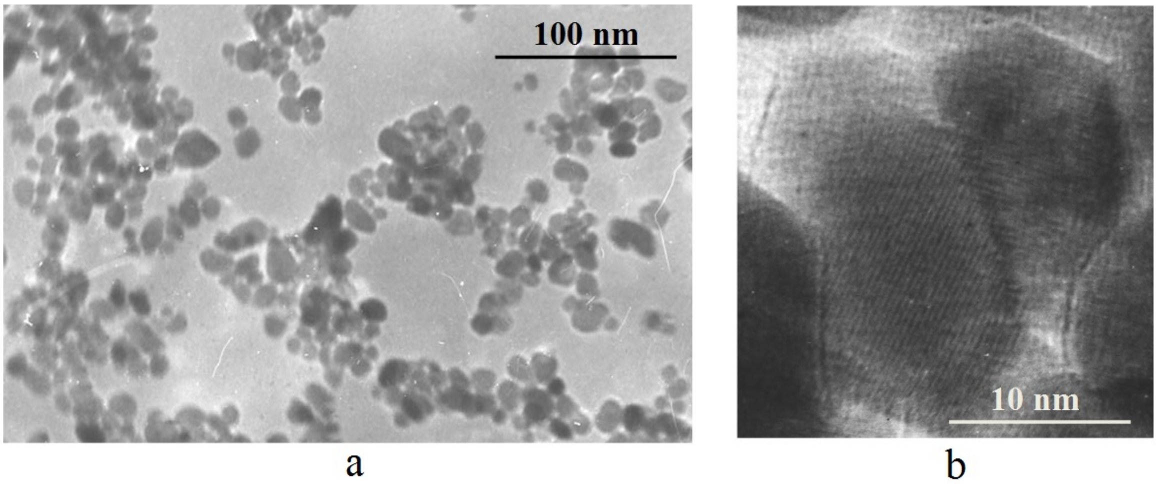

FIG. 3. Microphotographs of ZrO_2 nanocrystals, obtained in hydrothermal conditions (a) and after heat treatment at 700°C

It follows from the kinetic studies (Fig. 2) that for the 900–1100°C temperature range, structural transformation t-$ZrO_2 \rightarrow m$-ZrO_2 ends completely, while the size of the m-ZrO_2 nanocrystals more than doubles to 50–60 nm (Fig. 2). Based on thermal analysis, in addition to the exothermic conversion, a slight water release is observed here, leading to mass loss by the sample of about 0.1 mass% [16]. It is noted that in the 900–1000°C temperature range, in addition to the growth of m-ZrO_2 nanocrystals, there is a growth of t-ZrO_2 nanocrystals (Fig. 2). This type of change in the nanoparticle dimensions is apparently due to activation of mass transfer at these temperatures both between the nanoparticles of one structural modification and transfer of matter from the non-equilibrium structural modification of t-ZrO_2 at this temperature to equilibrium m-ZrO_2.

The findings, as well as the fact that t-$ZrO_2 \rightarrow m$-ZrO_2 transformation may occur essentially without a change in particle size supports the weak impact of the dimensional effect on nanoparticle t-ZrO_2 stability at low temperatures, as indicated in a number of publications [1, 2]. The stabilizing effect of the water, localized in the anion sublattice of the zirconium dioxide nanoparticle is the primary factor which determines the stability of t-ZrO_2 nanoparticles at temperatures up to 500°C.

4. Conclusion

It has been shown that the occurring changes in ZrO_2 nanoparticles in the 300–500°C temperature range are linked to the release of water, accompanied by an exothermic effect, to all appearances determined by structural re-arrangement in the t-ZrO_2 nanocrystals, initiated by dehydration, and resulting in a more orderly arrangement of the atoms in the anion sublattice.

The t-$ZrO_2 \rightarrow m$-ZrO_2 transition in the 600 to 800°C temperature range essentially occurs without a change in nanocrystallite size, but with a noticeable water loss. Removal of the stabilizing water from the t-ZrO_2 structure also results in a transition of the metastable tetragonal modification of zirconium dioxide to that of the monoclinic ZrO_2 modification which is stable at these temperatures.

In the 800 to 1100°C temperature range, mass transfer from the non-equilibrium t-ZrO_2 nanocrystallites to the m-ZrO_2 equilibrium phase makes a significant contribution to the increase in the percentage of m-ZrO_2 nanocrystals.

Acknowledgments

The author would like to thank Prof. V. V. Gusarov for interest in the work and help in the interpretation of results.

This work was supported by the Russian Foundation for Basic Research (project 13-08-01207).

References

[1] Garvie R.C. The Occurrence of Metastable tetragonal zirconia as a crystallite size effect. *The Journal of Physical chemistry*, 1965, **69**(4), P. 1238.

[2] Shukla S., Seal S. Mechanism of room temperature metastable tetragonal phase stabilisation in zirconia. *International materials reviews*, 2005, **50**(1), P. 45.

[3] Bugrov A.N., Almjasheva O.V., Effect of hydrothermal synthesis conditions on the morphology of ZrO_2 nanoparticles. *Nanosystems: pysics, chemistry, mathematics*, 2013, **4**(6), P. 810.

[4] Oleinikov N.N., Pentin I.V., Murav'eva G.P., Ketsko V.A. Highly disperse metastable ZrO_2-based phases. *Russian Journal of Inorganic Chemistry*, 2001, **46**(9), P. 1275.

[5] Pozhidaeva O.V., Korytkova E.N., Romanov D.P., Gusarov V.V. Formation of ZrO_2 nanocrystals in hydrothermal media of various chemical compositions. *Russian Journal of General Chemistry*, 2002, **72**(6), P. 849.

[6] Kolen'ko Yu.V., Maksimov V.D., Garshev A.V., Mukhanov V.A., Oleynikov N.N., Churagulov B.R. Physicochemical properties of nanocrystalline zirconia hydrothermally synthesized from zirconyl chloride and zirconyl nitrate aqueous Solutions. *Russian Journal of Inorganic Chemistry*, 2004, **49**(8), P. 1133.

[7] Li F., Li Y., Song Z., Ma F., Xu K., Cui H. Evolution of the crystalline structure of zirconia nanoparticles during their hydrothermal synthesis and calcination: Insights into the incorporationsof hydroxyls into the lattice. *J. Eur. Ceram. Soc.*, 2015, **35**(8), P. 2361.

[8] Dwivedi R., Maurya A., Verma A., Prasad R., Bartwal K.S. Microwave assisted sol-gel synthesis of tetragonal zirconia nanoparticles. *Journal of Alloys and Compounds*, 2011, **509**, P. 6848.

[9] Almjasheva O.V., Fedorov B.A., Smirnov A.V., Gusarov V.V. Size, morphology and structure of the particles of zirconia nanopowder obtained under hydrothermal conditions. *Nanosystems: physics, chemistry, mathematics*, 2010, **1**(1), P. 26–37.

[10] D. Isfahani T., Javadpour J., Khavandi A., Dinnebier R., Reza Rezaie H., Goodarzi M. Mechanochemical synthesis of zirconia nanoparticles: Formation mechanism and phase transformation. *Int. Journal of Refractory Metals and Hard Materials*, 2012, **31**, P. 21.

[11] Davis B.H. Effect of pH on crystal phase of ZrO_2 precipitated from solution and calcined at 600°C. *Commun. Am. Ceram. Soc.*, 1984, **67**(8), P. 168.

[12] dos Santos V., da Silveira N.P., Bergmannc C.P. In-situ evaluation of particle size distribution of ZrO_2-nanoparticles obtained by sol-gel. *Powder Technology*, 2014, **267**, P. 392.

[13] Mommer N., Lee T., Gardner J.A. Stability of monoclinic and tetragonal zirconia at low oxygen partial pressure. *J. Mater. Res.*, 2000, **15**(2), P. 377.

[14] Sharikov F. Yu., Almjasheva O. V., Gusarov V. V. Thermal Analysis of Formation of ZrO_2 nanoparticles under hydrothermal conditions. *Russian Journal of Inorganic Chemistry*, 2006, **51**(10), P. 1538.

[15] Sharikov F.Yu., Meskin P.E., Ivanov V.K., Churagulov B.R., Tret'yakov Yu.D. Hydrothermal synthesis of nanosized zirconia as probed by heat-flow calorimetry. *Doklady Chemistry*, 2005, **403**(2), P. 152.

[16] Al'myasheva O.V., Ugolkov V.L., Gusarov V.V. Thermochemical analysis of desorption and adsorption of water on the surface of zirconium dioxide nanoparticles. *Russian Journal of Applied Chemistry*, 2008, **81**(4), P. 609.

[17] Karakchiev L.G., Avvakumov E.G., Vinokurova O.B., Gusev A.A., Lyakhov N.Z. Formation of nanodispersed zirconia during sol-gel and mechanochemical processes. *Russian Journal of Inorganic Chemistr*, 2003, **48**(10), P. 1447.

[18] Pechenyuk S.I., Mikhailova N.L., Kuz'mich L.F. Physicochemical investigation of titanium(IV) and zirconium(IV) oxohydroxide xerogels. *Russian Journal of Inorganic Chemistry.* 2003, **48**(9), P. 1420.

[19] Osend M.I.i,. Moya J.S., Serna C.J., J. Soria Metastble of tetragonal zirconya powders. *J. Am. Ceram. Soc.*, 1985, **68**, P. 145.

[20] Mondal A., Ram S. Reconstructive phase formation of ZrO_2 nanoparticles a new orthorhombic crystal structure from an energized porous $ZrO(OH)_2$ xH_2O precursor. *Ceramics International.* 2004, **30**, P. 239.

[21] Inoue M., Sato K., Nakamura T., Inui T. Glycothermal synthesis of zirconia-rare earth oxide solid solutions. *Catalysis Letters*, 2000, **65**, P. 79.

[22] Lecloux A.J. Synthesis and characterization of monodisperse spherical zirconia particles. *Journal of Sol-Gel Science and Technology*, 1997, **8**, P. 207.

[23] Strekalovsky V.N., Polezhaev Y.M., Palguev S.F. *Oxides with impurity disordering: composition, structure, phase transformations.* M .: Nauka. 1987. 160 p.(In Russian).

[24] Srdi´c V.V., Winterer M. Comparison of nanosized zirconia synthesized by gas and liquid phase methods. *J. Eur. Ceram. Soc*, 2006, **26**(15), P. 3145.

[25] Guo X. Hydrothermal degradation mechanism of tetragonal zirconia. *J. of Mater. Sci.*, 2001, **36**(15), P. 3737.

[26] Murase Y., Kato E. Role of water vapor in crystallite growth and tetragonal-monoclinic phase transformation of ZrO_2. *J. Am. Ceram. Soc.*, 1983, **66**, P. 196.

[27] Yoshimura M. Phase Stability of Zirconia. *Am. Ceram. Soc. Bull.*, 1998, **67**, P. 1950.

[28] Pozhidaeva O.V., Korytkova E.N., Drozdova I.A., Gusarov V.V. Phase State and Particle Size of Ultradispersed Zirconium Dioxide as Influenced by Conditions of Hydrothermal Synthesis. *Russian Journal of General Chemistr*, 1999, **69**(8), P. 1265.

[29] Kollong R. *Nonstoichiometry.* M.: Mir. 1974. P. 288 (In Russian)

[30] Becker J., Bremholm M., Tyrsted C., Pauw B., K. Marie ∅. Jensen, Eltzholt J., Christensen M., Iversen B.B. Experimental setup for in situ X-ray SAXS/WAXS/ PDF studies of the formation and growth of nanoparticles in near- and supercritical fluids. *J. Appl. Cryst.*, 2010, **43**, P. 729.

[31] Krzhizhanovskaya M.G., Filatov S.K., Almjasheva O.V., Bubnova R.S., Meyer D.C., Paufler P., Gusarov V.V. The XRD study of ZrO_2 nanopowders. Book of abstracts. "Nanoparticles, nanostructures and nanocomposites". Topical meeting of the European Ceramic Soc. 5-7 July 2004. St. Peterburg, 2004, P. 31.

NANOSYSTEMS: PHYSICS, CHEMISTRY, MATHEMATICS, 2015, 6 (5), P. 704–714

Cryometry and excess functions of fullerenols and trismalonates of light fullerenes – $C_{60}(OH)_{24\pm2}$ and $C_{70}[=C(COOH)_2]_3$ aqueous solutions

M. Yu. Matuzenko[3], D. P. Tyurin[3], O. S. Manyakina[3], K. N. Semenov[1],
N. A. Charykov[2,3], K. V. Ivanova[1], V. A. Keskinov[3]

[1]St. Petersburg State University, St. Petersburg, Russia
[2]St. Petersburg State Electro-technical University (LETI), St. Petersburg, Russia
[3]St. Petersburg State Technological Institute (Technical University), St. Petersburg, Russia
keskinov@mail.ru

PACS 61.48.-c **DOI 10.17586/2220-8054-2015-6-5-704-714**

Cryometry investigations of the $C_{60}(OH)_{24\pm2}$ – H_2O and $C_{70}[=C(COOH)_2]_3$ – H_2O binary systems were conducted over the 0.1 – 10 g concentration range of fullerenols per 1 dm^3 of solutions. The decreases of the temperatures at the onset of H_2O – ice crystallization were determined. Excess functions of aqueous solutions – water and fullerenols (trismalonates) activities and activity coefficients and excess Gibbs energy of the solutions were calculated. All solutions demonstrated huge deviations from those of ideal solutions. The last fact, to our opinion, is caused by a very specific – hierarchical type of association of fullerenols (trismalonates) solution components, which was proved by the results of visible light scattering analysis.

Keywords: Cryometry, activities, activity coefficients, fullerenols, trismalonates, water solution.

Received: 11 April 2015

Revised: 15 April 2015

1. Introduction

This article is the continuation of a series of articles devoted to the synthesis, identification and physico-chemical properties investigation of nanoclusters, which represented the moderately water soluble derivatives of light fullerenes C_{60} and C_{70} [1–14] – poly-hydroxyl fullerenols (fullerenol-d $C_{60}(OH)_{24\pm2}$ and malonic ester – trismalonate $C_{70}[=C(COOH)_2]_3$). In previous articles' authors have reported on the volume, refraction, electrical, transport properties of these water soluble nanoclusters and their aqueous solutions, also investigations of solubility in water in poly-thermal conditions and in some ternary water-salt systems and complex thermal analysis of nanocluster crystal-hydrates were performed.

2. Reasons for direct excess functions in fullerenols (trismalonates) – H_2O solutions determination

We are not aware of any direct experimental data concerning the determination of excess thermodynamic data (primarily activity coefficients) in binary (or more component) solutions of fullerenes or their derivatives in any solutions. This fact may, to our opinion, be explained by the very low solubility of such nanoclusters in the main part of the solvents (see, for example [15–17]). The synthesis of well water soluble nanoclusters (such as: poly-hydroxyl fullerenols $C_{60}(OH)_n$, $C_{70}(OH)_n$; some ethers – for example: trismalonic esters – trismalonate $C_{60}[=C(COOH)_2]_3$, $C_{70}[=C(COOH)_2]_3$, some adducts with amino-acids (for example arginine $C_{60}(C_6H_{12}NaN_4O_2)_8H_8$ or alanine [18]), the solubility of which in water depends on the type of nanocluster and temperature, may be from tens to hundreds of grams of nanocluster per dm^3 of water. This fact makes it possible to determine excess functions of the solution by standard methods, for example, cryometry (described in this article) or by the determination of water activity by isopiestic method. Such determination is, to our opinion, may be very interesting because of the following reasons.

Visible light scattering analysis in light fullerenols (trismalonates) – H_2O solutions at room temperature was provided repeatedly (see [1,5,14]). In all cases, one can see the following:

- No monomer molecular nanoclusters (with linear dimension diameter $d_0 \approx 1.5 - 2.0$ nm) were seen in all investigated solutions, even in the dilute solution ($C = 0.1$ g/dm^3).
- The diameters of the first type aggregates (first order clusters of percolation) have similar sizes – some tens of nm $d_1 \approx 20 - 80$ nm over the whole concentration range.
- The diameters of the second type aggregates (second order clusters of percolation) also have similar sizes – hundreds nm $d_2 \approx 100 - 400$ nm.
- The third type aggregates (third order clusters of percolation) have not been seen at any concentrations except in the most concentrated solution at $C > 1$ g/dm^3, where clusters with extremely huge linear dimension (some microns) are formed: $d_3 > 1000$ nm – the solution 'becomes very heterogeneous' but stable as a colloid system.
- So, to describe these facts in the aggregation process, a stepwise model of particle growth was invoked, in other words, a hierarchical type of association of fullerenols (trismalonates) components in water solution is observed. We consider that monomer spherical molecules form the first type spherical aggregates. Next, the initial spherical associates form the second type spherical associates. Next, the second type spherical associates form the third type spherical associates (the last ones correspond to the colloidal heterogeneous system).

3. The possibility of determining excess functions in fullerenol (trismalonates) – water solutions

In order to check the possibility of determining the excess function of $C_{60}(OH)_{24\pm2}$ – H_2O and $C_{70}[=C(COOH)_2]_3$ – H_2O in the selected concentration range by cryometry method, the following conditions must be met:

- The solubility in the $C_{60}(OH)_{24\pm2}$ – H_2O and $C_{70}[=C(COOH)_2]_3$ – H_2O binary systems at ~273.15 K is great enough so that the solution is formally homogeneous, i.e. does not consist of solid crystal hydrates of $C_{60}(OH)_{24\pm2}$ or $C_{70}[=C(COOH)_2]_3$. Preliminary experiments show that in both cases, the solubilities of both nanoclusters at 273.15 ± 1 K is ≈ 360 g/dm^3 for $C_{70}[=C(COOH)_2]_3$ and ≈ 210 g/dm^3 for $C_{60}(OH)_{24\pm2}$. So, if we choose the concentration range not more than tens g/dm^3 we can be sure that no solid crystal hydrates can co-crystallize with water ice during crystallization of the respective solutions.
- Additionally one must be sure that solutions of the nanoclusters are really homogeneous – do not delaminate and are not colloidal in nature. In this case, only more or less dilute solutions may satisfy these requirements (see lower points 10, 11 in Table 1 were not taken into account).
- The last requirement is that the temperature decrease ΔT should be more or less significant – hundredth, or even better, tenth of a K. This requirement is easily satisfied.

TABLE 1. Cryometry data and excess function in the binary solutions fullerenol-60-d – H_2O (marked by *) and trismalonate-C_{70} – H_2O (marked by **) at 273.15 K

Number	*Molar fraction of fullerenol-60-d in solution $x_{\text{fullerenol-60-d}}$ (rel.un.)	*Temperature of water crystallization decrease ΔT (K)	**Molar fraction of trismalonate-C_{70} in solution $x_{\text{fullerenol-70-d}}$ (rel. un.)	**Temperature of water crystallization decrease ΔT (K)
1	0.000	0.000	0.000	0.000
2	$1.607 \cdot 10^{-6}$	0.047	$1.736 \cdot 10^{-6}$	0.045
3	$3.981 \cdot 10^{-6}$	0.070	$4.430 \cdot 10^{-6}$	0.064
4	$7.933 \cdot 10^{-6}$	0.099	$8.616 \cdot 10^{-6}$	0.089
5	$1.586 \cdot 10^{-5}$	0.149	$1.714 \cdot 10^{-5}$	0.126
6	$3.952 \cdot 10^{-5}$	0.234	$4.275 \cdot 10^{-5}$	0.183
7	$7.905 \cdot 10^{-5}$	0.350	$8.506 \cdot 10^{-5}$	0.271
8	$1.185 \cdot 10^{-4}$	0.469	$1.281 \cdot 10^{-4}$	0.343
9	$1.579 \cdot 10^{-4}$	0.565	$1.710 \cdot 10^{-4}$	0.410
10			$5.130 \cdot 10^{-4}$	0.785***
11			$8.510 \cdot 10^{-4}$	1.095***

Number	*$\ln a_{\text{H2O}}$ (water activity) (rel. un.)	**$\ln a_{\text{H2O}}$ (water activity) (rel. un.)	*a_{H2O} (water activity) (rel. un.)	**a_{H2O} (water activity) (rel. un.)
1	0.000	0.000	1.00000	1.00000
2	$-4.236 \cdot 10^{-4}$	$-4.056 \cdot 10^{-4}$	0.99958	0.99959
3	$-6.309 \cdot 10^{-4}$	$-5.775 \cdot 10^{-4}$	0.99937	0.99942
4	$-8.922 \cdot 10^{-4}$	$-8.027 \cdot 10^{-4}$	0.99911	0.9992
5	-0.00134	-0.00113	0.99866	0.99887
6	-0.00211	-0.00165	0.99789	0.99835
7	-0.00315	-0.00244	0.99685	0.99756
8	-0.00422	-0.00309	0.99579	0.99692
9	-0.00508	-0.00369	0.99493	0.99632

Number	*$\ln \gamma_{\text{H2O}}$ (water activity coefficient) (rel. un.)	**$\ln \gamma_{\text{H2O}}$ (water activity coefficient) (rel. un.)	*derivative $\frac{d \ln \gamma_{\text{H2O}}}{dx_{\text{fullerenol-d}}}$ (rel. un.)	**derivative $\frac{d \ln \gamma_{\text{H2O}}}{dx_{\text{trismalonate-C70}}}$ (rel. un.)
1	0.00000	0.00000	-262.6	-230.3
2	$-4.22 \cdot 10^{-4}$	$-4.03 \cdot 10^{-4}$	-174.4	-147.0
3	$-6.26 \cdot 10^{-4}$	$-5.73 \cdot 10^{-4}$	-75.71	-57.99
4	$-8.84 \cdot 10^{-4}$	$-7.94 \cdot 10^{-4}$	-60.303	-45.28
5	-0.00132	-0.00112	-43.51	-28.68
6	-0.00207	-0.00161	-28.42	-18.436
7	-0.00307	-0.00236	-25.71	-15.83
8	-0.0041	-0.00296	-23.47	-13.49
9	-0.00492	-0.00352	-20.82	-13.05

Number	*derivative $\frac{d\ln\gamma_{\text{fullerenol-d}}}{dx_{\text{fullerenol-d}}}$ (rel. un.)	**derivative $\frac{d\ln\gamma_{\text{trismalonate-C70}}}{dx_{\text{trismalonate-C70}}}$ (rel. un.)	$^{*}\ln\gamma_{\text{fullerenol-60-d}}$ (rel. un.)	$^{**}\ln\gamma_{\text{trismalonate-C70}}$ (rel. un.)
1	–	–	–	–
2	$1.08\cdot10^{8}$	$8.38\cdot10^{7}$	2628	2737
3	$1.901\cdot10^{7}$	$1.31\cdot10^{7}$	2737	2829
4	$7.60\cdot10^{6}$	$5.24\cdot10^{7}$	2780	2860
5	$2.74\cdot10^{6}$	$1.67\cdot10^{6}$	2807	2878
6	719101	431233	2835	2896
7	325211	186088	2862	2914
8	198035	105294	2885	2931
9	131834	76302	2906	2947

Number	$^{*}\ln a_{\text{fullerenol-60-d}}$ (rel. un.)	$^{**}\ln a_{\text{trismalonate-C70}}$ (rel. un.)	$^{*}\varphi_{\text{fullerenol-60-d}}$ (rel. un.)	$^{**}\varphi_{\text{trismalonate-C70}}$ (rel. un.)
1	–	–	–	–
2	2614	2724	−195	−205
3	2724	2816	−219	−228
4	2768	2848	−235	−244
5	2795	2867	−252	−261
6	2824	2886	−278	−286
7	2852	2905	−302	−309
8	2875	2922	−318	−326
9	2897	2938	−330	−338

Number	$^{*}G^{\text{ex}}/RT$ (rel. un.)	$^{**}G^{\text{ex}}/RT$ (rel. un.)	$^{*}G^{\text{mix}}/RT$ (rel. un.)	$^{**}G^{\text{mix}}/RT$ (rel. un.)
1	0.00000	0.00000	0.00000	0.00000
2	−0.00186	−0.00178	−0.00186	−0.00178
3	−0.00275	−0.00254	−0.00275	−0.00254
4	−0.00388	−0.00353	−0.00388	−0.00353
5	$1.903\cdot10^{-5}$	$2.123\cdot10^{-5}$	$1.894\cdot10^{-5}$	$2.114\cdot10^{-5}$
6	$4.844\cdot10^{-5}$	$5.381\cdot10^{-5}$	$4.825\cdot10^{-5}$	$5.360\cdot10^{-5}$
7	$9.831\cdot10^{-5}$	$1.081\cdot10^{-4}$	$9.795\cdot10^{-5}$	$1.077\cdot10^{-4}$
8	$1.488\cdot10^{-4}$	$1.640\cdot10^{-4}$	$1.482\cdot10^{-4}$	$1.634\cdot10^{-4}$
9	$1.999\cdot10^{-4}$	$2.203\cdot10^{-4}$	$1.993\cdot10^{-4}$	$2.196\cdot10^{-4}$

*** – unstable, heterogeneous solution.

4. Cryometry investigation in the $C_{60}(OH)_{24\pm2}$ - H_2O and $C_{70}[=C(COOH)_2]_3$ – H_2O binary systems. Main thermodynamic equations

Let us introduce designation:

$$\Delta F = F^S - F^L, \quad \Delta T = T_0^f - T, \tag{1}$$

where T_0^f – is the melting point for pure solvent, for water $T_0^f = 273.15$ K, T – current temperature (K), ΔF – molar change of thermodynamic function F, F^S – molar function F for the solid phase, F^L – molar function F for the liquid phase.

Condition of chemical phase equilibrium liquid (l) – solid (s) for pure solvent – water (w):

$$\mu w_0^S = \mu w_0^L + RT \ln a_w, \tag{2}$$

where: μw_0^S, μw_0^L – standard chemical potential of the solvent – water, in the solid and liquid phases, correspondingly, a_w – water activity in the scale of molar fractions in symmetrical normalization scale. Thus:

$$-\Delta H_w^f + \Delta C_P \left(T - T_0^f\right) + T\left[\Delta S_w^f - \Delta C_P \ln\left(T/T_0^f\right)\right] = RT \ln a_w, \tag{3}$$

$$\ln\left(T/T_0^f\right) = \ln\left(T_0^f - \Delta T/T_0^f\right) = \ln\left(1 - \Delta T/T_0^f\right) \approx -\Delta T/T_0^f, \tag{4}$$

where: ΔH_w^f, ΔS_w^f, ΔC_P – molar enthalpy, entropy and change of isobaric heat capacity of water at the temperature T_0^f. So:

$$-\Delta H_w^f \left[1 - T/T_0^f\right] + \Delta C_P \left[T - T_0^f - T\ln\left(T/T_0^f\right)\right] = RT \ln a_w, \tag{5.1}$$

$$-\Delta H_w^f \Delta T/T_0^f + \Delta C_P \Delta T\left(-1 + T/T_0^f\right) = RT \ln a_w, \tag{5.2}$$

$$\frac{-\Delta H_w^f \Delta T - \Delta C_P \Delta T^2}{R\left(T_0^f - \Delta T\right) T_0^f} = \ln a_w. \tag{5.3}$$

Later, we shall use formula (5.3) as a base one for the calculation of the solution's excess functions. In all calculations, we will use symmetrical normalization of the excess functions, as if nanoclusters are very weak electrolytes – practically non-electrolytes (see, for example [4, 6, 12]). So, we assume that:

$$a_{\text{H2O}}\left(x_{\text{H2O}} = 1\right) = \gamma_{\text{H2O}}\left(x_{\text{H2O}} = 1\right) = 1, \tag{6.1}$$

$$a_{\text{nanocluster}}\left(x_{\text{nanocluster}} = 1\right) = \gamma_{\text{nanocluster}}\left(x_{\text{nanocluster}} = 1\right) = 1, \tag{6.2}$$

where: a_i, γ_i – activity and activity coefficients of i-th solution component.

Experimental data were obtained with the help of metastatic Beckman thermometer. Data are represented in the Fig. 1 and Table 1. The arrow in the Fig. 1 shows the temperature decrease in the case of an ideal non-electrolyte solution. So, one can see how huge temperature decrease is observed in our cases for water soluble nanocluster solutions.

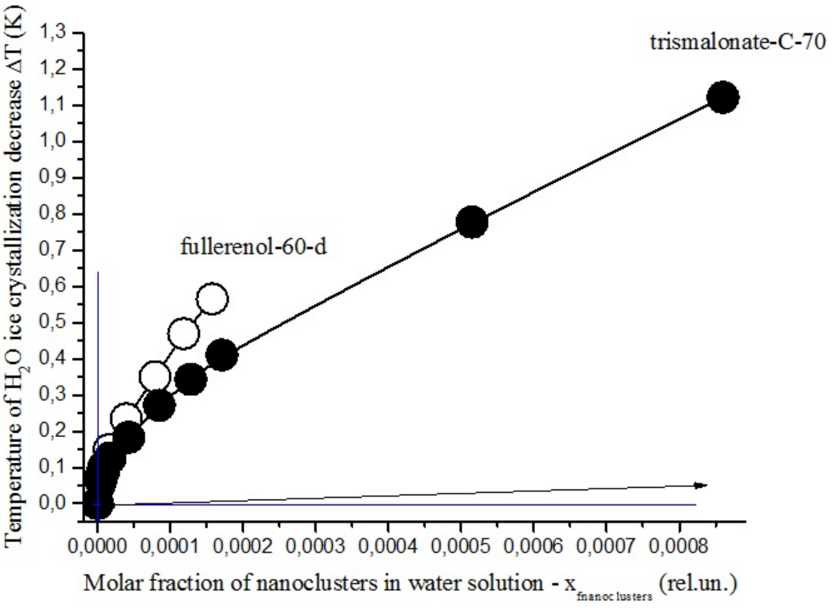

FIG. 1. The decrease of the temperatures of the beginning of the H_2O – ice crystallization in fullerenols (trismalonates) – H_2O solutions ($\Delta T = 273.15 - T$)

5. Partial excess functions of water and fullerenols (trismalonates) components in the $C_{60}(OH)_{24\pm2}$ – H_2O and $C_{70}[=C(COOH)_2]_3$ – H_2O binary systems

The graphics for the dependence ln of water activity ($\ln a_{\text{H2O}}$), ln of water activity coefficient ($\ln \gamma_{\text{H2O}}$), against molar fraction of fullerenols (trismalonates) in aqueous solutions are represented in Fig. 2, 3 in Table 1. The dependence of the derivative of ln of water (nanocluster) activity coefficients ($d \ln \gamma_{\text{H2O}} / d\text{x}_{\text{fullerenol-d(trismalonates-C-70)}}$) and ($d \ln \gamma_{\text{fullerenol-d(trismalonate-C-70)}} / d\text{x}_{\text{fullerenol-d(trismalonate-C-70)}}$) in fullerenols (trismalonates) – H_2O solutions against molar fraction of fullerenols (trismalonates) in aqueous solutions are also represented in Fig. 4, 5 (curves – approximation, points – experimental data). The approximation is also represented in the Fig. 4, 5. For calculation we used the Gibbs-Duheim equation:

$$\left(\frac{\partial \ln a_{\text{nanocluster}}}{\partial \ln \text{x}_{\text{nanocluster}}}\right)_T = -\frac{\text{x}_{\text{H2O}}}{\text{x}_{\text{nanocluster}}} \left(\frac{\partial \ln a_{\text{H2O}}}{\partial \ln \text{x}_{\text{H2O}}}\right)_T . \tag{7}$$

The dependence of ln of fullerenols (trismalonates) activity coefficients ($\ln \gamma_{\text{fullerenol-d(trismalonate-C-70)}}$) and the ln of fullerenols (trismalonates) activity ($\ln a_{\text{fullerenol-d(trismalonate-C-70)}}$) in fullerenols (trismalonates) – H_2O solutions against molar fraction of fullerenols (trismalonates) in aqueous solutions are represented in Fig. 6, 7 and Table 1.

6. Excess and Mixing Gibbs energy in the binary systems: $C_{60}(OH)_{24\pm2}$ – H_2O and $C_{70}[=C(COOH)_2]_3$ – H_2O. Miscibility gap and micro-heterogeneous behavior of the solutions

We have also calculated the dependence of the excess Gibbs energy of the solutions (G^{ex}) in fullerenols (trismalonates) – H_2O solutions against the molar fraction of fullerenols (trismalonates) in aqueous solutions (Fig. 8) and the dependence of the Gibbs energy of solution mixing (G^{mix}) and the miscibility gap in fullerenols (trismalonates) – H_2O solutions against molar fraction of fullerenols (trismalonates) (Fig. 9) and also Table 1:

$$G^{\text{ex}} = RT \left[\ln \gamma_{\text{nanocluster}} + \text{x}_{\text{H2O}} \ln \gamma_{\text{H2O}}\right], \tag{8}$$

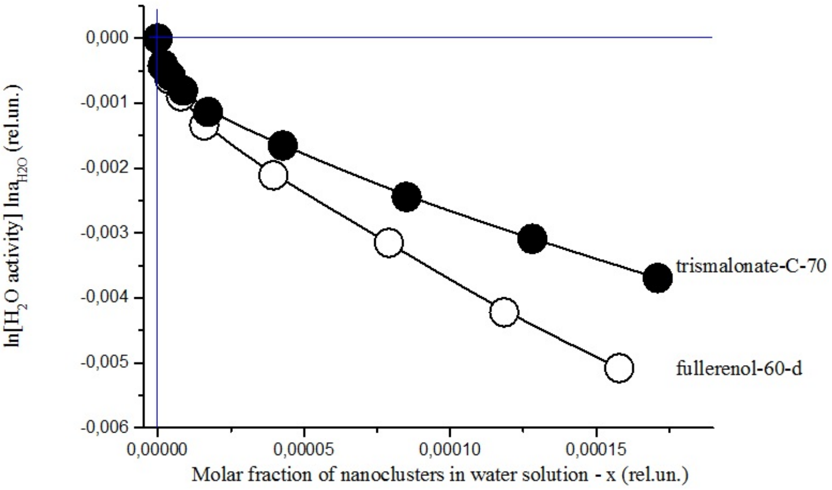

FIG. 2. The dependence of ln of water activity ($\ln a_{\mathrm{H2O}}$) in fullerenols (trismalonates) – H_2O solutions against molar fraction of fullerenols (trismalonates) in aqueous solutions.

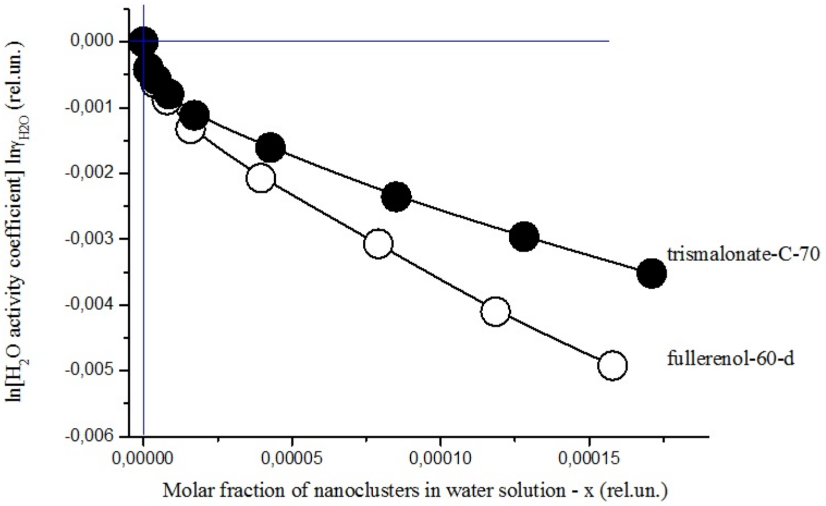

FIG. 3. The dependence of ln of water activity coefficients ($\ln \gamma_{\mathrm{H2O}}$) in fullerenols (trismalonates) – H_2O solutions against molar fraction of fullerenols (trismalonates) in aqueous solutions.

$$G^{\mathrm{mix}} = RT\left[\mathrm{x}_{\mathrm{nanocluster}} \ln a_{\mathrm{nanocluster}} + \mathrm{x}_{\mathrm{H2O}} \ln a_{\mathrm{H2O}}\right]. \tag{9}$$

One can see the inflection points in the Fig. 8, 9 where the second derivatives: $\left[\partial^2 G^{\mathrm{mix}}/\partial \mathrm{x}^2_{\mathrm{nanocluster}}\right]_{T,P}$ and $\left[\partial^2 G^{\mathrm{ex}}/\partial \mathrm{x}^2_{\mathrm{nanocluster}}\right]_{T,P}$ change signs or derivatives $\left[\partial G^{\mathrm{mix}}/\partial \mathrm{x}_{\mathrm{nanocluster}}\right]_{T,P}$ and $\left[\partial G^{\mathrm{ex}}/\partial \mathrm{x}_{\mathrm{nanocluster}}\right]_{T,P}$ cross through zero. Geometrically, this means that convexity in the graphics $G^{\mathrm{ex}}\left(\mathrm{x}_{\mathrm{nanocluster}}\right)$ and $G^{\mathrm{mix}}\left(\mathrm{x}_{\mathrm{nanocluster}}\right)$ is replaced by the concavity. Additionally, if the behavior of the first function is arbitrarily the sign of the derivative, then $\left[\partial^2 G^{\mathrm{mix}}/\partial \mathrm{x}^2_{\mathrm{nanocluster}}\right]_{T,P}$ in the concentration range of diffusion stability should be positive. So, we can consider that in the region $\mathrm{x}_{\mathrm{nanocluster}} > 2 \cdot 10^{-5}$ rel. un., the homogeneous solution exfoliates and becomes micro-heterogeneous. Experiments with light scattering show us that it is concentration region of the transition of the first type aggregates (first order clusters of percolation) with the linear dimensions $d_1 \approx 20 - 80$ nm to the second type aggregates (second

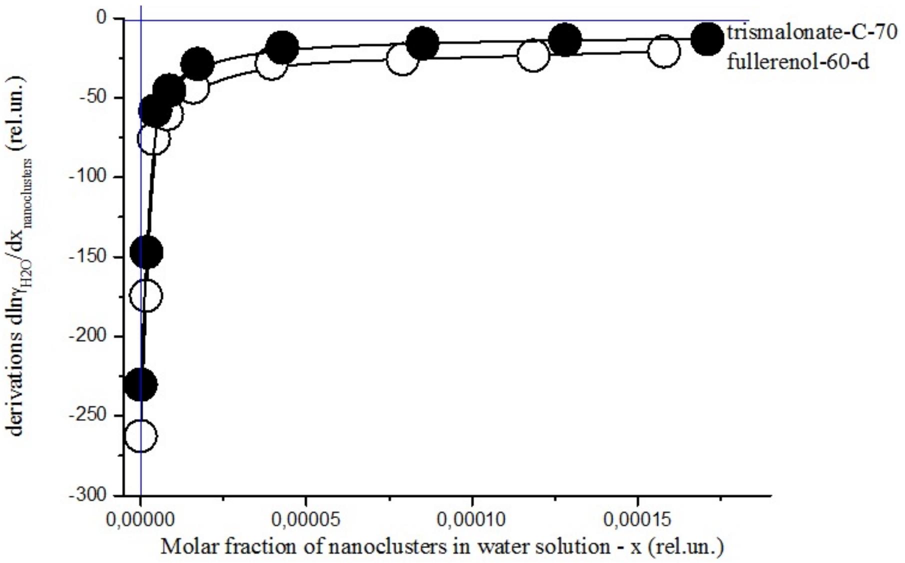

FIG. 4. The dependence of the derivative of ln of water activity coefficients $(d\ln\gamma_{\text{H2O}}/dx_{\text{fullerenol-d(trismalonates-C-70)}})$ in fullerenols (trismalonates) – H_2O solutions against molar fraction of fullerenols (trismalonates) in aqueous solutions (curves – approximation, points – experimental data).

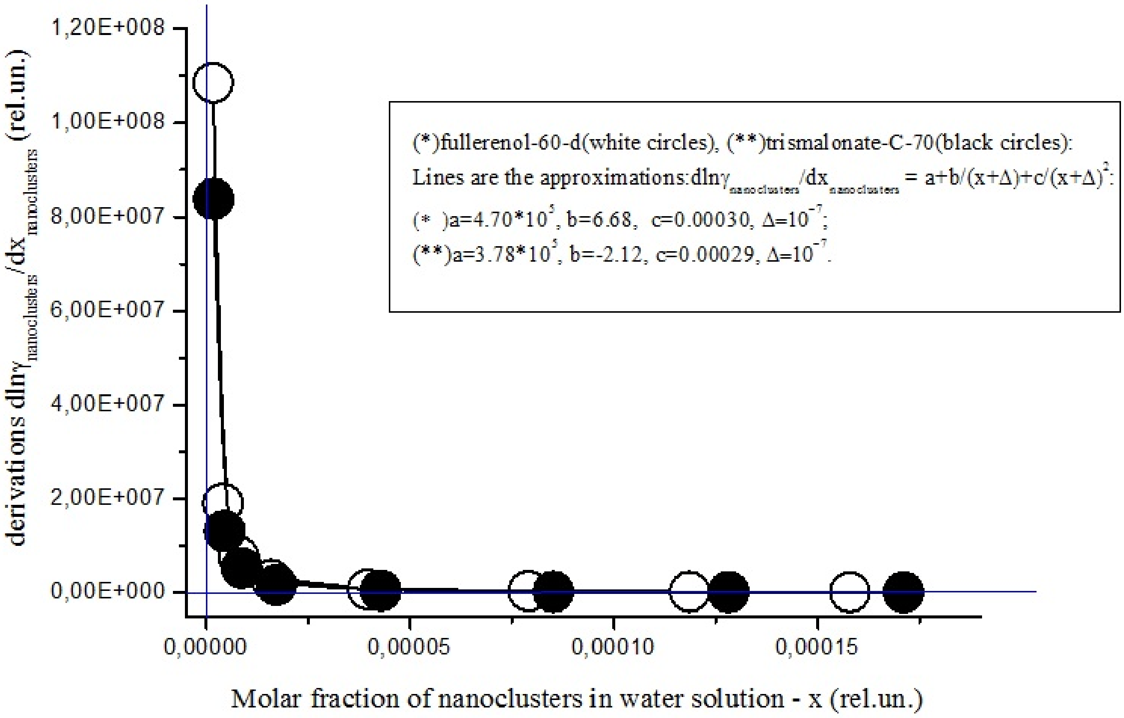

FIG. 5. The dependence of the derivative of ln of fullerenols (trismalonates) activity coefficients $(d\ln\gamma_{\text{fullerenol-d(trismalonate-C-70)}}/dx_{\text{fullerenol-d(trismalonate-C-70)}})$ in fullerenols (trismalonates) – H_2O solutions against molar fraction of fullerenols (trismalonates) in aqueous solutions.

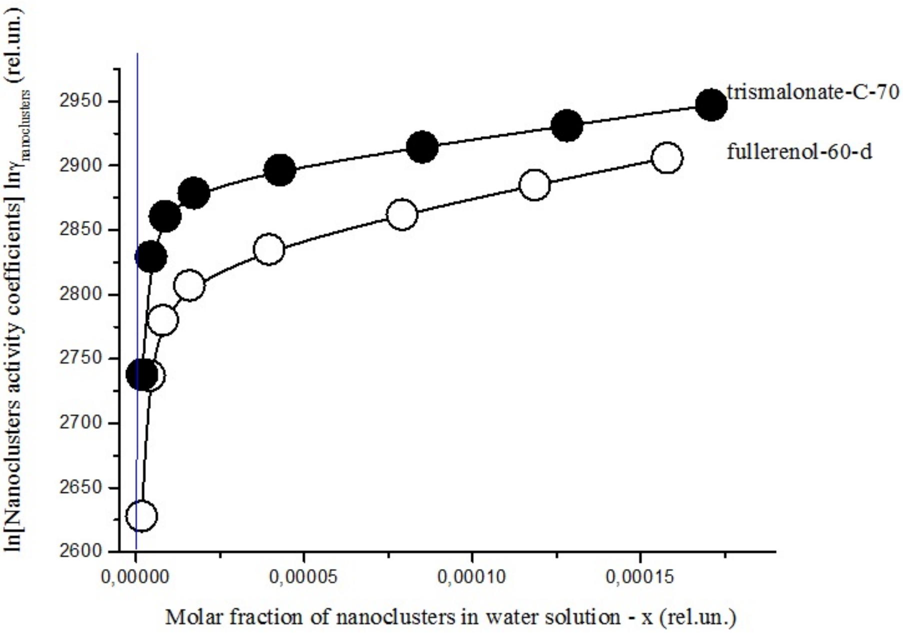

FIG. 6. The dependence of $\ln$ of fullerenols (trismalonates) activity coefficients ($\ln \gamma_{\text{fullerenol-d(trismalonate-C-70)}}$) in fullerenols (trismalonates) – H_2O solutions against molar fraction of fullerenols (trismalonates) in aqueous solutions.

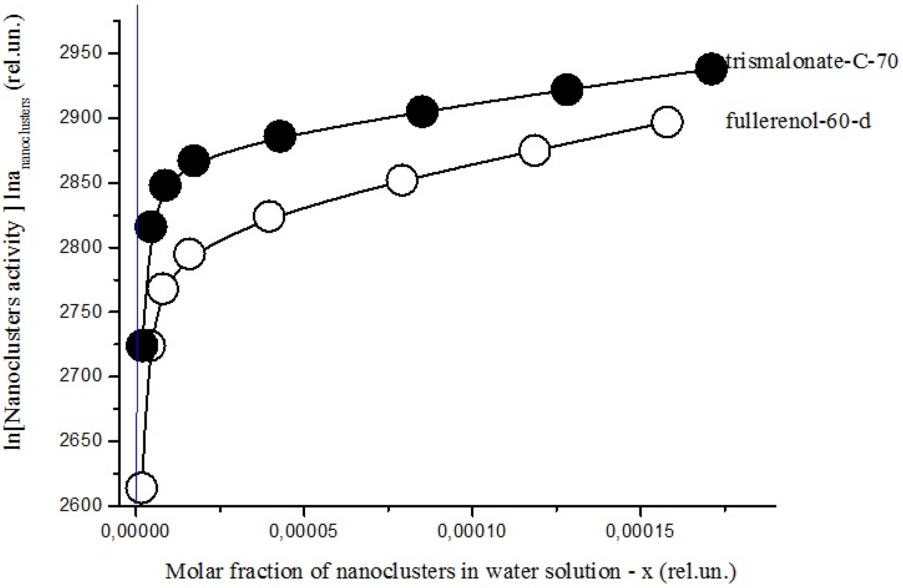

FIG. 7. The dependence of $\ln$ of fullerenols (trismalonates) activity ($\ln a_{\text{fullerenol-d(trismalonate-C-70)}}$) in fullerenols (trismalonates) – H_2O solutions against molar fraction of fullerenols (trismalonates) in aqueous solutions.

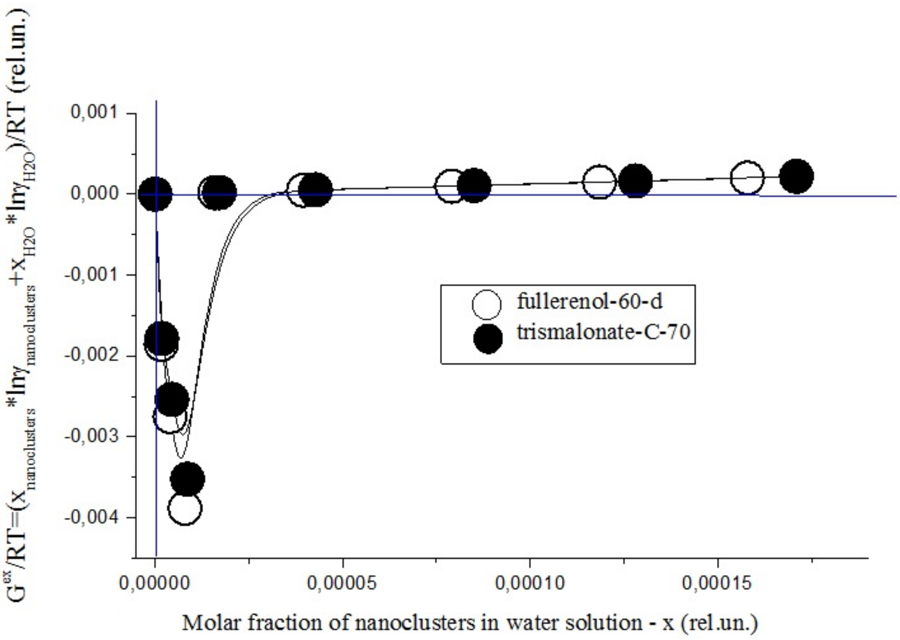

FIG. 8. The dependence of the excess Gibbs energy of the solutions (G^{ex}) in fullerenols (trismalonates) – H_2O solutions against molar fraction of fullerenols (trismalonates) in aqueous solutions

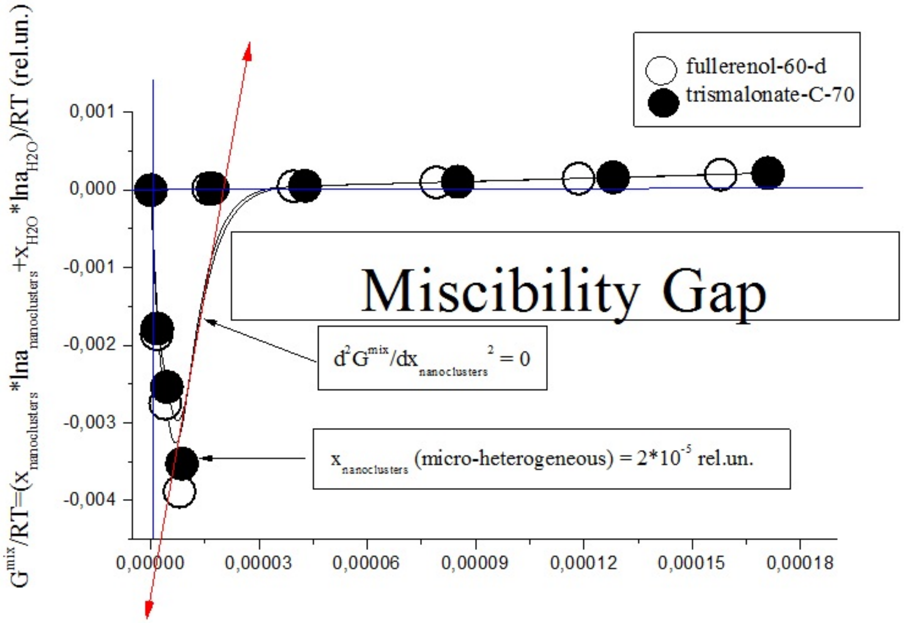

FIG. 9. The dependence of the Gibbs energy mixing of the solutions (G^{mix}) and the miscibility gap in fullerenols (trismalonates) – H_2O solutions against molar fraction of fullerenols (trismalonates) in aqueous solutions

order clusters of percolation) with the linear dimensions $d_2 \approx 100 - 400$ nm. In other words, this is the concentration range where a transition occurs from a nano-heterogeneous system to a micro-heterogeneous one.

Acknowledgements

Investigations were supported by Russian Foundation for Basic Research – RFBR (Project No. 15-08-08438) and with the help of the equipment of Resource Center 'Geomodel' (St.-Petersburg State University).

References

[1] K.N. Semenov, N.A. Charykov, I.V. Murin, Yu.V. Pukharenko. Physico-Chemical Properties of C_{60}-tris-malonic-derivative Water Solutions. *J. of Molecular Liquids*, 2015, **202**, P. 50–58.

[2] K.N. Semenov, N.A. Charykov, I.V. Murin, Yu.V. Pukharenko. Physico-chemical properties of the fullerenol-70 water solutions. *J. of Molecular Liquids*, 2015, **202**, P. 1–8.

[3] D.P. Tyurin, K.N. Semenov, et al. Dissociation of Fullerenol-d water solutions and their electric conductivity. *Rus. J. of Phys. Chem.*, 2015, **89** (5), P. 764–768.

[4] I.A. Pestov, V.A. Keskinov, et al. Solubility of $[C_{60}(=C(COOH)_2)_3$ in ternary system $[C_{60}(=C(COOH)_2)_3]$–$SmCl_3$–H_2 at 25 °C. *Rus. J. of Phys. Chem.*, 2015, **89** (6), P. 990–992.

[5] K.N. Semenov, N.A. Charykov, et al. Dependence of the dimension of the associates of water-soluble tris-malonate of light fullerene – $C_{60}[= C(COOH)_2]_3$ in water solutions at 25 °C. *Nanosystems: Physics, Chemistry, Mathematics*, 2015, **6** (2), P. 294–298.

[6] D.P. Tyurin, K.N. Semenov, et al. Dissociation of Fullerenol-70-d in Aqueous Solutionsand Their Electric Conductivity. *Russian Journal of Physical Chemistry A*, 2015, **89** (5), P. 771–775.

[7] K.N. Semenov, I.G. Kanterman, et al. Solid–Liquid Phase Equilibria in the Fullerenol-d–$CuCl_2$–H_2O System at 25 °C. *Russian Journal of Physical Chemistry*, 2014, **88** (6), P. 1073–1076.

[8] K.N. Semenov, N.A. Charykov, et al. Synthesis and identification water-soluble tris-malonate of light fullerene – $C_{60}[(=C(COOH)_2]_3$. *Nanosystems: physics, chemistry, mathematics*, 2014, **5** (2), P. 315–319.

[9] K.N. Semenov, N.A. Charykov, et al. Volume properties of water solution and refraction at 25 °C water-soluble tris-malonate of light fullerene – $C_{60}[= C(COOH)_2]_3$. *Nanosystems: physics, chemistry, mathematics*, 2014, **5** (3), P. 427–434.

[10] K.N. Semenov, N.A. Charykov, et al. Poly-thermal solubility and complex thermal analysis of water-soluble tris-malonate of light fullerene – $C_{60}[= C(COOH)_2]_3$. *Nanosystems: physics, chemistry, mathematics*, 2014, **5** (3), P. 435–440.

[11] K.N. Semenov, I.G. Kanterman, et al. Solubility in the Ternary System Fullerenol-d–Uranyl Sulfate–Water at 25 °C. *Radiokhimiya*, 2014, **56** (5), P. 493–495.

[12] K.N. Semenov, N.A. Charykov, et al. Concentration dependence of electric conductivity and pH for aqueous solutions of water soluble light fullerene $C_{60}[= C(COOH)_2]_3$ trismalonate. *Nanosystems: physics, chemistry, mathematics*, 2014, **5** (5), P. 709–717.

[13] K.N. Semenov, N.A. Charykov, et al. Fullerenol-d Solubility in Fullerenol-d – Inorganic Salt-Water Ternary Systems at 25 °C. *Industrial & Engineering Chemistry Research*, 2013, **52**, P. 16095–16100.

[14] K.N. Semenov, N.A. Charykov, V.A. Keskinov. Fullerenol Synthesis and Identification. Properties of the Fullerenol Water Solutions. *J. Chem. Eng. Data*, 2011, **56**, P. 230–239.

[15] K.N. Semenov, N.A Charykov. Solubility of light fullerenes and fullerenol in biocompatible with human beings solvents. Chapter in Handbook: *Grapes: Cultivation, Varieties and Nutritional Uses*. Nova Sciences Publishers, Inc., Editor R.P.Murphy et al., 2011, P. 1–48.

[16] K.N. Semenov, N.A. Charykov. Phase Equilibria in the FullereneContaining Systems. Handbook on Fullerene: Synthesis, Properties and Applications, Editor R.F.Verner, C.Benvegny, 2012, P. 1–91.

[17] K.N. Semenov, N.A. Charykov. *Solubility of light fullerenes and it's derivatives*. Germany: LAMBERT Academic Publishing, 2011, 237 p.

[18] L.B. Gan, C.P. Luo, et al. Water-soluble fullerene derivatives, synthesis and characterization of β-alanine C_{60} adducts. *Chinese Chemical letters*, 1994, **5** (4), P. 275–278.

NANOSYSTEMS: PHYSICS, CHEMISTRY, MATHEMATICS, 2015, 6 (5), P. 715–725

Cryometry and excess functions of the adduct of light fullerene C_{60} and arginine – $C_{60}(C_6H_{12}NaN_4O_2)_8H_8$ aqueous solutions

M. Yu. Matuzenko[1], A. A. Shestopalova[1], K. N. Semenov[2], N. A. Charykov[3,1], V. A. Keskinov[1]

[1]St. Petersburg State Technological Institute (Technical University), St. Petersburg, Russia
[2]St. Petersburg State University, St. Petersburg, Russia
[3]St. Petersburg State Electro-technical University (LETI), St. Petersburg, Russia
keskinov@mail.ru

PACS 61.48.+c **DOI 10.17586/2220-8054-2015-6-5-715-725**

Cryometry investigation of $C_{60}(C_6H_{12}NaN_4O_2)_8H_8$ - H_2O solutions was made over concentrations ranging from 0.1 – 10 g of fullerene-arginine adduct per 1 dm^3. Freezing point depression was measured for these aqueous solutions. Excess functions for water and fullerene-arginine adduct activities, activity coefficients and excess Gibbs energy of the solutions were calculated. All solutions demonstrate huge deviations from ideality. The last fact, to our opinion, is caused by the very specific – hierarchical type of association of fullerene-arginine adducts in aqueous solution components, which is proved by the results of our visible light scattering analysis.

Keywords: cryometry, activities, activity coefficients, fullerene-arginine adduct, water solution.

Received: 11 April 2015

Revised: 15 April 2015

1. Introduction

This article is a continuation in the series of articles devoted to the synthesis, identification and physico-chemical properties investigation of nanoclusters, which represented the fairly water soluble derivatives of light fullerenes C_{60} and C_{70} [1–14] – poly-hydroxylated fullerenols (fullerenol-d $C_{60}(OH)_{24\pm2}$ and malonic ether – trismalonate $C_{70}[=C(COOH)_2]_3$). In previous articles, the authors have reported on the volume, refraction, electrical, transport properties of water soluble nanoclusters and their aqueous solutions. Also, the investigations of solubility in water under poly-thermal conditions as well as in some ternary water-salt systems and complex thermal analysis of nanocluster crystal-hydrates were made.

2. The synthesis of the adduct of light fullerene C_{60} with arginine $C_{60}(C_6H_{13}N_4O_2)_8H_8$

Arginine hydrochloride (L–$C_6H_{14}N_4O_2\cdot HCl$) (5 g) and sodium hydroxide (2.5 g) were dissolved in 30 ml of water and 200 ml CH_3CH_2OH. In the other vessel fullerene C_{60} (0.5 g) was dissolved in 80 ml o–$C_6H_4(CH_3)_2$. Then both solutions were combined, mixed and remained at room temperature for 120 hours. A deep-brown exfoliating solution was formed. The colorless organic phase was separated from the aqueous inorganic one. The aqueous phase was salted using excess methanol (CH_3OH) over 24 hours. At that time, the sedimentation of the of the light fullerene C_{60} adduct with arginine was completed. The precipitate was filtered and washed repeatedly with a mix of CH_3OH with concentrated HCl. Recrystallization of precipitate was performed 3 times. Finally, the precipitate was dried at 60 °C for 8 hours. Previously, the synthesis of an original β-alanine C_{60} adduct was described [18]. Correspondingly, the L-arginine – light fullerene C_{60} adduct was formed – $C_{60}(C_6H_{12}NaN_4O_2)_8H_8$ with a yield $\approx$ 80 %.

3. Reasons for direct excess functions in fullerene-arginine adduct – water solutions determination

The authors do not know of any direct experimental data concerning the determination of the excess thermodynamic data (primarily activity coefficients) in binary (or more component) solutions of fullerenes or their derivatives in any solutions. This fact may, to our opinion, be explained by the very low solubility of such nanoclusters in the majority of solvents (see, for example [15–17]). For fairly water soluble nanoclusters (e.g.: poly-hydroxylated fullerenols $C_{60}(OH)_n$, $C_{70}(OH)_n$; some esters – for example: trismalonic esters – trismalonate $C_{60}[=C(COOH)_2]_3$, $C_{70}[=C(COOH)_2]_3$, some adducts with amino-acids (for example arginine $C_{60}(C_6H_{12}NaN_4O_2)_8H_8$ or alanine [18]), their solubility in water, which depends on the type of nanocluster and temperature, may vary from tens to hundreds grams of nanocluster per dm^3 of solvent. This fact permitted us to determine excess functions of the solution by standard methods, for example, cryometry (as described in the present article) or by the determination of water activity by isopiestic method. Such determination is, to our opinion, may be very interesting because of the following reasons.

Visible light scattering analysis in $C_{60}(C_6H_{12}NaN_4O_2)_8H_8$ – water solutions (as well as in light fullerenols (trismalonates)-water solutions) at room temperature was provided repeatedly (see [1, 5, 14]). In all cases, one can observe the following:

- No monomer molecular nanoclusters (with linear dimension diameter $d_0 \approx 1.5 – 2.0$ nm) are seen in all investigated solutions, even in the dilute solution ($C = 0.1$ g/dm^3).
- The diameters of the first type aggregates (the first order clusters of percolation) have the similar order – tens of nm $d_1 \approx 20 – 80$ nm over the entire concentration range.
- The diameters of the second type aggregates (the second order clusters of percolation) also have a similar order – hundreds nm $d_2 \approx 100 – 400$ nm.
- The third type associates (the third order clusters of percolation) have not been seen at any concentrations except in the most highly concentrated solution at $C > 1$ g/dm^3, where clusters with extremely huge linear dimension (on the order of microns) are formed: $d_3 > 1000$ nm – the solution 'becomes very heterogeneous' but stable as a colloidal system.
- Thus, to describe such facts in the aggregation process, a stepwise model of particle growth was invoked, in other words, a hierarchical type of association of fullerenols (trismalonates) components was observed in aqueous solutions. We consider that monomer spherical molecules form the first type of spherical aggregates, then, the first type spherical associates form a second type of spherical associates. Next, the second type of spherical associates form a third type spherical associates (the last ones correspond to a heterogeneous colloidal system). A typical figure of the distribution for $C_{60}(C_6H_{12}NaN_4O_2)_8H_8$ nanoclusters in aqueous solutions at comparatively high concentrations is represented below – in Fig. 1 (the third type associates).

4. The possibility of the determination of the excess functions in $C_{60}(C_6H_{12}NaN_4O_2)_8H_8$ – water solutions

In order to check the possibility of determining the excess functions in $C_{60}(C_6H_{12}NaN_4O_2)_8H_8$ – H_2O solutions in the selected concentration range by cryometry method one must be sure of the following:

- Solubility in the binary system $C_{60}(C_6H_{12}NaN_4O_2)_8H_8$ – H_2O at a temperature of 273.15 K is great enough such that the solution is formally homogeneous, i.e. does not consist of solid $C_{60}(C_6H_{12}NaN_4O_2)_8H_8$ crystal hydrates. Preliminary experiments show

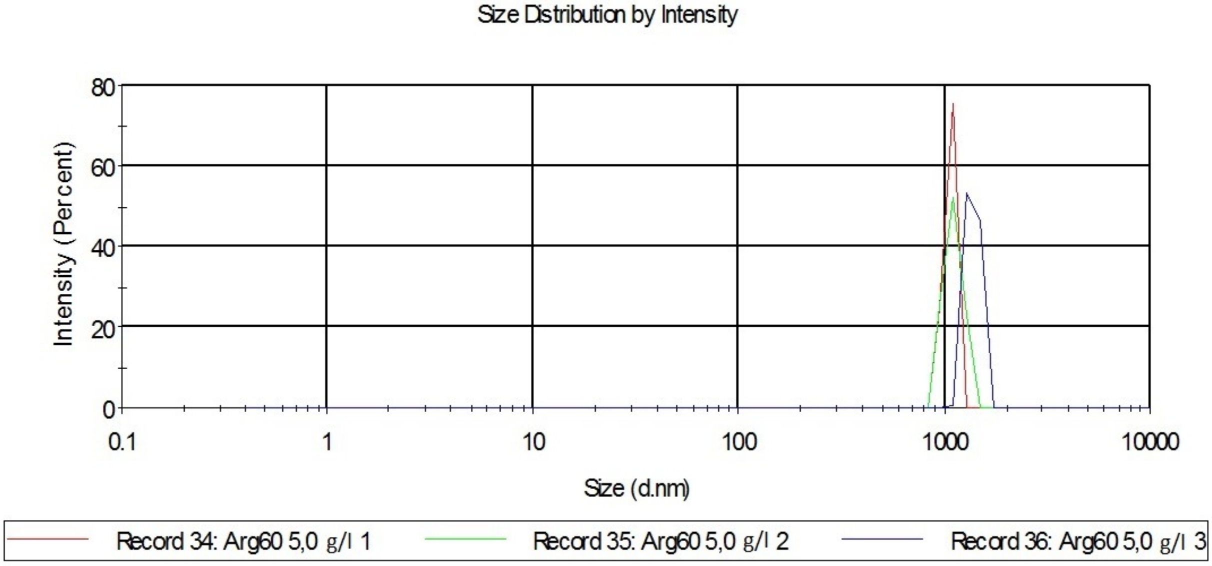

FIG. 1. The linear dimension of the particles on the base of the adducts $C_{60}(C_6H_{12}NaN_4O_2)_8H_8$ in aqueous (δ) solutions at $C = 5$ g/dm^3 (different curves correspond to the different times of observation (signal integration)

that in both cases, the solubility of $C_{60}(C_6H_{12}NaN_4O_2)_8H_8$ nanoclusters at 273.15±1 K is $\approx$ 70 g/dm^3. So, if we set the concentration range at not more than tens g/dm^3, we can be sure that no solid crystal hydrates can co-crystallize with water ice during the crystallization.

- Additionally, one must be sure that the nanocluster solutions are really homogeneous – do not delaminate and are not colloidal. In our case, only more or less diluted solutions may satisfy these request (see lower).
- The last condition is that the temperature decrease ΔT should be more or less significant – hundredths, or even better tenth of a degree K. Fortuitously, this request is easily satisfied.

5. Cryometry investigation in the binary system: $C_{60}(C_6H_{12}NaN_4O_2)_8H_8$ – H_2O. The decrease of the temperatures of the beginning of the H_2O – ice crystallization in $C_{60}(C_6H_{12}NaN_4O_2)_8H_8$ – water solutions. Cryometry of water solutions of water soluble fullerene derivatives. Main thermodynamic equations

Let us introduce designation:

$$\Delta F = F^S - F^L, \quad \Delta T = T_0^f - T, \tag{1}$$

where T_0^f – melting point of pure solvent, for water $T_0^f = 273.15$ K, T – current temperature (K), ΔF – molar change of thermodynamic function F, F^S – molar function F for the solid phase, F^L – molar function F for the liquid phase.

The conditions for chemical phase equilibrium liquid (L) – solid (S) for the pure solvent – water (W) were as follows:

$$\mu \mathrm{w}_0^S = \mu \mathrm{w}_0^L + RT \ln a_W \tag{2}$$

where: $\mu \mathrm{w}_0^S$, $\mu \mathrm{w}_0^L$ – standard chemical potential of the solvent – water, in the solid and liquid phases, correspondingly, a_W – water activity in the scale of molar fractions in symmetrical normalization scale. Thus:

$$-\Delta H_W^f + \Delta C_P \left(T - T_0^f\right) + T\left[\Delta S_W^f - \Delta C_P \ln\left(T/T_0^f\right)\right] = RT \ln a_W, \tag{3}$$

$$\ln\left(T/T_0^f\right) = \ln\left(T_0^f - \Delta T/T_0^f\right) = \ln\left(1 - \Delta T/T_0^f\right) \approx -\Delta T/T_0^f, \tag{4}$$

where: ΔH_W^f, ΔS_W^f, ΔC_P – molar enthalpy, entropy and change of isobaric heat capacity of water at the temperature T_0^f. So:

$$-\Delta H_W^f\left[1 - T/T_0^f\right] + \Delta C_P\left[T - T_0^f - T\ln\left(T/T_0^f\right)\right] = RT\ln a_W, \tag{5.1}$$

$$-\Delta H_W^f \Delta T/T_0^f + \Delta C_P \Delta T\left(-1 + T/T_0^f\right) = RT\ln a_W, \tag{5.2}$$

$$\frac{-\Delta H_W^f \Delta T - \Delta C_P \Delta T^2}{R\left(T_0^f - \Delta T\right)T_0^f} = \ln a_W. \tag{5.3}$$

Later, we shall use formula (5.3) as the basis for calculating the excess solution functions. In all calculations, we will use symmetrical normalization of the excess functions, as if nanoclusters are very weak electrolytes – practically non-electrolytic (see nanocluster-water systems close to our system, for example [4, 6, 12]). Accordingly, we assume that:

$$a_{\text{H2O}}(x_{\text{H2O}} = 1) = \gamma_{\text{H2O}}(x_{\text{H2O}} = 1) = 1, \tag{6.1}$$

$$a_{\text{nanocluster}}(x_{\text{nanocluster}} = 1) = \gamma_{\text{nanocluster}}(x_{\text{nanocluster}} = 1) = 1, \tag{6.2}$$

where: a_i, γ_i – activity and activity coefficients of i-th solution component.

Experimental data were obtained with the help of metastatic Beckman thermometer. Data are represented in the Fig. 2 and Table 1. Arrow in the Fig. 2 shows the temperature decrease in the case of an ideal non-electrolyte solution. Thus, one can see the huge temperature decrease we observed for our water soluble nanoclusters solutions.

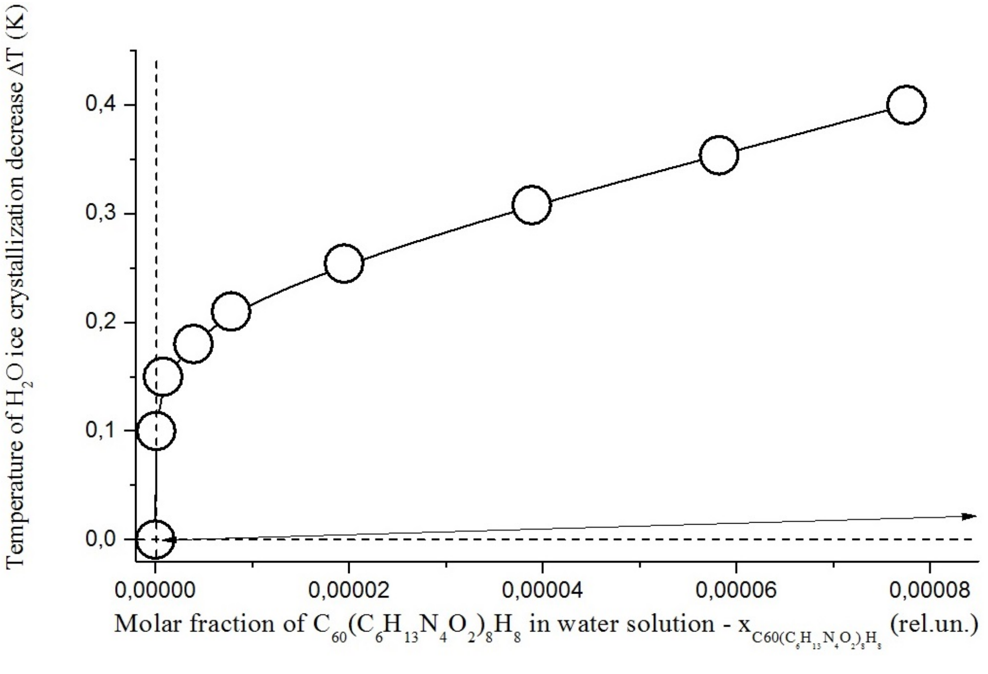

FIG. 2. The decrease of the temperatures of the beginning of the H_2O – ice crystallization in $C_{60}(C_6H_{12}NaN_4O_2)_8H_8$ – water solutions ($\Delta T = 273.15 - T$)

TABLE 1. Cryometry data and excess function in the binary $C_{60}(C_6H_{12}NaN_4O_2)_8H_8$ – H_2O solutions at 273.15 K

Number	Molar fraction of $C_{60}(C_6H_{13}N_4O_2)_8H_8$ in solution $x_{C60(C6H13N4O2)8H8}$ (rel.un.)	Temperature of water crystallization decrease ΔT (K)	$\ln a_{H2O}$ (water activity) (rel.un.)	a_{H2O} (water activity) (rel.un.)
1	0.000	0.000	0.000	1.00000
2	$7.868 \cdot 10^{-8}$	0.099	$-9.561 \cdot 10^{-4}$	0.99904
3	$7.868 \cdot 10^{-7}$	0.151	-0.00146	0.99854
4	$3.923 \cdot 10^{-6}$	0.179	-0.00172	0.99827
5	$7.828 \cdot 10^{-6}$	0.210	-0.00202	0.99797
6	$1.949 \cdot 10^{-5}$	0.254	-0.00245	0.99755
7	$3.887 \cdot 10^{-5}$	0.308	-0.00297	0.99703
8	$5.821 \cdot 10^{-5}$	0.354	-0.00341	0.99658
9	$7.758 \cdot 10^{-5}$	0.401	-0.00387	0.99613

Number	$\ln \gamma_{H2O}$ (water activity coefficient) (rel.un.)	derivative $\frac{d \ln \gamma_{H2O}}{dx_{C60(C6H13N4O2)8H8}}$ (rel.un.)	derivative $\frac{d \ln \gamma_{C60(C6H13N4O2)8H8}}{dx_{C60(C6H13N4O2)8H8}}$ (rel.un.)	$\ln \gamma_{C60(C6H13N4O2)8H8}$ (rel.un.)
1	0.000	-12000	$4.2 \cdot 10^{10}$	
2	$-9.561 \cdot 10^{-4}$	-6300	$1.3 \cdot 10^{10}$	$9.2 \cdot 10^{6}$
3	-0.00146	-410	$5.2 \cdot 10^{8}$	3750
4	-0.00172	-81	$2.1 \cdot 10^{7}$	4100
5	-0.00202	-55	$7.0 \cdot 10^{6}$	4130
6	-0.00243	-31	$1.6 \cdot 10^{6}$	4150
7	-0.00293	-24	$6.2 \cdot 10^{5}$	4170
8	-0.00336	-22	$3.8 \cdot 10^{5}$	4180
9	-0.00379	-22	$2.8 \cdot 10^{5}$	4200

Number	$\ln a_{C60(C6H13N4O2)8H8}$ (rel.un.)	G^{ex}/RT (rel.un.)	G^{mix}/RT (rel.un.)	
1	0.00000	0.00000	0.00000	
2	$9.2 \cdot 10^{6}$	-8.83	-8.83	
3	3740	0.00149	0.00148	
4	4090	0.0143	0.0143	
5	4120	0.0303	0.0302	
6	4140	0.0784	0.0782	
7	4160	0.159	0.158	
8	4170	0.239	0.239	
9	4190	0.322	0.321	

6. Excess partial functions of water $C_{60}(C_6H_{12}NaN_4O_2)_8H_8$ components in the binary system: $C_{60}(C_6H_{12}NaN_4O_2)_8H_8$ – H_2O

The graph of the dependence ln of water activity ($\ln a_{\mathrm{H2O}}$), ln of water activity coefficient ($\ln \gamma_{\mathrm{H2O}}$), against the molar fraction of $C_{60}(C_6H_{12}NaN_4O_2)_8H_8$ in aqueous solutions are represented in Figs. 3, 4 and in Table 1. The dependence of the derivative of ln of water (nanocluster) activity coefficients ($d\ln\gamma_{\mathrm{H2O}}/d\mathrm{x}_{\mathrm{nanocluster}}$) and ($d\ln\gamma_{\mathrm{nanocluster}}/d\mathrm{x}_{\mathrm{nanocluster}}$) in $C_{60}(C_6H_{12}NaN_4O_2)_8H_8$ – water solutions against the molar fraction of $C_{60}(C_6H_{12}NaN_4O_2)_8H_8$ in aqueous solutions are also represented in Figs. 5, 6 (curves – approximation, points – experimental data). The approximation is represented in the Figs. 5, 6 also. For calculation, we have used the Gibbs-Duheim equation:

$$\left(\frac{\partial \ln a_{\mathrm{nanocluster}}}{\partial \ln \mathrm{x}_{\mathrm{nanocluster}}}\right)_T = -\frac{\mathrm{x}_{\mathrm{H2O}}}{\mathrm{x}_{\mathrm{nanocluster}}}\left(\frac{\partial \ln a_{\mathrm{H2O}}}{\partial \ln \mathrm{x}_{\mathrm{H2O}}}\right)_T . \tag{7}$$

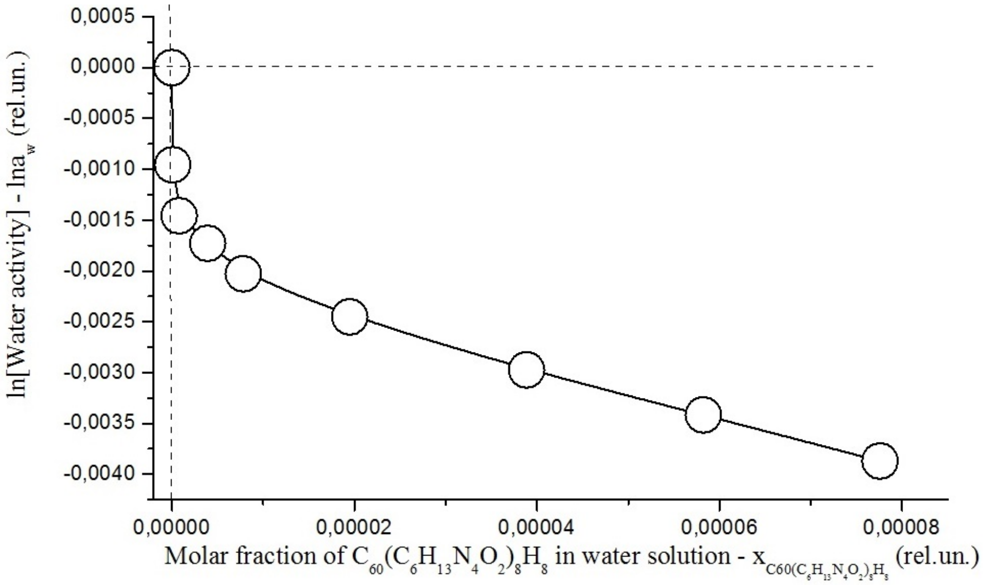

FIG. 3. The dependence of ln of water activity ($\ln a_{\mathrm{H2O}}$) in $C_{60}(C_6H_{12}NaN_4O_2)_8H_8$ – water solutions against the molar fraction of $C_{60}(C_6H_{12}NaN_4O_2)_8H_8$ in aqueous solutions

The dependence of the ln of $C_{60}(C_6H_{12}NaN_4O_2)_8H_8$ activity coefficients ($\ln\gamma_{\mathrm{nanocluster}}$) and ln of $C_{60}(C_6H_{12}NaN_4O_2)_8H_8$ activity ($\ln a_{\mathrm{nanocluster}}$) in $C_{60}(C_6H_{12}NaN_4O_2)_8H_8$ – water solutions against the molar fraction of $C_{60}(C_6H_{12}NaN_4O_2)_8H_8$ in aqueous solutions are represented in Figs. 7, 8 and Table 1.

7. Excess and Mixing Gibbs energy in the binary system: $C_{60}(C_6H_{12}NaN_4O_2)_8H_8$ – H_2O. Miscibility gap and micro-heterogeneous behavior of the solutions

We have also calculated the dependence of the excess Gibbs energy of the solutions (G^{ex}) in $C_{60}(C_6H_{12}NaN_4O_2)_8H_8$ – water solutions against the logarithm of the $C_{60}(C_6H_{12}NaN_4O_2)_8H_8$ molar fraction in aqueous solutions (Fig. 9) and the dependence of the Gibbs energy mixing for solutions (G^{mix}) and the miscibility gap in $C_{60}(C_6H_{12}NaN_4O_2)_8H_8$ – water solutions against the logarithm of the $C_{60}(C_6H_{12}NaN_4O_2)_8H_8$ molar fraction (Fig. 10) and also Table 1:

$$G^{\mathrm{ex}} = RT\left[\ln\gamma_{\mathrm{nanocluster}} + \mathrm{x}_{\mathrm{H2O}}\ln\gamma_{\mathrm{H2O}}\right], \tag{8}$$

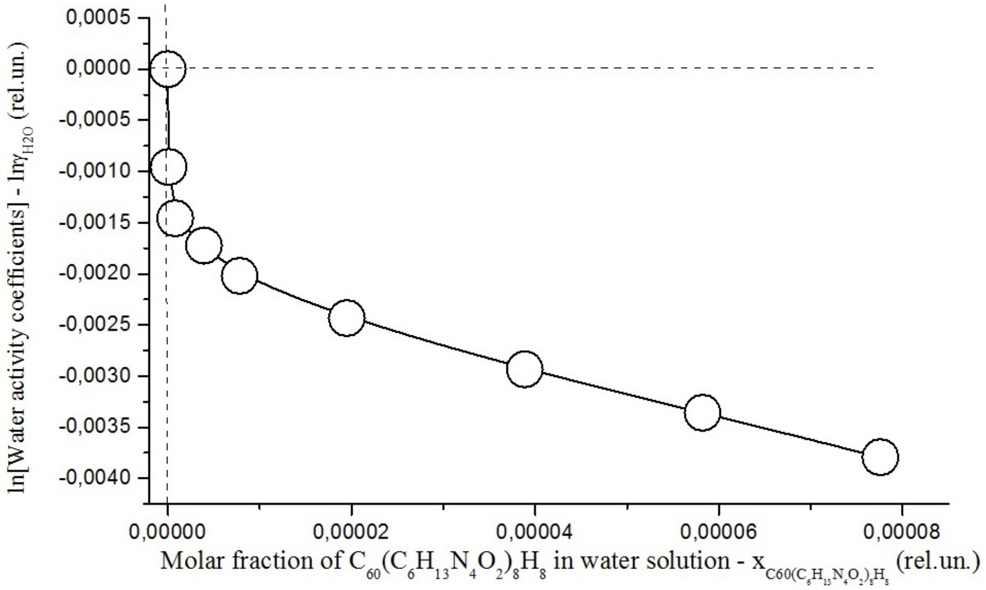

FIG. 4. The dependence of $\ln$ of water activity coefficients ($\ln\gamma_{\text{H2O}}$) in $C_{60}(C_6H_{12}NaN_4O_2)_8H_8$ – water solutions against the molar fraction of $C_{60}(C_6H_{12}NaN_4O_2)_8H_8$) in aqueous solutions

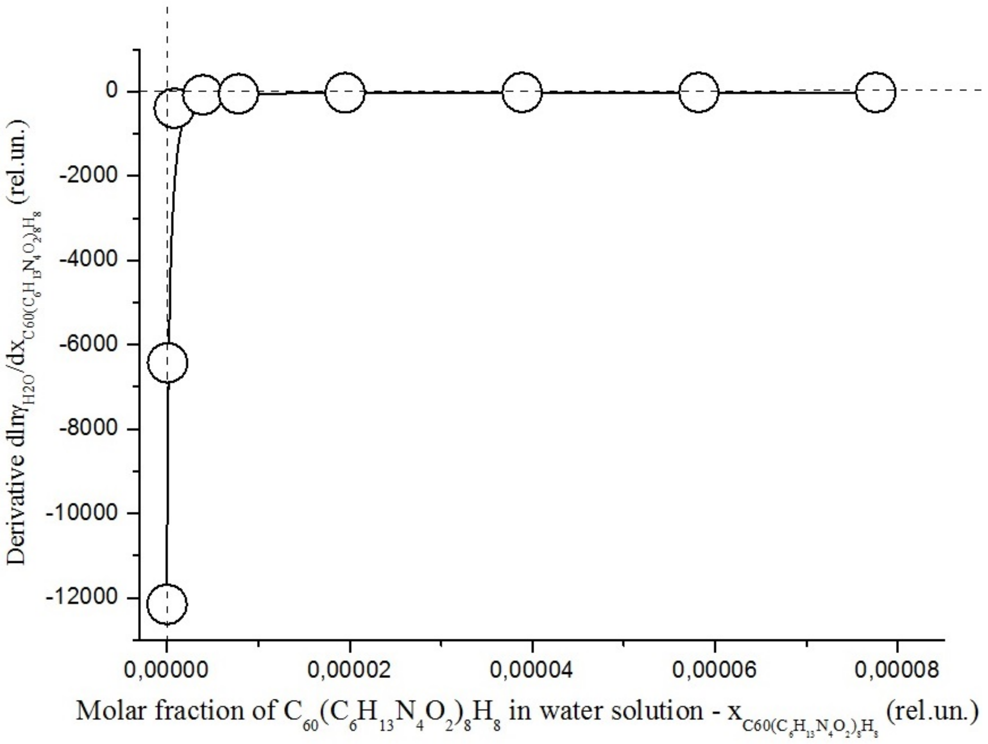

FIG. 5. The dependence of the derivative of $\ln$ of water activity coefficients ($d\ln\gamma_{\text{H2O}}/dx_{\text{nanocluster}}$) in $C_{60}(C_6H_{12}NaN_4O_2)_8H_8$ – water solutions against the molar fraction of $C_{60}(C_6H_{12}NaN_4O_2)_8H_8$ in aqueous solutions (curves – approximation, points – experimental data)

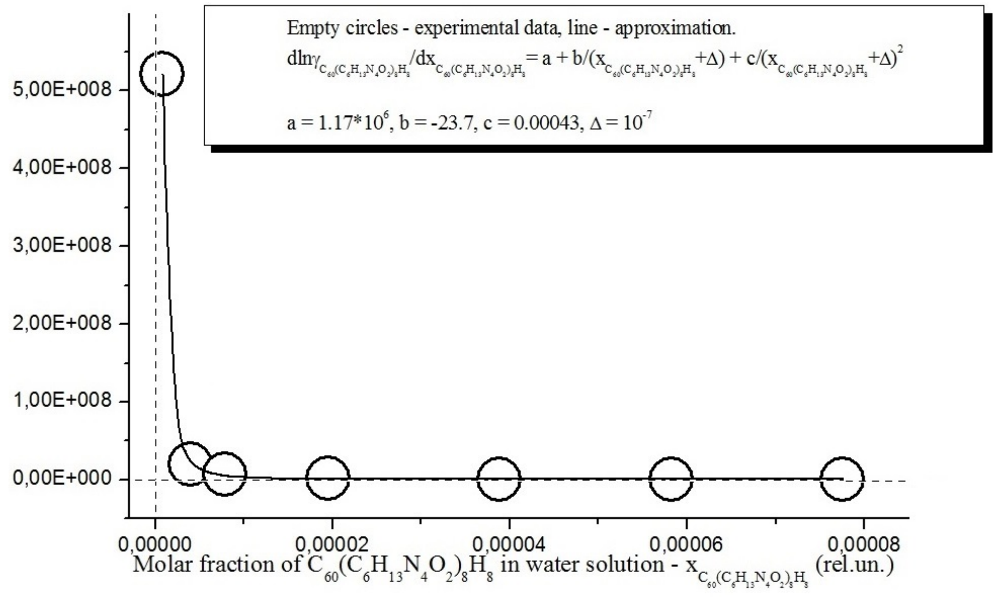

FIG. 6. The dependence of the derivative of ln of $C_{60}(C_6H_{12}NaN_4O_2)_8H_8$ activity coefficients $(d\ln\gamma_{\text{nanocluster}}/dx_{\text{nanocluster}})$ in $C_{60}(C_6H_{12}NaN_4O_2)_8H_8$ – water solutions against the molar fraction of $C_{60}(C_6H_{12}NaN_4O_2)_8H_8$ in aqueous solutions

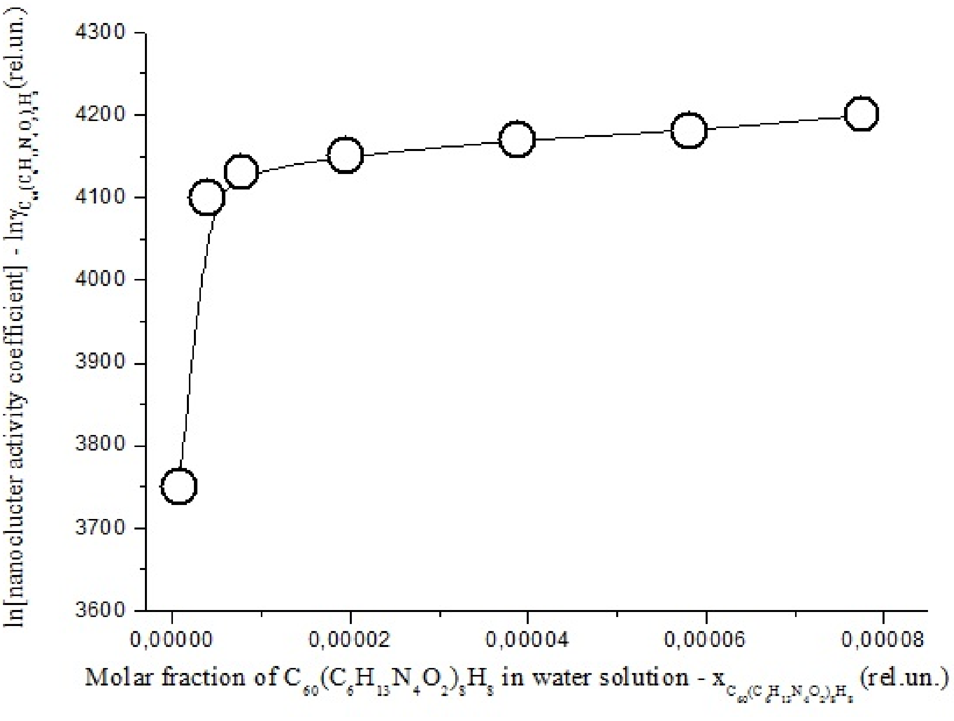

FIG. 7. The dependence of ln of $C_{60}(C_6H_{12}NaN_4O_2)_8H_8$ activity coefficients $(\ln\gamma_{\text{nanocluster}})$ in $C_{60}(C_6H_{12}NaN_4O_2)_8H_8$ – water solutions against the molar fraction of $C_{60}(C_6H_{12}NaN_4O_2)_8H_8$ in aqueous solutions

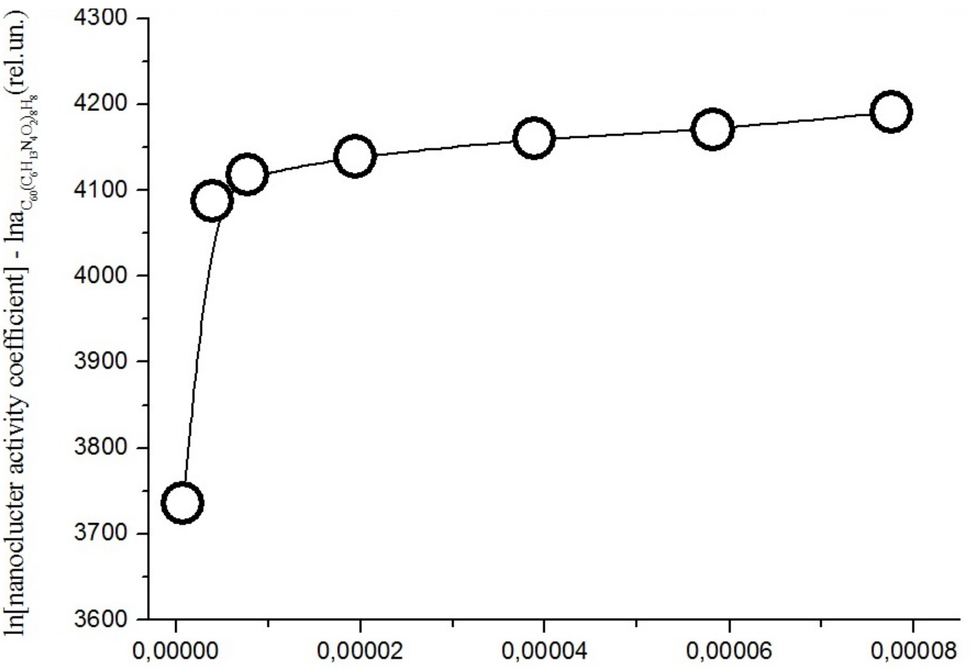

FIG. 8. The dependence of ln of $C_{60}(C_6H_{12}NaN_4O_2)_8H_8$ activity (lnananocluster) in $C_{60}(C_6H_{12}NaN_4O_2)_8H_8$ – water solutions against the molar fraction of $C_{60}(C_6H_{12}NaN_4O_2)_8H_8$ in aqueous solutions

$$G^{\text{mix}} = RT\left[x_{\text{nanocluster}}\ln a_{\text{nanocluster}} + x_{\text{H2O}}\ln a_{\text{H2O}}\right]. \tag{9}$$

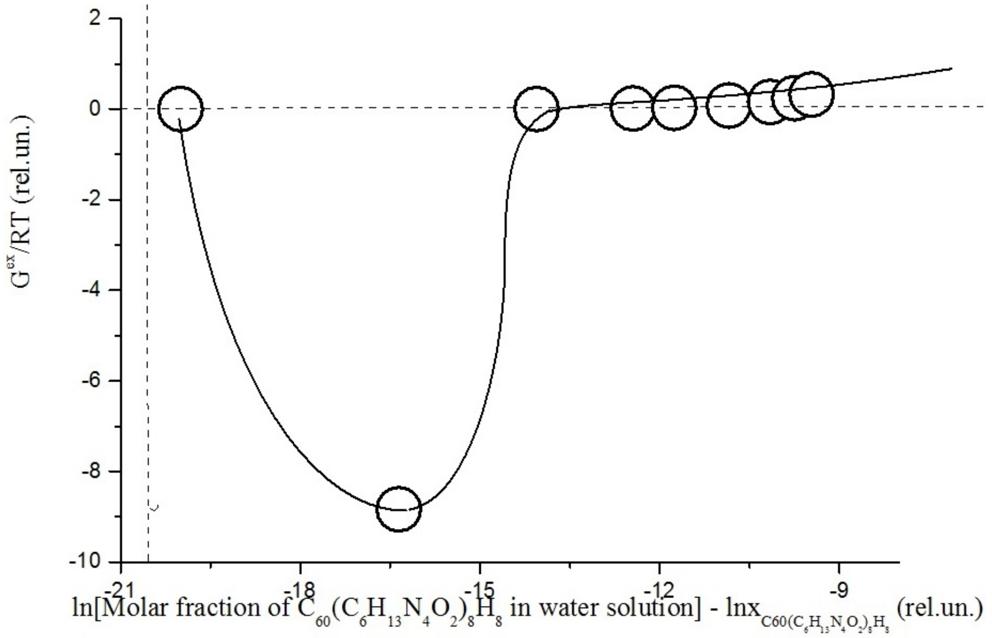

FIG. 9. The dependence of the excess Gibbs energy for solutions (G^{ex}) in $C_{60}(C_6H_{12}NaN_4O_2)_8H_8$ – water solutions against logarithm of molar fraction of $C_{60}(C_6H_{12}NaN_4O_2)_8H_8$ in aqueous solutions

One can see the inflection points in the Figs. 9, 10 where the second derivatives: $\left[\partial^2 G^{\text{mix}}/\partial x^2_{\text{nanocluster}}\right]_{T,P}$ and $\left[\partial^2 G^{\text{ex}}/\partial x^2_{\text{nanocluster}}\right]_{T,P}$ change signs or derivatives

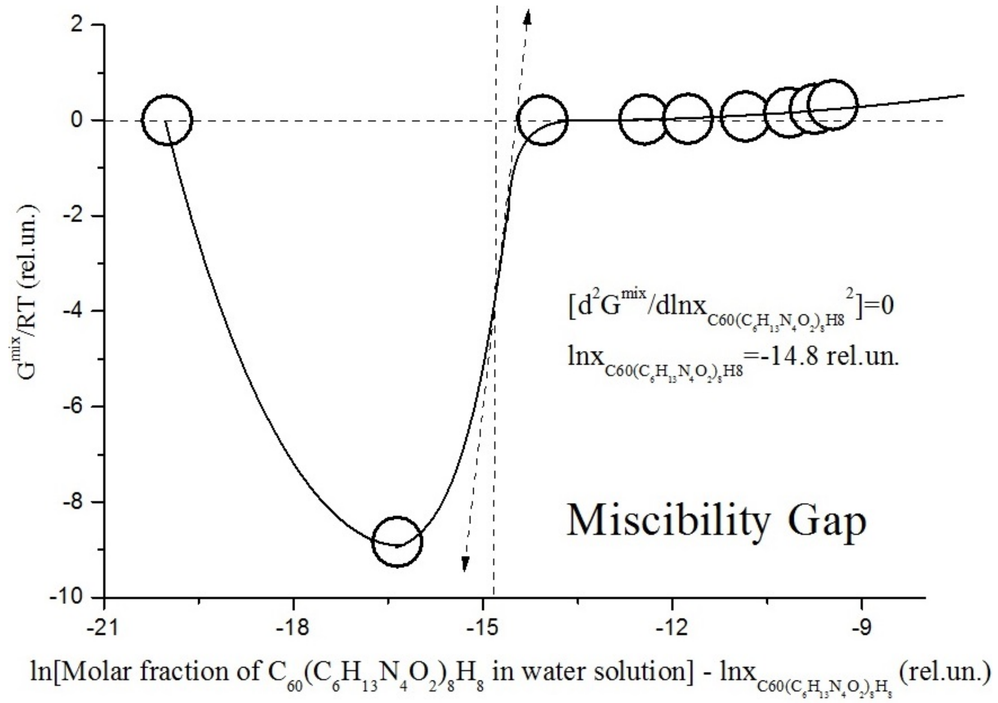

FIG. 10. The dependence of the Gibbs energy mixing for solutions (G^{mix}) and the miscibility gap in $C_{60}(C_6H_{12}NaN_4O_2)_8H_8$ – water solutions against logarithm of molar fraction of $C_{60}(C_6H_{12}NaN_4O_2)_8H_8$ in aqueous solutions

$\left[\partial^2 G^{\text{mix}}/\partial \mathrm{x}^2_{\text{nanocluster}}\right]_{T,P}$ and $[\partial^2 G^{\text{ex}}/\partial \mathrm{x}^2_{\text{nanocluster}}]_{T,P}$ cross through zero. Naturally, this fact takes place together with the crossing through zero of such functions: $\left[\partial^2 G^{\text{mix}}/\partial \ln(\mathrm{x}_{\text{nanocluster}})^2\right]_{T,P}$ and $[\partial^2 G^{\text{ex}}/\partial \ln(\mathrm{x}_{\text{nanocluster}})^2]_{T,P}$. Geometrically, this means that the convexity in the graph $G^e x(\mathrm{x}_{\text{nanocluster}})$ and $G^{\text{mix}}(\mathrm{x}_{\text{nanocluster}})$ is replaced by concavity. And, if the behavior of the first function – G^{ex} is arbitrarily, the sign of the derivation, $\left[\partial^2 G^{\text{mix}}/\partial \mathrm{x}^2_{\text{nanocluster}}\right]_{T,P}$, over the concentration range of diffusion stability, should be positive. Thus, we can consider that in the region $\mathrm{x}_{\text{nanocluster}} > 4 \cdot 10^{-7}$ rel.un. homogeneous solutions exfoliate and becomes micro-heterogeneous. Light scattering experiments show us that this occurs at the concentration region of the transition from the first type aggregates (the first order clusters of percolation) with the linear dimensions $d_1 \approx$ 20 – 80 nm to that of the second type aggregates (the second order clusters of percolation) with the linear dimensions $d_2 \approx$ 100 – 400 nm. In other words, there are the concentrations where the system transitions from a nano-heterogeneous one to that of a micro-heterogeneous type.

Acknowledgements

Investigations were supported by Russian Found of Basic Research – RFBR (Project No. 15-08-08438) and with the help of the equipment of Resource Center 'Geomodel' (St. Petersburg State University).

References

[1] K.N. Semenov, N.A. Charykov, I.V. Murin, Yu.V. Pukharenko. Physico-Chemical Properties of C_{60}-tris-malonic-derivative Water Solutions. *J. of Molecular Liquids*, 2015, **202**, P. 50–58.

[2] K.N. Semenov, N.A. Charykov, I.V. Murin, Yu.V. Pukharenko. Physico-chemical properties of the fullerenol-70 water solutions. *J. of Molecular Liquids*, 2015, **202**, P. 1–8.

[3] D.P. Tyurin, K.N. Semenov, et al. Dissociation of Fullerenol-d water solutions and their electric conductivity. *Rus. J. of Phys. Chem.*, 2015, **89** (5), P. 764–768.

[4] I.A. Pestov, V.A. Keskinov, et al. Solubility of $[C_{60}(=C(COOH))_2]_3$ in ternary system $[C_{60}(=C(COOH)_2)_3]$–$SmCl_{3-2}$ at 25 °C. *Rus. J. of Phys. Chem.*, 2015, **89** (6), P. 990–992.

[5] K.N. Semenov, N.A. Charykov, et al. Dependence of the dimension of the associates of water-soluble tris-malonate of light fullerene — $C_{60}[= C(COOH)_2]_3$ in water solutions at 25 °C. *Nanosystems: Physics, Chemistry, Mathematics*, 2015, **6** (2), P. 294–298.

[6] D.P. Tyurin, K.N. Semenov, et al. Dissociation of Fullerenol-70-d in Aqueous Solutions and Their Electric Conductivity. *Russian Journal of Physical Chemistry A*, 2015, **89** (5), P. 771–775.

[7] K.N. Semenov, I.G. Kanterman, et al. Solid–Liquid Phase Equilibria in the Fullerenol-d–$CuCl_2$–H_2O System at 25 °C. *Russian Journal of Physical Chemistry*, 2014, **88** (6), P. 1073–1076.

[8] K.N. Semenov, N.A. Charykov, et al. Synthesis and identification water-soluble tris-malonate of light fullerene – $C_{60}[(=C(COOH)_2]_3$. *Nanosystems: physics, chemistry, mathematics*, 2014, **5** (2), P. 315–319.

[9] K.N. Semenov, N.A. Charykov, et al. Volume properties of water solution and refraction at 25 °C water-soluble tris-malonate of light fullerene- C_{60} $[= C(COOH)_2]_3$. *Nanosystems: physics, chemistry, mathematics*, 2014, **5** (3), P. 427–434.

[10] K.N. Semenov, N.A. Charykov, et al. Poly-thermal solubility and complex thermal analysis of water-soluble tris-malonate of light fullerene – $C_{60}[= C(COOH)_2]_3$. *Nanosystems: physics, chemistry, mathematics*, 2014, **5** (3), P. 435–440.

[11] K.N. Semenov, I.G. Kanterman, et al. Solubility in the Ternary System Fullerenol-d–Uranyl Sulfate–Water at 25 °. *Radiokhimiya*, 2014, **56** (5), P. 493–495.

[12] K.N. Semenov, N.A. Charykov, et al. Concentration dependence of electric conductivity and pH for aqueous solutions of water soluble light fullerene C_{60} $[= C(COOH)_2]_3$ trismalonate. *Nanosystems: physics, chemistry, mathematics*, 2014, **5** (5), P. 709–717.

[13] K.N. Semenov, N.A. Charykov, et al. Fullerenol-d Solubility in Fullerenol-d–Inorganic Salt–Water Ternary Systems at 25 °C. *Industrial & Engineering Chemistry Research*, 2013, **52**, P. 16095–16100.

[14] K.N. Semenov, N.A. Charykov, V.A. Keskinov. Fullerenol Synthesis and Identification. Properties of the Fullerenol Water Solutions. *J. Chem. Eng. Data*, 2011, **56**, P. 230–239.

[15] K.N. Semenov, N.A Charykov. Solubility of light fullerenes and fullerenol in biocompatible with human beings solvents. Chapter in Handbook: *Grapes: Cultivation, Varieties and Nutritional Uses*. Nova Sciences Publishers, Inc., Editor R.P. Murphy et al., 2011, P. 1–48.

[16] K.N. Semenov, N.A. Charykov. Phase Equilibria in the Fullerene Containing Systems. *Handbook on Fullerene: Synthesis, Properties and Applications*, Editor R.F. Verner, C. Benvegny, 2012, P. 1–91.

[17] K.N. Semenov, N.A. Charykov. *Solubility of light fullerenes and it's derivatives*. Germany: Lambert Academic Publishing, 2011, 237 p.

[18] L.B. Gan, C.P. Luo. Water-soluble fullerene derivatives, synthesis and characterization of β-alanine C_{60} adducts. *Chinese Chemical letters*, 1994, **5** (4), P. 275–278.

NANOSYSTEMS: PHYSICS, CHEMISTRY, MATHEMATICS, 2015, 6 (5), P. 726–732

Stabilization of water-in-oil emulsions with complex of silica particles and hexylamine

A. V. Nushtaeva

Penza State University of Architecture and Construction,
Physics and Chemistry, Penza, Russia

nushtaeva.alla@yandex.ru

PACS 82.70.Kj, 68.05.-n, 68.08.-p **DOI 10.17586/2220-8054-2015-6-5-726-732**

The properties of emulsions stabilized by complexes of silica particles with hexylamine are analyzed. It is shown that water-in-oil emulsions were obtained only if the hexylamine volume fraction was greater than that of the silica (Aerosil) volume fraction in the aqueous phase. So, in the case of water-in-oil emulsions, hexylamine is a completely equivalent co-stabilizer together with silica, rather than just a solid surface modifier. It is assumed that at high concentrations this short-chain surfactant, together with silica, forms hybrid organic-inorganic particles that are attached at the oil/water interface and promotes the formation of oil droplets in the water.

Keywords: solid particles, solid-stabilized emulsions, oil-in-water emulsions, hybrid particle.

Received: 23 January 2015

1. Introduction

Solid particles have been recently widely applied alone or together with surfactants for the stabilization of emulsions [1–8] and foams [9–13]. Solid-stabilized emulsions and foams differ from classical surfactant-stabilized systems in that they have some specific properties: (1) extremely high stability; (2) specific rheological properties connected with the structure formation at the interface and in the liquid continuous phase. Micrometer-sized hollow clusters (colloidosomes) are obtained from the solid-stabilized drops [14, 15]. Such emulsions are used as a template for creating nano-microporous materials [16, 17].

Solid particles are considered to be the main stabilizers in an surfactant-solids emulsifying complex, while the surfactant is considered to be a co-stabilizer or modifier. It is usually assumed that the role of surfactant is to reduce the hydrophobicity the particle's surface. For example, cationic surfactants are easily adsorbed at the surface of silica, which is negatively charged in the presence of water. As a result, the silica particle's surface is modified by organic molecules orienting with their hydrophobic hydrocarbon radicals out toward the water. As a result, the surface charge decreases and the contact angle θ increases. The modified solid particles are attached more strongly at the interface, forming a compact protective interlayer.

A short-chain surfactant hexylamine was used together with silica to stabilize emulsions and foams [8, 10–13, 18–21]. Hexylamine adsorption at the silica particle's surface leads to an increase in the contact angle of wetting by water [12, 13] and the angle of selective wetting at the oil/water interface [20, 21] and hence, to an increase in the stability of emulsions and foams. In the case of emulsions, the growing concentration of hexylamine even leads to a phase inversion which correlates with the contact angle inversion [20, 21].

Using hexylamine-silica complex, we obtained extremely stable emulsions of both types: direct (oil-in-water, O/W) and reverse (water-in-oil, W/O) [18, 19]. At higher silica concentrations, the emulsions did not separate, even when sitting for several months [8].

The aim of this study was to compare the results of applying short-chain (hexylamine) and long-chain surfactants (cetyltrimethylammonium bromide) as co-stabilizers with solid particles and to clarify the role of hexylamine in stabilizing the complex.

2. Materials and methods

2.1. Materials

Different types of silica were used as solid stabilizer: 1) fumed silica powder – Aerosil A-200 and A-380 with specific surface area of 200 and 380 m^2/g respectively; 2) Ludox HS-40 – 40 % suspension in water with surface area of 220 m^2/g; 3) hydrolytic silica S-3 with the particle radius 230 nm obtained via the hydrolysis of silicon esters in an alcoholic medium by the Stober method [22].

The surfactants used as a co-stabilizer were hexylamine and cetyltrimethylammonium bromide (CTAB).

Distilled water was used as the aqueous phase for the preparation of suspension of silica and emulsions.

Saturated hydrocarbons (heptane and decane) or diesel fuel were used as the organic phase for emulsion.

2.2. Preparation and characterization of emulsions

The emulsions were obtained by shaking the organic and aqueous phases containing silica and surfactant in a test tube. An emulsion was considered to be stable if it did not separate into distinct phases over the course of a day or more.

2.3. Determination of silica aggregate size

The silica aggregate size was determined by turbidimetric analysis of a 0.1 % aqueous suspension of silica.

In the case of the turbidimetric method, the optical density D was measured using a photometer at the analytical wavelength λ = 590 nm and a cuvette length L = 3.011 cm immediately after shaking. The turbidity τ and characteristic turbidity $[\tau]$ were calculated as follows:

$$\tau = \frac{2.303D}{L}, \quad [\tau] = \frac{\tau}{v_{\mathrm{Hex}}}. \tag{1}$$

A characteristic $\varphi(z)$ [23] was calculated from value $[\tau]$:

$$\varphi(z) = \frac{[\tau]\,\lambda}{\alpha^2}, \tag{2}$$

where $\alpha = \frac{3}{4\pi}\left|\frac{m^2-1}{m^2+2}\right|$ is a parameter containing ratio $m = n_{\mathrm{d}}/n_{\mathrm{H_2O}}$ of refractive index of dispersed phase n_{d} = 1.45 (silica) and medium $n_{\mathrm{H_2O}}$ = 1.333.

A table in [23] contains pairs of values $\varphi(z)$ and z. We found the theoretical value $\varphi(z)_{\mathrm{theor}}$ nearest to the experimentally obtained value $\varphi(z)_{\mathrm{exp}}$ and calculated magnitude z by formula:

$$z_{\mathrm{exp}} = \frac{\varphi(z)_{\mathrm{exp}} \cdot z_{\mathrm{theor}}}{\varphi(z)_{\mathrm{theor}}}. \tag{3}$$

The average radius of the silica aggregate was equal to:

$$R = \frac{z\lambda}{8\pi}. \tag{4}$$

2.4. Determination of hexylamine droplet size

The size of hexylamine droplets dispersed in water was determined via a turbidimetric method at hexylamine concentrations ranging from 0.003 – 0.151 mol/L.

Optical density D was measured using a photometer at the following values: λ = 340 nm and L = 3.011 cm immediately after shaking. Characteristic turbidity $[\tau]$, parameters $\varphi(z)$, z and the average droplet radius of hexylamine were calculated by equations (1) – (4). Refractive index for hexylamine was accepted n_d = 1.375 (as for hexane).

3. Results and discussion

It has been found experimentally that amount of short-chain surfactant like hexylamine required to form emulsions (in complex with silica) is large enough compared to amount of long-chain surfactant like CTAB (Table 1). Here, the relative concentration of co-stabilizer n_s (mol/g) was calculated as:

$$n_\mathrm{s} = \frac{\mathrm{C_s}}{\mathrm{C_{SiO_2}}},$$

where $\mathrm{C_s}$ is the initial concentration of surfactant, mol/L; $\mathrm{C_{SiO_2}}$ is silica concentration, g/L. The volume fraction of oil during the shaking was equal $\varnothing_\mathrm{oil}$ = 0.5 or $\varnothing_\mathrm{oil}$ = 0.33 for the desired formation of direct emulsions and $\varnothing_\mathrm{oil}$ = 0.66 for the desired formation of reverse emulsions.

TABLE 1. Comparison of the relative concentrations of hexylamine and CTAB required to form O/W and W/O emulsions

Type and concentration of silica, % (mass)	Type and volume fraction of oil	Type and relative concentration of surfactant n_s, mol/g	
		Lower boundary of O/W	Lower boundary of W/O
		hexylamine	
1% erosil-380	decane, $\varnothing_\mathrm{oil} = 0.5$	0.002	0.014
2% erosil-380		0.001	0.010
3% erosil-380		$3 \cdot 10^{-4}$	0.007
		CTAB	
2% erosil-200	diesel fuel, $\varnothing_\mathrm{oil} = 0.33$ and $\varnothing_\mathrm{oil} = 0.66$	$5 \cdot 10^{-7}$	$7 \cdot 10^{-6}$
2% Ludox-HS-40	heptane, $\varnothing_\mathrm{oil} = 0.5$	$5 \cdot 10^{-6}$	—
3 % S-3	heptane, $\varnothing_\mathrm{oil} = 0.33$ and $\varnothing_\mathrm{oil} = 0.66$	$1 \cdot 10^{-6}$	$4.6 \cdot 10^{-6}$

The emulsions O/W and W/O had been achieved at relative concentrations of hexylamine which were 3 orders of magnitude higher than the relative concentrations of CTAB because the short-chain hydrophobicizer is required in larger amounts to achieve the definite contact angle value.

For the silica-CTAB complex, the maximum angle θ was equal to 53 ° (the water receding angle) [7] and the W/O emulsions could be obtained only if the oil volume fraction was dominant at the CTAB concentration $(1 - 5)\cdot 10^{-4}$ mol/L. At higher concentrations, CTAB itself stabilizes the O/W emulsion in competition with solids, moreover CTAB forms a second adsorption layer which is oriented with hydrophilic groups toward the water and the contact angle again decreases [24]. Therefore, the phase inversion region and even more the W/O emulsion instability region were not achieved in the case of CTAB.

As for hexylamine, increasing the concentration to n_s = 0.004 – 0.014 mol/g (for 1 – 5 % silica) caused an inversion of the contact angle (from $\theta < 90$ ° to $\theta > 90$ °) [20] and conversion from O/W to W/O emulsions. Increasing the hexylamine concentration to n_s = 0.01 – 0.02 mol/g resulted in a contact angle θ value that was approximately 180 ° [20] and the W/O emulsions became instable. Apparently, the second and subsequent adsorption layers of hexylamine on the silica surface are not oriented. This may explain the increasing contact angle to the point of practically complete hydrophobicity and loss of emulsion stability.

If CTAB is highly soluble in water, then hexylamine is poorly soluble. In the case of hexylamine-silica-stabilized emulsions, the aqueous phase is a three-phase system that contains solid particles of silica and liquid droplets of hexylamine.

When hexylamine and silica concentrations were expressed in terms of volume fractions in the aqueous phase (taking into account the density of silica 2.2 g/cm^3 and of hexylamine 0.766 g/cm^3), their magnitudes were comparable (Table 2). Moreover, W/O emulsions were formed when the volume fraction of hexylamine υ_{Hex} exceeded the volume fraction of the solids υ_{SiO_2}.

TABLE 2. The boundaries of the emulsion stability region for complex Aerosil-hexylamine at $\varnothing_{\text{oil}} = 0.5$ (decane)

υ_{SiO2}, % (vol)	υ_{Hex}, % (vol)		
	Lower boundary of O/W	Phase inversion	Upper boundary of W/O
0.5	0.26	1.32 – 1.85	2.77
0.9	0.26	1.85 – 2.64	4.62
1.4	0.13	1.85 – 2.64	5.28
2.3	0.07	1.85 – 2.64	6.60
3.3	0.04	2.77 – 3.70	6.60

Therefore, in W/O emulsions, hexylamine is a completely equivalent stabilizer together with silica, rather than simply a solid surface modifier.

Note also that in our experiment, a short-lived W/O emulsion was formed at shaking of hexylamine-water system with decane. The life-time of such emulsion was only a few seconds, but it showed a trend: colloidal droplets of hexylamine have the 'ability' to stabilize the W/O emulsion.

Silica particles with initial sizes of a few nanometers always formed stable aggregates in powder or in water alone [25]. The average radius of Aerosil A-380 aggregates used in experiments with hexylamine was 38 ± 5 nm.

As hexylamine is almost insoluble in water, so turbidimetric analysis of the hexylamine-water binary system was carried out to determine the size of hexylamine droplets dispersed in water.

There was linear growth of the turbidity of the system from 0.067 to 1.635 cm^{-1} with increasing concentrations. However, the characteristic turbidity calculation showed that hexylamine droplet radius remained constant $R = 45 \pm 8$ nm regardless of the concentration (Fig. 1). The average radius of Aerosil A-380 aggregates, also determined by characteristic turbidity, was 38±5 nm. Thus, the hexylamine droplet had a similar size to the silica aggregate.

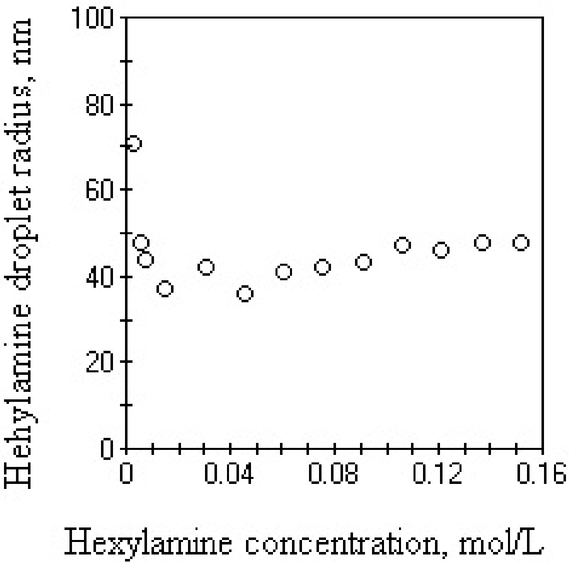

FIG. 1. Radius of hexylamine droplets in hexylamine-water binary system

Thus, the hexylamine-water system is a nanoemulsion. However, this system is not stable, unlike thermodynamically stable nanoemulsions with very low interfacial tension 10^{-2} – 10^{-5} mN/m [26]. Hexylamine constitutes a separate a bulk layer which becomes visible at a concentration of 0.151 mol/L. Instability of the association arises from the large interfacial tension between water and hexylamine, approximately 50 mN/m [10].

Accordingly, hexylamine's role appears to be not only in surface hydrophobization. We suggest that at high concentrations, this surfactant forms a hybrid organic-inorganic particle together with silica (Fig. 2) and the attachment of such hybrid particles at the decane/water interface promotes formation of oil droplets in the aqueous phase.

4. Conclusion

The amount of short-chain hexylamine required to form emulsions together with silica is large compared to the amount of long-chain surfactant. W/O emulsions were formed when the volume fraction of hexylamine exceeded that of the solid particles. It is assumed that at high concentrations, this surfactant and silica form hybrid organic-inorganic 'particle' which promotes the formation of oil droplets in water.

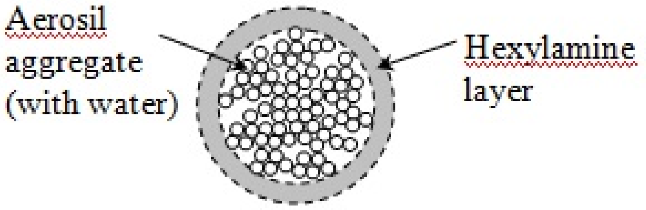

FIG. 2. Assumed scheme of hybrid particle formed in the ternary system silica-hexylamine-water at high concentration of hexylamine

References

[1] Aveyard R., Binks B.P., Clint J. Emulsions stabilized by solely colloidal parti-cles. *Adv. Colloid Interface Sci.*, 2003, **100–102**, P. 503–546.

[2] Binks B.P., Murakami R. Phase inversion of particle-stabilized materials from foams to dry water. *Nature Materials*, 2006, **5**, P. 865–869.

[3] Horozov T.S., Aveyard R., Clint J., Neumann B. Particle zips: vertical emul-sion films with particle monolayers at their surfaces. *Langmuir*, 2005, **21**, P. 2330–2341.

[4] Yan N., Gray M.R., Masliyah J.H. On water-in-oil emulsions stabilized by fine solids. *Colloids and Surfaces. A: Physicochem. Engineering Aspects*, 2001, **193**, P. 97–107.

[5] Abend S., Lagaly G. Bentonite and double hydroxides as emulsifying agents. *Clay Minerals*, 2001, **36**, P. 557–570.

[6] Tcholakova S., Denkov N.D., Lips A. Comparison of solid particles, globular proteins and surfactants as emulsifiers. *Phys. Chem. Chem. Phys.*, 2008, **10** (12), P. 1608–1627.

[7] Kruglyakov P.M., Nushtaeva A.V. Emulsion stabilized by solid particles: in-fluence of the capillary pressure. In: *Emulsions: Structure, Stability and Inter-actions*, D.N. Petsev (Ed.). Elsevier, Amsterdam, 2004, P. 641–676.

[8] Nushtaeva A.V., Shumkina A.V., Kruglyakov P.M., Elaneva S.I. Effect of Aqueous Phase Structuring on the Properties of Model Emulsion Films Stabi-lized with Solid. *Colloid Journal*, 2011, **73** (6), P. 821–829.

[9] Alargova R.G., Warhadpande D.S., Velev O.D., Paunov V.N. Foam superstabilization by polymer microrods. *Langmuir*, 2004, **20** (24), P. 10371–10374.

[10] Gonzenbach U.T., Studart R.R., Tervoort E., Gauker L.J. Ultrastable particle-stabilised foams. *Angew. Chem. Int. Ed. Engl.*, 2006, **43**, P. 3526–3530.

[11] Gonzenbach U.T., Studart R.R., Tervoort E., Gaukler L.J. Tailoring the mi-crostructure of particle-stabilized wet foams. *Langmuir*, 2007, **23**, P. 1025–1032.

[12] Kruglyakov P.M., Elaneva S.I., Vilkova N.G. About mechanism of foam stabi-lization by solid particles. *Adv. Colloid and Interface Sci.*, 2011, **165**, P. 108–118.

[13] Vilkova N.G., Elaneva S.I., Karakashev S.I. The hexylamine concentration influence on the properties of the foams and foam films stabilized by Ludox. *Mendeleev Commun.*, 2012, **22**, P. 227–228.

[14] Dinsmore A.D., Hsu M.F., et al. Colloidosomes: selectively permeable capsules composed of colloidal particles. *Science*, 2002, **298**, P. 1006–1009.

[15] Mao Zh., Xu H., Wang D. Molecular mimetric self-assembly of colloidal parti-cles. *Advanced Functional Materials*, 2010, **20** (7), P. 1053–1074.

[16] Simovic S., Heard P., Prestidge C.A. Hybrid lipid-silica microcapsules engi-neered by phase coacervation of Pickering emulsions to enhance lipid hydroly-sis. *Phys. Chem. Chem. Phys.*, 2010, **12**, P. 7162–7170.

[17] Wong C.H., Tervoort E., et al. Macroporous polymers from particle-stabilized foams. *J. Ma-ter. Chem.*, 2009, **19**, P. 5129–5133.

[18] Nushtaeva A.V., Shumkina A.V. Properties of emulsion and free emulsion (aqueous) films stabilized with hexylamine-modified silica. *Colliod Journal*, 2013, **75** (3), P. 326–332.

[19] Nushtaeva A.V. Stabilization of emulsions and emulsion films by silica with hexylamine. *Mendeleev Commun.*, 2012, **22** (4), P. 225–226.

[20] Nushtaeva A.V. Contact angles of selective wetting of hexylamine-modified silica. *Colloids and Surfaces A: Physicochem. Engineering Aspects*, 2014, **451**, P. 101–106.

[21] Nushtaeva A.V., Vilkova N.G., Mishina S.I. The effect of modifier concentration on the stability of emulsions and foams stabilized with colloidal silica particles. *Colloid Journal*, 2014, **76** (6), P. 717–724.

[22] Stöber W., Fink A., Bohn E. Controlled growth of monodisperse silica spheres in the micron size range. *J. Colloid Interface Sci.*, 1968, **26**, P. 62–69.

[23] Grigorov O.N., Karpova I.F., et al. *Guide to practical work on colloidal chemistry*, Khimia, Moscow, 1964. [In Russian]

[24] Churaev N.V., Sobolev V.D. Physical chemistry of wetting phenomena. In: *Colloid Stability: The role of surface forces*, Part II, T.F. Tadros (Ed.), Wiley-VCH Verlag GmbH and Co. KGaA, Weinheim, Germany, 2007, P. 127–152.

[25] Iler R.K. *The chemistry of silica: solubility, polymerization, colloid and surface properties, and biochemistry*. Wiley-Interscience, 1979, 866 p.

[26] Tadros Th.F., Vincent B. Emulsion stability. In: *Encyclopedia of Emulsion Technology*. P. Becher (Ed.), Marcel Dekker, New York, 1983, P. 129–285.

NANOSYSTEMS:

PHYSICS, CHEMISTRY, MATHEMATICS

INFORMATION FOR AUTHORS

The journal publishes research articles and reviews, and also short scientific papers (letters) which are unpublished and have not been accepted for publication in other magazines. Articles should be submitted in English. All articles are reviewed, then if necessary come back to the author to completion.

The journal is indexed in Chemical Abstract Service of the American Chemical Society and in Russian Scientific Citation Index.

Author should submit the following materials:

1. Article file in English, containing article title, the initials and the surname of the authors, Institute (University), postal address, the electronic address, the summary, keywords, MSC or PACS index, article text, the list of references.
2. Files with illustrations, files with tables.
3. The covering letter in English containing the article information (article name, MSC or PACS index, keywords, the summary, the literature) and about all authors (the surname, names, the full name of places of work, the mailing address with the postal code, contact phone number with a city code, the electronic address).
4. The expert judgement on possibility of publication of the article in open press (for authors from Russia).

Authors can submit a paper and the corresponding files to the following addresses: nanojournal.ifmo@gmail.com, popov1955@gmail.com.

Text requirements

Articles should be prepared with using of text editors MS Word or LaTEX (preferable). It is necessary to submit a pdf copy. In the name of files the English alphabet is used. The recommended size of short communications (letters) is 4-6 pages, research articles – 6-15 pages, reviews – 30 pages.

Recommendations for text in MS Word:

Formulas should be written using Math Type. Figures and tables with captions should be inserted in the text. Additionally, authors present separate files for all figures and Word files of tables.

Recommendations for text in LaTex:

Please, use standard LaTex without macros and additional style files. The list of references should be included in the main LaTex file. Single LaTex file of the paper with the corresponding pdf file should be submitted.

References in the article text are given in square brackets. The list of references should be prepared in accordance with the following samples:

[1] N. Surname. *Book Title*. Nauka Publishing House, Saint Petersburg, 2000, 281 pp.

[2] N. Surname, N. Surname. Paper title. *Journal Name*, 2000, **1**(5), P. 17-23.

[3] N. Surname, N. Surname. Lecture title. In: Abstracts/Proceedings of the Conference, Place and Date, P. 17-23, 2000.

[4] N. Surname, N. Surname. Paper title (2010). URL: http://books.ifmo.ru/ntv.

[5] N. Surname, N. Surname. Patent Name. Patent No. 11111, Bul. No. 33, 5 pp., 2010.

[6] N. Surname, N. Surname. Thesis Title. Thesis for full doctor degree in math. and physics, Saint Petersburg, 105 pp., 2000.

Requirements to illustrations

Illustrations should be submitted as separate black-and-white files. Formats of files – jpeg, eps, tiff.

N A N O
Ф&Х&М

NANOSYSTEMS:

PHYSICS, CHEMISTRY, MATHEMATICS

Журнал зарегистрирован
Федеральной службой по надзору в сфере связи, информационных технологий и массовых коммуникаций
(свидетельство ПИ № ФС 77 - 49048 от 22.03.2012 г.)
ISSN 2220-8054

Учредитель: федеральное государственное автономное образовательное учреждение высшего образования
«Санкт-Петербургский национальный исследовательский университет информационных технологий, механики и оптики»

Издатель: федеральное государственное автономное образовательное учреждение высшего образования
«Санкт-Петербургский национальный исследовательский университет информационных технологий, механики и оптики»

Отпечатано в Учреждении «Университетские телекоммуникации»
Адрес: 197101, Санкт-Петербург, Кронверкский пр., 49

Подписка на журнал НФХМ
На первое полугодие 2016 года подписка осуществляется через
ОАО Агентство «Роспечать»
Подписной индекс 57385 в каталоге «Издания органов научно-технической информации»